

AD _____

Award Number: DAMD17-00-1-0443

TITLE: A Multileaf Collimator for Modulated Electron Radiation
Therapy for Breast Cancer

PRINCIPAL INVESTIGATOR: Yulin Song

CONTRACTING ORGANIZATION: Stanford University
Stanford, CA 94305-5401

REPORT DATE: April 2003

TYPE OF REPORT: Annual Summary

PREPARED FOR: U.S. Army Medical Research and Materiel Command
Fort Detrick, Maryland 21702-5012

DISTRIBUTION STATEMENT: Approved for Public Release;
Distribution Unlimited

The views, opinions and/or findings contained in this report are those of the author(s) and should not be construed as an official Department of the Army position, policy or decision unless so designated by other documentation.

Best Available Copy

20040503 031

REPORT DOCUMENTATION PAGEForm Approved
OMB No. 074-0188

Public reporting burden for this collection of information is estimated to average 1 hour per response, including the time for reviewing instructions, searching existing data sources, gathering and maintaining the data needed, and completing and reviewing this collection of information. Send comments regarding this burden estimate or any other aspect of this collection of information, including suggestions for reducing this burden to Washington Headquarters Services, Directorate for Information Operations and Reports, 1215 Jefferson Davis Highway, Suite 1204, Arlington, VA 22202-4302, and to the Office of Management and Budget, Paperwork Reduction Project (0704-0188), Washington, DC 20503

1. AGENCY USE ONLY (Leave blank)		2. REPORT DATE April 2003	3. REPORT TYPE AND DATES COVERED Annual Summary (1 Apr 2000 - 31 Mar 2003)	
4. TITLE AND SUBTITLE A Multileaf Collimator for Modulated Electron Radiation Therapy for Breast Cancer			5. FUNDING NUMBERS DAMD17-00-1-0443	
6. AUTHOR(S) Yulin Song				
7. PERFORMING ORGANIZATION NAME(S) AND ADDRESS(ES) Stanford University Stanford, CA 94305-5401 E-Mail: yulin@reyes.stanford.edu			8. PERFORMING ORGANIZATION REPORT NUMBER	
9. SPONSORING / MONITORING AGENCY NAME(S) AND ADDRESS(ES) U.S. Army Medical Research and Materiel Command Fort Detrick, Maryland 21702-5012			10. SPONSORING / MONITORING AGENCY REPORT NUMBER	
11. SUPPLEMENTARY NOTES Original contains color plates: ALL DTIC reproductions will be in black and white				
12a. DISTRIBUTION / AVAILABILITY STATEMENT Approved for Public Release; Distribution Unlimited				12b. DISTRIBUTION CODE
13. ABSTRACT (Maximum 200 Words) Irradiation is an effective adjuvant therapy to lumpectomy, mastectomy, and chemotherapy for breast cancers of different stages. However, the conventional tangential photon beam treatment has two major limitations. Firstly, part of the lung and heart (in the case of the left breast treatment) may be exposed to high radiation dose. Secondly, the contralateral breast may receive a significant amount of scatter dose. Consequently, irradiation-related complications such as arm edema, myocardial infarction, severe breast fibrosis, and secondary breast cancer may occur in the patients who have undergone conventional photon beam treatment. To reduce radiation dose to normal structures, we have investigated treating breast cancers using MERT. To deliver MERT plans effectively, we designed and manufactured a prototype EMLC based on the results of Monte Carlo simulations and a Varian 25 x 25 cm ² electron applicator. The performance of the EMLC was experimentally evaluated and the results were compared with those of Monte Carlo simulations and a PMLC. We have also developed a complete system of Monte Carlo-based inverse treatment planning system for MERT plans. The system incorporates the Monte Carlo simulated electron pencil beams into the inverse planning process. Additionally, we have characterized the EMLC using a multiple-source beam model for fast Monte Carlo simulation. Furthermore, we have also studied the effect of beam delivery on optimized modulated electron radiation therapy plans in the final dose calculation.				
14. SUBJECT TERMS Modulated Electron Radiation Therapy (MERT), Multileaf Collimator (MLC), Electron Multileaf Collimator EMLC				15. NUMBER OF PAGES 176
				16. PRICE CODE
17. SECURITY CLASSIFICATION OF REPORT Unclassified	18. SECURITY CLASSIFICATION OF THIS PAGE Unclassified	19. SECURITY CLASSIFICATION OF ABSTRACT Unclassified	20. LIMITATION OF ABSTRACT Unlimited	

Table of Contents

Cover.....	1
SF 298.....	2
Table of Contents.....	3
Introduction.....	4
Body.....	7
Key Research Accomplishments.....	29
Reportable Outcomes.....	31
Conclusions.....	35
References.....	36
Appendices.....	38

1. INTRODUCTION

For many years, breast cancer has been the second most common disease for women in the United States. On average, one out of seven females will be diagnosed with breast cancer during their lifetimes. Currently, radiation therapy is still one of the most effective treatment modalities for all stages of localized breast cancer. Especially for early stage (T1 – T2) patients, breast conservation with lumpectomy followed by irradiation has been very successful. At present time, the most widely used radiotherapy technique for treating breast cancer consists of two opposed tangential photon fields. However, this technique has three major limitations. First of all, part of the lung and heart (in the case of the left breast treatment) may be exposed to a high radiation dose due to tumor location, patient size or in the case of chest-wall treatment. Secondly, because of lack of electron build-up in a photon beam, the skin surface receives a low dose. Thirdly, the contralateral breast may receive a significant amount of scatter dose. Consequently, irradiation-related complications such as arm edema, myocardial infarction, severe breast fibrosis, and secondary breast cancer may occur in the patients who have undergone conventional photon beam treatment.

The state of the art computer-controlled medical linear accelerators and multi-leaf collimators (MLCs) have become widely available now. These, combined with newly developed intensity modulated radiation therapy (IMRT) treatment planning systems (TPS), provide significant improvement in the delivery and control of external beam radiation through beam-intensity modulation. Although the photon beam IMRT is a powerful tool for treating the tumors that extend deeply into tissue below the skin surface, it is not suitable for treating very shallow targets like breast cancers due to the low surface doses and large depth of photon beam penetration. For photon beam IMRT, the slow attenuation of photon beams can still deliver a significant dose to the critical structures that are far from the target. Thus, using photon beam IMRT, the problem one above may be significantly improved, but problem two will remain, and problem three

may become more serious as treatment time increases with the number of segments and fields used (increase leakage or scattering dose).

A promising alternative approach is modulated electron radiation therapy (MERT) (1, 2). The rapid dose falloff of electron beams makes electron therapy an attractive treatment modality for some shallow targets like breast cancers. In addition, compared to photon beams, electron beams have negligible scatter radiation. Furthermore, because MERT mainly uses normal incident electron beams, it is less affected by patient's respiration as compared with tangential photon beams. Conceptually, each MERT plan consists of multiple ports (gantry angles) with different electron energies (energy modulation) and optimized beam intensity (intensity modulation). Dose conformity in the depth direction may be achieved by electron energy modulation, which is unique to MERT. Dose conformity and uniformity in the lateral direction may be achieved by intensity modulation using an electron-specific MLC (EMLC). Through both intensity and energy modulations, MERT is capable of delivering highly conformal doses to targets with complex shapes and of sparing surrounding normal tissue, particularly, the distal critical structures. Thus, it is expected that with MERT, problem one may be significantly improved and problems two and three can be completely eliminated due to the nature of electron beams.

However, because of severe electron in-air scattering, the conventional photon beam MLC (PMLC) is not suitable for the delivery of MERT plans. An electron beam collimated by a PMLC has a relatively large penumbra (3) due to the location and the thickness of the PMLC. A PMLC is normally located at a large distance (40 ~ 60 cm) from the patient skin surface. As an example, out of the most popular medical linear accelerators, the distance from the leaf bottom to the isocenter is 46.1 cm for Varian CLINAC 2100C, 62.7 cm for Elekta SL 75-5, and 62.1 cm for Siemens Digital Mevatron. When electrons travel this long distance from the PMLC to the patient skin, the beam penumbra will be broadened and the useful sharpness of the beam edge will be smeared

out due to the extended electron source and in-air multiple scattering (4). The thickness of a PMLC is optimized to minimize the leakage dose for photon beams (5). The leaf thickness is 6.13 cm for Varian CLINAC 2100C, 7.5 cm for Elekta SL 75-5, and 7.6 cm for Siemens Digital Mevatron. According to a study by Ebert and Hoban (6), the amount of electrons scattered from the end or side of an MLC leaf is proportional to the area irradiated by the beam. For thick leaves, large areas of leaf ends and sides will be exposed to the electron beam, and will therefore produce a large amount of scattered electrons into the beam, which will broaden the beam penumbra.

To deliver MERT plans effectively, we designed and manufactured a prototype EMLC based on the results of Monte Carlo simulations and a conventional Varian 25 x 25 cm² electron applicator (Varian Medical Systems, Palo Alto, CA). Based on the manufacturer's specifications of the beam production system and the EMLC design, electron beams collimated by this EMLC were simulated for a Varian CLINAC 2100C linear accelerator using the EGS4/BEAM code (7, 8). In addition, the EMLC was also experimentally evaluated using various methods.

The goals of this **Post-doctoral Traineeship** were two-fold. The first one was to provide the PI with a valuable opportunity to learn and apply modern radiotherapy techniques to breast cancer treatment and to train the PI for a career as a breast cancer research scientist and a radiation oncology physicist. The second goal was to simulate, design, manufacture, and evaluate a prototype EMLC specifically for the delivery of MERT plans. The project had four specific aims:

1. *Design an EMLC using the Monte Carlo simulation.*

The EGS4/BEAM Monte Carlo system and the source model developed in our lab (9) were used to simulate EMLCs with various leaf materials and geometric configuration. The optimal EMLC configuration was determined according to the clinical requirements, which included the minimum beam penumbra, maximum beam flatness, and minimum

radiation leakage produced by the EMLC and the minimum weight, size, and manufacturing cost of the EMLC.

2. Manufacture a prototype EMLC for MERT

A manually driven prototype EMLC was manufactured at our machine shop based on the optimal configuration determined by the Monte Carlo simulations. A fully functional computer-controlled EMLC was beyond the scope of this project due to its technical complexity, manufacturing cost, and time requirement.

3. Develop special software required for the use of EMLC

Monte Carlo simulated electron pencil beams collimated by the EMLC was incorporated into the inverse treatment planning process. An existing photon leaf sequence algorithm was modified specifically for the EMLC. The EMLC was modeled and incorporated into our multiple-source beam model for Monte Carlo simulation. The final dose delivered using the EMLC for the optimized plan was calculated using the Monte Carlo method.

4. Evaluate the functionality of the EMLC

Extensive experimental measurements were performed using the developed EMLC prototype to evaluate its functionality and check whether it met design specifications. The experiments were performed using film dosimetry, ion chambers, TLD, diode detectors, and the beam imaging system (BIS) (10).

In this report, I will summarize the highlights of my training and research as originally proposed in the **Postdoctoral Traineeship** application by Dr. Steve B. Jiang (original PI).

2. BODY

Training

The Department of Radiation Oncology at Stanford University School of Medicine has established a comprehensive postdoctoral training program in radiation oncology physics since 1996. A unique feature of this program is that it emphasizes not only the

cutting-edge research covering radiation therapy, computer simulation and modeling, image processing, molecular imaging, and image-guided radiation therapy, but also provides extensive clinical training to its postdoctoral fellows, ranging from the conventional 3D-conformal radiation therapy (3D-CRT) to the state of the art intensity modulated radiation therapy (IMRT) and frameless radiosurgery such as CyberKnife. Under the leadership of Dr. Arthur L. Boyer, the Director of the Radiation Physics Division, this program has become one of the best postdoctoral training programs in radiation physics in the United States. So far, all graduates from this program have successfully found academic positions in radiation oncology departments across the United States. Each year, the Department of Radiation Oncology at Stanford University offered two courses to its radiation oncology residents and postdoctoral fellows: the Physics of Radiation Therapy and Radiobiology. These are the most important courses for ABR certification examination for radiation oncologists and radiation oncology physicists. Both courses were one-semester long and covered the major aspects of radiation therapy and radiobiology with emphasis on the practical details. The courses also covered some of the hot topics such as gene therapy, molecular imaging, and image-guided radiation therapy. In addition, I also attended the weekly Cancer Education Seminar Series hosted by Stanford University School of Medicine, in which leading cancer researchers and clinicians presented their research results. In order to learn more advanced radiation therapy techniques, I also attended some of the important professional conferences and meetings. These include the 2001 ASTRO Annual Meeting in San Francisco, 2003 AAPM Annual Meeting in San Diego, and the 7th International Symposium on 3D-DRT and IMRT in San Francisco.

The Department of Radiation Oncology also held its annual IMRT Symposium and AcQSim Symposium, which all postdoctoral fellows were required to attend. AcQSim is a software package for optimizing CT-based localization and treatment planning. The Department of Radiation Oncology also had weekly clinical radiation physics seminars, in which guest speakers, faculty, and postdoctoral fellows presented

their research results. Under the direct guidance of Dr. Arthur L. Boyer, I have learned the basic theories of Monte Carlo simulation, modulated electron radiation therapy (MERT), intensity modulated radiation therapy (IMRT), and sweeping window arc therapy (SWAT). I have also learned IMRT treatment planning, X-Knife RT-2 treatment planning, CyberKnife Stereotactic Radiosurgery treatment planning, and HDR brachytherapy treatment planning. Additionally, I have also learned how to operate Varian CLINAC linear accelerators, Marconi CT scanner, and Wellhöfer dosimetry data acquisition system. Furthermore, I have also had opportunities to learn film dosimetry and to participate in the commissioning of radiation treatment planning systems (TPS) for IMRT treatment. As an important part of my postdoctoral training, I was also assigned clinical duties such as IMRT treatment planning, chart check, and machine QA.

Research

Recently, MERT has been exploited extensively for breast cancer treatment. In this technique, the electron beam intensity pattern, energy, and incident direction are optimized to deliver the optimal radiation dose to the target. This technique requires a proper beam-shaping device for the intensity-modulated beam delivery. We proposed to develop an EMLC specifically MERT. The EMLC will be located near the patient's skin and have much thinner leaves, and optimal shape of leaf ends and sides. We hypothesize that the quality of the electron beams and thus, the clinical effect of the MERT will be further improved if we shape the electron beams using the EMLC instead of using the conventional photon MLC since the photon MLC was designed and optimized specifically for photon beams, not for electron beams.

1. Design an EMLC using the Monte Carlo simulation

An essential requirement for MERT is to deliver, both accurately and efficiently, small-field electron beams (beamlets) of different energies and intensities. Traditionally, electron beams are shaped using a cutout and different energies at treatment depths may be achieved using variable incident energies. However, it would be very time consuming

to make cutouts for MERT beam delivery and the treatment time would become unacceptably long for routine clinical applications. Bolus can be used for missing tissue compensation and/or limited depth modulation. However, 3D bolus requires sophisticated techniques to build and it does not provide intensity modulation. As to the existing photon MLC (PMLC), although electron beam collimation can be achieved in some helium-filled scanned beam systems (11-14), there are some key limitations on accurate beam delivery with commonly accessible clinical accelerators. It has been found that a source to surface distance (SSD) of 70 cm is necessary to provide a clinically acceptable field using the PMLC in a Varian CLINAC 2100C linear accelerator. Beams collimated by a PMLC were found to be inferior to applicator fields in penumbra and uniformity. Monte Carlo simulations showed that the beam penumbra can be reduced significantly by either replacing the treatment head air with helium, together with a helium filled balloon between the accelerator and the patient skin or moving the MLC at least 11 cm towards the patient, or both (14). According to accelerator engineers, however, it is extremely difficult (if not impossible) to replace the air in an accelerator head with helium without major changes in the accelerator design. Therefore, an electron specific MLC has been proposed, which is located at the same level as a Cerrobend cutout, about 40 cm closer to the patient than the PMLC (15). An EMLC will be as accurate as a cutout in field shaping and as efficient as a PMLC for intensity modulation. It is generally believed that one of the reasons for the low use of electron beams in small cancer clinics is the extra manpower required to make customized cutouts for every patient. If so, the development of an EMLC will not only meet the needs for MERT, but also provide an efficient and effective device for beam shaping for conventional electron therapy.

We have performed extensive Monte Carlo simulations of electron fields collimated by 1.0 cm wide leaves to study the effect of material type and leaf thickness. Monte Carlo simulations were carried out on a cluster of 22 Pentium Pro CPUs (200 MHz) and 10 Pentium III CPUs (450 MHz), all running EGS4/BEAM, MCDOSE, and their utilities under the Linux operating system. Although the beam penumbral widths did

not change significantly for leaf thickness smaller than 2.0 cm, the beam intensity outside the field was affected by the leaf thickness and the atomic number of the leaf material.

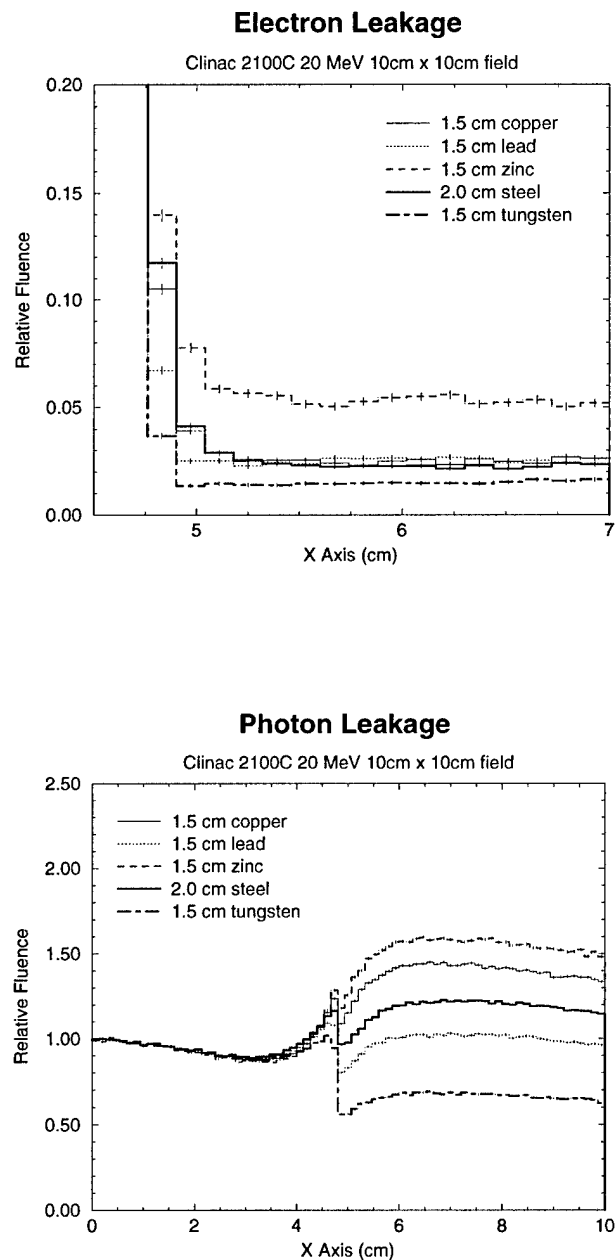


Figure 1. Monte Carlo simulated electron (top) and photon (bottom) planar fluence in the penumbral region and outside the treatment field for a 20 MeV electron beam collimated by an EMLC of different leaf materials and thicknesses.

As shown in Figure 1, for a 20 MeV electron beam, 1.5 cm thick zinc leaves reduced the electron fluence outside the field to about 5% of the central axis value. These electrons were mainly generated by the bremsstrahlung photons in the MLC leaves. This was confirmed by the photon fluence as shown, where 1.5 cm zinc MLC leaves resulted in about 60% higher photon fluence outside the field compared to the central axis photon fluence. Some electrons were also scattered off the leaf ends and by air. For 1.5 cm copper, 1.5 cm lead, and 2.0 cm steel, the electron fluence was about 2.5% of the central axis value. The electron fluence was reduced to about 1.5% if the leaves were made of 1.5 cm tungsten. This was reflected by the 30% less photon fluence under the tungsten MLC leaves compared to the central axis photon fluence. Clearly, tungsten is superior to other materials in terms of leaf leakage. If we increased the tungsten leaf thickness to 2.0 cm, the electron fluence would be reduced to less than 1% of the central axis value and the photon leakage would be reduced to about 50% of the central axis value (not shown).

To study the overall effect of the leaf leakage, leaf scattering, air scattering, and the extended source in an electron beam, we compared the dose distributions for single fields and multiple abutting fields collimated by an electron MLC with 1.5 cm thick tungsten leaves. We compared the Monte Carlo calculated dose distributions for a single 4 cm x 4 cm electron field and a multiple abutting field of the same size formed by four 1 cm x 4 cm electron fields (15). For a 20 MeV electron beam, the dose at the phantom surface for the abutting field shows about 4% fluctuation compared to a single electron field. This is potentially due to the effect of leaf shape and extended source. The dose outside the field for the abutting field is about 3 times higher than that for the single field, which is mainly caused by the leaf leakage due to the longer beam-on time to deliver the four 1 cm x 4 cm fields and electron scattering off the leaf ends. This increased leakage is comparable to that for photon IMRT, where the beam-on time is generally 3 ~ 5 times longer than a conventional photon treatment. The dose at 3.0 cm depth shows little difference between the abutting field and the single field except for the dose near the field edges and outside the field. For a 6 MeV electron beam, the dose at the phantom surface

for the abutting field is almost the same as that for the single field. The effect of leaf leakage is very small for a 6 MeV beam and the dose immediately outside the field is thought mainly due to the effect of electron scattering in the air. It seems that field abutting with 1.0 cm beamlets collimated by an electron MLC can provide adequate beam characteristics for MERT for the beam energies investigated. However, the dose outside the field needs to be minimized through beam energy and leaf sequence optimization.

We have also studied electron beam collimation using a photon MLC (16). One of the advantages of using a photon MLC is the possibility of easily combining both photon and electron beams in the same plan. An essential requirement for matching a photon beam and an electron beam at different depths is that both beams share the same source position. Several modifications to the design of a Varian CLINAC 2300CD accelerator have been proposed (14), one of which was to replace the intervening air with helium. This could significantly reduce the effect of electron scattering in the air on the beam penumbra. However, filling the accelerator head with helium requires major modifications to the existing accelerator design. Also, the beam properties deteriorated significantly for energies below 6 MeV even for helium filled treatment head based on the results of our previous DOD project (16).

To solve this problem, we have investigated an alternative solution - a thin leaf MLC at the electron cutout level to reduce the air scattering effect. As can be seen in Figure 2, the unfocused PMLC leaf ends could scatter the electrons very significantly to degrade the beam characteristics near the field edges. The Varian MLC has rounded leaf ends, which are expected to have similar or worse dosimetric characteristics as the unfocused MLC studied here. Focused leaf ends could greatly improve the beam edges and provided even slightly better dose profiles inside the field for a 20 MeV electron beam compared to an electron MLC, primarily due to the reduction of electron scattering in the accelerator head (helium vs. air). The dose outside the field was slightly lower for the electron MLC than for the photon MLC. For a 6 MeV beam, an electron MLC gave

slightly better surface dose profiles both inside and outside the field than the focused and unfocused photon MLC (Figure 3). The difference in the dose profiles decreases with depth (not shown). Note that in these comparisons, we have placed the phantom surface at 20 cm below the photon MLC and 7 cm below the electron MLC to minimize the effect of electron scattering in the air or helium between the MLC and the phantom (a fair comparison for using both MLCs). It is evident that an electron MLC will have similar dosimetric characteristics as a photon MLC with focused leaf ends, but without the need to replace the air in the accelerator head with helium.

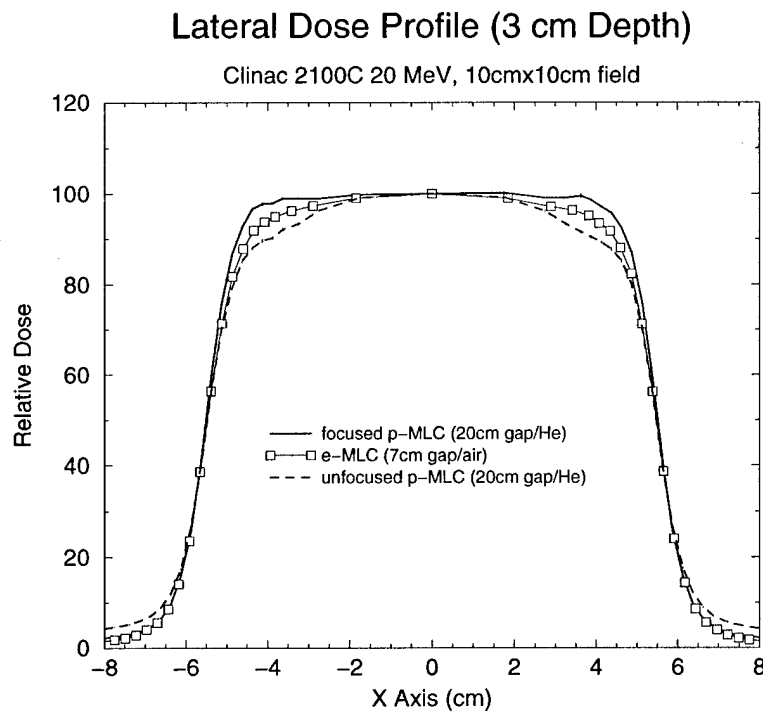


Figure 2 Monte Carlo calculated 20 MeV, 10 cm x 10 cm field electron beam profiles at 0.5 cm depth in water.

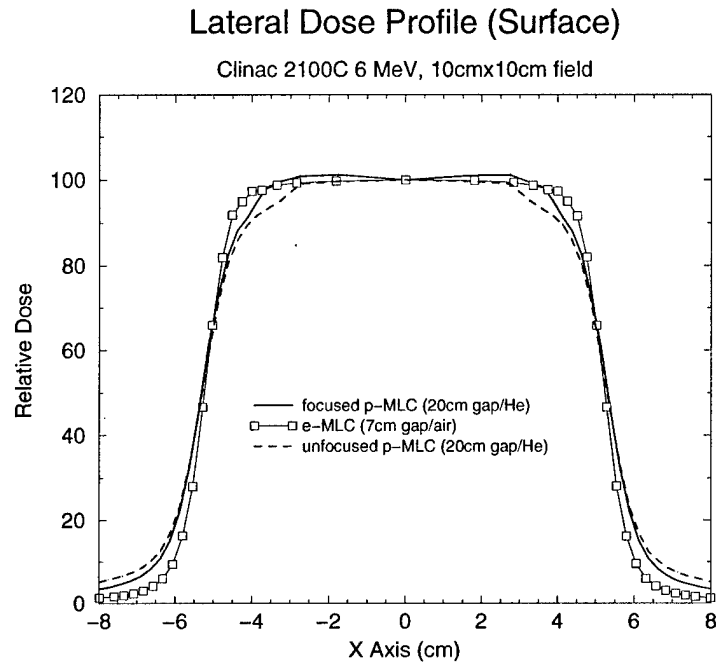


Figure 3. Monte Carlo calculated 6 MeV, 10 cm x 10 cm field electron beam profiles at 0.5 cm depth in water.

We have evaluated the Monte Carlo results using the established clinical criteria. The three important factors are beam delivery accuracy (beam penumbra), beam delivery efficiency (treatment time), and cost-effectiveness. An electron MLC is more accurate than a photon MLC for MERT beam delivery. It has smaller beam penumbra for small beamlet delivery compared to a photon MLC for the currently available clinical accelerators such as the Varian CLINAC accelerators. A photon MLC also requires the air in the treatment head to be replaced by helium to reduce electron scattering effects, but it is very difficult for some accelerators if not impossible because of the accelerator configuration. An EMLC is more efficient than electron cutouts for MERT beam delivery. A MERT treatment will require many cutouts for a single treatment, which will take much longer time to deliver. In the long run, the EMLC based MERT beam delivery will be more economical than using the cutouts.

Based on our Monte Carlo simulation results (15, 16), we designed a manually-driven EMLC for this project. Since our primary goal was to study the EMLC physical characteristics, the major concerns were the EMLC leaf shape and material. The mechanical characteristics of the proposed EMLC are listed in the table below:

Leaf material	Tungsten alloy
Leaf width	0.5 cm (nominal) projected at 100 cm SSD, leaves will travel in the x direction
Leaf length	20 cm, installed on a carriage movable along x direction
Leaf thickness	1.5 cm
Leaf end shape	Straight edge (unfocused)
Leaf side shape	Straight edge (unfocused) and/or side surface focused to a virtual source position.
Leaf location	The bottom of the leaves will be at about 95 cm SSD
Field size	Maximum 25 cm x 25 cm defined at 100 cm SSD

These parameters were determined based on our investigation results. We have chosen a 0.5 cm leaf width because thinner leaves will not provide effective beamlet collimation, especially for energies below 12 MeV, while wider leaves will deteriorate spatial resolution in the y direction (across the leaves). The EMLC leaf length was chosen to keep the overall dimension and weight low. The leaves will be installed on a movable carriage to compensate the limited leaf travel in the x direction. The 1.5 cm thickness is considered to be optimal for tungsten leaves in terms of leaf leakage (about 1.5% for 20 MeV electrons) and end scatter. Thicker leaves will further reduce leaf leakage, but will degrade beamlet penumbra. Straight leaf ends will ensure minimum interleaf leakage when a leaf pair is closed. Focused leaf sides will give slightly better beamlet penumbra in the y direction than unfocused leaf sides. For equal leaf width projected at 100 cm SSD, the actual leaf width will vary depending on the off-axis position. For easy

construction (therefore low cost), the actual leaf width can be made the same for a nominal 0.5 cm leaf width. The effective leaf positions in the y direction will be determined experimentally and used in the beamlet dose calculation and treatment optimization.

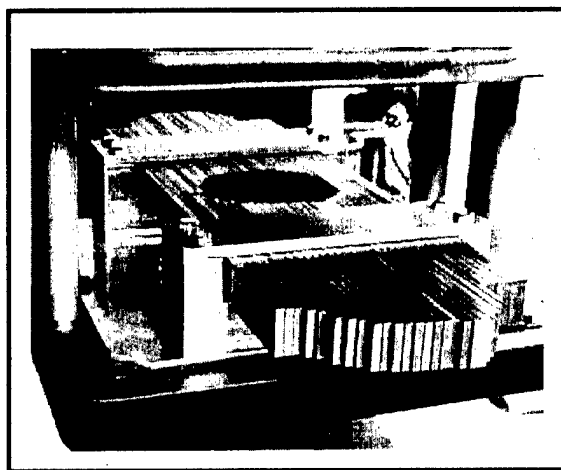


Figure 4. The EMLC placed on the top of the last scraper A 25 x 25 electron cone

2. Manufacture a prototype EMLC for MERT delivery

Based on the above-described design, the mechanical construction of the EMLC was done in our machine shop. We have made a prototype manually-driven EMLC to test the Monte Carlo simulations and for the experimental work scheduled for this project (Figure 4). The EMLC consists of 30 steel leaf pairs, which were made using conventional steel bars for convenience and cost-effectiveness (Tungsten leaves are difficult to machine and cost too much to built it for this project). Leaf ends and sides are parallel to the beam axis, i.e., unfocused. Each leaf is 0.476 cm wide (about 0.5 cm wide projected at 100 cm SSD), 20 cm long, and 2.54 cm thick. The leaves were mounted on a steel frame attached to the bottom scraper of a 25 cm x 25 cm electron applicator on a Varian CLINAC 2100C (Varian Medical Systems, Palo Alto, CA). This was the best

possible configuration that could be achieved without modifying the electron applicator itself. The leaves can slide in the steel frame and the leaf positions can be easily set using a pre-cut cardboard for a beam segment. The field shape is maintained by tightening screws from the side. The largest radiation field available using the electron MLC was 15.7 cm x 15.7 cm projected at 100 cm SSD. Since the cost of an electron applicator was well beyond the budget of this project, Varian Medical Systems donated an electron applicator specially used for this study. Their contributions are very important to the development of the EMLC.

The geometry of this prototype EMLC was simulated using the BEAM system. The simulations began with the upper phase space file and proceeded through the remainder of the accelerator and prototype EMLC geometry. At the isocenter plane, particles were collected into a phase space file, which was then used for dose calculation on a homogeneous water phantom composed of $3 \times 3 \times 2 \text{ mm}^3$ voxels. The goal was to verify the accuracy of the Monte Carlo simulations, so extensive measurements were performed. The prototype EMLC was installed onto the treatment head of a Varian CLINAC 2100C and film (Kodak X-omat V, Eastman Kodak Company, Rochester, NY) measurements were performed in solid water. Measurements were taken for all three energies under study at an SSD of 100 cm (the upper surface of the solid water phantom coincided with the isocenter plane). The film was scanned using a Vidar scanner system. The RIT 315 software package was used to generate isodose distribution for comparison with the simulated dose results. An appropriate film calibration curve was created to convert the optimal density (OD) of the film to the delivered dose. In addition, a final BEAM simulation and dose calculation were also performed with the photon MLC as the final electron collimation system. Again, no attempt was made to simulate the specific number of leaves and leaf widths found in a real accelerator; instead, the leaf parameters were adjusted such that the projected photon MLC leaf positions exactly matched the positions of the electron MLC. These simulations were performed in a helium

atmosphere, and the resulting dose distributions compared with the electron MLC simulation results.

3. Develop special software required for the use of EMLC

We have developed a complete system of Monte Carlo-based inverse treatment planning for modulated electron radiation therapy. The system incorporates the Monte Carlo simulated electron pencil beams into the inverse planning process. We have also modified an exiting photon beam leaf sequence algorithm to make it suitable for MERT plan delivery. Additionally, we have characterized the EMLC using a multiple-source beam model for fast Monte Carlo simulation. Furthermore, we have also studied the effect of beam delivery on optimized modulated electron radiation therapy plans in the final dose calculation.

In the inverse treatment planning process we have developed, a key assumption is that the dose delivered by the beamlets is not significantly different from the dose delivered by an MLC. This is not true in reality. The problem is that beamlets are a purely abstract concept; we can arbitrarily choose to simulate some particles and not others. In a physical system, particles throughout the whole field are active, and the MLC serves as an imperfect mask to select out a portion of those particles. The MLC imperfections can take the form of scatter and leakage, which may perturb the delivered doses. As a result, the MLC-delivered dose may differ significantly from the beamlet predicted dose. The magnitude of this effect depends on the specific plan and leaf configuration; as such, the effect cannot be known *a priori*. It is important to emphasize that in-air electron scattering is not included as one of these delivery effects. Because the reconstruction plane is at least several cm above the patient skin surface, any Monte Carlo simulation must include transport of particles through the air gap. This applies for both beamlets simulation and for simulation of the actual EMLC delivery. Thus, the in-air scatter is already included in the beamlets calculations. This disparity between planned and delivered dose is not limited to modulated electron therapy. Even, in photon IMRT, beamlets do not exactly predict the dose delivered by an MLC. The most notable

violation is the tong-and-groove effect. Delivery with an MLC imposes further differences between planned and delivered doses. In the inverse treatment planning system, the beamlet weight may take on any non-zero value. However, because of practical restrictions on delivery time, these weights are typically stratified into discrete levels. This will move the plan away from the optimized intensity map, and will likely have an adverse impact on the dose homogeneity and conformity. In this section, I will briefly describe the Monte Carlo-based inverse treatment planning system without touching on the involved mathematical theory.

Based on manufacturer's specifications of the beam production system and the electron applicator design, the electron beams produced by a Varian CLINAC 2100C linear accelerator and collimated by the EMLC were simulated using the EGS4/BEAM code. Monte Carlo simulations were carried out using a group of 22 Pentium Pro CPUs (200 MHz) and 10 Pentium III CPUs (450 MHz), all running EGS4/BEAM, MCDOSE (23, 24), and their utilities under the Linux operating system. All simulation parameters, such as the electron and photon energy cutoffs (ECUT and PCUT), the maximum fractional energy loss per electron step (ESTEPE), and the number of initial electron histories, were specified in the EGS4/BEAM input file. In this study, we used ECUT = 700 KeV and PCUT = 10 KeV, below which all remaining energy was assumed to deposit on the spot. ESTEPE was set to 0.04. The EMLC was included in the EGS4/BEAM simulations as an MLC component module. The number of initial electron histories ranged from 2-30 million, depending on the electron energy. Phase space data were scored at a plane of 100 cm SSD after the particles had transported through the linac treatment head, the EMLC, and the air gap beneath it. The 1σ statistical uncertainty in the dose was, in general, less than 2% of the D_{\max} value. Based on this simulated electron beam, the MERT plans were then created using our modified EGS4/MCDOSE and other related codes.

The CT scans were obtained from our department's patient database. The CT images were acquired with the patients in supine position. During CT scanning, a

thermoplastic facial mask with three fiducials was used for the purpose of patient immobilization and target localization for the subsequent treatments. For each patient, about 90 images with a slice thickness of 3.0 mm were acquired over the entire treatment area. Each CT image had an in-plane resolution of 512 x 512 pixels, with each voxel being 0.94 x 0.94 x 3.0 mm³ in size. The CT images were transferred to an AcQSim system (Marconi Medical Systems, Inc., Cleveland, OH) for further processing. The clinical tumor volume (CTV) and critical structures were contoured on the axial CT images by a radiation oncologist using the AcQsim workstation. The gross tumor volume (GTV) was defined based on diagnostic imaging and clinical findings. It consisted of gross primary and nodal tumors. The CTV was constructed by expanding the GTV 1.0 cm in all directions to cover microscopic extension of the tumor. The PTV was obtained by adding a 0.5 cm margin uniformly to CTV to account for patient setup uncertainty and organ shift. Like photon beam IMRT, any structures whose dose needed to be kept below a certain limit or whose statistics were to be calculated in the MERT plan had to be contoured. Only those contoured targets and structures were considered in the plan and included in the final statistics. In addition, in order for our MERT inverse planning programs to work properly, all regions of interest were delineated as separate structures. No structure overlapping was allowed for the current version of our programs. The CT images, along with the outlined structures, were transferred to a workstation using the DICOM 3.0 format and then converted into a format that was compatible with EGS4/MCDOSE code so that they could be sent to our designated Monte Carlo treatment planning machines. The final CT images used in MERT planning had an in-plane resolution of 128 x 128 pixels with a voxel size of 0.35 x 0.35 x 0.30 cm³ that balanced resolution with the Monte Carlo dose calculation time. Additionally, the CT numbers were converted into mass densities and material types for Monte Carlo simulations. Based on the CT numbers, each voxel was designated as being one of the three materials: air, tissue or bone. This provided the approximate effective atomic numbers, cross-sections, and stopping powers for each voxel. Figure 5 shows the simplified MERT treatment planning flowchart.

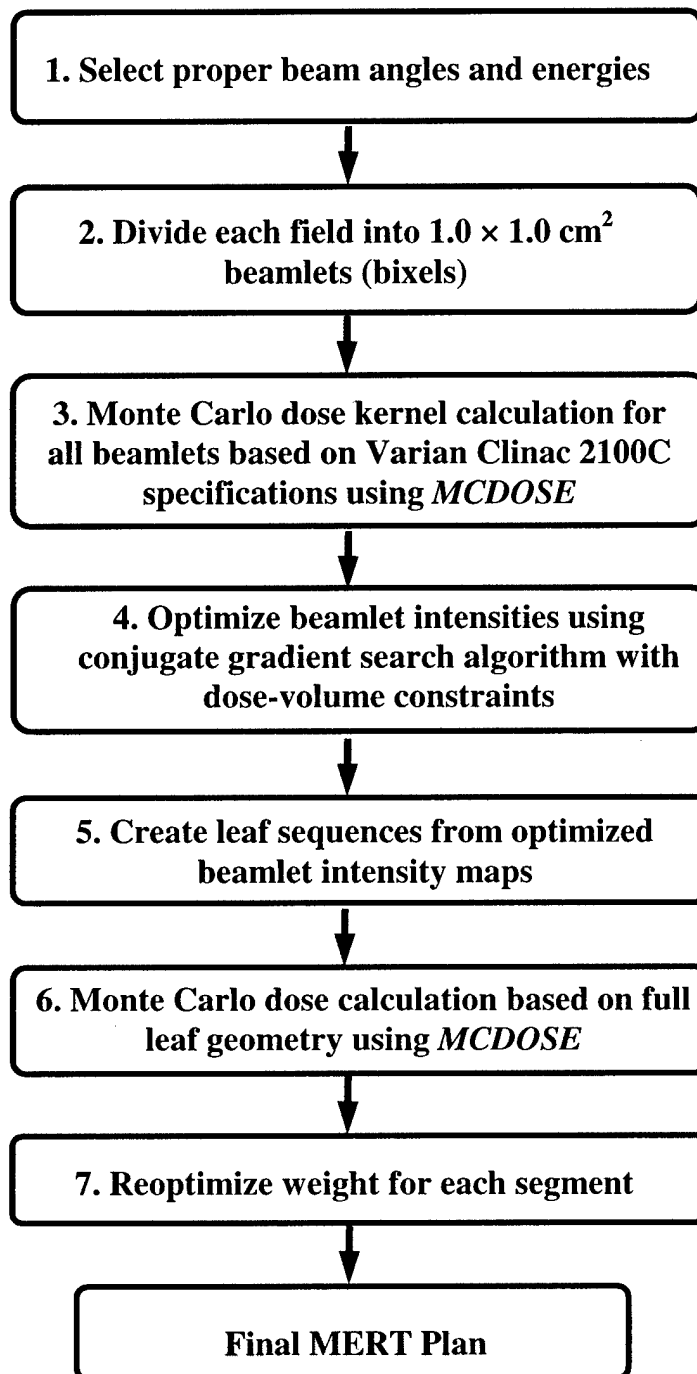


Figure 5. MERT treatment planning flow chart.

To facilitate the description of the flowchart, we will use the term *field* to specify each beam angle/electron energy combination and reserve the term *port* to indicate a single beam orientation (gantry angle). Thus, a plan in which five electron energies are delivered at a single gantry angle may be said to have one port and a total of five fields. Like the photon beam IMRT, the first step in creating a MERT plan was to select a set of suitable beam orientations, i.e., gantry angles, to fully cover the target volume while sparing the adjacent critical structures as much as possible. Each port was then divided into $1.0 \times 1.0 \text{ cm}^2$ beamlets, i.e., the smallest beam elements for dose calculation. All beamlets smaller than $1.0 \text{ cm} \times 1.0 \text{ cm}$ at the edge of the field were rounded to $1.0 \text{ cm} \times 1.0 \text{ cm}$. This means that beam intensity within a $1.0 \times 1.0 \text{ cm}^2$ beamlet would not be further differentiated. The beamlet size was defined at the isocenter plane. The goal of this step was to determine how many beamlets were required to simulate for each port. The user specified the isocenter, gantry, collimator, and couch angles, the desired beamlet size, and the dimension of the search space. A program calculated which beamlets intersected the target and created a text file containing these beamlets and their coordinates. This file was used by MCDOSE to pre-calculate the beamlet dose kernels. The total number of beamlets was the sum of the beamlets over all ports. A beamlet could be turned off, i.e., assigned a weight of zero, but continued to remain active throughout optimization. After the selection of a proper set of beam angles, we needed to decide which electron energies to use for each beam angle. To do so, we computed a tumor depth map for each beam angle, whose pixel size was the same as that of a beamlet, i.e., $1.0 \times 1.0 \text{ cm}^2$. Based on the tumor depth distribution and assuming that the electrons lost energy at about 2 MeV/cm in tissue, we were able to determine a suitable set of electron energies for each beam angle. Since, in most of the cases, the target was not spherical in shape, different beam angles could have different sets of electron energies. The obvious advantage of this approach was the removal of those electron energies that contributed less to the target dose and, thus, the reduction in the number of fields used and delivery time.

The next step was to calculate beamlet dose kernels using MCDOSE. The beamlet dose kernel was the Monte Carlo calculated dose array for all structures due to a single beamlet. Each element of the dose kernel represented the dose delivered to a dose calculation point or voxel assuming a unit beamlet weight. These values were also referred to as dose deposition coefficients. Thus, the purpose of this step was, given a set of unit beamlet weights, to calculate the dose distribution in every structure that we were interested in. To optimize beamlet weights or intensity maps, a quadratic objective function augmented with dose-volume constraints was constructed. This was based on the assumption that there existed a quadratic relationship between the delivered dose and the biological effect. The overall objective function contained a linear component for each structure. Within each structure, each of the individual constraints contributed linearly to the objective function. Following the construction of the objective function, the optimization of beamlet weights was initiated. The core of the optimization procedure was the well-known conjugate gradient search algorithm. The major advantage of the gradient search technique was its fast convergence speed, as compared to stochastic optimization techniques, such as simulated annealing. We believe that the gradient search algorithm was a good choice for future routine clinical implementation of MERT. During the optimization, care was exercised to avoid negative weights. These non-physical results were eliminated by scaling step sizes to avoid stepping over the boundary of the acceptable solution space and by projecting gradients onto the boundaries.

Following the beamlet weight optimization, the resulting fifteen optimized continuous intensity maps were stratified into five discrete intensity levels in preparation for leaf sequencing. We believe that five intensity levels provided a reasonably good approximation to the original intensity maps. The fifteen discrete intensity maps were then converted to fifteen step-and-shoot leaf sequences (17) based on the technique proposed by Bortfeld et al. (18). Since the dose distribution delivered by the ideal beamlets could be different from that delivered by the leaf sequences, a Monte Carlo dose calculation was performed again based on the fifteen discrete intensity maps

reconstructed from the corresponding fifteen leaf sequences. With these new dose kernels, the leaf sequence segment weights were re-optimized. This second optimization differed from the first one in two aspects. The first optimization was entirely based on idealized beamlets, without considering the EMLC geometry nor the leaf scatter effect, while the second optimization took into account not only the EMLC geometry, but also leaf end transmission bremsstrahlung leakage. Thus, the first optimization produced the best dose distribution possible, while the second one gave the actual delivered dose.

In the proposed planning scheme, the first optimization generates an approximate or preliminary plan. By applying a leaf-sequencing algorithm to the beamlet weights, the leaf positions are determined. This can be thought of as deciding in which general areas different energies are needed, and also grouping certain sections of the fields as being “similar” in intensity requirements. The second round of optimization leaves the leaf positions fixed and adjusts the intensities of each segment. This optimization can, in part, compensate for bremsstrahlung leakage. Additionally, it can improve on the results of stratification into equal levels. After second round simulations and optimization, all leaf effects have been included. Thus, the resulting doses can be taken to be an accurate representation of the doses that would actually be delivered, at least insofar as the Monte Carlo transport physics can be considered accurate. The resulting dose distributions are a significant improvement over the single optimization plans, with leakage effects at least partially ameliorated.

4. Evaluate the functionality of the EMLC experimentally

Ideally, the EMLC leaves should be placed in such a position that the bottom of the leaves is as close to the patient skin as possible in order to produce a clinically acceptable field. However, because of the existing electronic circuitry used to detect the insertion of the electron cutout at the last scraper of a standard Varian 25 x 25 cm² electron applicator, it was impossible to place the EMLC leaves at that position without changing the existing electron applicator design significantly. Thus, initially, the steel

frame of the EMLC leaves was temporarily inserted into the electron cutout mount and the leaves were placed about 1 cm above the last scraper. This configuration resulted in a 10 cm air gap between the bottom of the EMLC leaves and the patient skin for a nominal 100 cm source-surface distance (SSD). To further lower the EMLC leaves and, thus, reduce in-air electron scattering and the penumbra, we have now removed the entire last scraper of the electron applicator and its electronic accessories. The EMLC frame was placed at the bottom of the modified electron applicator and stabilized with eight screws. This modification reduced the air gap to 5.0 cm between the bottom of the EMLC leaves and the patient skin. Since the electronic circuitry for detecting the electron cutout was completely removed, we were able to avoid activating interlocks associated with electron beam accessory malfunction while inserting the EMLC assembly into the linac treatment head. Thus, even if the linac was in the electron mode, the gantry could still be rotated, making the delivery of MERT plans with multiple beam angles possible. Figure 6 shows a photo of the modified EMLC inserted on the treatment head of a Varian CLINAC 2100C linear accelerator.

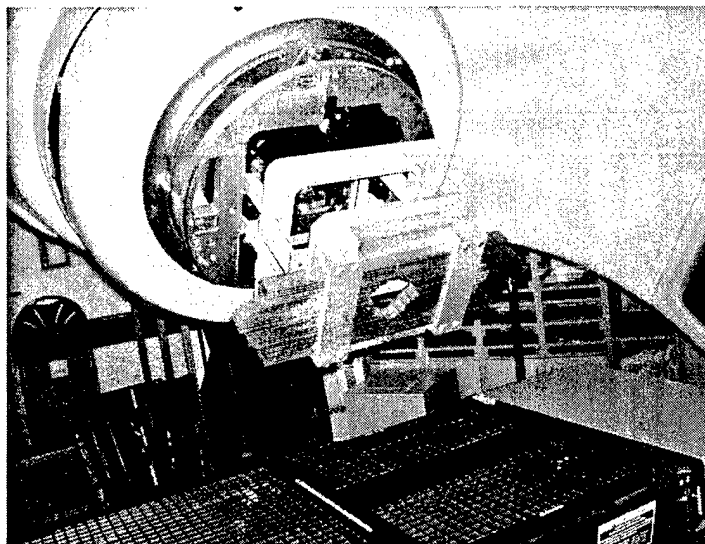


Figure 6 A photo of newly modified EMLC.

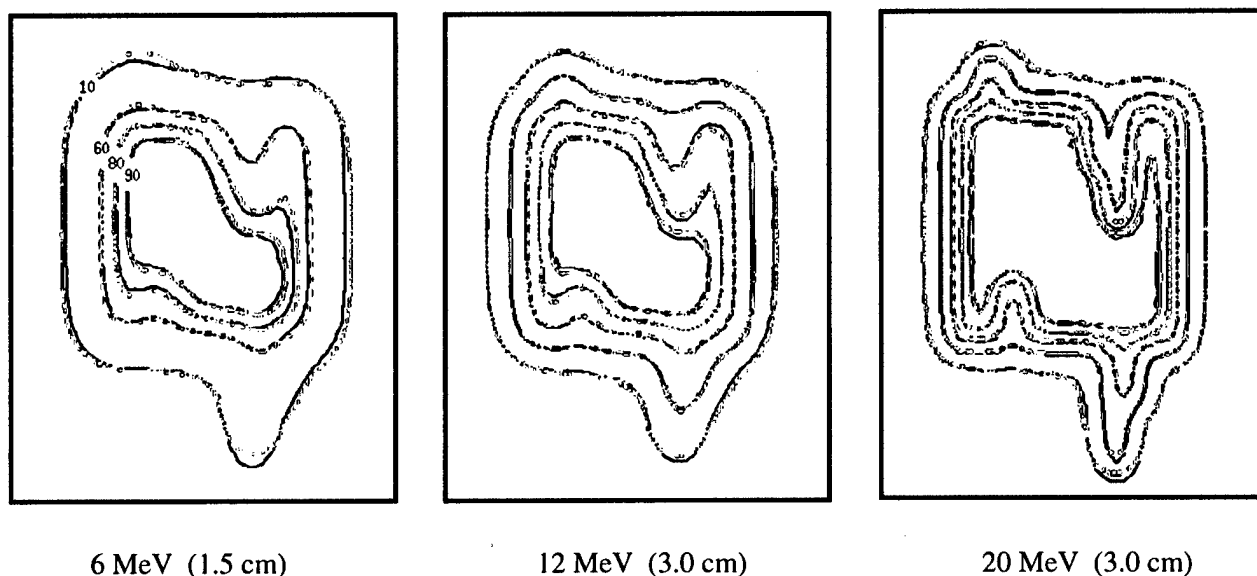


Figure 7. Comparison of Monte Carlo simulations (black) and film measurements (color).

The dosimetric characteristics of EMLC were evaluated experimentally using various techniques. Film (Kodak X-omat V, Eastman Kodak Company, Rochester, NY) dosimetry of the prototype EMLC was performed on a Varian CLINAC 2100C linear accelerator. Measurements were taken at energies of 6, 12, and 20 MeV and at the surface, 1.5 and 3.0 cm depths in a solid water phantom to evaluate the quality of the electron beams collimated by the EMLC. The films were scanned using a VXR-12 PLUS film digitizer (VIDAR Systems Corporation, Herndon, VA) and calibrated according to the AAPM TG-25 recommendations. Dose distributions, flatness and symmetry, and the extent of the beam penumbra were accessed using the RIT113 radiation therapy film dosimetry system (Radiological Imaging Technology, Colorado Springs, CO) and compared with the simulated dose results. Figure 7 shows the representative results of Monte Carlo simulations vs. film measurements. Figure 8 shows the representative results of beam imaging system (BIS) measurements. Our results showed that there was an excellent agreement between the film measurements and the Monte Carlo simulated

data at all electron energies in terms of dose distribution. We found that the EMLC provided significant improvements in dose penumbras and field resolution as compared to the photon MLC. We also found that MERT was able to provide similar or better target dose coverage compared with photon IMRT. However, MERT could significantly reduce the dose to critical structures.

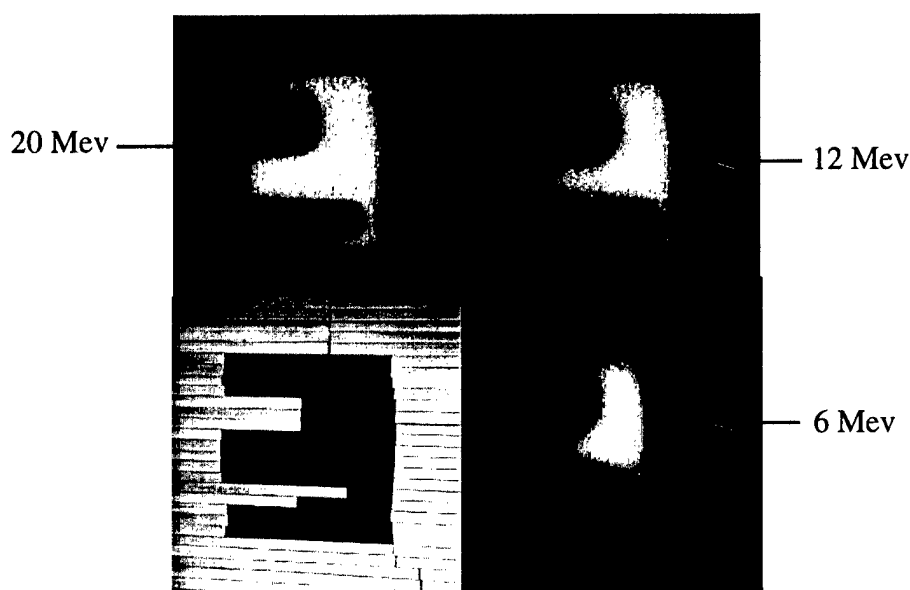


Figure 8 Representative results of beam imaging system (BIS) measurements

Note:

The original PI, Steve B. Jiang, Ph.D., left Stanford University School of Medicine in September 2000. Stanford University, with the approval of the U.S Army Medical Research Acquisition Activity (USAMRAA), transferred the PIship to me (Yulin Song, Ph.D., the author of this report) on January 17, 2002. As a result, my mentor, Dr. Arthur L. Boyer, requested the U.S. Army to extend the term of the **Traineeship** for one more year without additional funds. The request was approved by the USAMRAA on March 24, 2002.

3. KEY RESEARCH ACCOMPLISHMENTS

- Established clinical criteria for MERT beam delivery: The clinical requirements for MERT beam delivery are accuracy, efficiency, and cost-effectiveness.
- Performed Monte Carlo simulations to investigate EMLC parameters: We have investigated different materials and geometric configurations for the prototype EMLC and compared the results with those of a photon MLC and electron cutouts.
- Evaluated EMLC parameters based on the clinical criteria: We have evaluated the Monte Carlo results based on the clinical criteria. We conclude that the EMLC is superior to the PMLC and electron cutouts. The EMLC is more accurate (smaller beam penumbra) than the PMLC and more efficient, and cost-effective than electron cutouts.
- Finalized the EMLC design parameters: We have finalized the EMLC design parameters based on the optimal leaf material and geometric configuration.
- Manufactured a prototype EMLC for experimental MERT beam delivery study: We have manufactured a prototype EMLC based on the project budget and our current linear accelerator.
- Developed software for the use of EMLC: We have incorporated the Monte Carlo simulated electron pencil beams in the inverse treatment planning process. We have also modified a photon beam leaf-sequencing algorithm for MERT beam delivery. We have investigated the characteristics of the EMLC using a multiple-source model for fast Monte Carlo simulations.

- Included the effects of the EMLC in the final dose calculation: We have incorporated the EMLC into the EGS/BEAM simulations as an MLC component module and created MERT plans for breast cancers.
- Evaluated the functionalities of the prototype EMLC: We have performed film and BIS dosimetry to experimentally evaluate the quality of the EMLC in terms of dose distribution, flatness, and symmetry, and the extent of the beam penumbra. We have also measured the corresponding data for a PMLC.

4. REPORTABLE OUTCOMES

----PUBLICATIONS:

Manuscript

1. **Yulin Song**, Arthur L. Boyer, Todd Pawlicki, Lei Xing, Steve Jiang, Yulong Yan, C-M Ma, and Michael C. Lee, "Modulated Electron Radiation Therapy (MERT): A Novel Treatment Modality for Parotid Cancers", *Technology in Cancer Research and Treatment* (Submitted), 2003.
2. Michael C. Lee, Jun Deng, Jinsheng Li, **Steve B. Jiang**, and C-M. Ma, "Monte Carlo based treatment planning for modulated electron radiotherapy", *Phys. Med. Biol.* **46**: 2177- 2199, 2001.
3. C-M. Ma, Todd Pawlicki, Michael C. Lee, **Steve B. Jiang**, Jinsheng Li, Jun Deng, Ed Mok, B. Yi, Gary Luxton, and Arthur L. Boyer, "Energy- and intensity-modulated electron beams for radiotherapy", *Phys Med Biol.* **45**: 2293-2311, 2000.
4. **Steve B. Jiang**, A. Kapur, and C-M. Ma, "Electron beam modelling and commissioning for Monte Carlo treatment planning", *Med. Phys.*, **27**:180-191, 2000.
5. Michael C. Lee, **Steve B. Jiang**, and C-M. Ma, "Monte Carlo and Experimental Investigations of Multileaf Collimated Electron Beams for Modulated Electron Radiotherapy", *Med. Phys.* **27**: 2708-18, 2000.

Abstracts

1. **Yulin Song**, Penny Peng, Arthur L. Boyer, and Lei Xing "Concurrent Boost Using Forward Multiple-Segment Planning and Step-and-Shoot Delivery: A Novel Technique of Breast-Conserving Radiation Therapy", To be presented at ASTRO 2003 Annual Meeting, Salt Lake City, Utah, USA, October 19-23, 2003.

2. Anthony Lo, **Yulin Song**, Arthur L. Boyer, Todd Pawlicki, and Lei Xing “Combing IMRT and MERT for Breast-Conserving Radiation Therapy”, To be presented at RSNA 2003, Chicago, USA, November 30-December 5, 2003.
3. Lei Xing, Zhenyu Shou, Jonathon Li, **Yulin Song**, Todd Pawlicki, Arthur L. Boyer, and Quynh-Thu Le “Dose Matching of Two IMRT Plans or an IMRT and a 3D Conformal Treatment Plan”, To be presented at ASTRO 2003 Annual Meeting, Salt Lake City, Utah, USA, October 19-23, 2003.
4. **Yulin Song**, Anthony K. Ho, Todd Pawlicki, and Anthony Lo, “A Comparative Dosimetric Study of CyberKnife Stereotactic Radiosurgery System and Intensity Modulated Radiation Therapy (IMRT) for Localized Cancers in the Head and Neck”, Presented at AAPM 2003 Annual Meeting, San Diego, CA, USA, August 10-14, 2003.
5. Arthur L. Boyer, Todd Pawlicki, Carlos Cardenas, and **Yulin Song**, “IMRT Using Audio and Optical Respiration Gating”, Presented at AAPM 2003 Annual Meeting, San Diego, CA, USA, August 10-14, 2003.
6. Todd Pawlicki, **Yulin Song**, Geoff Zhang, Thomas Guerrero, Karl Prado, Naresh B. Tolani, Joseph A. Both, and Arthur L. Boyer, “Automated Monte Carlo Commissioning for Photons Using the NXEGS Software”, Presented at AAPM 2003 Annual Meeting, San Diego, CA, USA, August 10-14, 2003.
7. **Yulin Song**, Michael C. Lee, and Arthur L. Boyer, “Energy and intensity modulated electron radiotherapy: A comparative dosimetric study of MERT and IMRT for head & neck cancer”, Presented at the 44th Annual Meeting of the American Association of Physicists in Medicine, Montreal, Canada, July 18-21, 2002.

8. Gary Luxton, **Yulin Song**, Jenny Hai, and Arthur L. Boyer, "TLD measurement system for comprehensive dosimetric quality assurance in IMRT", Presented at the 44th Annual Meeting of the American Association of Physicists in Medicine, Montreal, Canada, July 18-21, 2002.
9. Arthur L. Boyer, **Yulin Song**, Yong Yang, and Lei Xing, "Sweeping window arc therapy", Presented at the 44th Annual Meeting of the American Association of Physicists in Medicine, Montreal, Canada, July 18-21, 2002.
10. **Yulin Song**, Steve B. Jiang, Michael C. Lee, C-M Ma, and Arthur L. Boyer, "A multileaf collimator for modulated electron radiation therapy (MERT) for breast cancer", Presented at the Era of Hope 2002 DoD Breast Cancer Research Program Meeting, Orlando, Florida, USA, September 25-28, 2002.
11. Lei Xing, Jonathan G. Li, **Yulin Song**, David Y. Yang, Don Goffinet, and Arthur L. Boyer, "Combining electron with intensity modulated photon beams for breast cancer", Presented at the Era of Hope 2002 DoD Breast Cancer Research Program Meeting, Orlando, Florida, USA, September 25-28, 2002.
12. C-M. Ma, Jinsheng Li, Todd Pawlicki, **Steve B. Jiang**, and Jun Deng, "MCDOSE – a Monte Carlo dose calculation tool for radiation therapy treatment planning", Proc. of the XIII International Conference on the Use of Computer in Radiation Therapy (ICCR), Eds: W Schlegel and T Bortfeld (Springer-Verlag, Heidelberg), 123-125, 2000.
13. C-M. Ma, Todd Pawlicki, Michael C Lee, **Steve B. Jiang**, Jinsheng Li, Jun Deng, Ed Mok, and Arthur L. Boyer, "Modulated electron beams for treatment of breast cancer", Presented at the XIII International Conference on the Use of Computer in Radiation Therapy (ICCR), Heidelberg, Germany, May 22 - 25, 2000.

14. C-M. Ma, and **Steve B. Jiang** "Monte Carlo methods in electron beams treatment planning", invited talk at the 41st Annual Meeting of the American Association of Physicists in Medicine, Nashville, TN, July 24-29, 1999.
15. Jun Deng, **Steve B. Jiang**, Todd Pawlicki, Jinsheng Li, and C-M Ma, "Electron beam commissioning for Monte Carlo dose calculation", Presented at ICCR, Heidelberg, Germany, May 22 – 25, 2000.
16. C-M Ma, Todd Pawlicki, **Steve B. Jiang**, Jinsheng Li, Jun Deng, David Findley, Ed Mok, and Arthur L. Boyer, "Implementation of a Monte Carlo dose calculation module in the FOCUS treatment planning system", CMS FOCUS 2000 User's Symposium, St. Louis, MO, April 10-11, 2000.
17. Jinsheng Li, Todd Pawlicki, Jun Deng, **Steve B. Jiang**, A. Kapur, Ed Mok and C-M Ma, "Clinical validation of a Monte Carlo dose calculation code for radiotherapy treatment planning (abstract), *Med. Phys.* 26:1083, 2000.
18. Jinsheng Li, Todd Pawlicki, Jun Deng, **Steve B. Jiang**, and C-M Ma, "Simulation of Beam Modifiers for Monte Carlo Treatment Planning", Presented at ICCR Heidelberg, Germany, May 22 – 25, 2000.
19. **Steve B. Jiang**, A. Kapur, and C-M Ma, "Electron beam modeling and commissioning for Monte Carlo treatment planning" (abstract), *Med. Phys.* 26:1084, 1999.

----FUNDING APPLIED FOR BASED ON WORK RESULTING FROM OR SUPPORTED IN PART BY THIS GRANT:

Modulated Electron Radiation Therapy

NIH: R01 Principle Investigator: C-M Charlie Ma, Ph.D. (April 1, 2001)

----EMPLOYMENT RECEIVED ON TRAINING SUPPORTED BY THIS POST-DOCTORAL TRAINEESHIP:

1. **Steve B. Jiang**, Ph.D., Assistant professor, the Department of Radiation Oncology, Massachusetts General Hospital, Harvard Medical School, Boston, MA.
2. **Yulin Song**, Ph.D., Assistant Attending Physicist (Assistant professor), the Department of Medical Physics, Memorial Sloan-Kettering Cancer Center, New York, NY

5. CONCLUSIONS

We have successfully completed the tasks described in the "Statement of Work" in this Post-doctoral Fellowship proposal. Based on the results of this study, we conclude that EMLC is able to provide sufficient beam collimation for MERT and Monte Carlo simulation provides an accurate technique for computing dose distributions from such a beam collimation system.

6. REFERENCES

1. Lee, M. C., Deng, J., Li, J., Jiang, S. B., and Ma, C-M, "Monte Carlo Based Treatment Planning for Modulated Electron Radiation Therapy", *Phys Med Biol*, **46**:2177-2199, 2001.
2. Ma, C-M, Pawlicki, T., Lee, M. C., Jiang, S. B., Li, J., Deng, J., Yi, B, Mok, E., and Boyer, A. L., "Energy-and Intensity-Modulated Electron Beams for Radiotherapy", *Phys Med Biol*, **45**:2293-2311, 2000.
3. Klein, E. E., "Modulated electron beams using multi-segmented multi-leaf collimation", *Radiother Oncol*, **48**(3):307-11, 1998.
4. Jiang, S. B., Luo, Z. M., and Ayyangar, K. M., "Incorporation of the electron energy-loss straggling into the Fermi-Eyges equation", *Rad Phys Chem*, **53**:477-482, 1998.
5. Zhu, Y, Boyer, A. L., and Desobry, G. E., "Dose distribution of x-ray fields as shaped with multileaf collimators", *Phys Med Biol*, **37**(1):163-174, 1992.
6. Ebert, M. A., and Hoban, P. W., "A Monte Carlo investigation of electron-beam applicator scatter", *Med Phys*, **22**(9):1431-1435, 1995.
7. Nelson, W. R., Hirayama, H., and Rogers, D. W. O., "The EGS4 Code System", *SLAC-Report-265*, Stanford Linear Accelerator Center, 1985.
8. Rogers, D. W. O., Faddegon, B. A., Ding, G. X., Ma, C-M., Wei, J., and Mackie, T. R., "BEAM: A Monte Carlo Code to Simulated Radiotherapy Treatment Units", *Med Phys*, **22**:503-524, 1995.

9. Jiang, S. B., Kapur, A., Ma, C. M., "Electron beam modeling and commissioning for Monte Carlo treatment planning", *Med Phys*, **27**:180-191, 2000
10. Ma, L., Geis, P. B., and Boyer, A. L., "Quality assurance for dynamic multileaf collimator modulated field using a fast beam imaging system", **24**(8):1213-20, 1997
11. Hyodynmaa, S., Gastafsson, A., and Brame, A., "Optimization of conformal electron beam therapy using energy- and fluence-modulated beams", *Med. Phys.*, **23**:659-666, 1996.
12. Lief, E. F., Larsson, A., and Humm, J. L., "Electron dose profile shaping by modulation of a scanning elementary beam", *Med. Phys.*, **23**:33-44, 1996.
13. Zackrisson, B., and Karlsson, M., "Matching of electron beams for conformal therapy of target volumes at moderate depths", *Radiotherapy and Oncology*, **39**:261-270, 1996.
14. Karlsson, M. G., Karlsson, M., Ma, C. M., and Satherberg, A., "MLC-collimated electron beams – a Monte Carlo based optimization", *World Congress on Med. Phys.* (Nice, France), 1997.
15. Ma, C. M., Pawlicki, T., Lee, M. C., Jiang, S. B., Li, J. S., Deng, J., Mok, E., Yi, B., Luxton, G., and Boyer, A. L., "Energy- and intensity-modulated electron beams for radiotherapy, *Phys. Med. Biol.* **45**:2293-2311, 2000.
16. Lee, M. C., Jiang, S. B., and Ma, C. M., "Monte Carlo and Experimental Investigations of Multileaf Collimated Electron Beams for Modulated Electron Radiotherapy", *Med. Phys.* **27**:2708-18, 2000.

17. Boyer, A. L., and Yu, C. X., "Intensity Modulated Radiation Therapy with Dynamic Multileaf Collimators", *Semin Radiat Oncol*, **9**:48-59, 1999.
18. Bortfeld, T., Kahler, D. L., Waldron, T. J., and Boyer, A. L., "X-ray Field Compensation with Multileaf Collimators", *Int J Radiat Oncol Biol Phy*, **28**:723-730, 1994.

15. APPENDICES

Copies of manuscripts and abstracts

Modulated Electron Radiation Therapy (MERT): A Novel Treatment Modality for Parotid Cancers

Yulin Song, Ph.D.¹, Arthur L. Boyer, Ph.D.^{1*}, Todd Pawlicki, Ph.D.¹, Lei Xing, Ph.D.¹,
Steve Jiang, Ph.D.², Yulong Yan, Ph.D.¹, C-M Charlie Ma, Ph.D.⁴, and Michael C. Lee, Ph.D.³

¹Department of Radiation Oncology
Stanford University School of Medicine
300 Pasteur Drive, Stanford, CA 94305

²Department of Radiation Oncology
Massachusetts General Hospital
Harvard Medical School
100 Blossom Street, Boston, MA 02114

³Department of Radiology
University of California at San Francisco
505 Parnassus Avenue, San Francisco, CA 94115

⁴Department of Radiation Oncology
Fox Chase Cancer Center
7701 Burholme Avenue, Philadelphia, PA 19111

Running Title Header: Radiotherapy for Parotid Cancers

Keywords: Monte Carlo, IMRT, MERT, EMLC, MLC, and Parotid Cancer

***Address Correspondence to:**

Arthur L. Boyer, Ph.D., Director and Professor
Division of Radiation Physics
Department of Radiation Oncology
300 Pasteur Dr., Room H0144
Stanford University School of Medicine
Stanford, CA 94305-5304
Tel: (650)-723-5549
Fax: (650)-498-5008
E-mail: boyer@reyes.stanford.edu

Abstract

In this study, we investigated treating parotid cancers using modulated electron radiation therapy (MERT) and compared MERT plans with photon beam intensity-modulated radiation therapy (IMRT) in terms of target dose coverage and normal tissue sparing. To deliver MERT plans effectively, we developed a prototype MERT delivery device – an electron multileaf collimator (EMLC) for routine clinical implementation of MERT.

The prototype electron multileaf collimator was fabricated by modifying a conventional 25 x 25 cm² electron applicator (Varian Medical Systems, Palo Alto, CA). Electron beams produced by a medical linear accelerator (Clinac 2100C, Varian Medical Systems, Palo Alto, CA) and collimated by this EMLC were simulated using the EGS4/BEAM code. The simulations were based on the manufacturer's specifications of the beam production system and the electron applicator design. The MERT plans with three coplanar beams (205⁰, 235⁰, and 255⁰) and five nominal energies (6, 9, 12, 16, 20 MeV) were created using modified EGS4/MCDOSE code. The corresponding IMRT plans with five coplanar beams were computed using a commercial treatment planning system (CORVUS, NOMOS Corp, Sewickley, Pennsylvania). Our preliminary data indicated that MERT was able to provide at least similar or better target dose coverage and uniformity compared with photon beam IMRT. However, MERT can significantly reduce the dose to critical structures. In the cases we studied, the maximum doses to the orbits, brainstem, optic chiasm, and spinal cord were reduced by 3.0, 16.2, 11.5, and 19.6 Gy, respectively, for a 50.0 Gy target dose, suggesting a distinct normal tissue sparing advantage for MERT.

Introduction

Each year, about 70,000 new head and neck cases were diagnosed in the United States (1) and tumors of the parotid gland are the most frequently encountered salivary gland tumors, accounting for about 3% of total head and neck cancers (2). Currently, the most widely used treatment is a combination of surgery and adjuvant postoperative radiotherapy for the malignant salivary tumors (3, 4). The minimally required operation for tumors of the parotid gland is a superficial parotidectomy with careful identification and preservation of the facial nerve (5). The parotid gland has two lobes, a superficial lobe and a deep lobe. Most tumors are located in the superficial lobe of the parotid gland and can be excised easily. Retrospective studies have indicated that this combined modality treatment can reduce the local recurrence rate by 5 - 40% (6, 7).

However, in certain situations, such as high surgical risk of damage to the facial nerve, advanced inoperable cancers, unfavorable cosmetic outcome after surgery, lymph node metastases, and deep-lobe malignant tumors, radiotherapy should be the preferred treatment (5). Because of its proximity to many critical structures, such as the oral cavity, brainstem, auditory apparatus, spinal cord, optical nerves, and the lenses of the eyes, parotid cancer treatment using radiation still remains a very challenging task. Currently, the most commonly used radiotherapy techniques for the treatment of the parotid cancers are: 1) an ipsilateral wedged pair of 6 MV photon beams oriented at oblique angles to encompass the entire parotid bed, 2) an ipsilateral field treated with high energy electrons (12, 16 or 20 MeV), and 3) a combination of high energy photon and electron beams (6 MV + 12 or 16 or 20 MeV) with proper weighting (8, 9, 10) (Figure 1). However, all these techniques have drawbacks. The first technique gives a low radiation dose to the contra-lateral parotid gland and high doses to the oral cavity, brainstem, cochlea, optical nerves, the lenses of the eyes, and spinal cord. In addition, because relatively high energy photon beams are used, the slow build-up effect of the photon beams results in a low skin dose. This is not acceptable for the treatment of the majority of the parotid cancers

because most parotid cancers are located in the superficial lobe of the parotid gland. Although high energy electrons may be the best in terms of normal tissue sparing, it is impossible to achieve depth dose conformity with a single electron energy only. The third technique typically employs a high energy electron beam (12-20 MeV) and a single 6 MV photon beam. However, good matching of photon and electron beams is not easy to achieve and poor matching may produce areas of high inhomogeneity within the tumor dose distribution.

Recently, with the availability of photon beam intensity modulated radiation therapy (IMRT) and computer-controlled multileaf collimators (MLC), there has been wide interest in using photon beam IMRT to treat head and neck cancers and parotid cancers in particular (9, 11-16). A common feature of the head and neck cancers is their complex geometry. IMRT has shown potential to produce a highly conformal dose distribution around the concave-shaped target volumes and a steep dose gradient near the organs at risk (OAR). These characteristics can spare radiosensitive normal structures and reduce complication rates (17-19). In addition, there has been an effort to exploit IMRT to improve local-regional tumor control through dose escalation. Now, many commercial inverse treatment planning systems and MLCs are available.

Although the photon beam IMRT is a powerful tool for treating the parotid tumors that extend deeply into tissue below the skin surface, it is not suitable to treat very shallow targets due to the low surface doses and large depth of photon beam penetration. For photon beam IMRT, the slow attenuation of photon beams can still deliver a high dose to the critical structures that are far from the target. A promising alternative approach is modulated electron radiation therapy (MERT) (20-21). The rapid dose falloff of electron beams makes electron therapy an attractive treatment modality for some shallow targets such as parotid tumors. Conceptually, each MERT plan consists of multiple ports (gantry angles) with different electron energies (energy modulation) and optimized beam intensity (intensity modulation). Dose conformity in the depth direction

may be achieved by electron energy modulation, which is unique to MERT. Dose conformity and uniformity in the lateral direction may be achieved by intensity modulation using an electron-specific MLC (EMLC). Through both intensity and energy modulations, MERT is capable of delivering highly conformal doses to targets with complex shapes and of sparing surrounding normal tissue, particularly, the distal critical structures.

However, because of severe electron in-air scattering, the conventional photon beam MLC is not suitable for the delivery of MERT plans. To deliver MERT plans effectively, we designed and manufactured a prototype EMLC based on the results of Monte Carlo simulations and a conventional Varian 25 x 25 cm² electron applicator (22). Based on the manufacturer's specifications of the beam production system and the EMLC design, electron beams collimated by this EMLC were simulated for a Varian Clinac 2100C linear accelerator using the EGS4/BEAM code (23, 24). Subsequently, using the simulated electron beams, MERT plans for parotid cancers were created. In the present study, we investigated the possibility of treating parotid tumors using modulated electron radiation therapy by comparing MERT plans with corresponding photon beam IMRT plans in terms of target dose coverage and normal tissue sparing.

Materials and Methods

Electron MLC

We have previously reported a prototype manually-driven electron specific MLC for the delivery of MERT plans (20, 21). Ideally, the EMLC leaves should be placed in such a position that the bottom of the leaves is as close to the patient skin as possible in order to produce a clinically acceptable field. However, because of the existing electronic circuitry used to detect the insertion of the electron cutout at the last scraper of a standard Varian 25 x 25 cm² electron applicator, it was impossible to place the EMLC leaves at that position without changing the existing electron applicator design significantly. Thus,

initially, the steel frame of the EMLC leaves was temporally inserted into the electron cutout mount and the leaves were placed about 1 cm above the last scraper. This configuration resulted in a 10 cm air gap between the bottom of the EMLC leaves and the patient skin for a nominal 100 cm source-surface distance (SSD) (**Figure 2 (A)**). To further lower the EMLC leaves and, thus, reduce in-air electron scattering and the penumbra, we have now removed the entire last scraper of the electron applicator and its electronic accessories. The EMLC frame was placed at the bottom of the modified electron applicator and stabilized with eight screws. This modification reduced the air gap to 5.0 cm between the bottom of the EMLC leaves and the patient skin (**Figure 2 (B)**). Since the electronic circuitry for detecting the electron cutout was completely removed, we were able to avoid activating interlocks associated with electron beam accessory malfunction while inserting the EMLC assembly into the linac treatment head. Thus, even if the linac was in the electron mode, the gantry could still be rotated, making the delivery of MERT plans with multiple beam angles possible.

MERT Plans

Based on manufacturer's specifications of the beam production system and the electron applicator design, electron beams produced by a Varian Clinac 2100C linear accelerator and collimated by the EMLC were simulated using the EGS4/BEAM code. Monte Carlo simulations were carried out using a group of 22 Pentium Pro CPUs (200 MHz) and 10 Pentium III CPUs (450 MHz), all running EGS4/BEAM, MCDOSE (23, 24), and their utilities under the Linux operating system. All simulation parameters, such as the electron and photon energy cutoffs (ECUT and PCUT), the maximum fractional energy loss per electron step (ESTEPE), and the number of initial electron histories, were specified in the EGS4/BEAM input file. In this study, we used ECUT = 700 KeV and PCUT = 10 KeV, below which all remaining energy was assumed to deposit on the spot. ESTEPE was set to 0.04. The EMLC was included in the EGS4/BEAM simulations as an MLC component module. The number of initial electron histories ranged from 2-30 million, depending on the electron energy. Phase space data were scored at a plane of 100

cm SSD after the particles had transported through the linac treatment head, the EMLC, and the air gap beneath it. Based on this simulated electron beam, the MERT plans were then created using our modified EGS4/MCDOSE code.

The CT scans of representative parotid cancer patients were obtained from our department's patient database. The CT images were acquired with the patients in supine position. During CT scanning, a thermoplastic facial mask with three fiducials was used for the purpose of patient immobilization and target localization for the subsequent treatments. For each patient, about 90 images with a slice thickness of 3.0 mm were acquired over the entire treatment area. Each CT image had an in-plane resolution of 512 x 512 pixels, with each voxel being 0.94 x 0.94 x 3.0 mm³ in size. The CT images were transferred to an AcQSim system (Marconi Medical Systems, Inc., Cleveland, OH) for further processing. The clinical tumor volume (CTV) and critical structures were contoured on the axial CT images by a radiation oncologist using the AcQSim workstation. The gross tumor volume (GTV) was defined based on diagnostic imaging and clinical findings. It consisted of gross primary and nodal tumors. The CTV was constructed by expanding the GTV 1.0 cm in all directions to cover microscopic extension of the tumor. The PTV was obtained by adding a 0.5 cm margin uniformly to CTV to account for patient setup uncertainty and organ shift. Like photon beam IMRT, any structures whose dose needed to be kept below a certain limit or whose statistics were to be calculated in the MERT plan had to be contoured. Only those targets and structures that were contoured were considered in the plan and included in the final statistics. In addition, in order for our MERT inverse planning programs to work properly, all regions of interest were delineated as separate structures. No structure overlapping was allowed for the current version of our programs. In this study, the critical structures to be protected were the spinal cord, brainstem, optical chiasm, optical nerve, and orbits. The CT images, along with the outlined structures, were transferred to a workstation using the DICOM 3.0 format and then converted into a format that was compatible with EGS4/MCDOSE code so that they could be sent to our designated

Monte Carlo treatment planning machines. The final CT images used in MERT planning had an in-plane resolution of 128×128 pixels with a voxel size of $0.35 \times 0.35 \times 0.30 \text{ cm}^3$ that balanced resolution with the Monte Carlo dose calculation time. Additionally, the CT numbers were converted into mass densities and material types for Monte Carlo simulations. Based on the CT numbers, each voxel was designated as being one of the three materials: air, tissue or bone. This provided the approximate effective atomic numbers, cross-sections, and stopping powers for each voxel.

Figure 3 shows the simplified MERT planning flowchart. To facilitate the description of the flowchart, we will use the term *field* to specify each beam angle/electron energy combination and reserve the term *port* to indicate a single beam orientation (gantry angle). Thus, a plan in which five electron energies are delivered at a single gantry angle may be said to have one port and a total of five fields. In this study, the MERT plans consisted of three ports and a total of fifteen fields, as summarized in **Tables 1 and 2**. Like the photon beam IMRT, the first step in creating a MERT plan was to select a set of suitable beam orientations, i.e., gantry angles, to fully cover the target volume while sparing the adjacent critical structures as much as possible. Each port was then divided into $1.0 \times 1.0 \text{ cm}^2$ beamlets, i.e., the smallest beam elements for dose calculation. This means that beam intensity within a $1.0 \times 1.0 \text{ cm}^2$ beamlet could not be further differentiated. The beamlet size was defined at the isocenter plane. The goal of this step was to determine how many beamlets were required to simulate for each port. The user specified the isocenter, gantry, collimator, and couch angles, the desired beamlet size, and the dimension of the search space. A program calculated which beamlets intersected the target and created a text file containing these beamlets and their coordinates. This file was used by MCDOSE to pre-calculate the beamlet dose kernels. The total number of beamlets was the sum of the beamlets over all ports. A beamlet could be turned off, i.e., assigned a weight of zero, but continued to remain active throughout optimization. After the selection of a proper set of beam angles, we needed to decide which electron energies to use for each beam angle. To do so, we computed a tumor

depth map for each beam angle, whose pixel size was the same as that of a beamlet, i.e., $1.0 \times 1.0 \text{ cm}^2$. Based on the tumor depth distribution and assuming that the electrons lost energy at about 2 MeV/cm in tissue, we were able to determine a suitable set of electron energies for each beam angle. Since, in most of the cases, the target was not spherical in shape, different beam angles could have different sets of electron energies. The obvious advantage of this approach was the removal of those electron energies that contributed less to the target dose and, thus, the reduction in the number of fields used and delivery time.

The next step was to calculate beamlet dose kernels using MCDOSE. The beamlet dose kernel was the Monte Carlo calculated dose array for all structures due to a single beamlet. Each element of the dose kernel represented the dose delivered to a dose calculation point or voxel assuming a unit beamlet weight. These values are also referred to as dose deposition coefficients. Thus, the purpose of this step was, given a set of unit beamlet weights, to calculate the dose distribution in every structure that we were interested in. To optimize beamlet weights or intensity maps, a quadratic objective function augmented with dose-volume constraints was constructed. This was based on the assumption that there existed a quadratic relationship between the delivered dose and the biological effect. The overall objective function contained a linear component for each structure. Within each structure, each of the individual constraints contributed linearly to the objective function. Following the construction of the objective function, the optimization of beamlet weights was initiated. The core of the optimization procedure was the well-known conjugate gradient search algorithm. A complete description of the conjugate gradient search algorithms may be found in any number of sources. The major advantage of the gradient search technique was its fast convergence speed, as compared to stochastic optimization techniques, such as simulated annealing. We believe that the gradient search algorithm was a good choice for future routine clinical implementation of MERT. During the optimization, care was exercised to avoid negative weights. These non-physical results were eliminated by scaling step sizes to avoid stepping over the

boundary of the acceptable solution space and by projecting gradients onto the boundaries.

Following the beamlet weight optimization, the resulting fifteen optimized continuous intensity maps were stratified into five discrete intensity levels in preparation for leaf sequencing. The fifteen discrete intensity maps were then converted to fifteen step-and-shoot leaf sequences (26) based on the technique proposed by Bortfeld et al. (27). Since the dose distribution delivered by the ideal beamlets could be different from that delivered by the leaf sequences, A Monte Carlo dose calculation was performed again based on the fifteen discrete intensity maps reconstructed from the corresponding fifteen leaf sequences. With these new dose kernels, the leaf sequence segment weights were re-optimized. This second optimization differed from the first one in two aspects. The first optimization was entirely based on idealized beamlets, without considering the EMLC geometry, while the second optimization took into account not only the EMLC geometry, but also leaf end transmission and Bremsstrahlung leakage. Thus, the first optimization produced the best dose distribution possible, while the second one gave the actual delivered dose.

The MERT plans with three coplanar beams (gantry angles: 205° , 235° , and 255°) were created using our modified EGS4/MCDOSE treatment planning system. The schematic layout of the beam orientations is shown in **Figure 4A**. The beam orientations were selected based on the goodness of target coverage by the beams. Each gantry angle or port was treated with five nominal electron energies (6, 9, 12, 16, and 20 MeV) separately. The intensities of each energy for each particular gantry angle were determined by the optimizer. The prescribed dose to the target was 50.0 Gy, with a conventional fractionation scheme of 2.0 Gy per fraction, 5 fractions per week, and 25 fractions in total. The goal of the treatment planning was to cover the entire target with isodose lines between 95% and 107% of the prescribed dose as recommended by ICRU Report No. 50 (25). Isodose lines were normalized to 55.0 Gy for all plans.

IMRT Plans

The CT images, together with the outlined structure set, were transferred from the AcQSim system to a commercial treatment planning system (CORVUS, NOMOS Corp, Sewickley, Pennsylvania). The corresponding photon beam IMRT plans were computed using our standard clinical protocol. As in the MERT planning, the PTV was defined by adding a 0.5 cm immobilization and localization uncertainty to the CTV. The CORVUS IMRT system allows the target volume to grow based on a user-specified positional uncertainty caused by tissue motion and setup errors. The isocenter of the beams was placed approximately at the geometric center of the target. The goal dose to the target was 50.0 Gy, with the minimum and maximum doses being 49.0 Gy and 54.0 Gy, respectively. The CORVUS IMRT system also allows the user to specify a percent target volume allowed below the goal dose. In this study, we used 4% for this value. For the critical structures, the limit dose ranged from 37.0 to 42.0 Gy, with the volume allowed above the limit dose being 5%. The maximum allowable dose to the critical structures was set to be 40.0 Gy. IMRT plans using other combinations of the dose volume constraints were also tried. It was found that above-described constraints optimized target dose coverage and conformity against critical structure sparing. The final IMRT plans consisted of five coplanar gantry angles, each being treated with a 4 MV photon beam. The gantry angles and beam energy were selected in such a way as to minimize unnecessary normal tissue and critical structure irradiation. However, in this study, beam orientations were not optimized. IMRT plans of different beam number and angle combinations were generated. Each of the plans was carefully reviewed and evaluated on the basis of target dose coverage and normal tissue sparing. Plan evaluation indicated that the plans with coplanar beams: 0° , 205° , 235° , 270° , and 320° gave the best results. Therefore, this beam arrangement was used in this study. Isodose lines were also normalized to 55.0 Gy for all IMRT plans. **Figure 4B** shows the IMRT beam orientations.

Tissue heterogeneity correction was performed during the beamlet intensity optimization and final dose calculation. Like the MERT planning system, the CORVUS IMRT system also uses an integral dose volume histogram-based cost function. The current version of the CORVUS IMRT software supports only one optimization technique, simulated annealing (28). To obtain the best possible beamlet intensities and thus, the optimal dose distribution, the optimizer mode was set to continuous. This mode determines the internal representation of the beamlet intensities and is, in general, the best choice for most treatment plans. All IMRT plans used in this study were created based on a Varian Clinac 2100C linear accelerator and delivered in the step-and-shoot mode. The machine was equipped with a 26-leaf pair photon MLC, capable of producing $1.0 \times 1.0 \text{ cm}^2$ beamlets.

Results and Discussion

Electron MLC

Figure 5 shows a photo of the EMLC assembly inserted on the treatment head of a Varian Clinac 2100C linear accelerator. The EMLC had 30 steel leaf pairs, with each leaf being 0.476 cm wide, 20.0 cm long, and 2.54 cm thick. Both sides and ends of the leaves were made parallel with the central beam axis. The maximum opening was $14.2 \times 15.5 \text{ cm}^2$ when all leaves were completely retracted, giving the largest radiation field of $15.0 \times 16.3 \text{ cm}^2$ projected at 100 cm SSD. The EMLC leaves could be pushed in and pulled out easily. For each of the beam segments, the corresponding field shape was obtained by manually positioning the leaves according to their coordinates, which were computed from the electron beam leaf-sequencing program. To set the field shapes more efficiently, currently, we first drew the field shapes on a piece of hard cardboard at a ratio of 1:1 and cut them out. The field shapes were then set using these pre-cut cardboard templates. In the near future, we will develop a faster and more accurate technique of setting field shapes.

In the past, attempts have been made to use a photon MLC for electron beam collimation (30). Using a photon MLC in this circumstance has its obvious advantages. On one hand, treatment planners could easily make plans that consist of both photon and electron beams. On the other hand, the plans could be delivered using the existing linear accelerators without any further capital investment. Unfortunately, because of the severe electron scattering in the air, the quality of the electron beam collimated by a photon MLC is significantly degraded and is no longer clinically useful. Here, we present a practical and viable approach to the electron beam collimation — an electron-specific MLC. Our results indicated that the newly modified EMLC was able to provide sufficient beam collimation for MERT plan delivery.

Intensity Maps

Figure 6A shows a 3-D beam's eye view of a representative parotid tumor viewed at the beam angle of 235° . **Figure 6B** shows the corresponding tumor depth map at the same beam angle, in which different pixel gray scale levels represent different depths of the target. Darker pixels indicate the area where the tumor extended deeper into the tissue at this particular beam angle. As clearly demonstrated in the tumor depth map, this case was a good candidate for a MERT treatment because the target was superficial and, in addition, it had an irregular boundary. Based on the tumor depth map, a histogram was created, showing the tumor depth distribution (**Figure 7**). Out of 115 pixels, 2 pixels had a mean depth of greater than 5.0 cm, 2 pixels had a mean depth between 4.0 and 5.0 cm, 20 pixels had a mean depth between 3.0 and 4.0 cm, and 43 pixels had a mean depth between 2.0 cm and 3.0 cm, 37 pixels had a mean depth between 1.0 and 2.0 cm, and 11 pixels had a mean depth between 0.0 and 1.0 cm. Thus, the electron beams of 12, 16, and 20 MeV would be the best choices for this case in terms of depth dose conformity at this beam angle.

However, for this preliminary study, we chose to use all available electron energies. **Figures 8A to 8E** show representative beam intensity maps for a MERT plan

for the 6, 9, 12, 16, and 20 MeV fields at the beam angle of 235° . In all figures, each pixel represents a $1 \times 1 \text{ cm}^2$ beamlet projected at the isocenter. Darker pixels indicate higher beam intensity levels, which correspond to a longer beam on time. White background indicates zero beam intensity. These are areas where beams were blocked all the time by the EMLC leaves. In reality, however, there was about 1% radiation leakage through the EMLC leaves. As can be seen in the intensity maps, the optimizer gave significant weights to the 12, 16, and 20 MeV fields, while small weights were assigned to the 6 and 9 MeV fields. It was these different electron energy weights that brought about the energy modulation. By carefully examining the intensity maps and the tumor depth map, we noticed that the MERT intensity maps largely reflected the tumor depth distribution. The superposition of these intensity maps yielded not only the optimal lateral dose conformity, but more importantly the optimal depth dose conformity. The numbers of segments needed to produce these intensity maps were 18 (for 6 MeV), 18 (for 9 MeV), 12 (for 12 MeV), 18 (for 16 MeV), and 14 (for 20 MeV), giving a total of 80 segments for this port. This number was comparable to the number of segments for a photon field in a typical IMRT head and neck plan. For comparison, the corresponding optimized photon beam IMRT intensity map for the 4 MV field at the same beam angle is shown in **Figure 8F**. This intensity map, actually consisting of two separate maps, was combined together manually. This was because the size of the target in the anterior-posterior direction was fairly large, the MLC leaves could not cover the entire target with one field only. Thus, this 235° port split into two sub-fields. Like the MERT intensity maps, each pixel in the photon beam IMRT map represents a $1 \times 1 \text{ cm}^2$ beamlet projected at the isocenter. Compared to its MERT counterparts, the photon beam IMRT intensity map shows a relatively uniform intensity distribution, indicating a lack of depth dose modulation. The combined photon beam IMRT intensity map required a total of 120 segments to deliver, divided into 62 and 58 segments for each sub-field, respectively. For both the MERT and the IMRT plans, we counted both “step” and “shoot” that were listed in the step-and-shoot leaf sequence files as a segment. Thus, in the case of the combined photon beam IMRT intensity map, it required 60 steps and 60 shoots to produce. Since

the delivery time is linearly proportional to the number of segments in a leaf sequence file, we can say that the MERT plan required relatively less time to deliver. It is worth pointing out that in this study, we used all five available electron energies, which, in most cases, is not necessary. Let us take the 6 and 9 MeV electron beams as examples. As shown in **Figures 8A and 8B**, the optimizer gave them very low weights. Their contributions to the dose distribution in the final MERT plan were not significant. Therefore, they could have been deleted from the plan, leaving only three electron beams in the plan. The final three leaf sequence files would have had less number of segments. The total delivery time would have been even less.

Dose Distributions

Figures 9A and 9D show the comparison of the MERT and IMRT isodose distributions for the central axial slices from a representative parotid cancer case. **Figures 9B and 9E** show the comparison of the isodose distributions for the central coronal slices from the same example. **Figures 9C and 9F** show the comparison of the isodose distributions for the central sagittal slices also from the same example. The isodose distributions are shown in color lines. In both plans, the isodose curves were normalized to 55.0 Gy, representing 10, 20, 30, 40, 50, 60, 70, 80, 90, and 100%, respectively. Only selected isodose lines are labeled in the figures. The red colored target in the IMRT plan represents the PTV, while the red colored target in the MERT plan represents the CTV. The final MERT dose distribution was computed based on 15 intensity maps reconstructed from corresponding 15 step-and-shoot leaf sequences. The beamlet size was $1 \times 1 \text{ cm}^2$ for both plans. It is evident from the isodose distributions that higher isodose lines covered the target fairly well in terms of conformity in both plans, with the MERT plan showing an overall better conformity for all isodose lines in all three anatomical planes. As to the lower isodose lines, the photon beam IMRT plan exhibited a relatively poor conformity. As anticipated, the exit doses of the photon beams penetrated much deeper regions than the doses delivered by the electron beams. This resulted in significant, but unnecessary doses to distal areas, including some of the critical structures.

This was clearly demonstrated in the axial and coronal slices of the IMRT plan, in which the 30% isodose line covered the spinal cord fully and the 40% isodose line covered the brain stem and the orbits partly,. In contrast, the corresponding MERT plan showed an excellent critical structure sparing because of the rapid falloff of the electron beams. The 30% isodose line covered only small portions of the spinal cord, the brain stem, and the right orbit. The left orbit was almost completely spared, as shown in **Figures 9D and 9E**. Thus, it is very clear that the MERT plan provided a better target dose coverage and homogeneity than the photon beam IMRT plan.

Dose-Volume Histograms (DVH)

To evaluate the plans objectively, we analyzed the cumulative dose-volume histograms (DVH) of the plans. The cumulative dose-volume histograms displayed quantitative statistical information about the target dose coverage and homogeneity and normal tissue sparing. Each cumulative DVH curve represents the fractional volume that received a particular dose or higher for that structure. It provides radiation oncologists and medical physicists with a very effective tool to evaluate completing treatment plans created with different parameters or even with different treatment planning systems (TPS). The DVHs for the target and the critical structures considered in this study from a representative parotid cancer case are shown in **Figure 10**. Based on the DVHs, it is evident that the MERT plan provided a more homogenous dose coverage to the target than the corresponding photon beam IMRT plan as the former's DVH is more vertical than the latter's. In the MERT plan, the maximum, minimum, and mean doses delivered to the CTV were 55.82, 40.50, and 50.32 Gy, respectively, while the corresponding doses delivered to the CTV in the IMRT plan were 60.38, 17.30, and 50.24 Gy, respectively, resulting in some undesirable hot and cold spots. Obviously, the photon beam IMRT plan exhibited some degree of dose inhomogeneity. In addition, in the photon beam IMRT plan, about 3% of the CTV received a dose of greater than or equal to 55 Gy and 5 % of the CTV received a dose of less than or equal to 45 Gy. In contrast, the MERT plan gave much better statistics. Less than 0.5% of the CTV received a dose of greater than or equal

to 55 Gy and approximately 1.5% of the CTV received a dose of less than or equal to 45 Gy. All these suggest that the MERT plan provide a better dose homogeneity. It has been known that conventional treatment modalities using electron beams exhibit a higher degree of dose inhomogeneity in comparison with photon beam techniques. In part, this is caused by tissue heterogeneity and skin surface irregularity. Here, we see that with electron energy and intensity modulations, it is possible to reduce the degree of dose heterogeneity and achieve a satisfactory dose distribution and uniformity.

Significant differences between the two DVHs for the critical structures indicated that the MERT plan also delivered much less doses to the critical structures than the photon beam IMRT plan. It is undoubtedly clear from **Figure 10** that the MERT plan showed a superior normal tissue sparing. The maximum, minimum, and mean doses to the spinal cord in the MERT plan were 16.62, 0.02, and 5.24 Gy, respectively, while the corresponding doses in the photon beam IMRT plan were 36.22, 0.60, and 17.50 Gy. Only 16% of the spinal cord volume in the MERT plan received a dose of greater than or equal to 10 Gy compared to 97% in the IMRT plan. Similar sparing for other structures were also observed in the MERT plan. The maximum, minimum, and mean doses given to the brainstem in the MERT plan were 13.65, 0.45, and 2.66 Gy, respectively. In contrast, the corresponding doses given in the photon beam IMRT plan were 29.88, 8.45, and 16.66 Gy, significantly higher than the doses delivered in the MERT plan. As to the orbits, both the MERT and the photon beam IMRT plans gave very low doses. Especially, the MERT plan delivered an extremely low dose to the contra-lateral orbit, with the maximum, minimum, and mean doses being 0.15, 0.01, and 0.05 Gy, respectively. This is very significant and clinically relevant since the tolerance dose for the lenses is only 10 ~ 15 Gy. In the cases we studied, the contra-lateral parotid gland was not contoured as an independent critical structure. However, based on the isodose distributions shown in **Figure 9**, it is clear that the dose delivered to the contra-lateral parotid gland for the MERT plan was well under the established tolerance dose of 20 ~ 30 Gy (29). Even if we increased the prescribed dose to 60 Gy, the dose delivered to the

contra-lateral parotid gland for the MERT plan would be still kept well within the tolerance. It is very important to point out that the mean dose to the non-target tissue in the photon beam IMRT plan was 7.54 Gy as compared with 3.95 Gy in the MERT plan. This is of clinical significance as the MERT plan could significantly reduce low radiation doses to large normal tissue volume.

For many years, parotid cancers have been largely treated using one of these three radiotherapy techniques: an ipsilateral wedged pair of photon beams oriented at oblique angles, an ipsilateral field treated with high energy electrons, and a combination of high energy photon and electron beams with carefully chosen weights. Unfortunately, because of the intrinsic limitation of the underlying physics, all these techniques are not able to produce treatment plans that provide both a high degree of target dose conformity and a significant normal tissue sparing. Recently, the photon IMRT has shown some success in treating certain head and neck cancers, but it is still not suitable to treat shallow tumors due to extremely low surface dose and excessively high exit dose. The low surface dose is not effective in killing tumor cells in superficial tissues. The high exit dose constitutes a significant risk to the normal function of the distal critical structures, such as the spinal cord and the contra-lateral orbit and parotid gland. Therefore, it would be desirable to develop a technique that can eliminate these drawbacks. As the results presented here indicate, through both electron intensity and energy modulations, MERT was able to deliver highly conformal doses to targets with complex shapes. In the mean time, it provided sufficient protection of the critical structures and substantial normal tissue sparing. Considering the radiation side effects and the quality of life limiting organs at risk like the contra-lateral parotid gland and orbit, it is necessary to keep the dose to the healthy tissue to a minimum and preserve the organ normal function as much as possible. In this respect, MERT had an undisputable advantage and a great potential.

Conclusions

Based on the results of this comparative dosimetric study, we conclude that EMLC was able to provide sufficient beam collimation for MERT treatments and for superficial targets, such as parotid cancers, MERT offered not only a better target dose coverage and uniformity, but also a superior normal tissue sparing. Therefore, it could become the treatment of choice for superficial tumors. As the development of the computer-controlled EMLC is underway, we believe that the widespread routine implementation of this novel technique for superficial tumors should be investigated.

Acknowledgements

This study was supported in part by grants DAMD17-00-1-0443 (Yulin Song and Steve Jiang), DAMD17-00-1-0444 (Todd Pawlicki), and DAMD17-01-1-0635 (Lei Xing) from the US Department of Defense. In addition, we would like to express our sincere thanks to Varian Medical System, Palo Alto, CA, for providing electron applicators for this study.

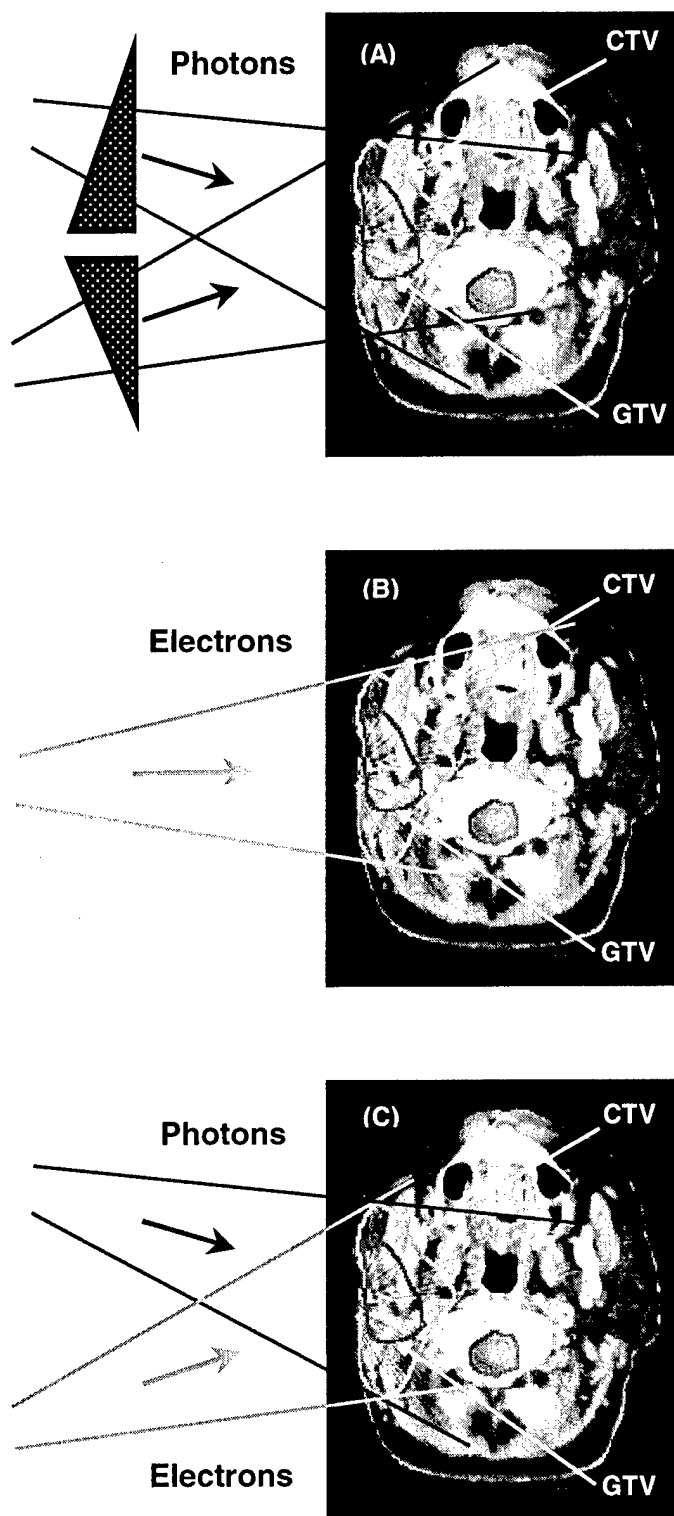


Figure 1

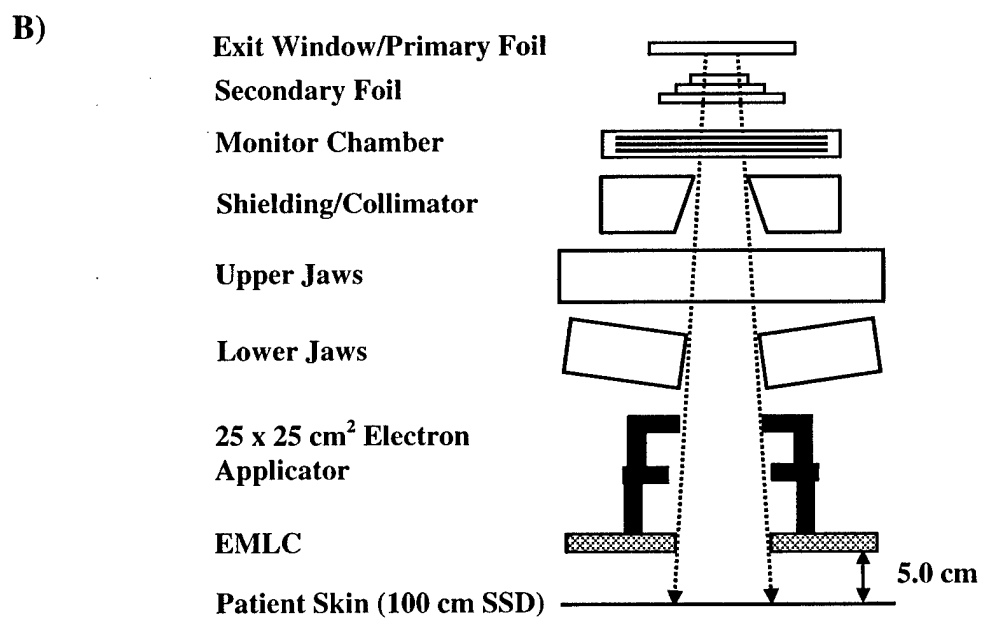
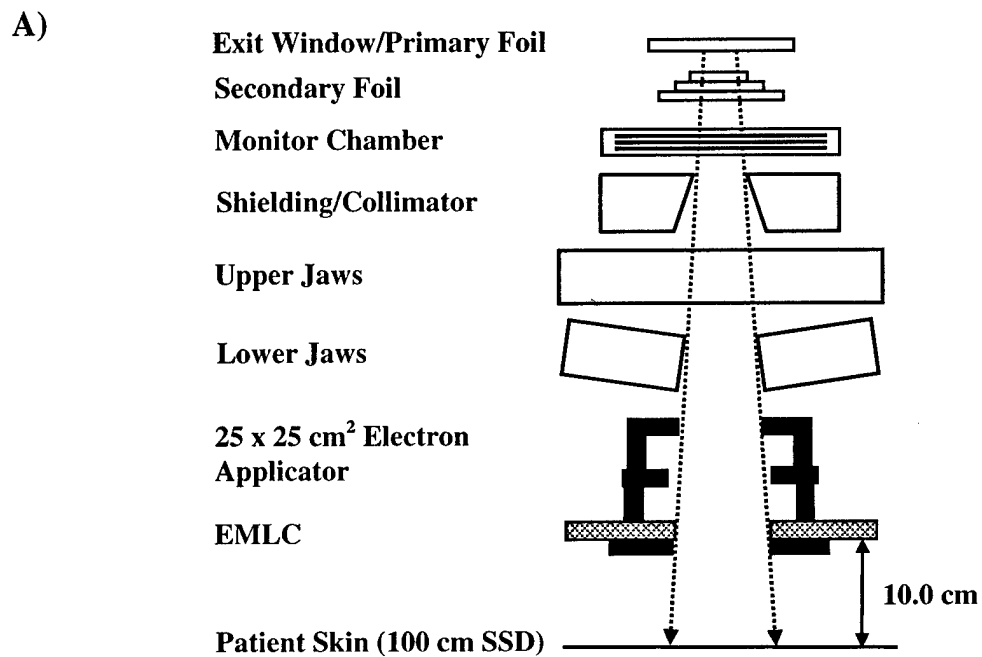


Figure 2

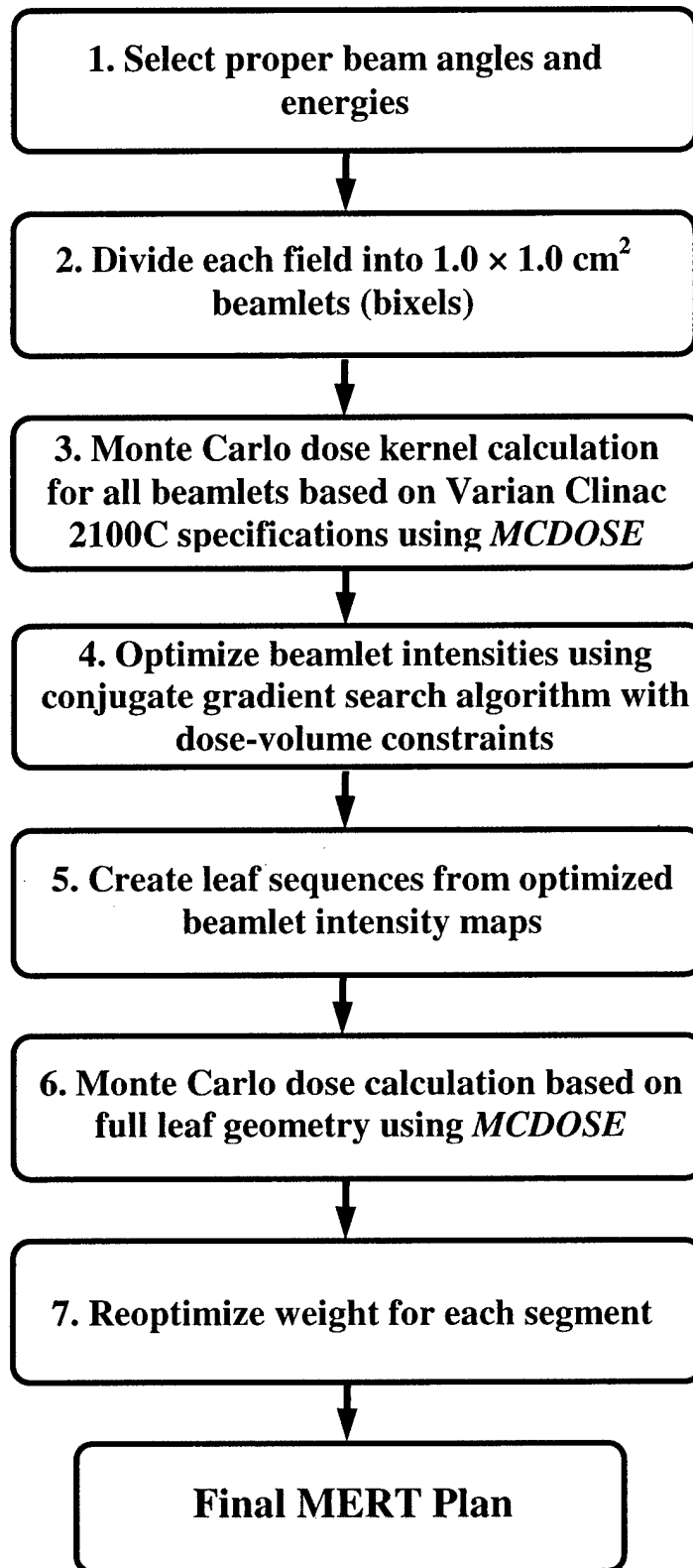


Figure 3

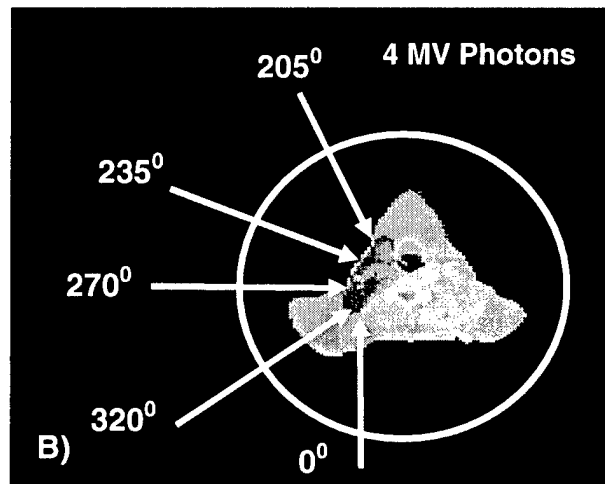
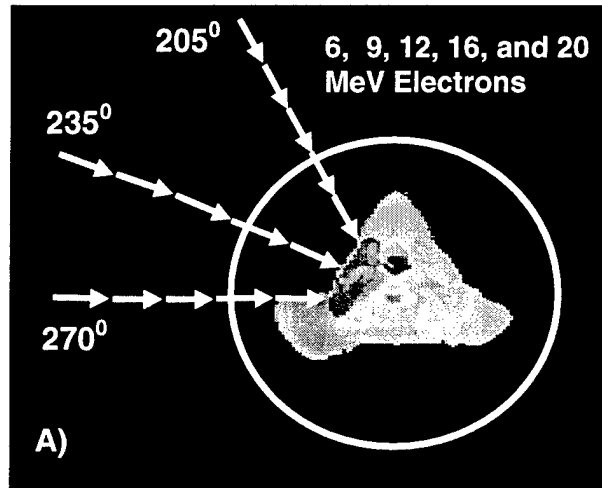


Figure 4

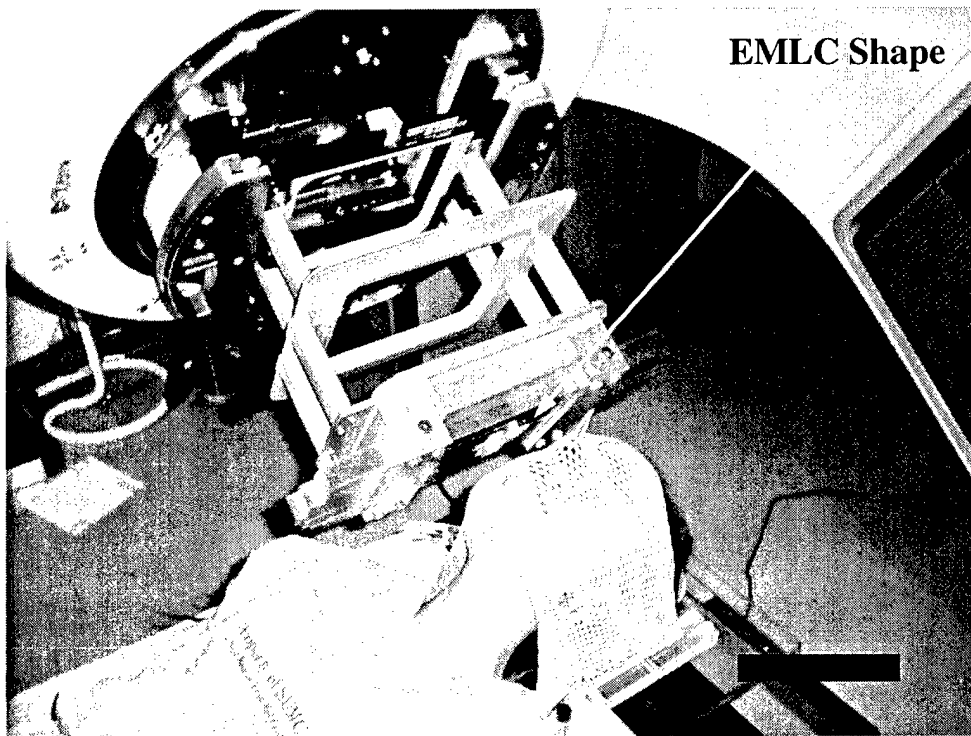
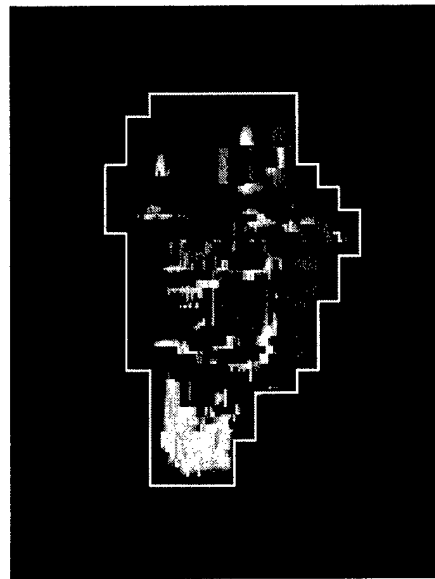


Figure 5

A



B

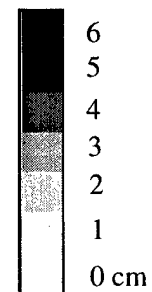
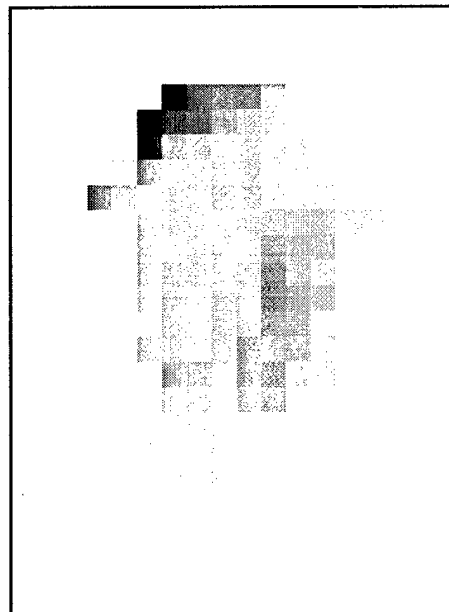


Figure 6

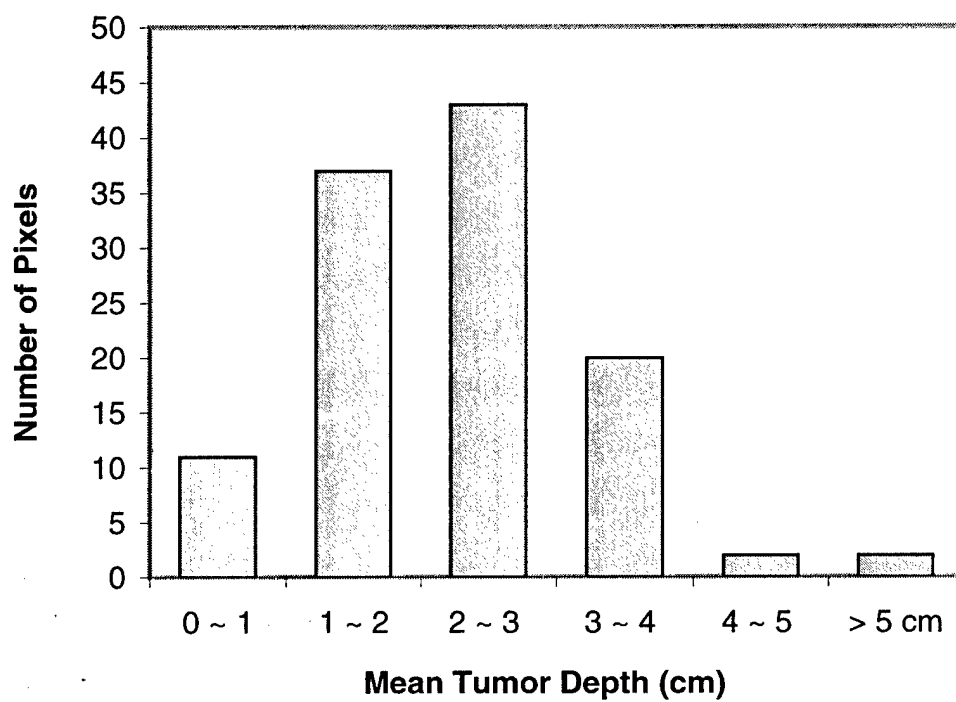
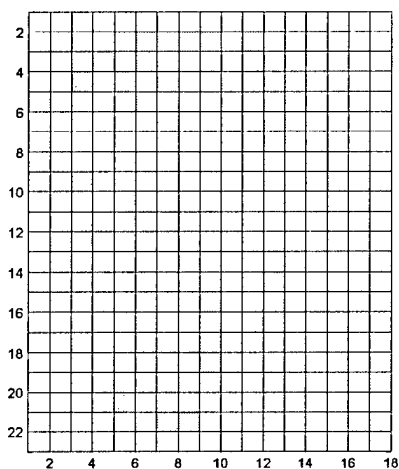
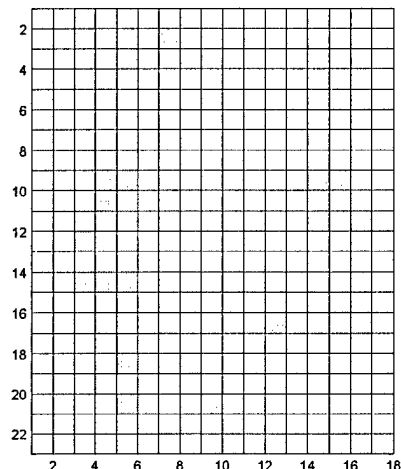


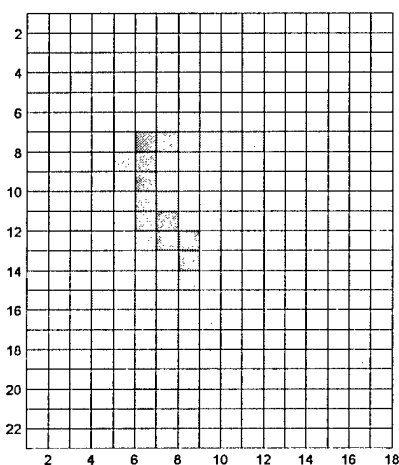
Figure 7



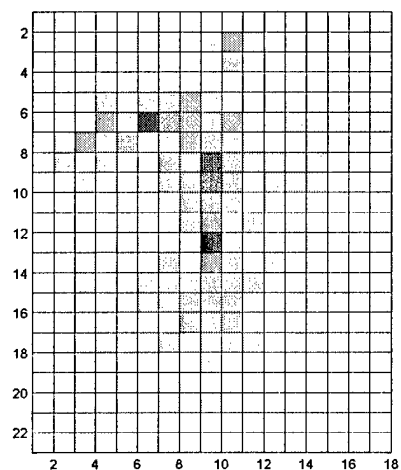
A. MERT plan 6 MeV field



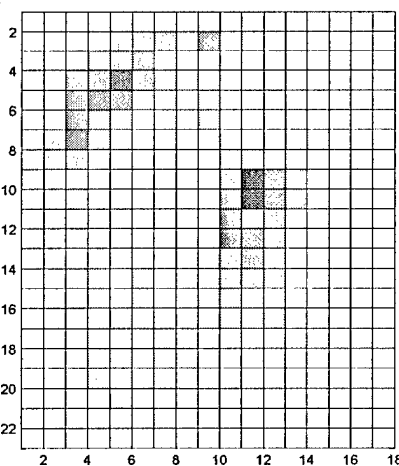
B. MERT plan 9 MeV field



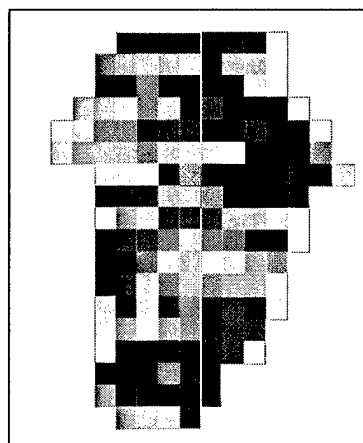
C. MERT plan 12 MeV field



D. MERT plan 16 MeV field



E. MERT plan 20 MeV field



F. IMRT plan 4 MV field

Figure 8

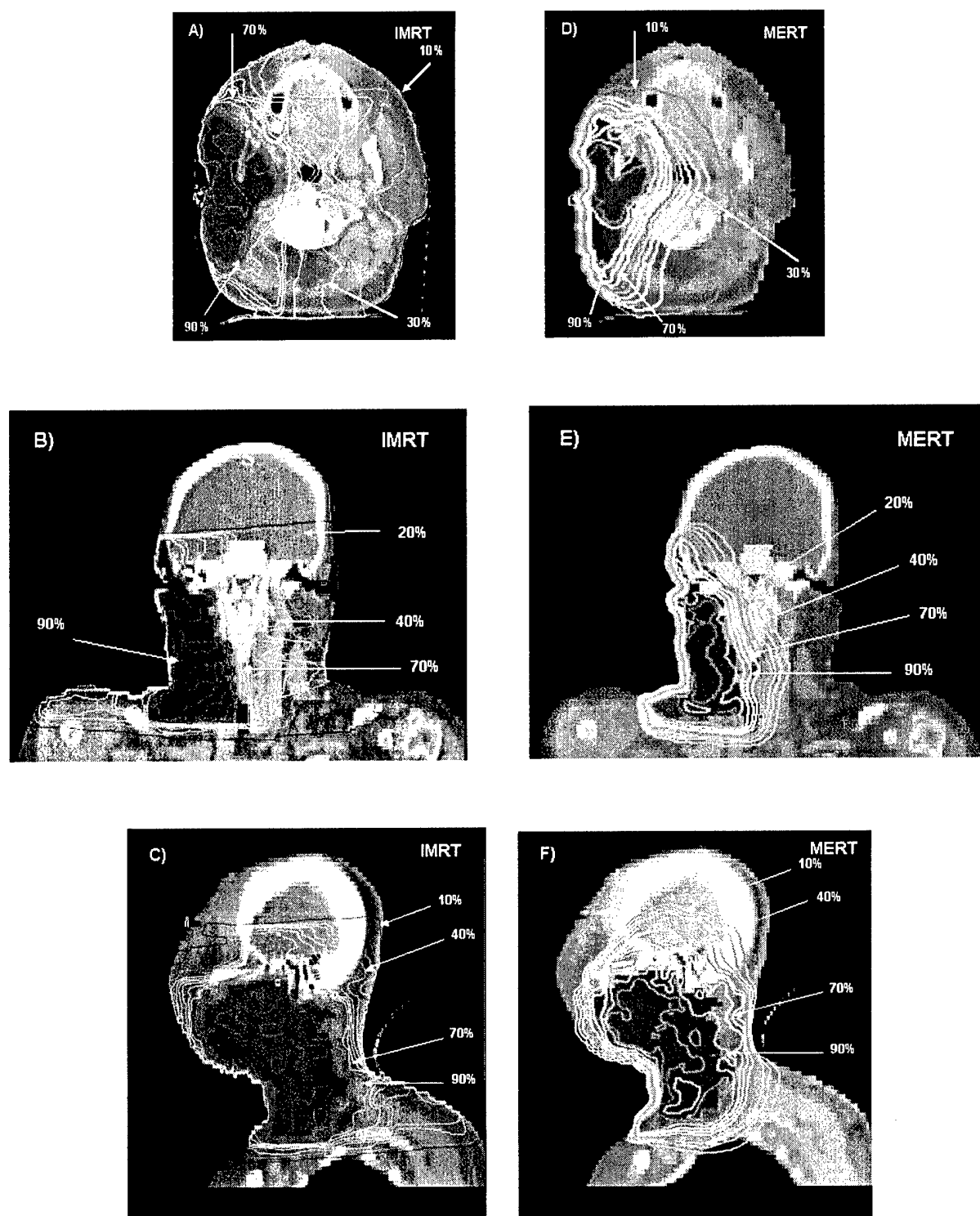


Figure 9

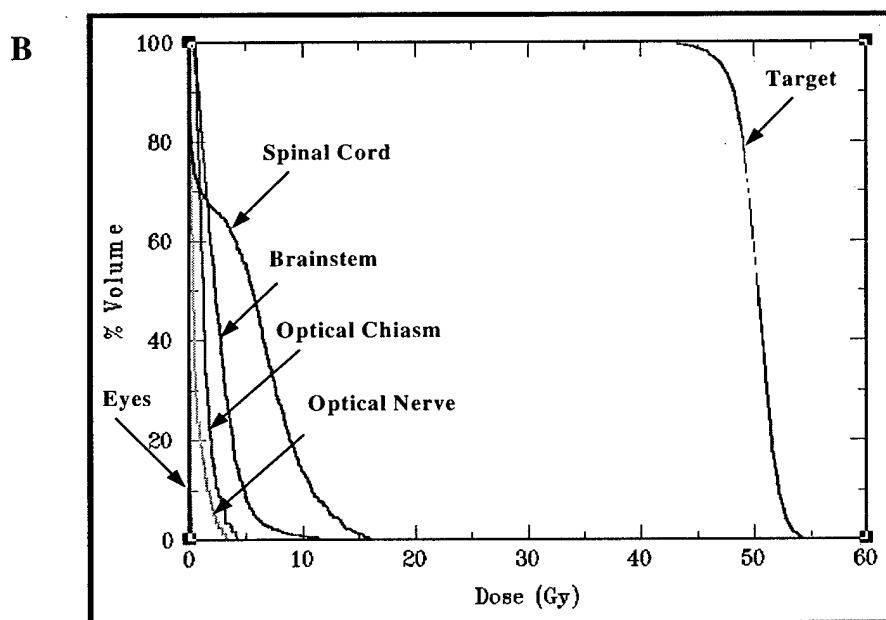
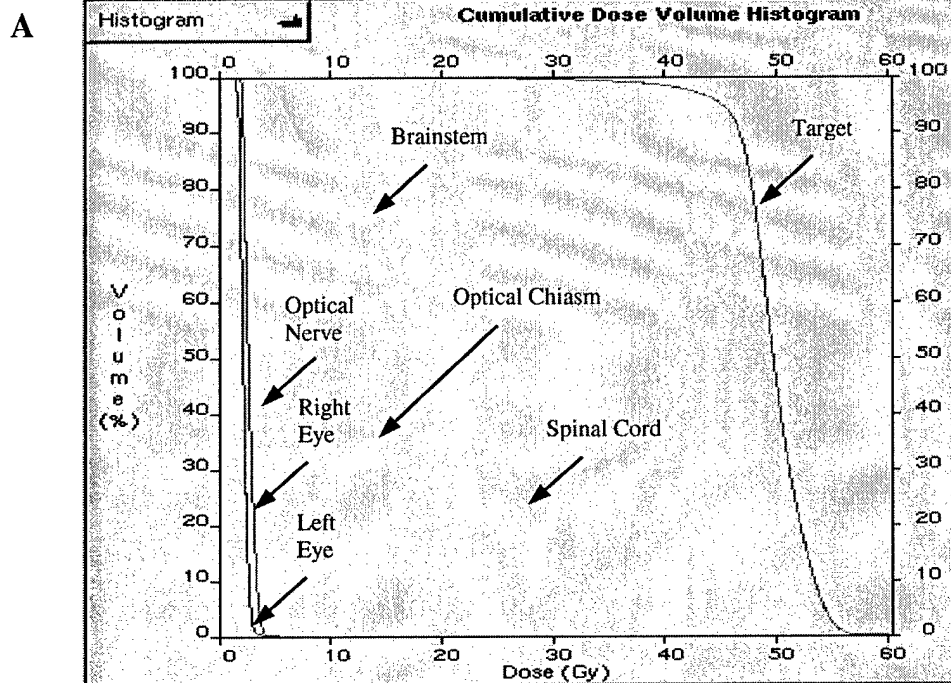


Figure 10

FIGURE LEGENDS

Figure 1

Conventional radiotherapy techniques for the treatment of parotid tumors. (A) An ipsilateral wedged pair of 6 MV photon beams oriented at oblique angles to cover the entire parotid bed, (B) An ipsilateral field treated with high energy electrons (12, 16 or 20 MeV), and (C) A combination of high energy photon and electron beams (6 MV + 12 or 16 or 20 MeV) with proper weighting.

Figure 2

Schematic drawings of the EMLC and a Varian Clinac 2100C treatment head. (A) The manually-driven EMLC was originally placed at the last scraper of a standard Varian 25 x 25 cm² electron applicator. This resulted in a considerably large air gap (10 cm) between the bottom of the EMLC leaves and the patient skin for a nominal 100 cm SSD. (B) To further lower the EMLC leaves, we have now removed the entire last scraper of the electron applicator and its electronic circuitry. The EMLC was placed immediately at the bottom of the modified electron applicator and stabilized with eight screws. This modification reduced the air gap to 5.0 cm between the bottom of the EMLC leaves and the patient skin.

Figure 3

The MERT treatment planning flowchart.

Figure 4

Schematic layouts of the beam orientations. (A) Each MERT plan consisted of three coplanar ports, oriented at 205°, 235°, and 255°, respectively. Each port was treated with five nominal electron energies (6, 9, 12, 16, and 20 MeV) consecutively. (B) Corresponding photon beam IMRT plan had five coplanar ports: 0°, 205°, 235°, 270°, and 320°, with each port being treated with a 4 MV photon beam.

Figure 5

A photo of the EMLC assembly mounted on a Varian Clinac 2100C linear accelerator. The air gap between the bottom of the EMLC leaves and the patient skin was 5.0 cm. The gantry angle was 235° .

Figure 6

A representative parotid tumor and corresponding tumor depth map. (A) A 3-D beam's eye view of a parotid tumor at the beam angle of 235° . (B) Corresponding tumor depth map, with darker pixels indicating the deeper parts of the tumor at this viewing angle.

Figure 7

A representative tumor depth histogram. The histogram was created based on Figure 6B, showing the number of pixels distribution as a function of mean tumor depth. Based on this distribution, a suitable set of electron energies were selected for this particular beam angle.

Figure 8

Representative beam intensity maps. (A-E) Intensity maps for the MERT plan for the 6, 9, 12, 16, and 20 MeV fields at the beam angle of 235° . (F) Corresponding photon beam IMRT intensity map for the 4 MV field at the same beam angle. This intensity map consisting of two separate intensity maps and combined together manually.

Figure 9

Comparison of the MERT and IMRT plan isodose distributions. (A, D) Isodose distributions for the central axial slices for a representative parotid cancer case. (B, E) Isodose distributions for the central coronal slices from the same case. (C, F) Isodose distributions for the central sagittal slices from the same case. The isodose curves,

normalized to 55.0 Gy, represent 10, 20, 30, 40, 50, 60, 70, 80, 90, and 100%, respectively. Only selected isodose lines are labeled here.

Figure 10

Comparison of dose volume histograms (DVH) for the photon beam IMRT (A) and MERT (B) plans. Clearly, the MERT plan shows a superior normal tissue sparing and a better dose distribution.

Table I. List of ports used in the MERT plans

Port No	Gantry Angle
1	205 ⁰
2	235 ⁰
3	270 ⁰

Table II. List of fields used in the MERT plans

Field No	Gantry Angle	Beam Energy (MeV)
1	205 ⁰	6
2	205 ⁰	9
3	205 ⁰	12
2	205 ⁰	16
5	205 ⁰	20
6	235 ⁰	6
7	235 ⁰	9
8	235 ⁰	12
9	235 ⁰	16
10	235 ⁰	20
11	270 ⁰	6
12	270 ⁰	9
13	270 ⁰	12
14	270 ⁰	16
15	270 ⁰	20

References

1. Parker, S., Tong, T., Bolden, S., and Wingo, P., "Cancer Statistics", *CA Cancer J Clin*, **47**:5-27, 1997.
2. Seifert, G., Brocheriou, C., Cardesa, A., and Eveson, J. W., "WHO International Classification of Tumors. Tentative Histological Classification of Salivary Gland Tumors", *Pathol Res Pract*, **186**(5):555-581, 1990.
3. Garden, A. S., El-Naggar, A. K., et al, "Postoperative Radiotherapy for Malignant Tumors of the Parotid Gland", *Int J Radiat Oncol Biol Phy*, **37**:79-85, 1997.
4. Spino, I. J., Wang, C. C., and Montgomery, W. W., "Carcinoma of the Parotid Gland. Analysis of Treatment Results and Patterns of Failure After Combined Surgery and Radiation Therapy", *Cancer*, **71**:2699-2705, 1993.
5. Lenhard, Jr., R. E., Osteen, R. T., and Gansler, T., "Clinical Oncology", *American Cancer Society*, 297-329, 2001.
6. North, C. A., Lee, D-J, Piantedosi, S., Zahurak, M. S., Johns, M. E., "Carcinoma of the Major Salivary Glands Treated by Surgery Plus Postoperative Radiotherapy", *Int J Radiat Oncol Biol Phy*, **18**:1319-1326, 1990.
7. Sykes, A. J., Logue, J. P., Slevin, N. J., Gupta, N. K., "An Analysis of Radiotherapy in the Management of 104 Patients with Parotid Carcinoma", *Clin Oncol*, **7**:16-20, 1995.
8. Yaparpalvi, R., Fontenla, D. P., Tyerech, S. K., Boselli, L. R., and Beitler, J. J., "Parotid Gland Tumors: A Comparison of Postoperative Radiotherapy Techniques Using Three Dimensional (3D) Dose Distributions and Dose-Volume Histograms (DVHS)", *Int J Radiat Oncol Biol Phy*, **40**(1):1319-1326, 1990.

9. Nutting, C. M., Rowbottom, C. G., Cosgrove, V. P., Henk, J. M., Dearnaley, D. P., Robinson, M. H., Conway, J., and Webb, S., "Optimization of Radiotherapy for Carcinoma of the Parotid Gland: A Comparison of Conventional, Three-Dimensional Conformal, and Intensity-Modulated Techniques", *Radiother Oncol*, **60**:163-172, 2001.
10. Garden, A. S., El-Naggar, A. K., Morrison, W. H., Callender, D. L., Ang, K. K., and Peters, L. J., "Postoperative Radiotherapy for Malignant Tumors of the Parotid Gland", *Int J Radiat Oncol Biol Phy*, **37**(1):79-85, 1997.
11. Boyer, A. L., Geis, P., Grant, W., and Carol, M., "Modulated Beam Conformal Therapy for Head and Neck Tumors", *Int J Radiat Oncol Biol Phy*, **39**:227-236, 1997.
12. Bragg, C. M., Conway, J., and Robinson, M. H., "The Role of Intensity-Modulated Radiotherapy in the Treatment of Parotid Tumors", *Int J Radiat Oncol Biol Phy*, **52**(3):729-738, 2002.
13. Wu, Q., Manning, M., Schmidt-Ullrich, R., and Mohan, R., "The Potential for Sparing of Parotids and Escalation of Biologically Effective Dose with Intensity-Modulated Radiation Treatments of Head and Neck Cancers: A Treatment Design Study", *Int J Radiat Oncol Biol Phy*, **46**(1):195-205, 2000.
14. Cozzi, L., Fogliata, A., Lomax, A., and Bolsi, A., "A Treatment Planning Comparison of 3D Conformal Therapy, Intensity Modulated Photon Therapy and Proton Therapy for Treatment of Advanced Head and Neck Tumors", *Radiother Oncol*, **61**:287-297, 2001.
15. Vineberg, K. A., Eisbruch, A., Coselmon, M. M., McShan, D. L., Kessler, M. L., and Fraass, B. A., "Is Uniform Target Dose Possible in IMRT Plans in the Head and Neck?", *Int J Radiat Oncol Biol Phy*, **52**(5):1159-1172, 2002.

16. Rowbottom, C. G., Nutting, C. M., Webb, S., "Beam-Orientation Optimization of Intensity-Modulated Radiotherapy: Clinical Application to Parotid Gland Tumors", *Radiother Oncol*, **59**:169-177, 2001.
17. Boyer, A. L., "The Physics of Intensity-Modulated Radiation Therapy", *Phys Today*, 38-44, September 2002.
18. Boyer, A. L., *et al*, "Intensity-Modulated Radiation Therapy: Current Status and Issues of Interest", *Int J Radiat Oncol Biol Phy*, **51**(4):880-914, 2001.
19. Xing, L., Cotrutz, C., Hunjun, S., Boyer, A. L., Adalsteinsson, E., and Spielman, D., "Inverse planning for functional image-guided IMRT", *Phys Med Biol*, **47**:3567-3578, 2002.
20. Lee, M. C., Deng, J., Li, J., Jiang, S. B., and Ma, C-M, "Monte Carlo Based Treatment Planning for Modulated Electron Radiation Therapy", *Phys Med Biol*, **46**:2177-2199, 2001.
21. Ma, C-M, Pawlicki, T., Lee, M. C., Jiang, S. B., Li, J., Deng, J., Yi, B , Mok, E., and Boyer, A. L., "Energy-and Intensity-Modulated Electron Beams for Radiotherapy", *Phys Med Biol*, **45**:2293-2311, 2000.
22. Song, Y., Jiang, S. B., Lee, M. C., Ma, C-M, and Boyer, A. L. "A Multileaf Collimator for Modulated Electron Radiation Therapy (MERT) for Breast Cancer", the Department of Defense Breast Cancer Research Program Meeting, Proceedings Volume I:17-5, 2002.
23. Nelson, W. R., Hirayama, H., and Rogers, D. W. O., "The EGS4 Code System", SLAC-Report-265, Stanford Linear Accelerator Center, 1985.

24. Rogers, D. W. O., Faddegon, B. A., Ding, G. X., Ma, C-M., Wei, J., and Mackie, T. R., "BEAM: A Monte Carlo Code to Simulated Radiotherapy Treatment Units", *Med Phys*, **22**:503-524, 1995.
25. ICRU, "Prescribing, Recording, and Reporting Photon Beam Therapy-Report 50", Washington, DC, *International Commission on Radiation Units and Measurements*, 1993.
26. Bortfeld, T., Kahler, D. L., Waldron, T. J., and Boyer, A. L., "X-ray Field Compensation with Multileaf Collimators", *Int J Radiat Oncol Biol Phy*, **28**:723-730, 1994.
27. Boyer, A. L., and Yu, C. X., "Intensity Modulated Radiation Therapy with Dynamic Multileaf Collimators", *Semin Radiat Oncol*, **9**:48-59, 1999.
28. Webb, S., "Optimization of Conformal Radiotherapy Dose Distribution by Simulated Annealing", *Phys Med Biol*, **34**:1349-1370, 1989.
29. Chao, K. S. C, Low, D. A., Perez, C. A., and Purdy, J. A., "Intensity Modulated Radiation Therapy in Head and Neck Cancers: The Mallinckrodt Experience", *Int J Cancer (Radiat Oncol Invest)*, **90**:92-103, 2000.
30. Karlsson, M. G., Karlsson, M. K., and Ma, C-M, "Treatment Head Design for Multileaf Collimated High-Energy Electrons", *Med Phys*, **26**:2125-2132, 1999.

Monte Carlo based treatment planning for modulated electron beam radiation therapy

Michael C Lee, Jun Deng, Jinsheng Li, Steve B Jiang¹ and C-M Ma

Radiation Physics Division, Department of Radiation Oncology,
Stanford University School of Medicine, Stanford, CA 94305-5304, USA

E-mail: mclee@reyes.stanford.edu

Received 5 March 2001

Published 19 July 2001

Online at stacks.iop.org/PMB/46/2177

Abstract

A Monte Carlo based treatment planning system for modulated electron radiation therapy (MERT) is presented. This new variation of intensity modulated radiation therapy (IMRT) utilizes an electron multileaf collimator (eMLC) to deliver non-uniform intensity maps at several electron energies. In this way, conformal dose distributions are delivered to irregular targets located a few centimetres below the surface while sparing deeper-lying normal anatomy. Planning for MERT begins with Monte Carlo generation of electron beamlets. Electrons are transported with proper in-air scattering and the dose is tallied in the phantom for each beamlet. An optimized beamlet plan may be calculated using inverse-planning methods. Step-and-shoot leaf sequences are generated for the intensity maps and dose distributions recalculated using Monte Carlo simulations. Here, scatter and leakage from the leaves are properly accounted for by transporting electrons through the eMLC geometry. The weights for the segments of the plan are re-optimized with the leaf positions fixed and bremsstrahlung leakage and electron scatter doses included. This optimization gives the final optimized plan. It is shown that a significant portion of the calculation time is spent transporting particles in the leaves. However, this is necessary since optimizing segment weights based on a model in which leaf transport is ignored results in an improperly optimized plan with overdosing of target and critical structures. A method of rapidly calculating the bremsstrahlung contribution is presented and shown to be an efficient solution to this problem. A homogeneous model target and a 2D breast plan are presented. The potential use of this tool in clinical planning is discussed.

¹ Present address: Department of Radiation Oncology, Massachusetts General Hospital and Harvard Medical School, Boston, MA 02114, USA.

1. Introduction

In an increasing number of centres, the treatment of tumours in close proximity to critical organs or targets possessing complex geometries is performed via intensity modulated radiation therapy (IMRT) with photon beams. While this technique is an extremely powerful tool for treating tumours that are located more than a few centimetres below the surface, the physics of x-ray energy deposition suggests that photon IMRT is not well suited to the treatment of shallow targets. Furthermore, in many cases the slow attenuation of photon beams makes conventional photon IMRT a poor choice for some targets with distal critical structures. In contrast, electron beams, with their comparatively higher surface doses and more rapid depth-dose fall-offs, are well suited to these targets. However, conventional electron beam delivery and treatment planning systems are ill-equipped for the delivery of complex dose distributions.

Modulated electron beam radiation therapy (MERT) is a new electron modality that has been developed to deliver highly conformal doses to shallow targets (Lief *et al* 1996, Hyödynmaa *et al* 1996, Zackrisson and Karlsson 1996, Åsell *et al* 1997, Ebert and Hoban 1997, Karlsson *et al* 1998, 1999, Åsell *et al* 1999, Ma *et al* 2000b). Dose conformality in the beam direction may be achieved by energy modulation, while lateral uniformity and conformity may be achieved by intensity modulation via a variable collimator. Many of the studies into MERT have used microtron based scanned beam systems. In principle, energies should be selectable with relative ease on these systems, while intensity modulation could be achieved by scanning the narrow electron beam. Studies using these systems have shown MERT to be feasible and potentially of great value; however, the cost and availability of such machines have greatly restricted research and development of scanned beam based MERT. Investigations into the use of the photon MLCs on accelerators that broaden electron beams with scattering foils have also been performed, including the possibility of using helium along the beam axis to reduce deleterious air scatter (Karlsson *et al* 1999, Lee *et al* 2000a).

As an alternative to these systems, an electron-specific multileaf collimator (eMLC) has been proposed (Lee *et al* 2000a, Ma *et al* 2000b). It has been demonstrated that a collimator consisting of 1.5 cm thick tungsten leaves located at the level of the last scraper of a 25×25 cm² electron applicator allows shaping of the field to a higher degree of resolution than is possible using the photon MLC. By superposition of a number of different field shapes, an intensity modulated field may be delivered. However, a system for generating such a plan required further research.

Any planning system requires the ability to perform accurate dose calculations. Because electron transport and scatter in matter is strongly influenced by density and material composition, dose calculation in heterogeneous media is extremely challenging. Conventional algorithms typically utilize variants of the 3D Hogstrom pencil beam algorithm, based on Fermi-Eyges transport theory (Hogstrom *et al* 1981). However, it has been well documented that in heterogeneous phantoms and small irregular fields, this algorithm results in large regions of dose error (Cygler *et al* 1987, Bielajew *et al* 1987, Mah *et al* 1989, Mackie *et al* 1994, Ma *et al* 1999). It has been demonstrated that the Monte Carlo method can provide accurate dose estimations under all circumstances (Cygler *et al* 1987, Mackie *et al* 1994, Kawrakow *et al* 1996, Mohan 1997, Kapur 1999, Ma *et al* 1999). Additionally, Monte Carlo transport algorithms can be used to accurately assess the perturbations to the electron fluence caused by beam modifiers, such as multileaf collimators (assuming an accurate source model). The combined effects of field size, shape, and collimator on absolute doses can then be included as planning considerations with a high degree of accuracy. Thus, while the need for Monte Carlo dose computation of photon IMRT plans has been debated, the importance of Monte Carlo in conventional electron plans is well established, and it follows that more complex MERT plans will also benefit from Monte Carlo computation.

Most photon IMRT planning systems divide a radiation field into small spatial elements, or beamlets, and separate out the dose contribution from each beamlet as the first step in planning. This beamlet simulation may be performed by analytical methods or by the Monte Carlo method (Boyer and Mok 1985, Pawlicki *et al* 1999, Laub *et al* 2000). By optimizing on the dose distributions, weights or intensities for each beamlet may be obtained and the resulting 2D intensity maps may be converted into an MLC leaf sequence for delivery. The assumption is that the dose computed on a beamlet-by-beamlet basis is the same as the dose delivered via the actual leaf sequence. Even in photon IMRT this is not the case, the MLC tongue-and-groove effect being the most notable violation (van Santvoort *et al* 1996, Yu 1998), with transmission through leaf ends and edges also being a factor (Chen *et al* 2000). In these instances, an additional correction must be applied to leaf sequences or simply during dose reconstruction so that planners may evaluate the true dose rather than an ideal dose.

This difference between beamlet and delivered doses is the primary challenge encountered in developing a MERT planning system. During delivery, electrons (and contaminant photons) have the opportunity to scatter off or through leaf ends and sides to a much greater degree than photons. Additionally particles incident on the closed portions of the leaves may generate secondary particles, in particular bremsstrahlung photons (Lee *et al* 2000a). These effects result in a leaf-delivered dose that may differ significantly from the beamlet predicted dose. The magnitude of this effect depends on the specific plan and cannot be known *a priori*.

Holmes (2001) has proposed a tomotherapy planning system that accounts for aperture-dependent non-idealities such as leakage and head scatter. In that system, leaf sequencing occurred as part of the optimization procedure, and thus aperture-dependent leakage and head scatter could be included for each 'field' delivered by the tomotherapy system. This work seeks to apply the same concept to MERT planning, though in this case Monte Carlo calculated aperture-dependent non-idealities are incorporated via a *post hoc* procedure rather than during the optimization.

The objective of this study was first to examine the differences between beamlet deliveries and dose distributions from simulations in which particles were transported in the eMLC. A Monte Carlo based treatment planning system was then developed in which the bremsstrahlung leakage and leaf-end scatter and transmission could be properly accounted for in the optimization process. A method of implicitly including the effect of particle transport in the leaves was developed, allowing for faster calculations. Using this system, a plan is generated for an artificial homogeneous phantom and for a CT phantom of an intact breast. Based on these results, potential directions for further research are discussed.

2. Methods

2.1. Monte Carlo simulations

Source parameter descriptions of 6, 9, 12, 16 and 20 MeV (nominal energy) electron beams were obtained using a procedure described elsewhere and summarized here. Electron beam simulations of a Varian Clinac 2100C (Varian Oncology Systems, Palo Alto, CA) were performed using the EGS4/BEAM code (Nelson *et al* 1985, Rogers *et al* 1995). A 25 × 25 cm² type III (open walled) applicator was used in these simulations. Vendor supplied geometries were used to define the component modules in the BEAM simulation, with photon jaw settings adjusted according to the nominal beam energy. It has been shown elsewhere that the resulting phase space data from these simulations, when used in EGS4/DOSXYZ or MCDOSE dose calculations, provide agreement with measured data to within 2% on depth-dose and transverse profiles, as well as output factor calculations (Kapur *et al* 1998, Kapur 1999, Lee *et al* 2000c).

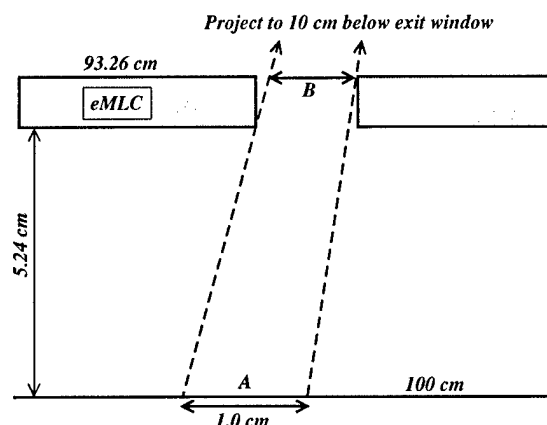


Figure 1. A schematic diagram of the beamlet and electron MLC geometry. The beamlet is defined as having a width of exactly 1.0 cm at 100 cm from the photon target, regardless of where the phantom surface is actually located. This is shown in A. The source plane is reconstructed at 93.26 cm, coincident with the upper surface of the eMLC. The beamlets are then defined at this plane B by ray tracing from the approximate location of the electron virtual source, 10 cm below the exit window. Only particles within B are reconstructed and beamlet simulation occurs without any collimation. When leaves are simulated, their positions are set based on the geometric projections of the leaf edges, as shown. Thus there is an inherent difference in beamlet simulation and actual delivery.

During the simulation, 'latch bit' settings were used to delineate particles originating or scattering off the first two scrapers of the applicator (source 1 and 2), and electrons (source 3) and photons (source 4) that were well described by a virtual point source (Ma *et al* 1997, Ma and Rogers 1997, Jiang *et al* 2000). This four-source model has been shown to provide agreement with both the direct phase-space simulation and measured data (Jiang *et al* 2000). During dose calculations particles were generated according to this source model, thus eliminating the need for calculation and storage of large phase-space data files.

Unless otherwise noted, electrons were transported down to 0.70 MeV total energy (ECUT) and photons transported to 10 keV energy (PCUT), at which point the remaining energy was deposited on the spot. It has been documented that an ECUT of 0.70 MeV, corresponding to a residual continuous slowing down approximation range in water of <0.5 mm, is sufficient for most dosimetric purposes (Rogers *et al* 1995). Transport through the leaves and in air was performed using PRESTA for step-length calculations (Bielajew and Rogers 1987). For transport in the phantom, photon splitting and electron track repetition were employed as variance reduction techniques (Kawrawkow and Fippel 2000, Ma *et al* 2000a).

Dose calculations were performed using the EGS4 user code MCDOSE (Nelson *et al* 1985, Ma *et al* 2000a). This code has been described in detail elsewhere and has been shown to provide agreement with DOSXYZ and measured data to within 2% (Li *et al* 2000b). The code was modified and used for MERT planning as described in the following sections.

2.1.1. Electron beamlets. For each energy and port, electron beamlets were simulated for use in the inverse planning algorithm in a manner analogous to Monte Carlo based photon IMRT planning (Pawlicki *et al* 1999). Beamlet size was set at the level of isocentre, with a resolution of 1 cm. The beamlet was then defined by a virtual aperture located at the position of the upper surface of the electron MLC, 93.26 cm below the photon target. The beamlet size was defined

to be given by projections taken from the plane containing the isocentre to the approximate location of the electron virtual source, 10 cm below the photon target as determined during beam commissioning. This geometry is shown schematically in figure 1. The virtual aperture could be simulated in one of two ways:

- (a) By taking the beamlet to be an opening in a perfectly absorbing infinitely thin collimator, that is, sampling from the full $25 \times 25 \text{ cm}^2$ field and transporting only those particles that land in the beamlet.
- (b) Sampling directly within the beamlet itself, and never generating any particles in the remaining regions.

For efficiency, method (b) was selected with weighting factors defined as follows.

Let us consider a subset of a two-dimensional fluence profile ('beamlet') defined by $x = x_1$ to x_2 and $y = y_1$ to y_2 with area A_{beamlet} . If we sample within this beamlet according to the true distribution, then each particle can be given a weighting factor equal to the ratio of the integral fluence within the beamlet to the overall integrated fluence. If, however, we sample *uniformly* within this region, then we must apply an additional weighting factor to remove the biasing due to the uniform sampling. If the intensities (number of particles in a bin) are given as $F(x, y)$ and we consider a point (x', y') , then

$$w(x', y') = \frac{A_{\text{beamlet}}}{A_{\text{bin}}} \frac{F(x', y')}{\sum_x \sum_y F(x, y)} \quad (1)$$

where A_{bin} is the area of the spatial bin to convert number of particles to fluence and the summation represents the total number of particles in the source parameter file.

As mentioned above, each source parameter file contains fluence information for four subsources. Because spatial bins are defined in the same way for each subsource, it is possible to assign a cumulative distribution function (CDF) for each bin, describing the relative intensities of each source. Particles are sampled according to this CDF and hence no additional weighting factor is needed for subsources. Note that contaminant photons from the treatment head are included in the source reconstruction during both beamlet and eMLC simulation. Particle origins are uniformly sampled on each subsource (i.e. an electron has an equal probability of coming from each edge of an electron scraper). The reader is referred to Jiang *et al* (2000) for complete details on source reconstruction for this four-source model, with the aforementioned weighting factors for beamlet sampling.

During beamlet simulation, particles are reconstructed at the upper surface of the eMLC at a distance 93.26 cm below the nominal photon target position. The remaining air gap to the phantom is then explicitly simulated, thus accounting for the in-air scatter, such that the final fluence at the phantom surface is essentially a convolution of the original fluence and the scatter kernel.

2.1.2. Electron MLC simulation. A proposed design for an electron specific MLC (eMLC) has been described elsewhere and is summarized below (Lee *et al* 2000a). Based on measurements with a prototype system and Monte Carlo simulations, it has been shown that 1.5 cm thick tungsten leaves located at the level of the last scraper provide adequate electron collimation for MERT. Leaf ends and sides may be unfocused, though in this study leaf sides were considered to be focused to a point 10 cm below the photon target (for the 2D targets studied here, this has no significant effect). Note that while this study utilized this specific eMLC design, the results are general to any collimator in which leaf end scatter and transmission and bremsstrahlung leakage are non-trivial.

The MCDOSE code was modified to include the simulation of particle transport in such a collimator, placed according to arbitrary table, collimator and gantry angles, with leaves set

according to a leaf sequence file. The geometry coding routines were based upon macros used for block simulations (Li *et al* 2000a, b). In all simulations, a region extending from the field edge 5 mm into the leaves of the eMLC was subject to explicit simulation of all particles, up to the global transport cut-offs. Margins of thickness greater than 3 mm have been shown to be adequate for accounting for edge effects in cut-outs (Mubata *et al* 2000). Outside this region, one of two rejection methods was used to accelerate the simulations. In one method all particles in this region were rejected, while in the second method electrons were discarded based on a 2 MeV total energy cut-off while photons were transported explicitly. An alternative method for computing bremsstrahlung leakage was investigated and is described separately in section 2.1.3.

Each segment of the MERT plan was given a different number of histories based upon the number of monitor units to be delivered. Note, however, that the absolute dose is decoupled from the number of histories delivered, because the absolute dose for each field is separately computed assuming a single monitor unit delivery, and then rescaled to the correct value. However, for increased speed, the number of particles simulated was proportional to the number of MU to be delivered. In particular, the overall statistical uncertainty at a point after N segments with relative intensities w is given by

$$\sigma_{\text{tot}}^2 = \sum_{i=1}^N (w_i \sigma_i)^2. \quad (2)$$

If we express all the intensities in units of the minimum intensity, w_{min} , such that $w_i = \alpha_i w_{\text{min}}$, we may write

$$\sigma_{\text{tot}}^2 = \sum_{i=1}^N (\alpha_i^2 w_{\text{min}}^2 \sigma_i^2). \quad (3)$$

If we desire to have all segments provide an equal contribution to the overall uncertainty, then $(\alpha_i^2 \sigma_i^2)$ must stay constant over i . This implies that the square of the uncertainties should scale linearly with the square of the intensities, or equivalently, the number of histories for a field should scale with the square of the intensities. The uncertainty in the final plans was less than 1% at 1σ for the voxels with a dose $D > 0.5 D_{\text{max}}$. By using a low uncertainty (at the cost of high computation time), the noise-convergence issue of Monte Carlo based inverse planning can be minimized (Jeraj and Keall 2000, Keall *et al* 2000).

2.1.3. Bremsstrahlung background approximation. In a subset of the simulations, leakage photons were included in the calculations without explicit transport through the leaves. Using the EGS4/BEAM system, two phase space files were generated, one directly above and one directly below a 1.5 cm tungsten slab. Only particles passing through a $10 \times 10 \text{ cm}^2$ square centred on the slab's upper surface were transported and scored. The photons in the lower phase space were placed into angular bins of 1.0° (taken with respect to the central axis) and within each angular bin, particles were separated into energy bins of 0.5 MeV. A 'total photon yield' S was defined as the number of photons in the lower phase space divided by the total number of particles in the upper phase space. Note that this differs from the standard definition of bremsstrahlung yield in that all photons are scored including, for example, transmission, rather than only bremsstrahlung, and the yield is given per incident particle rather than per incident electron.

The Monte Carlo simulation employed the bremsstrahlung production cross sections of Koch and Motz (1959). The validity of the Monte Carlo method for studying thick-target bremsstrahlung has been discussed at length in the literature (e.g. Seltzer and Berger 1985, Faddegon *et al* 1990, 1991).

During source reconstruction, electrons that would be incident upon the upper surface of the eMLC are discarded (recall that the source plane and the top of the eMLC are coincident). A random number η is selected in the interval (0, 1], and if $\eta < (S/N_{\text{split}})$ then a photon of weight N_{split} is generated according to the joint angular/spectral distribution and simulated beginning from the bottom surface of the MLC. In these simulations, N_{split} was set at 10, thus utilizing a Russian roulette-style variance reduction technique. The assumption was made that the bremsstrahlung phase space was invariant across the field, and that at a given point the photon distribution was radially symmetric. The low-energy electrons produced in the leaves were also ignored. This greatly simplifies and accelerates both source model generation and reconstruction, and it is shown in section 3.1.3 that these assumptions allow for sufficient accuracy for treatment planning.

2.1.4. Absolute dose calibration. In general, Monte Carlo results are given in dose per incident particle. To convert to absolute dose, the dose distribution from a $15 \times 15 \text{ cm}^2$ field is calculated (for each separate energy) and the central axis maximum taken to be a calibration factor, $D_{\text{ref}}^{\text{ref}}$ (here, subscripts refer to fields and superscripts refer to measurement points). This value is given in cGy/particle. Then, an arbitrary point A in the reference field may be converted to absolute dose per monitor unit D , given in cGy MU^{-1} by

$$D = \frac{D_{\text{ref}}^A}{D_{\text{ref}}^{\text{ref}}} \quad (4)$$

Because some particles are ignored for various reasons during conversion from phase space to source parameter (particles going backwards, positrons, field size limits, etc), this simple calculation is only valid for a single source parameter file. To be used in any field (in particular, here, the $25 \times 25 \text{ cm}^2$ field), equation (4) may be expanded as

$$\frac{D_{25 \times 25}^A}{D_{\text{ref}}^{\text{ref}}} = \frac{D_{25 \times 25}^A}{D_{25 \times 25}^{\text{ref}}} \times \frac{D_{25 \times 25}^{\text{ref}}}{D_{\text{ref}}^{\text{ref}}} \quad (5)$$

The term $D_{25 \times 25}^{\text{ref}}$ can be calculated directly by simulating a $25 \times 25 \text{ cm}^2$ field. The second factor, $D_{25 \times 25}^{\text{ref}}/D_{\text{ref}}^{\text{ref}}$ cannot be taken from source parameter based Monte Carlo calculations, for reasons described above, i.e. some particles are not included during source parameter generation. However, this energy-dependent parameter may be taken from Monte Carlo simulations based on complete phase-space data or from measured applicator factors, defined as the ratio of absolute doses at the central axis maxima.

2.2. Optimization

The optimization method used was developed by Jiang (1998) and the salient features are described here. The system utilizes a steepest descent search algorithm, with a quadratic objective function augmented by dose-volume constraints. As usual, deviations from the prescribed dose p_0 contribute to the objective function in the following form

$$F_{\text{target}} = \sum_{i \in T} (d_i - p_0)^2 \quad (6)$$

with T denoting points in the target. The soft dose-volume constraints are given by Zangwill's penalty function (Buchanan and Turner 1992). In particular,

$$F_{\text{target}}^{\text{penalty}} = w_{\text{target}}^{\text{low}} \sum_{i \in T} \xi_i^{\text{low}} (d_i - p_1)^2 + w_{\text{target}}^{\text{high}} \sum_{i \in T} \xi_i^{\text{high}} (d_i - p_2)^2 \quad (7)$$

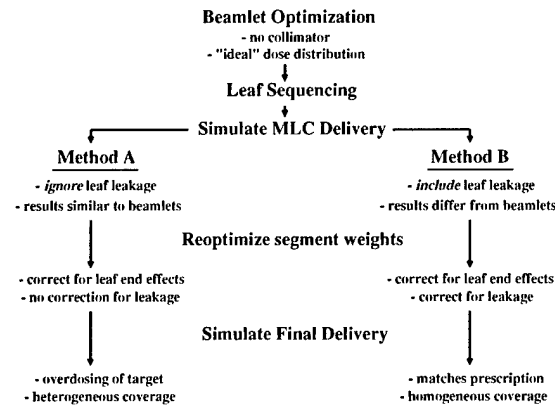


Figure 2. A schematic summary of the overall treatment plan. Each stage is discussed in detail in the text. 'Method A' utilizes a simplified leaf model and is shown to result in an inferior plan. 'Method B' utilizes either explicit particle transport in the leaves or a bremsstrahlung approximation, and results in a delivered doses that match well with prescriptions.

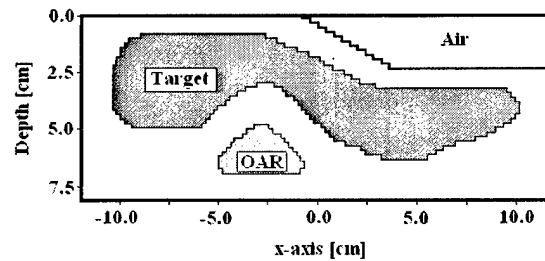


Figure 3. Schematic diagram of the test phantom. The target structure and organ at risk (OAR) are shaded and labelled accordingly. An extended air gap exists in the positive x region with the accelerator isocentre located at the origin of the diagram. The phantom material is ICRU tissue. The phantom extends 10 cm above and below the plane of the page.

where d_i is the dose at a point i , p_1 and p_2 are the upper and lower limits on target dose, w are the weights for the constraints and ξ_i is defined as 1 if the point i is too high/low and the volume constraint (number of points already in violation) has been reached. Similarly, critical structures are protected by adding upper-limit penalties in a dose-volume fashion. The overall objective function is then defined as

$$F_{\text{obj}} = F_{\text{target}} + r(F_{\text{target}}^{\text{penalty}} + F_{\text{critical}}^{\text{penalty}}) \quad (8)$$

where r rises with each Zangwill iteration. Further details on this method of optimization may be obtained from Jiang (1998).

3. Results and discussion

The general outline of the treatment planning procedure is given in figure 2. On occasion, the text will refer to 'method A' or 'method B'. These will correspond with the appropriate branch of the flowchart in figure 2.

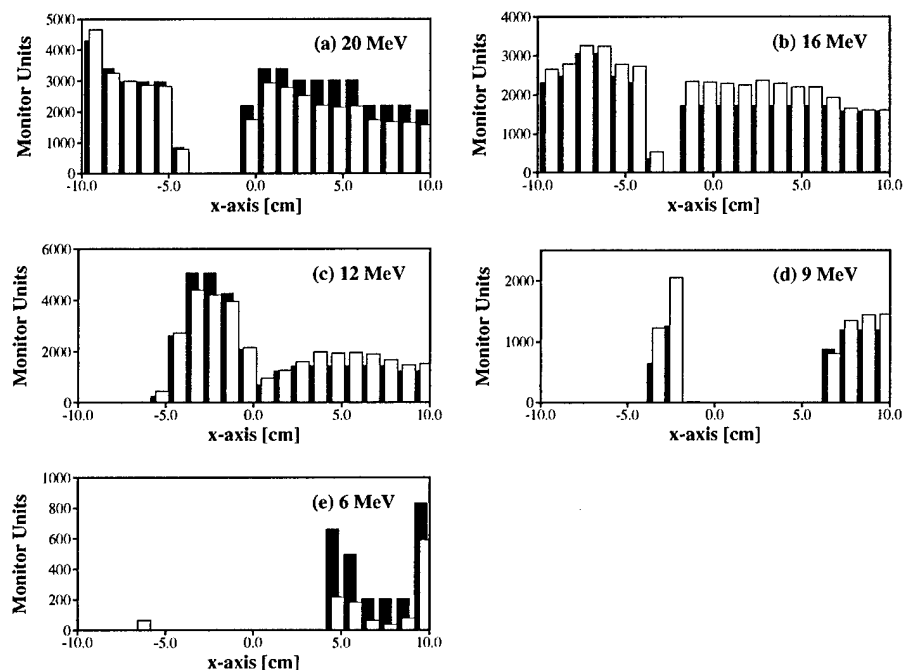


Figure 4. Intensity maps generated for the homogeneous phantom by optimization of electron beamlets: (a) 20 MeV, (b) 16 MeV, (c) 12 MeV, (d) 9 MeV, (e) 6 MeV. Shown are □, after initial beamlet optimization and ■, after final segment optimization. Note that the intensities shown for beamlets are prior to rebinning.

3.1. Homogeneous phantom

3.1.1. Geometry and beamlets. The first phantom geometry to be considered was a two-dimensional homogeneous phantom with a sloped surface, shown schematically in figure 3. The two-dimensional system was chosen so that beamlet weights and dose distributions could be more easily assessed. The target was chosen to be concave with a critical structure placed within the concavity. A small region around the target was chosen to represent the normal tissue dose. The lateral extent of the target was approximately 20 cm. In the third dimension, i.e. out of the page, as shown, the target region was 4 cm wide and was surrounded by homogeneous ICRU tissue to a total width of 20 cm. The isocentre was placed at the surface of the phantom, centred on the x-axis.

An array consisting of 20 beamlets, each with an area of $1 \times 7 \text{ cm}^2$, was delivered into the phantom at each of the five available energies, covering the area from $x = -10.0$ to 10.0 cm . The 7 cm beamlet size along the y-axis was chosen to be sufficiently large such that the central target voxels were covered by a uniform field.

The beamlet weights were optimized to provide the intensity map shown in figure 4. The general trend is as expected based on energies and depths. That is, the higher (20 and 16 MeV) beams are restricted to the deeper target regions, while the lower energies are used in regions where sparing of the critical structure is necessary. The resulting cumulative dose-volume histogram (DVH) is shown in figure 5. Note that the target is well covered at the level of dose prescription and the coverage is uniform to within the statistics given in table 1.

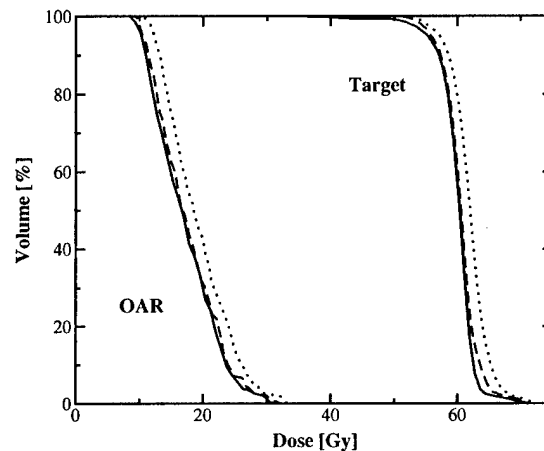


Figure 5. Cumulative DVHs for the homogeneous phantom based on a leaf sequence derived from the beamlet optimization (before the second optimization). Shown are DVHs for target and critical structures. The results are for beamlet simulation (—), full simulation of leaves (· · · · ·), and with leaf end scatter but no leakage (- - -). The full simulation is what would actually be delivered, including a significant overdosing because of bremsstrahlung from the leaves. This overdose is not predicted by the other simulations.

Table 1. Dose constraints used during optimization of plans. For the target, a prescription dose of 60 Gy was assigned for the homogeneous phantom and 50 Gy for the breast phantom. In both cases, the average dose met this prescription to within 1%. Dose volume constraints are given as maximum or minimum dose allowed for a given volume (Prescr.). When this constraint is violated, penalties are assessed according to equation (7).

	Structure	Dose (Gy)	Relative weight	% Volume exceeding dose limit		
				Prescr.	Initial opt.	Final opt.
Homogeneous phantom	Target	>61.0	100.0	1.0	35.7	35.1
		<59.0	100.0	0.0	25.9	27.6
	OAR	>30.0	50.0	5.0	1.5	2.4
		>20.0	50.0	25.0	29.7	32.1
		>5.0	50.0	75.0	100.0	100.0
Breast phantom	Target	>50.5	100.0	0.0	38.0	34.6
		<49.5	100.0	0.0	38.7	33.7
	Rt Lung	>1.0	25.0	50.0	61.8	100.0
		>3.3	25.0	30.0	43.6	55.4
		>9.2	25.0	20.0	19.1	22.7

3.1.2. Simulation of the leaf sequence. This intensity profile was converted to a step-and-shoot leaf sequence (for a single, wide leaf) via the close-in method (Bortfeld *et al* 1994). The leaf sequencing method was chosen arbitrarily, but it is expected that the results should be general to any given leaf sequencing system (see section 3.2, for example). The delivery of this leaf sequence was then simulated with the leaves accounted for using two different methods: (A) no particles transported in leaves and consequently, no bremsstrahlung production in the leaves, and (B) explicit transport of electrons down to 2.0 MeV (ECUT) and photons to

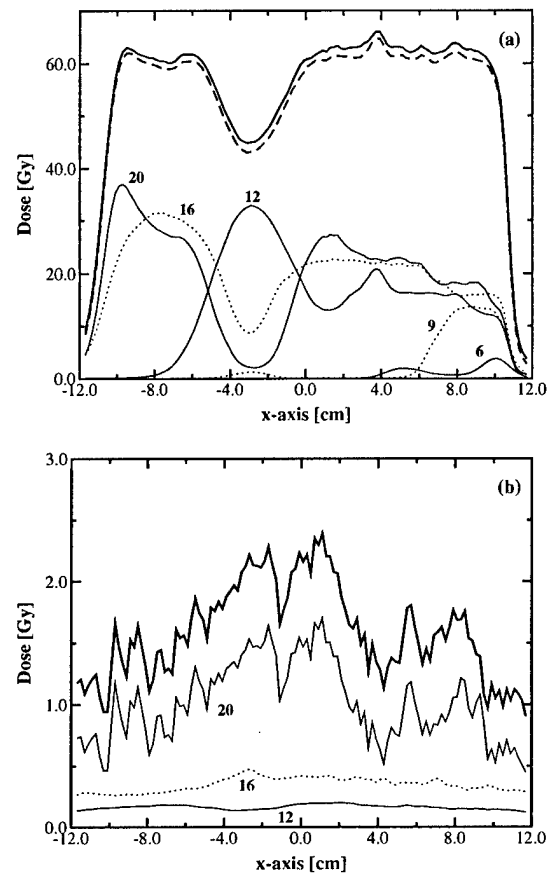


Figure 6. Dose profile from the simulated delivery of a plan based on beamlet optimization results (before the second optimization). (a) Dose profile taken at a depth of 4.0 cm below isocentre. Thin curves (full and dotted for clarity) represent individual energies while the thick curves indicate total dose, — with, - - - without bremsstrahlung. (b) A difference plot representing the bremsstrahlung contribution for each energy and the total plan (thick curve). For clarity, 9 and 6 MeV have been omitted. These low energies result in considerably less bremsstrahlung leakage than the energies displayed.

10 keV (PCUT). In all cases, complete simulation of all particles down to the global cut-offs was performed in an area within 5 mm of the leaf boundaries.

The DVHs for these deliveries are shown in figure 5. There are significant differences in the DVHs based on the type of leaf simulation. When bremsstrahlung is ignored (method A), the delivered DVH closely matches the DVH generated during beamlet delivery, with small differences caused by the finite thickness of the leaves and scatter off the leaf ends. The similarity between these two curves suggests that the beamlets and leaf delivery are implemented properly both in relative and absolute dose calculation. The difference between the beamlet optimization result and simulation via method A is due to the combined effects of leaf end scatter and rebinning the weights into 10 intensity levels. These effects are observed to have only a small impact on the resulting DVHs for this case.

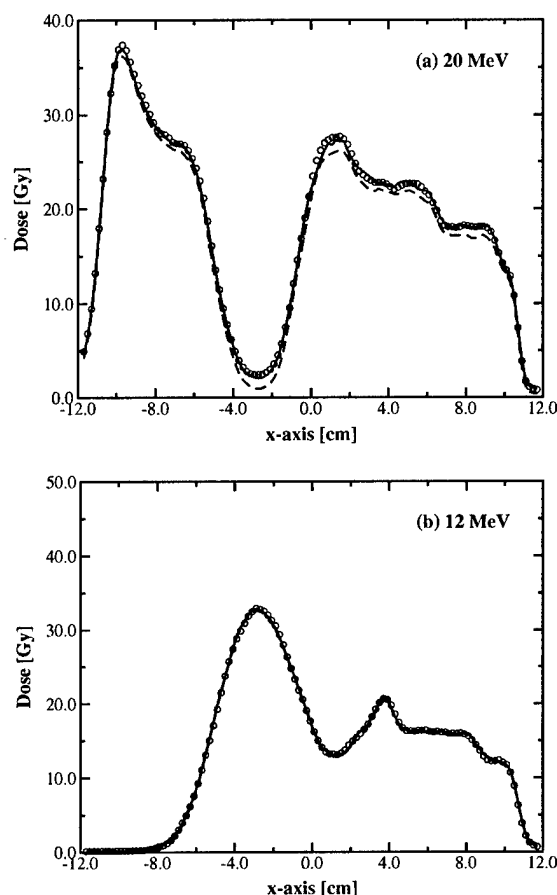


Figure 7. Dose profiles taken at a depth of 4.0 cm below isocentre for (a) 20 MeV and (b) 12 MeV. Shown are explicit simulation (—), no bremsstrahlung production in leaves (---), and approximated leakage (○). Note the magnitude of the bremsstrahlung dose (the difference between no transport and explicit simulation) at 20 MeV and the agreement between the approximate and explicit simulation.

This, however, represents only the ideal case and one that cannot be delivered with a real collimator system. When the actual eMLC delivery is simulated, including bremsstrahlung production in the leaves (method B), it is apparent that a significant increase in dose occurs in both the critical structure and target. This suggests that bremsstrahlung leakage is an essential element in the dose calculation.

Figure 6(a) shows the contribution of each energy to the total dose at a depth of 4.0 cm. As expected, the dose distribution of each energy roughly follows the intensity maps of figure 4. The difference in absolute dose between the complete plan delivered with and without bremsstrahlung leakage, taken at the same depth, is shown in figure 6(b). What is immediately apparent is that, as expected, the primary contributor to bremsstrahlung background is the 20 MeV field. Profiles at different depths show similar results. It is also observed that the

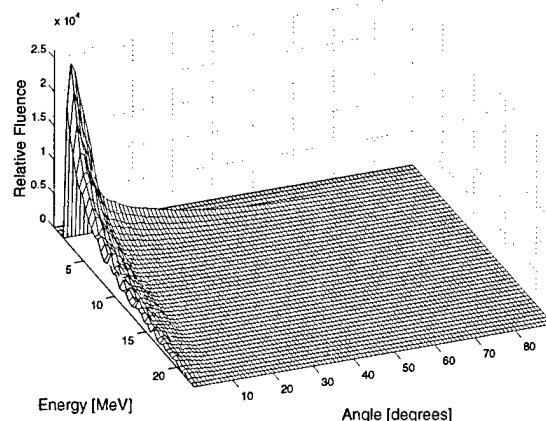


Figure 8. The joint angular/spectral distribution for bremsstrahlung photons generated in a 1.5 cm tungsten slab irradiated by the 20 MeV field of a Varian Clinac 2100C. The distribution is given as an average over the entire field. The z-axis is presented in arbitrary units of planar fluence. Integrated over all angles, the most probable energy for this distribution is 2.25 MeV with a mean energy of 5.06 MeV.

effect is not uniform, and is thus not likely to be corrected by a global change in monitor units delivered.

This leaf effect can be studied in more detail by examining dose profiles for individual energies, as shown for 20 and 12 MeV in figure 7. Examining the 20 MeV profile in figure 7(a), taken at a depth of 4.0 cm, it can be seen that the full leaf simulation gives a slightly higher dose across the field, especially in the region corresponding to the critical structure. In this region, adequate coverage was achieved by the use of the 12 MeV field because the target stopped at a shallower depth. Because the 20 MeV would penetrate into the critical structure, it was blocked in this region. However, while primary electrons are blocked, bremsstrahlung is generated by the electron interactions in the leaves.

Thus, there exists here a situation where the open field (12 MeV) delivers dose as predicted by the beamlet simulation, but leakage dose from closed fields (20 MeV) is not accounted for during beamlet optimization. In this case, an appropriate correction can be found by inspection: the intensity of the portions of the 12 MeV overlaying the critical structure should be reduced in such a way as to (at least partially) offset the dose being delivered by the bremsstrahlung from the 20 MeV field. Of course, this only offers an approximate correction to one region which may not be the optimal correction even for this limited problem, and does not correct for leaf end scatter. As noted, leaf end scatter plays a small role in this case, but situations may arise in which it has a larger impact than bremsstrahlung production, especially if low-energy fields are delivered with higher intensities. A more robust and automated solution is necessary for use in treatment planning. This can be achieved by the optimization of segment weights.

3.1.3. Bremsstrahlung approximation. These results clearly indicate that the effect of bremsstrahlung leakage must be included during treatment planning. However, transporting particles through the leaves becomes prohibitively slow when multisegment, multienergy plans are considered. A method to approximate the leakage was then developed to circumvent this problem.

Table 2. A comparison of the three different methods of leaf simulation. All values are taken at a depth of 2.5 cm. The open portion of the field extended from the central axis towards the $+x$ direction. The 'dose out of field' was computed as the average of the dose from -10.0 cm to -3.5 cm. Relative speeds are presented normalized to the full, or explicit, simulation. See section 2.1.3 for details on each simulation method. The same number of initial particles were simulated in each case. The statistical uncertainty was approximately 0.5% at 1σ .

Field	Leaf simulation method	Relative speed	Max. dose in field		Dose out of field	
			(Gy)	Rel. error	(Gy)	Rel. error
20 MeV 5×7 cm ²	Explicit	1.0	10.05	—	0.16	—
	No trans.	5.1	9.98	<1%	0.01	-92.4%
	Approx.	4.3	10.01	<1%	0.16	<1%
20 MeV 1×7 cm ²	Explicit	1.0	8.27	—	0.15	—
	No trans.	13.3	8.14	-1.54%	0.01	-96.3%
	Approx.	8.2	8.50	+1.03%	0.16	<1%

Just as a source model is used to generate electrons and photons from the treatment head, a bremsstrahlung source model was used to re-create photons at the lower surface of the eMLC, as described in section 2.1.3. The joint angular/spectral distribution for a 20 MeV field as generated by EGS4/BEAM simulation is plotted in figure 8. As expected, the photons are primarily forward directed with a significant low-energy portion. The approximation was tested on simple static fields and found to reproduce full simulation results to within 2%. The improvement in speed and specific dose values can be found in table 2. In particular, for the 1 cm field where only about 3% of the eMLC is open (as is the case in many plan segments), the simulation could be accelerated by approximately a factor of 8.

A second set of simulations was executed for these leaf settings, again with full leaf simulation. The BLCMIN parameter of the PRESTA algorithm was set to 1.5 to maintain smaller step sizes than are necessary for accurate transport (Bielajew and Rogers 1987). It has been reported that this may lead to a small but significant change in the bremsstrahlung yield in thick targets (Faddegon *et al* 1990, 1991). However, no significant changes were observed in the bremsstrahlung dose distributions, and so the default PRESTA values were retained (for speed) in all subsequent simulations. However, it is noted that the true bremsstrahlung spectrum, yield and angular distributions may indeed differ significantly from the approximate source used here, though the effect on the resulting dose is trivial compared with the primary electron dose.

In section 3.1.2, it was proposed that optimizing segment weights may correct for bremsstrahlung leakage. This will be most effective if the bremsstrahlung angular spread is sufficiently narrow such that open regions received only trivial photon dose during the delivery of that segment. Indeed, this assumption is validated by the results shown in table 2. For the 1 cm wide field, the difference between maximum doses with explicit leakage and no leakage is approximately 1.6% on a statistical uncertainty of 1.0%. The overdose caused by the approximation in the open field region is similarly within 2%. This error is due to the approximation that the bremsstrahlung angular distribution is the same at all points, rather than tilted away from the central axis (as the incident electrons are). However, especially as this effect decreases with increasing field size, it was considered an acceptable level of error.

The method presented is one possible method to simulate the effect of the leaves in an acceptable time frame, and was used for the CT phantom in section 3.2. For the homogeneous phantom currently under discussion, DVHs and isodose lines for simulations performed using

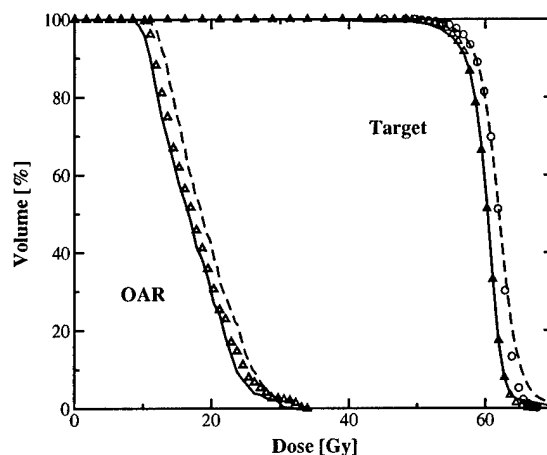


Figure 9. Cumulative DVHs for the homogeneous phantom for target and critical structure, after beamlet optimization (—), simulated delivery of this plan with leaves in place, i.e. without second optimization (---), and simulated delivery with leaves after segment optimization, i.e. final plan (Δ). Note that the original beamlet optimization and the final plan are nearly indistinguishable in target coverage. Also shown is the delivered target DVH for a plan in which a second optimization occurred, but in which segments only included leaf scatter, and not bremsstrahlung (O).

this approximation and explicit full leaf simulation were found to be indistinguishable. Thus, unless otherwise specified, figures and discussion regarding explicit simulation of leaves are equally applicable to the approximate bremsstrahlung approach.

3.1.4. Optimization of segment weights. During the simulated delivery of the leaf sequence, the dose distribution from each segment was stored separately. A segment was defined as the beam delivered by a field defined by a set of leaf positions, that is, a single static field in a step-and-shoot sequence. Treating each of these segments as if they were beamlets, the weights, or monitor units delivered per segment, were re-optimized with the same parameters as before. The initial conditions for the optimization were taken from the original monitor unit settings, i.e. those derived from the first beamlet optimization. The results of this second optimization are shown in table 1.

It is crucial to recall that this second optimization is based on a realistic geometry and includes such details as leaf end transmission and bremsstrahlung leakage. In contrast, the results of the first optimization are based on idealized beamlets, i.e. with no real collimator geometry involved. This first optimization gives the best dose distribution with a given optimization (given a perfectly absorbing and infinitely thin collimator), while the second optimization is the actual delivered dose. What is observed is that if the non-idealities caused by the eMLC are included in the second stage optimization (i.e. the segment optimization), the final result does not deviate far from the ideal case (i.e. the beamlet optimization). The target dose and coverage are very similar, with a slight increase in dose to critical structures. Note that of course the bremsstrahlung dose cannot be completely negated, and that there is a small increase in dose to normal tissues as a result, but this occurs deeper than the target and critical structure and thus represents doses of less than 2% of the prescription dose.

These results are further detailed in figure 9, where the DVHs are shown after various stages of planning. Idealized beamlets are optimized to give a dose distribution that agrees very well

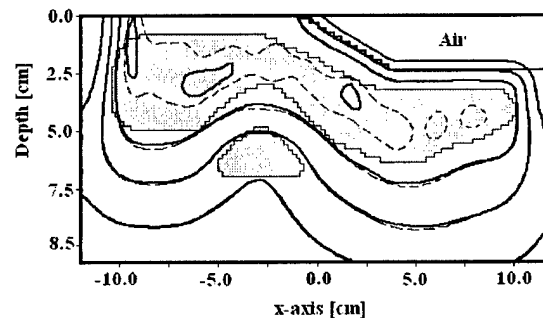


Figure 10. Isodose lines for the homogeneous phantom. Shown are the simulated deliveries of plans generated accounting for leaf effects (—) and plans that ignored the effect of the leaves (---). The structures are labelled in figure 3. Lines represent absolute doses: starting closest to the target and moving outwards, 62.5, 50, 30, 10 Gy. Recall that the prescription dose was 60 Gy. Target doses in both cases satisfied the minimum prescription dose requirements, but there is significant overdosing of the target in the plan that did not account for leaf effects.

with the prescription on table 1, shown as full curve in the figure. However, actually delivering this plan adds the effect of the collimator leakage and scatter. The resulting DVH is shown as a broken curve, and is right shifted and also has a change in the slope, suggesting much poorer target coverage than was predicted by the idealized plan. However, once segment weights are re-optimized, the DVHs, shown as symbols, indicate that target coverage is very similar to that of the ideal beamlets, despite the non-idealities of the real collimator. The dose to critical structures rises slightly with the addition of the leaves, due to the leakage, but the final optimization does reduce this effect somewhat. The resulting intensity maps are shown in figure 4.

It is noted that this optimization is a somewhat smaller problem than the initial optimization. In particular, whereas the initial optimization was in 100 dimensions (20 beamlets \times 5 energies), this second optimization has a dimensionality equal to the total number of segments in all ports: in this case, 33. Additionally, the initial values of the segment weights are much closer to the optimal solution than the initial beamlet weights, which were set to zero.

3.1.5. Final dose distributions. As implemented, the optimization procedure involves storage of complete information about dose in structures (target, OAR) but only stores dose for a limited set of healthy tissue voxels. Thus, while the DVHs generated in the second optimization are complete, plotting isodose lines and a full accounting of normal tissue dose requires a final dose calculation based upon the entire plan. While it is possible that this step could be avoided in a clinical implementation (given sufficient computer resources), it was also a necessary step for this study to fully quantify the error introduced by ignoring the leaf transport.

Figure 9 shows the DVHs for the final deliveries planned based on full leaf transport simulations and also a plan generated with only leaf scatter accounted for. Both plans were based on an intensity map generated by the same ideal beamlets. This initial optimization result gave the leaf positions for the deliveries. At this point, both simulations are identical. Then, the delivery of the leaf sequence was simulated with leaf leakage included in one case and ignored in the other. In the case where bremsstrahlung from the leaves was ignored, the finite thickness of the leaves and end scatter and transmission was still included. The segment weights for these two simulations were then re-optimized, such that a final set of leaf positions

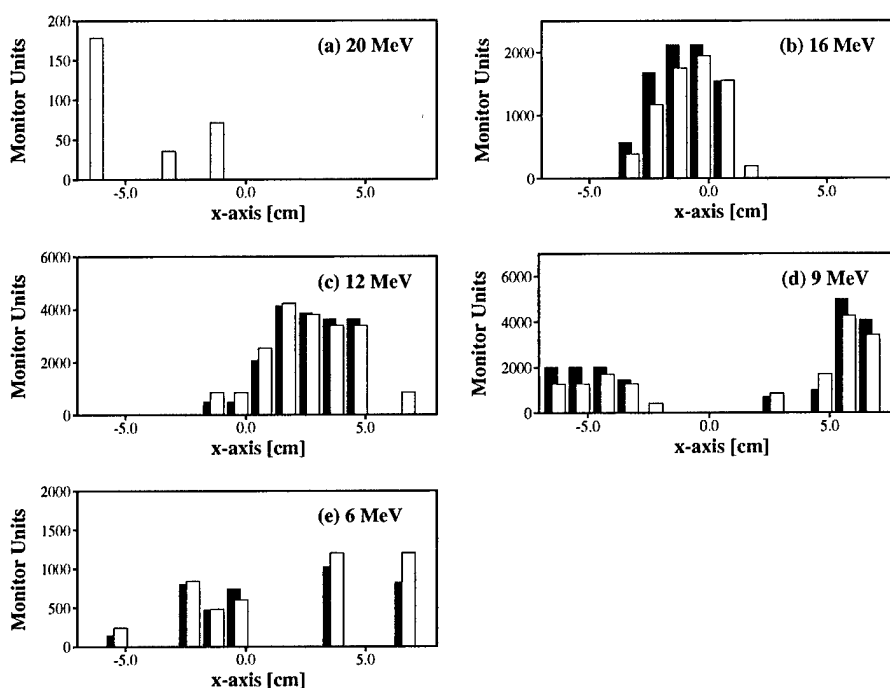


Figure 11. Intensity maps for the AP field of the 2D breast plan, generated by optimization of electron beamlets, for the AP directed port: (a) 20 MeV, (b) 16 MeV, (c) 12 MeV, (d) 9 MeV, (e) 6 MeV. Shown are □, after beamlet optimization and ■, after segment optimization.

(based on the first optimization) and monitor units (based on the second optimization) were obtained. These were then simulated with complete simulation of the collimator system, to observe the dose distributions from actual deliveries based on these planning procedures.

As expected, figure 9 shows that the delivery that was planned without leaf leakage resulted in an overdose to the target and critical structures. This is expected to be true for any situation in which the leaf transport and leakage is not properly included in the simulation, not just simulations in which all transport is ignored. Note that the DVHs for the plan generated with the bremsstrahlung approximation are virtually indistinguishable from the full simulation DVHs, and are thus not shown.

Isodose plots are shown in figure 10 for the plans generated with the leaf effect included in the optimization and for plans that did not take this leaf effect into account. What is apparent is that failing to include leaf effects in planning leads to an overdosing, shown by the 62.5 Gy isodose line.

3.2. Two-dimensional breast CT phantom

As a demonstration of this method in a more realistic scenario, a plan was generated for irradiation of an intact breast. For this proof-of-principle study, the breast was taken as a single CT slice. Extension to 3D cases requires further study on the effect of leaf sequences on MERT planning, and will be addressed in future research. Details of the planning parameters and results can be seen in table 1.

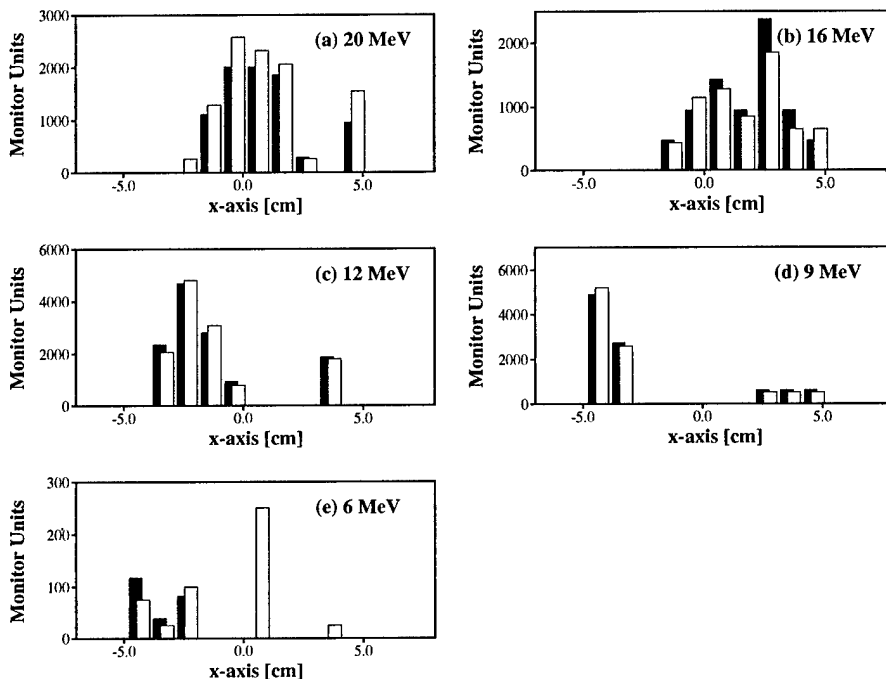


Figure 12. Intensity maps for the RL field of the 2D breast plan, generated by optimization of electron beamlets, for the right lateral port: (a) 20 MeV, (b) 16 MeV, (c) 12 MeV, (d) 9 MeV, (e) 6 MeV. Shown are \square , after beamlet optimization and \blacksquare , after segment optimization.

For this plan, two ports with different gantry angles and isocentres were employed, with five energies delivered through each port. One port is directed in the anterior-posterior (AP) direction while the second port was directed from the right lateral (RL) direction. The planning proceeded using the method developed in the discussion of the homogeneous phantom (i.e. via method B). Beamlets were delivered and optimized, a leaf sequence was derived for the eMLC, delivery was simulated using the bremsstrahlung approximation and the segment weights were re-optimized. While the homogeneous leaf sequence was generated using the close-in method, this leaf sequence was generated using the intensity solid paradigm method of Siochi (1999), as a demonstration of the generality of the planning procedure. No other modifications to the planning scheme described above were necessary for simulation of this multiport/multi-isocentre plan.

The intensity maps for the AP fields are shown in figure 11 and the RL fields are shown in figure 12. Unlike the single-port homogeneous plan discussed earlier, the intensity maps are less intuitive and are, in a qualitative sense, less smoothly varying than the homogeneous phantom discussed earlier. The addition of a second gantry angle and homogeneous material makes this optimization more similar to photon IMRT in that intensity maps can only be roughly estimated by inspecting the geometry. However, the general trend of reducing 20 MeV field intensities and compensating for this with increased intensity at the lower energies is maintained. Further research will examine the effect of smoothing these profiles, as has been suggested for photon IMRT.

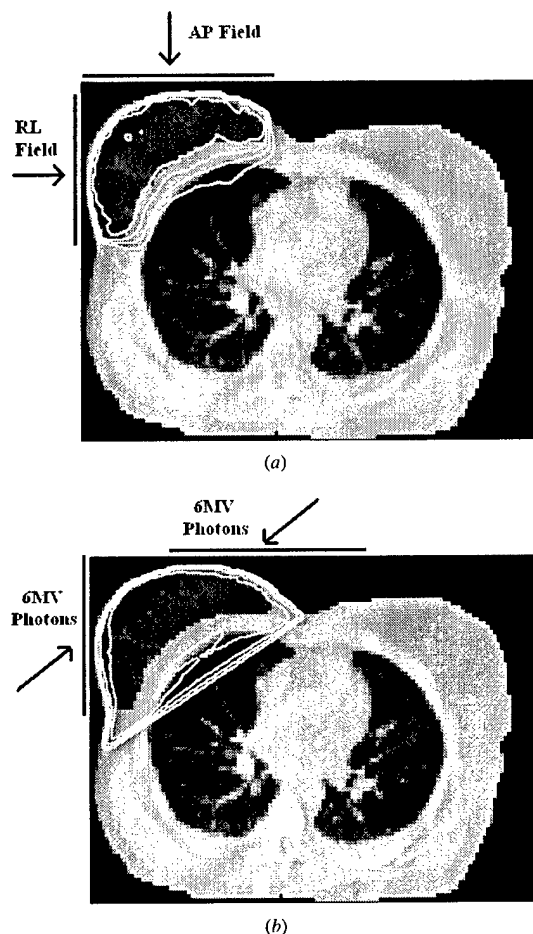


Figure 13. Isodose lines for the 2D breast plan. (a) MERT final delivery after both beamlet and segment optimization are complete. (b) A pair of tangential photon beams. Starting closest to the target and moving outwards, 48, 40, 30, 20 Gy.

(This figure is in colour only in the electronic version, see www.iop.org)

The resulting dose distribution for the MERT plan is shown in figure 13(a). A second set of isodose lines are plotted in figure 13(b) for a pair of 6 MV tangential photon beams directed onto the breast as per standard protocols. The lateral photon field utilized a 45° wedge and the relative weights of the two fields was optimized. The corresponding DVHs are shown in figure 14. The low lung dose in the MERT plan is a combination of two factors: the two-port set-up and the use of lower-energy beams for the thinner portions of the breast. Note that achieving a homogeneous dose with two electron ports necessitates intensity modulation. Note, also, that the DVH volumes are presented as percentages of this slice only, and not as a percentage of the entire lung.

This represents a case where conventional treatments are often non-optimal, as tangential photon beams often result in heterogeneous dose, scatter dose to the contralateral breast and

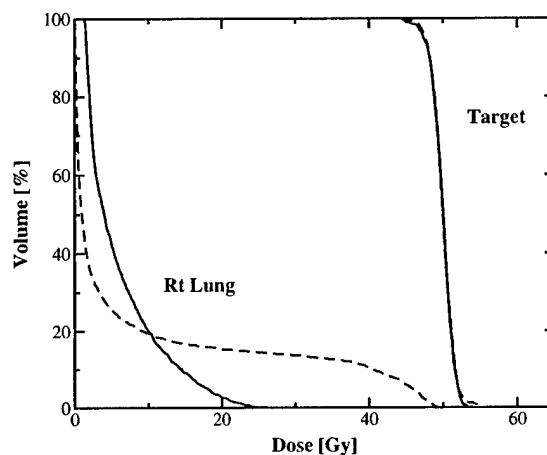


Figure 14. Cumulative DVHs for the 2D breast plan. —, simulation of final delivery plan with leaves in place and - - -, tangential 6 MV photon beams. Note that volumes actually represent area in this slice, as the plan was conducted in two dimensions.

the necessity of a large margin to compensate for breathing motion. In this case, the breathing motion was assumed to be primarily expansion in the direction normal to the tangential beams. While this two-port MERT plan is also affected by breathing motion, the effect is somewhat lessened as the beams still retain an acute angle of incidence relative to the breathing motion. In contrast, the photon plan includes a much larger region of the breast in the high-dose region, as a large margin must be included because breathing motion is in a direction largely orthogonal to the beam angles. A complete study of the impact of breathing motion on the two treatment modalities will be of significant interest, but is beyond the scope of this work. Regardless of the margin, the curvature of the chest wall and the lateral extent of the clinical target region dictate that some amount of normal tissue and lung will be included in the high-dose region.

Note that this case has been presented as a proof-of-principle for both the potential role of MERT in a clinical scenario and of the efficacy of this planning scheme. Examining the utility of MERT at different anatomical sites and a full comparison with other treatment modalities is beyond the scope of this paper.

4. Conclusions

This study has demonstrated the feasibility of MERT with a scattering foil linear accelerator. Two primary objections voiced against MERT have been that the in-air scatter is too great to have an acceptable resolution and that this scatter will hinder the optimization process. The scattering problem has been minimized by the design of the electron MLC. There is certainly an appreciable amount of air scatter, especially at the lower energies; however, it has been shown that this does not significantly affect dose distributions in the model targets. Furthermore, optimization of electron beamlets will be inherently inaccurate if poor electron transport algorithms are used to account for in-air transport. This problem has been overcome with the use of Monte Carlo transport algorithms. The beamlet dose profiles may have wide penumbras or other non-ideal characteristics, but as long as this information is incorporated into optimization, the final result will be physically correct.

While this study has employed a specific model of an electron MLC and a specific Monte Carlo dose calculation system and optimization software, it should be noted that these results can be generalized to other situations. That is, the effect of any real collimator that perturbs the delivered beam away from the idealized beamlets can be at least partially accounted for by this two-step optimization procedure. Also, any dose calculation system and optimization software may be used, provided that transport in non-patient regions such as the air gap and eMLC can be performed accurately.

With rapidly increasing Monte Carlo calculation speeds and improvements in computer hardware, it is likely that calculating MERT plans in the manner described will soon be possible on a time scale easily comparable to advanced analytical photon planning algorithms. Thus it is important to pursue additional research in MERT planning, focusing on development of three-dimensional planning techniques. Currently, three-dimensional plans may be generated using the methods presented. However, it is anticipated that the method used to organize individual leaves into a synchronous leaf sequence will have some bearing on the ability to compensate for leakage. Further research will also examine specific treatment planning considerations, such as changing the number of energy and intensity levels, as well as adding additional gantry angles or isocentres, and combining photons and electrons in a single plan.

Acknowledgments

We would like to thank our colleagues A L Boyer, G Luxton, B Shahine, T Pawlicki, T Guerrero and J Jolly for their support and helpful discussions regarding this work. We would also like to thank S Brain, B Tofighrad and T Koumrian for help with computer and software support. This work has been funded in part by grants CA78331 from the NIH, BC971292 and BC000838 from the US Department of Defense, and NIH Training Grant 5T32GM08294-11.

References

- Åsell M, Hyödynmaa S, Gustafsson A and Brahme A 1997 Optimization of 3D conformal electron beam therapy in inhomogeneous media by concomitant fluence and energy modulation *Phys. Med. Biol.* **42** 2083–100
- Åsell M, Hyödynmaa S, Söderström S and Brahme A 1999 Optimal electron and combined electron and photon therapy in the phase space of complication-free cure *Phys. Med. Biol.* **44** 235–52
- Bielajew A F 1994 Monte Carlo modelling in external-beam radiotherapy—why leave it to chance? *Proc. 11th Int. Conf. on the Use of Computers in Radiation Therapy* ed A R Hounsell, J M Wilkinson and P C Williams (Manchester: North Western Medical Physics Department, Christie Hospital NHS Trust) pp 2–5
- Bielajew A F and Rogers D W O 1987 PRESTA—the parameter reduced electron step algorithm for electron Monte Carlo transport *Nucl. Instrum. Methods B* **18** 165–81
- Bielajew A F, Rogers D W O, Cygler J and Battista J J 1987 A Comparison of electron pencil beam and Monte Carlo calculational methods *The Use of Computers in Radiation Therapy* ed I A D Bruinvis (Amsterdam: Elsevier) pp 65–8
- Bortfeld T R, Kahler D L, Waldron T J and Boyer A L 1994 X-ray field compensation with multileaf collimators *Int. J. Radiat. Oncol. Biol. Phys.* **28** 723–30
- Boyer A L and Mok E C 1985 A photon dose distribution model employing convolution calculations *Med. Phys.* **12** 169–77
- Buchanan J L and Turner P R 1992 *Numerical Methods and Analysis* (New York: McGraw-Hill)
- Chen Y, Boyer A L and Ma C-M 2000 Calculation of x-ray transmission through a multileaf collimator *Med. Phys.* **27** 1717–26
- Cygler J, Battista J J, Scrimger J W, Mah E and Antolak J 1987 Electron dose distributions in experimental phantoms: a comparison with 2D pencil beam calculations *Phys. Med. Biol.* **32** 1073–83
- Ebert M A and Hoban P W 1997 Possibilities for tailoring dose distributions through the manipulation of electron beam characteristics *Phys. Med. Biol.* **42** 2065–81
- Faddegon B A, Ross C K and Rogers D W O 1990 Forward directed bremsstrahlung of 10–30 MeV electrons incident on thick targets of Al and Pb *Med. Phys.* **17** 773–85

- Faddegon B A, Ross C K and Rogers D W O 1991 Angular distribution of bremsstrahlung from 15 MeV electrons incident on thick targets of Be, Al and Pb *Med. Phys.* **18** 727–39
- Hogstrom K R, Mills M D and Almond P R 1981 Electron beam dose calculations *Phys. Med. Biol.* **26** 445–59
- Holmes T W 2001 A method to incorporate leakage and head scatter corrections into a tomotherapy inverse treatment planning algorithm *Phys. Med. Biol.* **46** 11–27
- Hyödynmaa S, Gustafsson A and Brahme A 1996 Optimization of conformal electron beam therapy using energy- and fluence-modulated beams *Med. Phys.* **23** 659–66
- Jansson T, Lindman H, Nygård K, Dahlgren C V, Montelius A, Öberg-Kreuger C, Asplund S and Bergh J 1998 Radiotherapy of breast cancer after breast-conserving surgery: an improved technique using mixed electron-photon beams with a multileaf collimator *Radiother. Oncol.* **46** 83–9
- Jeraj R and Keall P 2000 The effect of statistical uncertainty on inverse treatment planning based on Monte Carlo dose calculation *Phys. Med. Biol.* **45** 3601–13
- Jiang S B 1998 Development of a compensator based intensity modulated radiation therapy system *PhD Thesis* Medical College of Ohio, Toledo, OH
- Jiang S B, Kapur A and Ma C-M 2000 Electron beam modelling and commissioning for Monte Carlo treatment planning *Med. Phys.* **27** 180–91
- Kapur A 1999 Monte Carlo dose calculations for clinical electron and intensity modulated photon beams in radiotherapy *PhD Thesis* Stanford University, Stanford, CA
- Kapur A, Ma C-M, Mok E C, Findley D O and Boyer A L 1998 Monte Carlo calculations of electron beam output factors for a medical linear accelerator *Phys. Med. Biol.* **43** 3479–94
- Karlsson M G, Karlsson M K and Ma C-M 1999 Treatment head design for multileaf collimated high-energy electrons *Med. Phys.* **26** 2125–32
- Karlsson M K, Karlsson M G and Zackrisson B 1998 Intensity modulation with electrons: calculations, measurements and clinical applications *Phys. Med. Biol.* **43** 1159–69
- Kawrakow I and Fippel M 2000 Investigation of variance reduction techniques for Monte Carlo photon dose calculation using XVMC *Phys. Med. Biol.* **45** 2163–83
- Kawrakow I, Fippel M and Friedrich K 1996 3D electron dose calculation using a voxel based Monte Carlo algorithm *Med. Phys.* **23** 445–57
- Keall P J, Siebers J V, Jeraj R and Mohan R 2000 The effect of dose calculation uncertainty on the evaluation of radiotherapy plans *Med. Phys.* **27** 478–84
- Klein E E, Li Z and Low D A 1996 Feasibility study of multileaf collimated electrons with a scattering foil based accelerator *Radiother. Oncol.* **41** 189–96
- Koch H W and Motz J W 1959 Bremsstrahlung cross-section formulas and related data *Rev. Mod. Phys.* **31** 920–55
- Korevaar E W, Heijmen B J M, Woudstra E, Huizenga H and Brahme A 1999 Mixing intensity modulated electron and photon beams: combining a steep dose fall-off at depth with sharp and depth-independent penumbras and flat beam profiles *Phys. Med. Biol.* **44** 2171–81
- Laub W, Alber M, Birkner M and Nüsslin F 2000 Monte Carlo dose computation for IMRT optimization *Phys. Med. Biol.* **45** 1741–54
- Lee M C, Jiang S B and Ma C-M 2000a Monte Carlo and experimental investigations of multileaf collimated electron beams for modulated electron radiotherapy *Med. Phys.* **27** 2708–18
- Lee M C, Jiang S B, Yi B and Ma C-M 2000b Monte Carlo simulations of multileaf collimated electrons *Proc. 13th Int. Conf. on the Use of Computers in Radiation Therapy* ed W Schlegel and T Bortfeld (Heidelberg: Springer) pp 176–8
- Lee M C, Kapur A, Jiang S B and Ma C-M 2000c Characterization of electron beams for modulated electron beam radiotherapy *CD-ROM Proc. of the World Congress on Medical Physics and Biomedical Engineering (23–28 July 2000)*
- Li J S, Pawlicki T, Deng J, Jiang S B and Ma C-M 2000a Simulation of Beam Modifiers for Monte Carlo Treatment Planning *Proc. 13th Int. Conf. on the Use of Computers in Radiation Therapy* ed W Schlegel and T Bortfeld (Heidelberg: Springer) pp 437–9
- Li J S, Pawlicki T, Deng J, Jiang S B, Mok E and Ma C-M 2000b Validation of a Monte Carlo dose calculation tool for radiotherapy treatment planning *Phys. Med. Biol.* **45** 2969–85
- Lief E P, Larsson A and Humm J L 1996 Electron dose profile shaping by modulation of a scanning elementary beam *Med. Phys.* **23** 33–44
- Ma C-M, Faddegon B A, Rogers D W O and Mackie T R 1997 Characterization of Monte Carlo calculated electron beams for radiotherapy *Med. Phys.* **24** 401–16
- Ma C-M, Li J S, Pawlicki T, Jiang S B and Deng J 2000a MCDOS—A Monte Carlo dose calculation tool for radiation therapy treatment planning *Proc. 13th Int. Conf. on the Use of Computers in Radiation Therapy* ed W Schlegel and T Bortfeld (Heidelberg: Springer) pp 123–5

- Ma C-M, Mok E, Kapur A, Pawlicki T, Findley D, Brain S, Forster K and Boyer A L 1999 Clinical implementation of a Monte Carlo treatment planning system for radiotherapy *Med. Phys.* **26** 2133-43
- Ma C-M, Pawlicki T, Lee M C, Jiang S B, Li J, Deng J, Yi B, Mok E, Luxton G and Boyer A L 2000b Energy- and intensity-modulated electron beam radiotherapy for breast cancer *Phys. Med. Biol.* **45** 2947-67
- Ma C-M and Rogers D W O 1997 BEAMDP users manual *National Research Council of Canada Report PIRS-0509c* (Ottawa: NRC)
- Mackie T R *et al* 1994 The OMEGA project: comparison among EGS4 electron beam simulations, 3D Fermi-Eyges calculations, and dose measurements *Proc. 11th Int. Conf. on the Use of Computers in Radiation Therapy* ed A R Hounsell, J M Wilkinson and P C Williams (Manchester: North Western Medical Physics Department, Christie Hospital NHS Trust) pp 152-3
- Mah E, Antolak J, Scrimger J W and Pattista J J 1989 Experimental evaluation of a 2D and 3D pencil beam algorithm *Phys. Med. Biol.* **34** 1179-94
- Mohan R 1997 Why Monte Carlo? *Proc. 12th Int. Conf. on the Use of Computers in Radiation Therapy* ed D D Leavitt and G Starkschall (Madison, WI: Medical Physics Publishing) pp 16-18
- Mubata C D, Verhaegen F and Nahum A E 2000 Speeding up Monte Carlo simulation of electron cut-outs in treatment planning *Proc. 13th Int. Conf. on the Use of Computers in Radiation Therapy* ed W Schlegel and T Bortfeld (Heidelberg: Springer) pp 440-2
- Nelson W R, Hirayama H and Rogers D W O 1985 The EGS4 code system *SLAC Report 265* (Stanford, CA: Stanford Linear Accelerator Center)
- Pawlicki T A, Jiang S B, Deng J, Li J S and Ma C-M 1999 Monte Carlo calculated beamlets for photon beam inverse planning *Med. Phys.* **26** 1064-5
- Rogers D W O 1991 The role of Monte Carlo simulation of electron transport in radiation dosimetry *Int. J. Appl. Radiat. Isot.* **42** 965-74
- Rogers D W O, Faddegon B A, Ding G X and Ma C-M 1995 BEAM: a Monte Carlo code to simulate radiotherapy treatment units *Med. Phys.* **22** 503-24
- Seltzer S M and Berger M J 1985 Bremsstrahlung spectra from electron interactions with screened atomic nuclei and orbital electrons *Nucl. Instrum. Methods B* **12** 95-134
- Siochi R A C 1999 Minimizing static intensity modulate delivery time using an intensity solid paradigm *Int. J. Radiat. Oncol. Biol. Phys.* **43** 671-80
- van Santvoort J P C and Heijmen B J M 1996 Dynamic multileaf collimation without 'tongue-and-groove' underdosage effects *Phys. Med. Biol.* **41** 2091-105
- Yu C X 1998 Design considerations for the sides of multileaf collimator leaves *Phys. Med. Biol.* **43** 1335-42
- Zackrisson B and Karlsson M 1996 Matching of electron beams for conformal therapy of target volumes at moderate depths *Radiother. Oncol.* **39** 261-70

Energy- and intensity-modulated electron beams for radiotherapy

C-M Ma, T Pawlicki, M C Lee, S B Jiang, J S Li, J Deng, B Yi, E Mok and
A L Boyer

Department of Radiation Oncology, Stanford University School of Medicine, Stanford,
CA 94305-5304, USA

E-mail: cma@reyes.stanford.edu

Received 5 January 2000, in final form 10 April 2000

Abstract. This work investigates the feasibility of optimizing energy- and intensity-modulated electron beams for radiation therapy. A multileaf collimator (MLC) specially designed for modulated electron radiotherapy (MERT) was investigated both experimentally and by Monte Carlo simulations. An inverse-planning system based on Monte Carlo dose calculations was developed to optimize electron beam energy and intensity to achieve dose conformity for target volumes near the surface. The results showed that an MLC with 5 mm leaf widths could produce complex field shapes for MERT. Electron intra- and inter-leaf leakage had negligible effects on the dose distributions delivered with the MLC, even at shallow depths. Focused leaf ends reduced the electron scattering contributions to the dose compared with straight leaf ends. As anticipated, moving the MLC position toward the patient surface reduced the penumbra significantly. There were significant differences in the beamlet distributions calculated by an analytic 3-D pencil beam algorithm and the Monte Carlo method. The Monte Carlo calculated beamlet distributions were essential to the accuracy of the MERT dose distribution in cases involving large air gaps, oblique incidence and heterogeneous treatment targets (at the tissue–bone and bone–lung interfaces). To demonstrate the potential of MERT for target dose coverage and normal tissue sparing for treatment of superficial targets, treatment plans for a hypothetical treatment were compared using photon beams and MERT.

(Some figures in this article are in colour only in the electronic version; see www.iop.org)

1. Introduction

Photon beams have been an effective modality for breast cancer treatment in radiation therapy. Although such conventional treatment with tangential photon fields has been successful, the following two problems (or potential areas of improvement) remain:

- (a) The inclusion of the lung and other normal tissues, and sometimes of a small volume of the heart, in the high-dose volume due to tumour location, patient size or in the case of chest-wall treatments.
- (b) High exit or scatter dose to the normal structures such as the lung, the heart and the contralateral breast.

Advances in the state of the art of computer-controlled medical linear accelerators have recently become available that, along with newly developed treatment planning techniques, may provide significant improvements in the delivery and control of external beam radiation through beam-intensity modulation (Boesecke *et al* 1988, Brahme 1988, Convery and

Rosenbloom 1992, Leibel *et al* 1992, Webb 1992, 1997, LoSasso *et al* 1993, Powlis *et al* 1993, Chui *et al* 1994, Mageras *et al* 1994, Brewster *et al* 1995, Fraass *et al* 1995, Kutcher *et al* 1995, Mackie *et al* 1995, McShan *et al* 1995, Ling *et al* 1996, Boyer *et al* 1997). It is expected that using photon IMRT, the problem (a) above may be significantly improved but (b) may become more serious as treatment time increases with the number of fields/segments used (increased leakage or scattering dose). Using the modulated electron radiotherapy (MERT) technique (Lief *et al* 1996, Hyödynmaa *et al* 1996, Zackrisson and Karlsson 1996, Åsell *et al* 1997, Ebert and Hoban 1997, Karlsson *et al* 1998, 1999), on the other hand, problem (a) may also be significantly improved and problem (b) may almost be eliminated due to the nature of the electron beams.

In the optimization process of MERT, dose conformity along the beam direction can be achieved by modulating the electron incident energy, making use of the sharp dose fall-off feature. A drawback is its large penumbra at large depths. Traditionally, electron beams are shaped using a cutout (or blocks) and beam penetration/intensity may be modified using a bolus. However, it is time-consuming to make such beam modifiers and the treatment time would be significantly increased if such beam modifiers are used for MERT. Efforts have been made to use computer-controlled MLC for electron beam modulation. The recent results by Karlsson *et al* (1999) showed that by replacing the air in the treatment head with a low-cost, custom-made helium balloon, the beam penumbral width (20/80) was reduced from 18 to 11 mm at 80 cm SSD. The beam characteristics are affected by the position of the MLC. However, by replacing the air between the MLC and the patient with a helium balloon, the beam penumbra become almost the same as that achieved by electron beam-shaping with an electron applicator that extends to the patient skin surface (Karlsson *et al* 1999). This means that many of the techniques so far developed with computer-controlled MLC and our experience with MLC photon beam modulation can be adopted for use with MERT.

The calculation of dose distributions for electron beam radiotherapy planning is challenging because electron scattering is strongly affected by changes in density and composition in the patients. The 3D pencil beam algorithm (Hogstrom *et al* 1981) is a fast analytical algorithm which has been adopted by most treatment planning systems. However, it has limitations with small irregular electron fields and in the presence of inhomogeneities (Cygler *et al* 1987, Bielajew *et al* 1987, Mah *et al* 1989, Mackie *et al* 1994, Ma *et al* 1999). The Monte Carlo simulation has been demonstrated to be a viable option for such complex situations, and also the only way to take into account back-scattering from denser materials in a patient (e.g. bone or metal inserts) (Shortt *et al* 1986, Cygler *et al* 1987, Mackie *et al* 1994, Kawrokwaw *et al* 1996, Mohan 1997, Kapur 1999, Ma *et al* 1999). The EGS4/BEAM system was developed for the simulation of radiotherapy beams from various radiotherapy treatment units, such medical accelerators (Rogers *et al* 1995). Excellent agreement (1–3%) has been achieved between the Monte Carlo dose distributions calculated using the simulated particle phase-space data and measurements (Rogers *et al* 1995, Kapur *et al* 1998, Zhang *et al* 1999, Ma *et al* 1999). We have installed a Monte Carlo patient dose calculation tool on a clinical treatment planning system (Ma *et al* 1999) and used Monte Carlo for treatment planning and dose delivery validation. This has reduced the uncertainty of the accelerator output for small irregular field electron beams from up to 10% to about 3% (Ma *et al* 1997, Kapur *et al* 1998).

Conformal radiotherapy was initially used to limit the normal tissue dose by conforming the treatment field to the beam's-eye-view projection of the target volume (Takahashi 1965). For photon beams, the MLC was used to collimate the fields and later to modulate the beam intensity in the field (Boesecke *et al* 1988, Brahme 1988, Convery and Rosenbloom 1992, Leibel *et al* 1992, Webb 1992, 1997, LoSasso *et al* 1993, Powlis *et al* 1993, Chui *et al* 1994, Mageras *et al* 1994, Brewster *et al* 1995, Kutcher *et al* 1995, Mackie *et al* 1995,

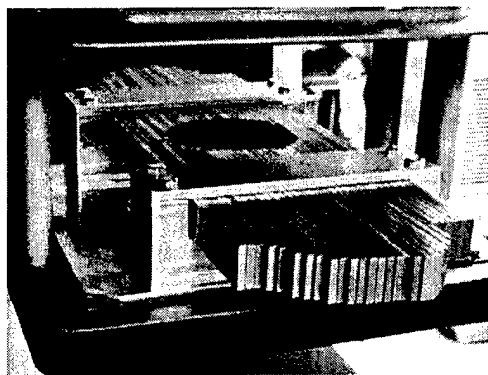


Figure 1. A prototype of an electron MLC mounted on the bottom scraper of a 25 cm \times 25 cm applicator on a Varian Clinac 2100C accelerator. The MLC has 30 pairs of steel leaves and the leaf positions are fixed by the tightening screws.

McShan *et al* 1995, Ling *et al* 1996, Boyer *et al* 1997). There have been a few studies on electron conformal therapy. Tailoring dose distributions using electron beams requires substantial beam manipulation, due to their scattering characteristics. Such manipulation is already possible with radiation sources such as microtrons where preferential energy selection and magnetically scanned pencil beams are possible (Lief *et al* 1996). Both intensity- and energy/intensity-modulated electron beams have been investigated to conform the dose to the target near the surface (Lief *et al* 1996, Hyödynmaa *et al* 1996, Zackrisson and Karlsson 1996, Ebert and Hoban 1997, Karlsson *et al* 1998). More recent work has studied the combination of photon IMRT and MERT for targets at greater depth (Karlsson *et al* 1999). Using the helium-balloon technique together with a computer-controlled MLC, it may be possible to deliver a set of intensity-modulated beams with different energies and incident angles.

In this work, we investigate the feasibility of optimizing energy- and intensity-modulated electron beams for radiotherapy treatment. We report here our Monte Carlo studies of a multileaf collimator specially designed for MERT and some preliminary experimental results. We also report on the dose calculation algorithms and their effects on treatment plan optimization for MERT. We will discuss the differences in the beam characteristics between a photon MLC and an electron MLC. We will compare the dose distributions between a conventional tangential photon treatment plan and a MERT treatment plan for a hypothetical breast treatment to demonstrate the potential of MERT for target dose coverage and normal tissue sparing.

2. Materials and method

2.1. The prototype electron MLC

We have developed a prototype manual-driven electron MLC for the beam delivery for MERT. As shown in figure 1, the electron MLC consists of 30 steel leaf pairs, which were made from the off-the-shelf steel bars for convenience and cost-effectiveness. Each leaf is 0.476 cm wide, 20 cm long and 2.54 cm thick with straight edges and ends. The leaves were mounted on a steel frame, which can be attached to the bottom scraper of a 25 cm \times 25 cm electron applicator on a Varian Clinac 2100C (Varian Oncology Systems, Palo Alto, CA). The leaves can slide in

the steel frame and the leaf positions can be easily set using a pre-cut cardboard for a beam segment. The field shape is maintained by tightening the screws from the side. The largest radiation field available using the electron MLC was 15.7 cm \times 15.7 cm projected at 100 cm source-surface distance (SSD).

Because of the existing electronic device for inserting the electron cutout, the leaves could not be placed at the last scraper level without modifying the existing applicator geometry. Instead, the steel frame was inserted using the electron cutout mount and the leaves were placed immediately above the last scraper. This resulted in a slightly greater air gap (7 cm) between the bottom of the electron MLC leaves and the phantom surface (assuming a 97 cm SSD) compared with that of an electron cutout (5 cm for a 100 cm SSD). The projected leaf width for a 5 cm air gap is 0.5 cm, while for a 7 cm air gap the projected leaf width is 0.51 cm (e.g. for the current configuration at 97 cm SSD). Further modifications are needed to the electron applicator geometry in order to lower the electron MLC leaves. The ideal location for the MLC leaves is the last scraper since electron cutouts will no longer be needed if an electron MLC is in place.

Film measurement was performed to study the characteristics of the electron beams collimated by the electron MLC. The film was calibrated following the AAPM TG-25 recommendations (AAPM 1991) and the exposures were taken by placing film at different depths in a solid water phantom. The film was scanned using a film scanner which has a spatial resolution of about 0.15 cm.

2.2. The Monte Carlo beam simulation

We have used the EGS4 (Nelson *et al* 1985) user code BEAM for the accelerator head simulation. Detailed descriptions of the software can be found in Rogers *et al* (1995). A detailed description of the clinical implementation of the Monte Carlo method at the Stanford Medical Center was given in a previous publication (Ma *et al* 1999).

For this work, we have used the previously simulated Monte Carlo beam data for 6, 12 and 20 MeV electron beams from a Varian Clinac 2100C linear accelerator and for 6 MV photon beams from a 2300CD accelerator (Varian Oncology Systems, Palo Alto, CA). The dimensions and materials for the accelerator components were incorporated according to the manufacturer's specifications. Electron beams emerging from the vacuum exit window were assumed to be monoenergetic and monodirectional with a beam radius of 0.1–0.2 cm (Kapur *et al* 1998). The energy cutoffs for electron transport in the accelerator simulation (ECUT and AE) were 700 keV (kinetic + rest mass) and for photon transport (PCUT and AP) 10 keV. The electron transport step length was confined such that the maximum fractional energy loss per electron step is 4% (i.e. ESTEPE = 0.04). The ICRU recommended compositions and stopping power values were used for the materials in the accelerator simulations (ICRU 1984). The phase-space data were scored at a plane either immediately above the photon MLC or above the lowest scraper. The number of particles was about 2–30 million in an electron beam file and about 50 million in a photon file.

Field shaping by the photon MLC or electron MLC was further simulated using the BEAM component module MLC. MLC could simulate either straight or 'double focused' leaf edges and ends. In this work, we have simulated electron beams collimated by a photon MLC with both straight and double focused MLC leaf shapes. The leaves were 7.5 cm thick and made of tungsten. The leaf center was 49 cm from the isocentre. The intervening air in the accelerator and between the MLC and the isocentre was in some cases replaced with helium to investigate the effect of electron scattering in the air. In the simulations of the electron beams collimated by an electron MLC, the leaves were placed on the bottom scraper of a 25 cm \times 25 cm applicator

with a 7 cm air gap between the bottom surface of the MLC and the isocentre. Tungsten leaves of 1.5 cm thickness with straight edges and ends were used in all the simulations and the phase space data were used in the subsequent dose calculations except for the leaf leakage study where different leaf materials and thicknesses were investigated for the electron MLC.

2.3. The Monte Carlo dose calculation

The EGS4 user code, MCDOSE (Ma *et al* 1999), was used in this work for the dose calculations. MCDOSE was designed for dose calculations in a 3D rectilinear voxel geometry. Voxel dimensions were completely variable in all three directions. Every voxel (volume element) could be assigned to a different material. The cross-section data for the materials used were available in a pre-processed PEGS4 cross-section data file. The mass density of the material in a MCDOSE calculation was varied based on the patient's CT data although the density effect corrections for the stopping powers of the material remain unchanged (Ma *et al* 1999). The voxel dimensions and materials were defined in a MCDOSE input file together with the transport parameters such as the energy cutoffs (ECUT and PCUT), the maximum fractional energy loss per electron step (ESTEPE), and the parameters required by PRESTA (Bielajew and Rogers 1987). Several variance reduction techniques have been implemented in the MCDOSE code to improve the calculation efficiency. These include photon interaction forcing, particle splitting, Russian roulette, electron range rejection and region rejection, particle track displacement and rotation, and correlated sampling. Detailed descriptions of these techniques have been given elsewhere (Rogers and Bielajew 1990, Ma and Nahum 1993, Rogers *et al* 1995, Kawrakow *et al* 1996, Keall and Hoban 1996, Ma *et al* 1999).

For patient dose calculations, the simulation phantom was built from the patient's CT data with up to $128 \times 128 \times 128$ voxels (uniform in any dimension). The side of a voxel varied from 0.2 to 0.4 cm. A separate program was developed to convert the patient's CT data from the FOCUS treatment planning system (Computerized Medical Systems, St Louis, MO) to desired dimensions, material types and densities. The organ contours were also obtained for dose calculation and analysis. The phase-space data obtained from a BEAM simulation were used as a source input with variable source positions and beam incident angles. To simulate the dose distribution of a finite size beamlet used by the inverse planning process, particles were transported to the MLC plane and only those within the beamlet area ($= 1 \text{ cm} \times 1 \text{ cm}$ projected at 100 cm SSD) were allowed to go through. This ignored the bremsstrahlung photon leakage and electron scattering by the leaf ends in the optimization process (the effect was corrected in the final dose calculation, as discussed below). After optimization, a leaf sequence was generated using a modified 'step and shoot' algorithm based on our early work (Ma *et al* 1998). The final MERT dose distribution was computed based on an intensity map (a 2D distribution of particle weighting factors) reconstructed from the leaf sequence. The bremsstrahlung leaf leakage effect was included in the intensity map using the leaf sequence and pre-calculated leaf leakage data for 1.5 cm thick tungsten leaves. MCDOSE produced data files that contained geometry specifications such as the number of voxels in all the three directions and their boundaries as well as the dose values and the associated (1σ) statistical uncertainties in the individual voxels and organs (structures). The EGS4 transport parameters were ECUT = AE = 700 keV, PCUT = AP = 10 keV and ESTEPE = 0.04. The number of particle histories simulated ranged from 2 million to 30 million for a MERT treatment. The 1σ statistical uncertainty in the dose was generally 2% or smaller of the D_{max} value. The CPU time required for a MERT simulation was about 1–3 h on a Pentium III 450 MHz PC with the variance reduction option switched on.

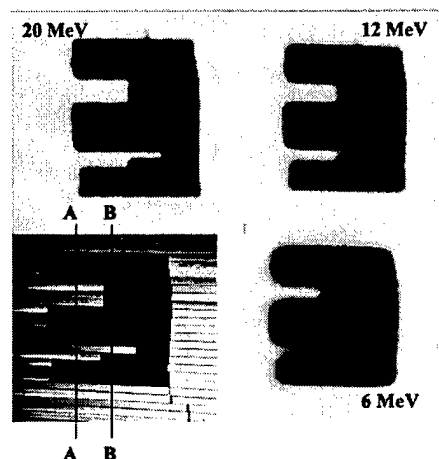


Figure 2. Beam intensity distributions measured by film on the surface of a solid water phantom for 6, 12 and 20 MeV electrons. The MLC leaf positions for the electron fields are also shown (bottom left).

2.4. The optimization process

The treatment planning optimization system used in this work is a home-developed system based on the work by Jiang (1998). First, the planner inputs the patient geometry and defines the treatment setup, such as the beam energy, number and orientations of beams, etc. The target volume and the critical structures are defined by the clinician. A reference monitor unit is assigned to each open rectangular beam and the dose deposition coefficients, which are defined as the dose contribution from a beamlet to a point, are calculated using the MCDOSE code.

Second, using the calculated dose deposition coefficients as input, the optimal intensity profile for each beam is achieved using a gradient method to minimize the objective function. For the target area, a quadratic form of objective function is specified. In addition, two target dose-uniformity constraints are used to ensure a uniform target dose distribution and to distinguish the clinical importance of cold and hot spots. For the critical structures, maximum-dose constraint and several levels of dose-volume constraints are assigned to each structure. For each objective function and constraint, an importance weight relative to the target objective function is assigned. All the constraints are mathematically transformed to the penalty functions of quadratic forms. The augmented objective function, which should be minimized, is a combination of the original objective functions and all penalty functions. The results of the optimization process are the intensity profiles for the individual fields (different incident energies and gantry angles). The same optimizer has been used for photon beam optimization with the Monte Carlo method and a finite-size pencil beam algorithm (Jiang 1998, Jiang *et al* 1999, Pawlicki *et al* 1999).

3. Results and discussion

3.1. Characteristics of electron beams collimated by an electron MLC

Figure 2 shows the electron fields collimated by the prototype electron MLC for 6, 12 and 20 MeV electron beams on a Varian Clinac 2100C machine. For convenience, a photo showing

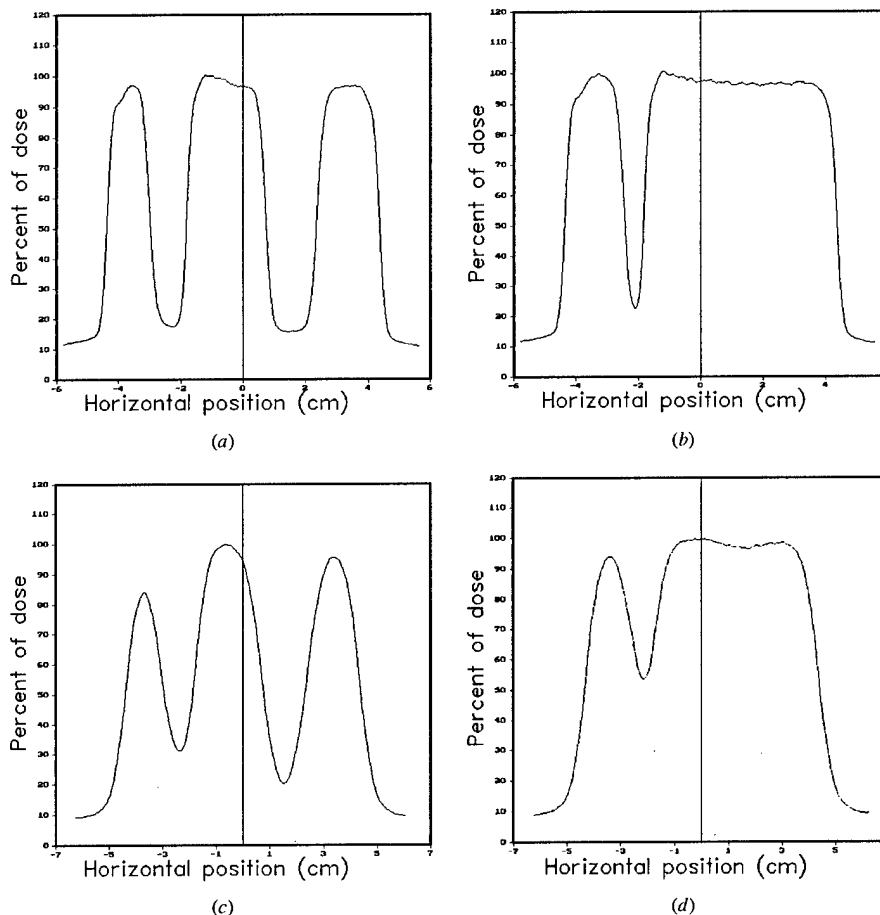


Figure 3. Beam profiles measured by film on the surface of a solid water phantom for the 6 MeV and 20 MeV electron fields shown in figure 2: (a) 20 MeV along A-A; (b) 20 MeV along B-B; (c) 6 MeV along A-A; (d) 6 MeV along B-B.

the MLC leaf positions for the field shape is also included in figure 2. Figure 2 shows the film measurement at the surface of a solid water phantom (97 cm SSD) for 6, 12 and 20 MeV electron beams. Figure 3 shows the measured profiles on the phantom surface along A-A and B-B for the 6 MeV and 20 MeV electron fields shown in figure 2. Figure 4 shows the beam profiles at 2 cm depth in the solid water phantom. It can be seen that for a 20 MeV electron beam, 0.5 cm leaf shapes are still distinguishable on the surface but become very blurred at 2 cm depth. For a 6 MeV electron beam, however, the effect of electron scattering becomes so severe that a leaf width smaller than 1.0 cm will not result in any improvement in the spatial resolution. However, a small leaf width may have the advantage of defining the field more precisely in the direction perpendicular to the leaves.

Based on these experimental results, we further performed Monte Carlo simulations of electron fields collimated by 1 cm wide leaves to study the effect of material type and

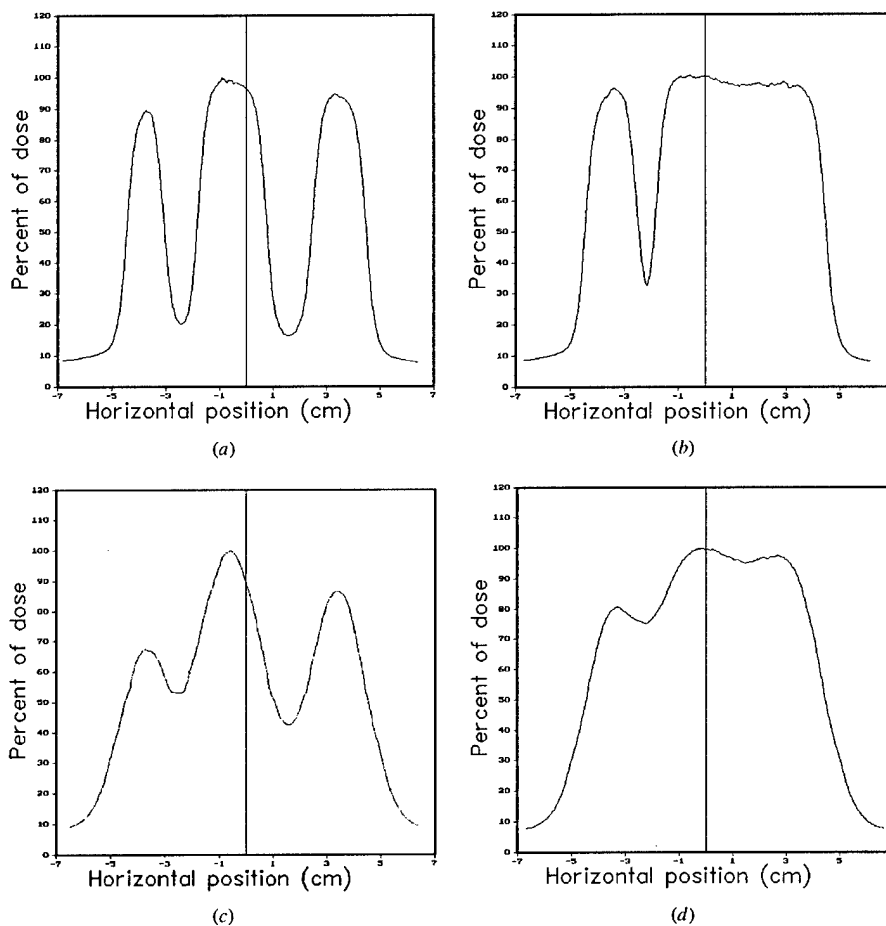
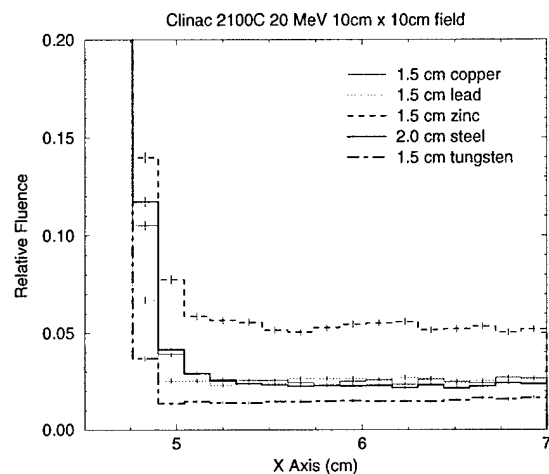
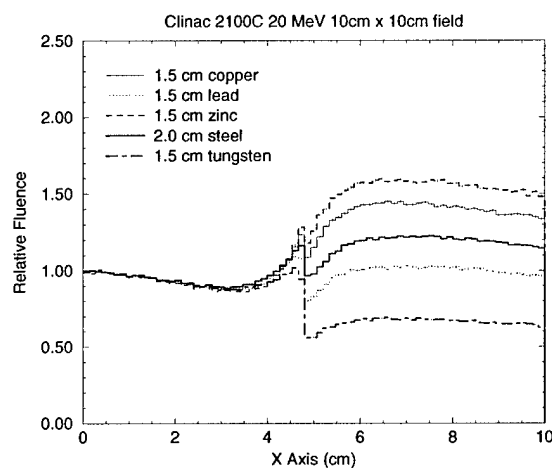


Figure 4. Beam profiles measured at 2 cm depth in a solid water phantom for the 6 MeV and 20 MeV electron fields shown in figure 2: (a) 20 MeV along A-A; (b) 20 MeV along B-B; (c) 6 MeV along A-A; and (d) 6 MeV along B-B.

leaf thickness. Although the beam penumbral widths did not change significantly for leaf thicknesses smaller than 2 cm, the beam intensity outside the field was affected by the leaf thickness and the atomic number of the leaf material. As shown in figure 5 for a 20 MeV electron beam, 1.5 cm thick zinc reduced the electron fluence outside the field to about 5% of the central axis value (figure 5(a)). These electrons were mainly generated by the bremsstrahlung photons in the MLC leaves. This was confirmed by the photon fluence as shown in figure 5(b), where 1.5 cm zinc MLC leaves resulted in about 60% higher photon fluence outside the field compared with the central axis photon fluence. Some electrons were also scattered off the leaf ends and by air. For 1.5 cm copper, 1.5 cm lead and 2 cm steel, the electron fluence was about 2.5% of the central axis value. The electron fluence was reduced to about 1.5% if the leaves were made of 1.5 cm tungsten. This was reflected by the 30% smaller photon fluence under the tungsten MLC leaves compared with the central axis photon fluence. Clearly, tungsten was superior to



(a)



(b)

Figure 5. Monte Carlo simulated electron (a) and photon (b) planar fluence in the penumbral region and outside the treatment field for a Varian Clinac 2100C 20 MeV electron beam collimated by an electron MLC of different leaf materials and thicknesses. The air gap between the electron MLC and the scoring plane is 7 cm.

other materials in terms of leaf leakage. If we increased the tungsten leaf thickness to 2 cm the electron fluence would be reduced to less than 1% of the central axis value and the photon leakage would be reduced to about 50% of the central axis value (not shown).

To study the overall effect of the leaf leakage, leaf scattering, air scattering and the extended source in an electron beam, we compared the dose distributions for single fields and multiple abutting fields collimated by an electron MLC with 1.5 cm thick tungsten leaves. Figure 6 shows the Monte Carlo calculated dose distributions for a single 4 cm × 4 cm electron field and a multiple abutting field of the same size formed by four 1 cm × 4 cm electron fields. For

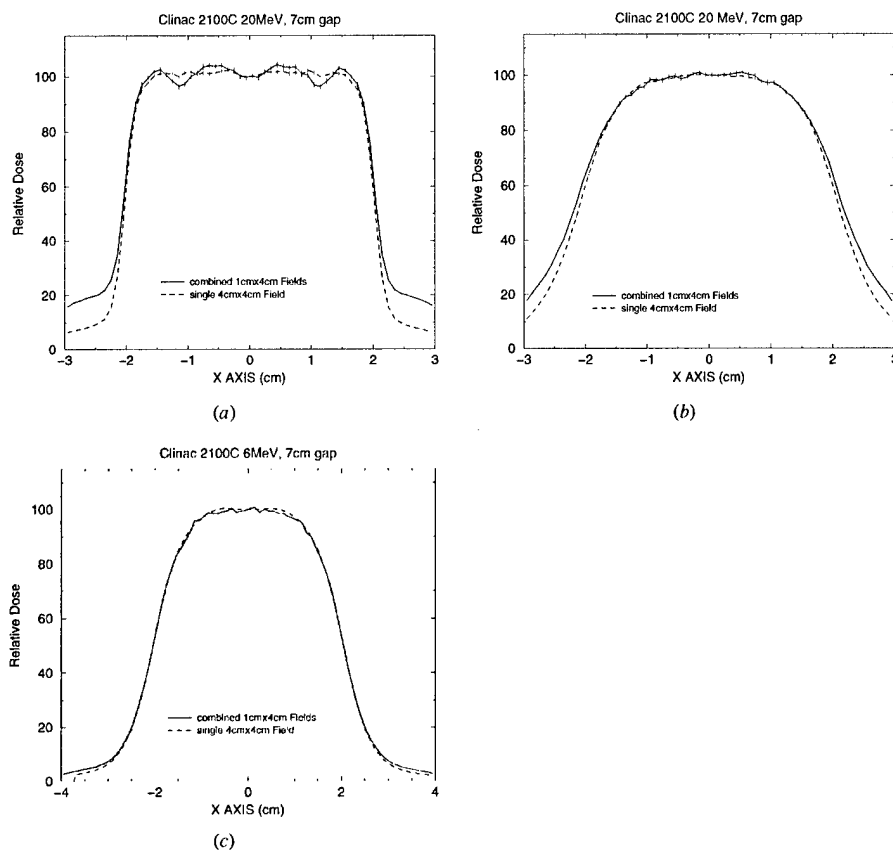


Figure 6. Monte Carlo calculated dose distributions in a water phantom for Varian Clinac 6 and 20 MeV electron beams collimated by an electron MLC of 1.5 cm thick tungsten leaves for a single $4\text{ cm} \times 4\text{ cm}$ electron field and a $4\text{ cm} \times 4\text{ cm}$ field formed by four $1\text{ cm} \times 4\text{ cm}$ electron fields: (a) dose at surface for a 20 MeV beam; (b) dose at 3 cm depth for a 20 MeV beam; (c) dose at surface for a 6 MeV beam.

a 20 MeV electron beam, the dose at the phantom surface for the abutting field shows about 4% fluctuation compared with a single electron field (figure 6(a)). This is potentially due to the effect of leaf shape and extended source. The dose outside the field for the abutting field is about three times higher than that for the single field, which is mainly caused by the leaf leakage due to the longer beam-on time to deliver the four $1\text{ cm} \times 4\text{ cm}$ fields and electron scattering off the leaf ends. The dose at 3 cm depth shows little difference between the abutting field and the single field except for the dose near the field edges and outside the field (figure 6(b)). For a 6 MeV electron beam, the dose at the phantom surface for the abutting field is almost the same as that for the single field (figure 6(c)). The dose outside the field for the abutting field is only slightly higher than that for the single field. The effect of leaf leakage is very small for a 6 MeV beam and the dose immediately outside the field is thought to be mainly due to the effect of electron scattering in the air. It seems that field abutting with 1 cm beamlets collimated by an electron MLC can provide adequate beam characteristics for MERT for the beam energies

investigated. However, the dose outside the field needs to be minimized through beam energy and leaf sequence optimization.

3.2. Comparisons of a photon MLC and an electron MLC

There have been studies on electron beam collimation using a photon MLC (Karlsson *et al* 1999). One of the advantages of using a photon MLC is the possibility of combining both photon and electron beams in the same plan. An essential requirement for matching a photon beam and an electron beam at different depths is that both beams share the same source position. Karlsson *et al* (1999) proposed several modifications to the design of a Varian Clinac 2300CD accelerator, one of which was to replace the intervening air with helium. This could significantly reduce the effect of electron scattering in the air on the beam penumbra. However, filling the accelerator head with helium requires major modifications to the existing accelerator design. In this work, we have investigated an alternative solution—a thin leaf MLC at the electron cutout level to reduce the air scattering effect. As can be seen in figure 7, the unfocused MLC leaf ends could scatter the electrons very significantly to degrade the beam characteristics near the field edges. The Varian MLC has rounded leaf ends, which are expected to have similar dosimetric characteristics as the unfocused MLC studied here. Focused leaf ends could greatly improve the beam edges and provided even slightly better dose profiles inside the field for a 20 MeV electron beam compared with an electron MLC (figures 7(a)–(c)), primarily due to the reduction of electron scattering in the accelerator head (helium versus air). The dose outside the field was slightly lower for the electron MLC than for the photon MLC. For a 6 MeV beam, an electron MLC gave slightly better surface dose profiles both inside and outside the field than the focused and unfocused photon MLC. However, the dose profiles became practically similar at the depth of the maximum dose and greater depths (not shown). Note that in these comparisons, we have placed the phantom surface at 20 cm below the photon MLC and 7 cm below the electron MLC to minimize the effect of electron scattering in the air or helium between the MLC and the phantom. It is evident that an electron MLC will have similar dosimetric characteristics as a photon MLC with focused leaf ends but without the need to replace the air in the accelerator head with helium.

3.3. Comparison of beamlet distributions

The accuracy of the beamlet distribution calculation may play an important role in the treatment planning optimization process. Ma *et al* (1999) reported significant differences in the final dose distributions of the optimized treatment plans computed by a commercial inverse treatment planning system with a finite-size pencil beam and the Monte Carlo method. Pawlicki *et al* (1999) demonstrated that inaccurate beamlet distributions may result in under-dosing in the target and over-dosing in the adjacent critical structures, and using the Monte Carlo calculated beamlets could potentially reduce the uncertainty in the photon IMRT dose distributions. This was demonstrated again by Jeraj and Keall (1999) using a Monte Carlo dose calculation based inverse planning algorithm.

It has been shown that the electron beam dose distributions calculated by the pencil beam algorithm as implemented in some commercial treatment planning systems could be fairly uncertain in the regions near material interfaces and inhomogeneities (Cygler *et al* 1987, Shortt *et al* 1986, Mackie *et al* 1994, Ma *et al* 1999). We have computed the beamlet dose distributions using the 3D pencil beam as implemented in the FOCUS treatment planning system (Computerized Medical Systems, St Louis, MO) and compared them with the Monte Carlo calculated beamlets. Figure 8 shows the dose distributions calculated using the Monte

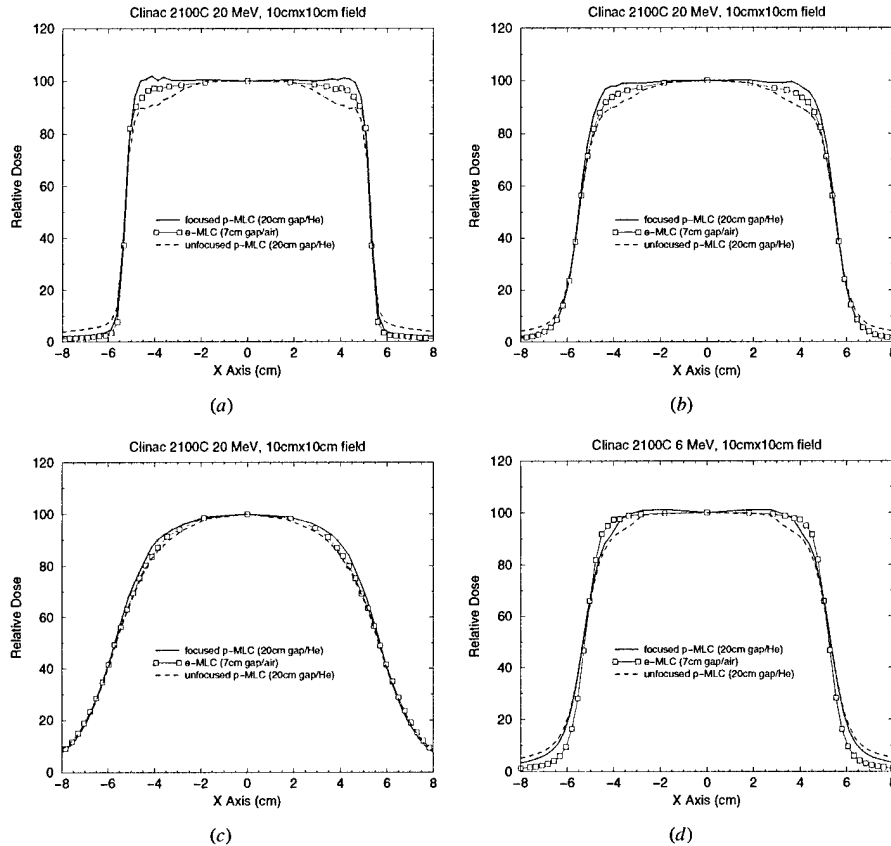


Figure 7. Monte Carlo calculated dose distributions in a water phantom for a 10 cm \times 10 cm field collimated by an electron MLC with 1.5 cm thick tungsten leaves and a photon MLC with 7.5 cm thick leaves on a Varian Clinac 2100C accelerator: (a) surface dose for a 20 MeV beam; (b) dose at 3 cm depth for a 20 MeV beam; (c) dose at 6 cm depth for a 20 MeV beam; (d) surface dose for a 6 MeV beam. The electron MLC has straight leaf ends. The photon MLC has either straight or double-focused leaves.

Carlo method (a, c, e) and the FOCUS 3D pencil beam algorithm (b, d, f) for a 1 cm \times 1 cm 12 MeV beamlet incident on a patient phantom built from CT data. For beamlets with normal incidence (figures 8(a) and (b)), the difference in the dose distributions in the heart was evident: the Monte Carlo calculated isodose lines varied with the heart contour while the pencil beam isodose lines remained symmetrical despite the change in material densities. Figures 8(c) and (d) show the beamlet distributions with a 10 cm air gap. The difference is clearly seen near the surface. The beamlet distributions again differed significantly in the lung for oblique incidence (figures 8(e) and (f)). The axis of the beamlet was intentionally placed to go through soft tissues and bones. The pencil beam isodose lines seemed to stretch according to the beam axis pathlength and showed no signs of electron build-down near the low-density material. These results provided enough evidence to show that to ensure the accuracy of the optimized dose distributions for MERT we should use the Monte Carlo method to compute the electron beamlets for the inverse planning process.

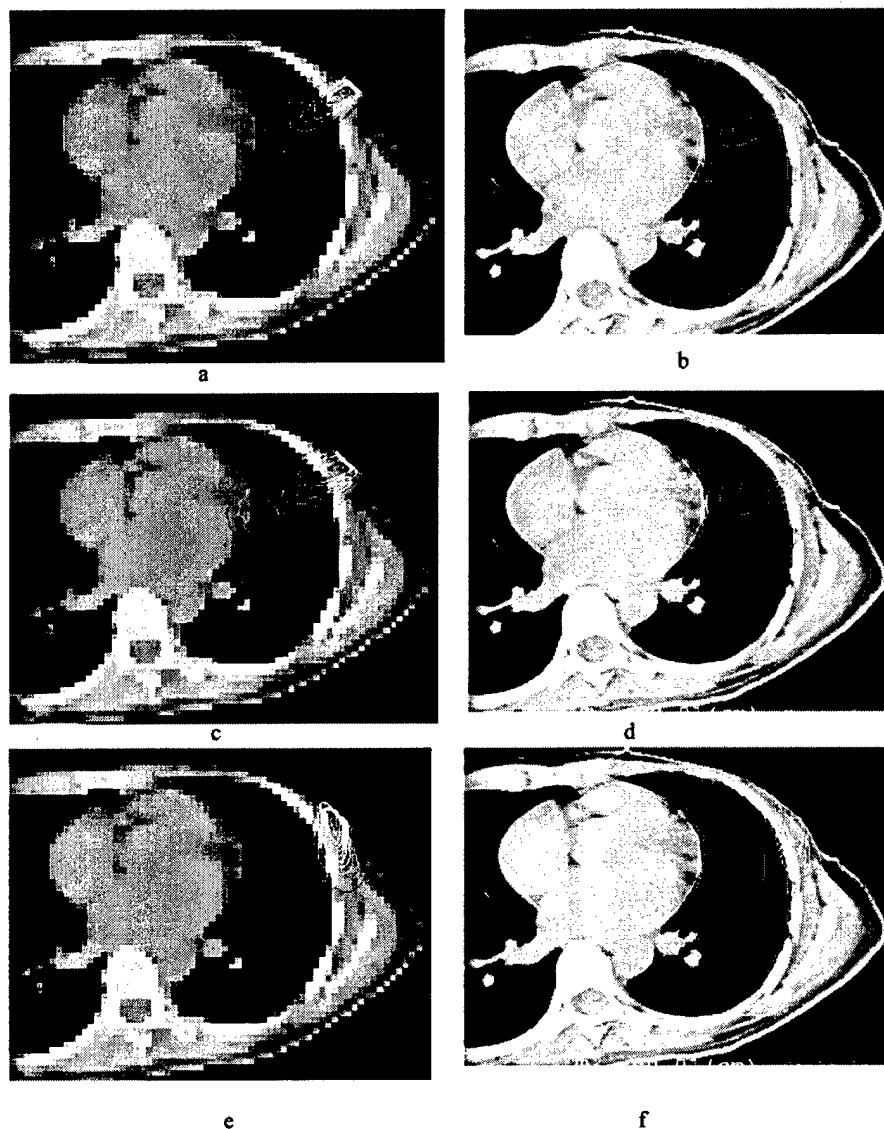


Figure 8. Dose distributions calculated using the Monte Carlo method (*a, c, e*) and the FOCUS 3D pencil beam algorithm (*b, d, f*) for a $1\text{ cm} \times 1\text{ cm}$ 12 MeV beamlet with normal incidence (*a* and *b*), normal incidence plus 10 cm air gap (*c* and *d*), and oblique incidence (*e* and *f*). The beamlet size is defined at 100 cm SSD. The isodose lines shown are 10, 20, 30, 40, 50, 60, 70, 80 and 90% of the maximum dose respectively.

3.4. MERT versus photons: a hypothetical treatment plan

Modulated electron radiotherapy is a general purpose technique that should be advantageous in many clinical situations. An exhaustive investigation of the specific advantages of MERT

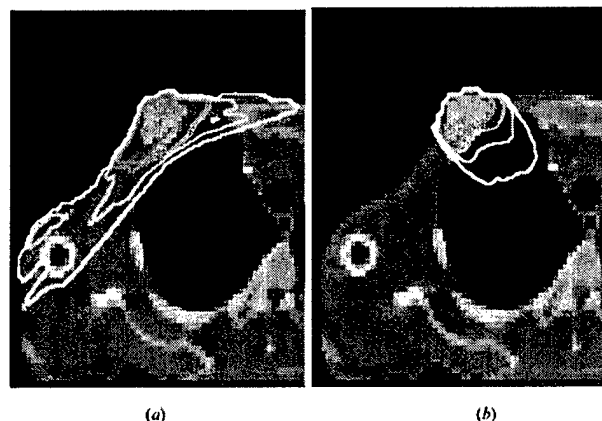


Figure 9. Treatment plans for a hypothetical breast case using tangential 6 MV photon beams (a) and MERT with 6, 12 and 20 MeV electron beams (b). Both plans were calculated using the Monte Carlo method. The isodose lines (90, 70, 50 and 30%) represented 50, 38.9, 25 and 16.7 Gy.

over traditional treatment modalities on a site by site basis is outside the scope of this work. However, to demonstrate the possibility of improving the dose homogeneity in the target and the reduction of the dose in surrounding normal tissues, we compare the dose distributions to treat a hypothetical target using tangential photon beams and MERT. The purpose of the comparison was to illustrate the concept of MERT but not to draw specific conclusions on the use of either technique. Previous investigators have used artificial phantoms and hypothetical targets to mimic different treatment sites (e.g. Hyödynmaa *et al* 1996, Åsell *et al* 1997, Ebert and Hoban 1997). We considered it to be clinically relevant to use a more realistic patient geometry (built from CT data) in our comparison, although the target definition and beam setup are somewhat arbitrary. Figure 9 shows the hypothetical treatment plan using tangential 6 MV photon beams and MERT with normally incident 6, 12 and 20 MeV electron beams. The intensity maps for each electron beam energy are shown in figure 10. The beamlet size was 1 cm \times 1 cm at 100 cm at isocentre. It is worth noting here, that as a matter of practicality, it is impossible to create the intensity maps shown in figure 10 using the conventional electron cutout approach but the electron MLC is a viable alternative. The dose distributions for both plans were calculated using the Monte Carlo method. The isodose lines (90, 70, 50 and 30%) were normalized in such a way that the 90% isodose surface would receive the prescribed target dose of 50 Gy. For the photon plan, the 90% dose line also included a margin in the lung to account for the effect of patient breathing. This was not needed for the electron plan as the electron beams were incident *en face* and the electron beamlet dose distributions do not vary significantly with breathing. Figure 11 shows the dose volume histograms (DVH) for the hypothetical treatment plans shown in figure 9. The target DVH together with the right lung DVH are shown in figure 11(a) (as percentage volume) and the right lung DVH and the 'total body' (including everything inside the external contour) DVH are shown in figure 11(b) (as absolute volume).

It is clear that MERT provided better dose homogeneity in the target region than tangential photon beams. Tangential photon beams produced hot spots in the target and cold spots near the skin (figure 11(a)). MERT significantly reduced the dose to the lung relative to tangential photon beams; the maximum dose to the lung was reduced from 50 Gy for a tangential treatment to 35 Gy for MERT (figure 11(a)). However, MERT increased the volume of the lung that

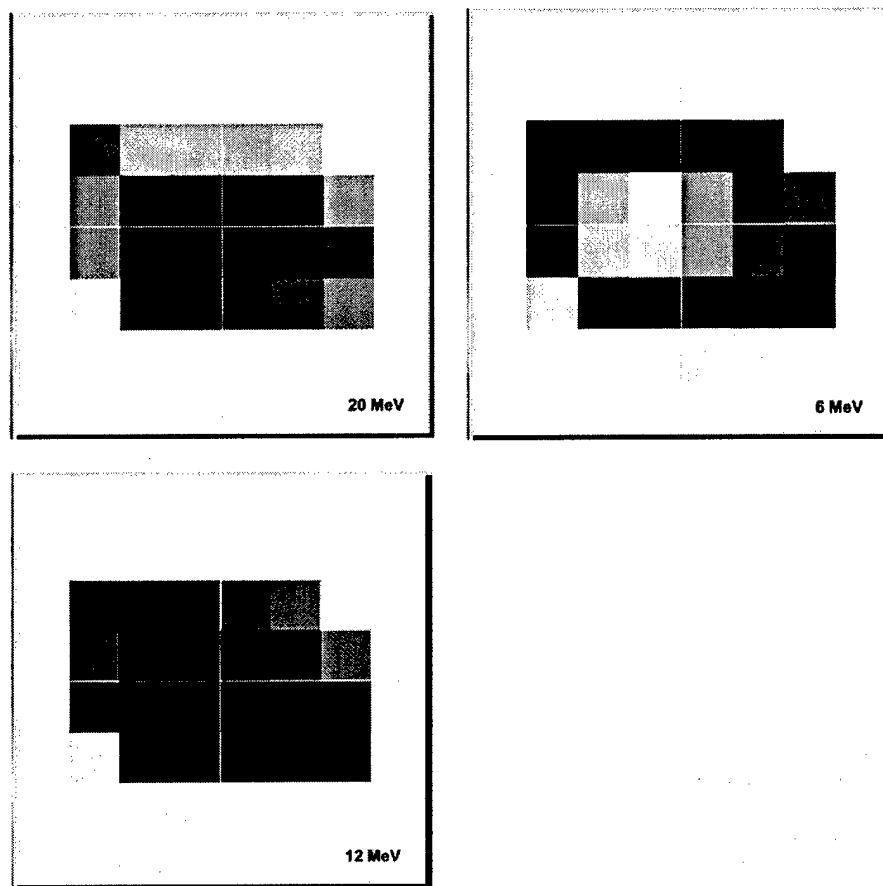


Figure 10. Intensity maps for the three electron beam energies. The beamlet size for each port was $1 \times 1 \text{ cm}^2$. Darker beamlets indicate a higher weight than the lighter beamlets and the grey scale for all three maps is in absolute terms.

received a lower dose (10% more volume received 5 Gy and 20% more volume received 2 Gy) compared with tangential photon beams. The clinical significance of the increased lung volume receiving such a low dose needs to be investigated. On the other hand, over 150 cm^3 of lung received much less dose with MERT compared with tangential photon beams, which could result in reduced lung complications (figure 11(b)). Another clear benefit with MERT is the exclusion of the surrounding normal tissue from the high dose volume (figure 11(b)). Over 1000 cm^3 of normal tissue received 10–30 Gy less dose in a MERT plan compared with this tangential photon beam plan.

4. Conclusions

In this work, we have investigated the feasibility of modulating both energy and intensity of electron beams for radiotherapy. This was achieved by combining electron beams of different

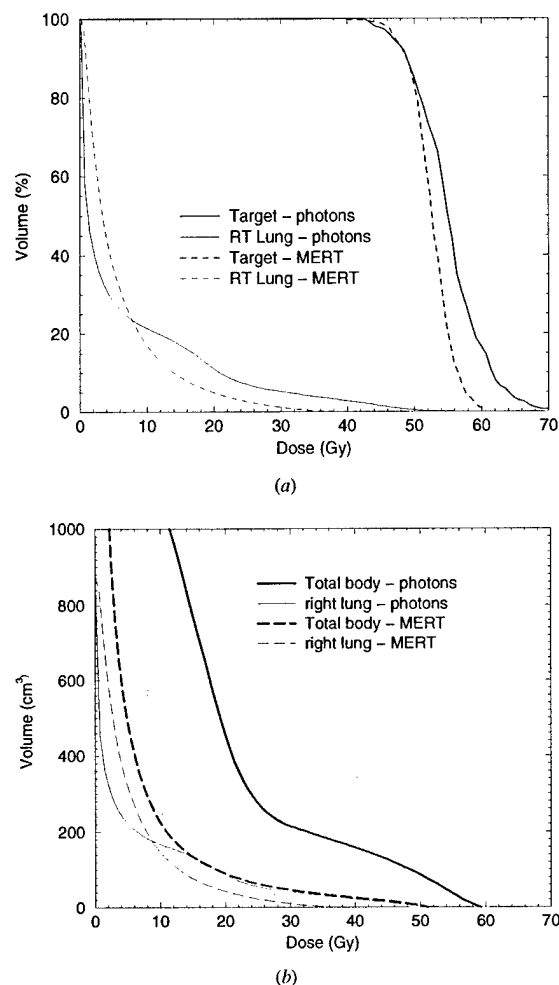


Figure 11. Dose volume histograms (DVH) for the breast treatment plans shown in figure 9: (a) DVH shown as percentage volume for the target (PTV) and the right lung and (b) DVH shown as absolute volume for the right lung and the 'total body' which includes everything inside the external contour.

nominal energies and variable intensity distributions. A prototype electron MLC was built to study the characteristics of MLC-collimated electron beams and the Monte Carlo simulations were used to investigate the effect of MLC leaf material, thickness, shape and location. The beamlet distributions calculated using a 3D electron pencil beam algorithm as implemented in a commercial treatment planning system and the Monte Carlo method were compared for electron beams of different energies, extended air gaps, oblique incidence and heterogeneous geometries. A hypothetical breast case was used to compare the dose distributions using tangential photons and MERT for target coverage (dose homogeneity) and normal tissue sparing (dose reduction in the lung and other surrounding normal tissues).

Our results showed that an electron MLC at the electron cutout location can provide adequate beam collimation for MERT without the need to replace the air in the accelerator head and between the MLC and the phantom with helium. The beam characteristics collimated by an electron MLC are comparable to those collimated by a focused photon MLC. However, the latter requires the accelerator head and between the MLC and the phantom to be filled with helium, which may be impractical for some accelerators because of the major modifications needed to the structure design. An electron MLC can also be used in place of a cutout. The Monte Carlo method can accurately simulate particle transport in cases involving extended air gaps, oblique incidence and heterogeneous anatomy, and is therefore suitable for the beamlet calculation for MERT treatment optimization. Our preliminary results based on a hypothetical breast case demonstrated the potential of MERT for uniform target coverage and normal tissue sparing. To fully explore the potential of MERT, further studies need to be carried out for realistic clinical cases and for other treatment sites such as the head and neck.

Acknowledgments

We would like to acknowledge Varian Oncology Systems, Palo Alto, CA, for providing detailed information on the Varian Clinac linear accelerators. We would like to thank our colleagues Fred van den Haak, for making the prototype electron MLC, and Sam Brain, Todd Koumrian, Behrooz Tofighrad and Michael Luxton for help with the computers and software support. This investigation was supported in part by grants CA78331 from the NIH, BC971292, BC990018 and BC990213 from the DOD, Seed Cycle 1 from the RSNA Research and Education Fund, and a consortium agreement with the NumeriX, LLC.

References

- AAPM 1983 AAPM TG-21, a protocol for the determination of absorbed dose from high-energy photons and electrons *Med. Phys.* **10** 741
- 1991 AAPM TG-25, Clinical electron beam dosimetry: report of AAPM Radiation Therapy Committee Task Group No. 25 *Med. Phys.* **18** 73–109
- Åsell M, Hyödynmaa S, Gustafsson A and Brahme A 1997 Optimization of 3D conformal electron beam therapy in inhomogeneous media by concomitant fluence and energy modulation *Phys. Med. Biol.* **42** 2083–100
- Bielajew A and Rogers D W O 1987 PRESTA—the parameter reduced electron step algorithm for electron Monte Carlo transport *Nucl. Instrum. Methods B* **18** 165–81
- Bielajew A F, Rogers D W O, Cygler J and Battista J J 1987 A comparison of electron pencil beam and Monte Carlo calculational methods *The Use of Computers in Radiation Therapy* ed I A D Bruinvis (Amsterdam: Elsevier) pp 65–8
- Boesecke R, Doll J, Bauer B, Schlegel W, Pastyr O and Lorenz M 1988 Treatment planning for conformation therapy using a multileaf collimator *Strahlenther. Onkol.* **164** 151–4
- Brewster L, Mohan R, Mageras G, Burman C, Leibel S and Fuks Z 1995 Three dimensional conformal treatment planning with multileaf collimators *Int. J. Radiat. Oncol. Biol. Phys.* **33** 1081–9
- Boyer A L, Geis P B, Grant W, Kendall R and Carol M 1997 Modulated-beam conformal therapy for head and neck tumors *Int. J. Radiat. Oncol. Biol. Phys.* **39** 227–36
- Brahme A 1988 Optimal setting of multileaf collimators in stationary beam radiation therapy *Strahlenther. Onkol.* **164** 343–50
- Chui C S, LoSasso T and Spirou S 1994 Dose calculations for photon beams with intensity modulation generated by dynamic jaw or multileaf collimators *Med. Phys.* **21** 1237–43
- Convery D J and Rosenbloom M E 1992 The generation of intensity-modulated fields for conformal radiotherapy by dynamic collimation *Phys. Med. Biol.* **37** 1359–74
- Cygler J, Battista J J, Scrimger J W, Mah E and Antolak J 1987 Electron dose distributions in experimental phantoms: a comparison with 2D pencil beam calculations *Phys. Med. Biol.* **32** 1073–83
- DeMarco J J, Solberg T D and Smathers J B 1998 A CT-based Monte Carlo simulation tool for dosimetry planning and analysis *Med. Phys.* **25** 1–11

- Ebert M A and Hoban P W 1997 Possibilities for tailing dose distributions through the manipulation of electron beam characteristics *Phys. Med. Biol.* **42** 2065-81
- Faddegon B A, Balogh J, Mackenzie R and Scora D 1998 Clinical considerations of Monte Carlo for electron radiotherapy treatment planning *Radiat. Phys. Chem.* **53** 217-28
- Fraass B A, McShan D L, Kessler M L, Matrone G M, Lewis J D and Weaver T A 1995 A computer-controlled conformal radiotherapy system I: overview *Int. J. Radiat. Oncol. Biol. Phys.* **33** 1139-57
- Hogstrom K R, Mills M D and Almond P R 1981 Electron beam dose calculations *Phys. Med. Biol.* **26** 445-59
- Hyödynmaa S, Gastafsson A and Brahme A 1996 Optimization of conformal electron beam therapy using energy- and fluence-modulated beams *Med. Phys.* **23** 659-66
- ICRU 1984 Radiation dosimetry: Stopping powers for electrons and positrons *ICRU Report 37* (Bethesda, MD: ICRU)
- Jeraj R and Keall P 1999 Monte Carlo-based inverse treatment planning *Phys. Med. Biol.* **44** 1885-96
- Jiang S B 1998 Development of a compensator based intensity modulated radiation therapy system *PhD Thesis* Medical College of Ohio, Toledo, OH
- Jiang S B, Boyer A L and Ma C-M 1999 A hybrid system for IMRT inverse planning and dose verification *Int. J. Radiat. Oncol. Biol. Phys.* **41** 123
- Kapur A 1999 Monte Carlo dose calculations for clinical electron and intensity modulated photon beams in radiotherapy *PhD Thesis* Stanford University, Stanford, CA, USA
- Kapur A, Ma C-M, Mok E and Findley D 1997 Characterization of small field electron beams for radiotherapy using Monte Carlo simulations *Proc. 12th Int. Conf. on the Use of Computers in Radiation Therapy (Salt Lake City, Utah)* (Madison, WI: Medical Physics Publishing) pp 157-8
- Kapur A, Ma C-M, Mok E, Findley D and Boyer A L 1998 Monte Carlo calculations of clinical electron beam output factors *Phys. Med. Biol.* **43** 3479-94
- Karlsson M G, Karlsson M K and Ma C-M 1999 Treatment head design for multileaf collimated high-energy electrons *Med. Phys.* **26** 2125-32
- Karlsson M K, Karlsson M G and Zackrisson B 1998 Intensity modulation with electrons: calculations, measurements and clinical applications *Phys. Med. Biol.* **43** 1159-69
- Kawrakow I, Fippel M and Friedrich K 1996 3D electron dose calculation using a voxel based Monte Carlo algorithm *Med. Phys.* **23** 445-57
- Keall P J and Hoban P 1996 Superposition dose calculation incorporating Monte Carlo generated electron track kernels *Med. Phys.* **23** 479-85
- Kutcher G J, Mageras G S and Leibel S A 1995 Control, correction and modeling of setup errors and organ motion *Semin. Radiat. Oncol.* **5** 134-45
- Leibel S A et al 1992 Three-dimensional conformal radiation therapy at the Memorial Sloan-Kettering Cancer Center *Semin. Radiat. Oncol.* **2** 274-89
- Lief E P, Larsson A and Humm J L 1996 Electron dose profile shaping by modulation of a scanning elementary beam *Med. Phys.* **23** 33-44
- Ling C C et al 1996 Conformal radiation treatment of prostate cancer using inversely-planned intensity-modulated photon beams produced with dynamic multileaf collimation *Int. J. Radiat. Oncol. Biol. Phys.* **35** 731-40
- LoSasso T, Chui C S, Kutcher G J, Leibel S A, Fuks Z and Ling C C 1993 The use of multileaf collimators for conformal radiotherapy of carcinomas of the prostate and nasopharynx *Int. J. Radiat. Oncol. Biol. Phys.* **25** 161-70
- Ma C-M, Mok E, Kapur A and Findley D 1997 Improvement of small-field electron beam dosimetry by Monte Carlo simulations *Proc. 12th Int. Conf. on the Use of Computers in Radiation Therapy (Salt Lake City, Utah)* (Madison, WI: Medical Physics Publishing) pp 159-62
- Ma C-M, Mok E, Kapur A, Pawlicki T A, Findley D, Brain S, Forster K and Boyer A L 1999 Clinical implementation of a Monte Carlo treatment planning system for radiotherapy *Med. Phys.* **26** 2133-43
- Ma C-M and Nahum A E 1993 Calculation of absorbed dose ratios using correlated Monte Carlo sampling *Med. Phys.* **20** 1189-99
- Ma C-M, Reckwerdt P, Holmes M, Rogers D W O and Geiser B 1995 DOSXYZ Users Manual *National Research Council Report PIRS-0509(B)* (Ottawa: NRC)
- Ma L, Boyer A L, Xing L and Ma C-M 1998 An optimized leaf setting algorithm for beam intensity modulation using dynamic multileaf collimators *Phys. Med. Biol.* **43** 1629-43
- Mackie T R, Holmes T W, Reckwerdt P J and Yang J 1995 Tomotherapy: optimized planning and delivery of radiation therapy *Int. J. Imaging Syst. Technol.* **6** 43-55
- Mackie T R et al 1994 The OMEGA project: comparison among EGS4 electron beam simulations, 3D Fermi-Eyges calculations, and dose measurements *Proc. 11th Int. Conf. on the Use of Computers in Radiation Therapy (Manchester, UK)* pp 152-3

- Mageras G S *et al* 1994 Initial clinical experience with computer-controlled conformal radiotherapy using the MM50 microtron *Int. J. Radiat. Oncol. Biol. Phys.* **30** 971–8
- Mah E, Antolak J, Scrimger J W and Pattista J J 1989 Experimental evaluation of a 2D and 3D pencil beam algorithm *Phys. Med. Biol.* **34** 1179–94
- McShan D L, Fraass B A, Kessler M L, Matrone G M, Lewis J D and Weaver T A 1995 A computer-controlled conformal radiotherapy system. II: sequence processor *Int. J. Radiat. Oncol. Biol. Phys.* **33** 1159–72
- Mohan R 1997 Why Monte Carlo? *Proc. 12th Int. Conf. on the Use of Computers in Radiation Therapy* (Salt Lake City, UT) (Madison, WI: Medical Physics Publishing) pp 16–18
- Nelson R, Hirayama H and Rogers D W O 1985 The EGS4 code system *Stanford Linear Accelerator Center Report SLAC-265* (Stanford, CA: SLAC)
- Pawlicki T A, Jiang S B, Deng J, Li J S and Ma C-M 1999 Monte Carlo calculated beamlets for photon beam inverse planning *Med. Phys.* **26** 1064–5
- Powlis W D *et al* 1993 Initiation of multileaf collimator conformal radiation therapy *Int. J. Radiat. Oncol. Biol. Phys.* **25** 171–9
- Rogers D W O and Bielajew A F 1990 Monte Carlo techniques of electrons and photons for radiation dosimetry *Dosimetry of Ionizing Radiation* vol III, ed K Kase, B E Bjarngard and F H Attix (New York: Academic) pp 427–539
- Rogers D W O, Faddegon B A, Ding G X, Ma C-M, Wei J S and Mackie T R 1995 BEAM: a Monte Carlo code to simulate radiotherapy treatment units *Med. Phys.* **22** 503–25
- Shortt K R, Ross C K, Bielajew A F and Rogers D W O 1986 Electron beam dose distributions near standard inhomogeneities *Phys. Med. Biol.* **31** 235–49
- Takahashi S 1965 Conformation radiotherapy-rotation techniques as applied to radiography and radiotherapy of cancer *Acta Radiol. Suppl.* **242** 1–142
- Wang L, Chui C and Lovelock M 1998 A patient-specific Monte Carlo dose-calculation method for photon beams *Med. Phys.* **25** 867–78
- Webb S 1992 Optimization by simulated annealing of three-dimensional conformal treatment planning for radiation fields defined by multi-leaf collimator: II. Inclusion of two-dimensional modulation of x-ray intensity *Phys. Med. Biol.* **37** 1689–704
- 1997 *The Physics of Conformal Radiotherapy: Advances in Technology* (Bristol: Institute of Physics Publishing)
- Yu C X, Symons J M, Du M N, Martinez A A and Wong J W 1995 A method for implementing dynamic photon beam intensity modulation using independent jaws and multileaf collimators *Phys. Med. Biol.* **40** 769–87
- Zackrisson B and Karlsson M 1996 Matching of electron beams for conformal therapy of target volumes at moderate depths *Radiother. Oncol.* **39** 261–70
- Zhang G G, Rogers D W O, Cygler J E and Mackie T R 1999 Monte Carlo investigation of electron beam output factors versus size of square cutout *Med. Phys.* **26** 743–50

Monte Carlo and experimental investigations of multileaf collimated electron beams for modulated electron radiation therapy

Michael C. Lee,^{a)} Steve B. Jiang, and C.-M. Ma

Department of Radiation Oncology, Stanford University School of Medicine, Stanford, California 94305-5304

(Received 17 November 1999; accepted for publication 2 October 2000)

Modulated electron radiation therapy (MERT) has been proposed as a means of delivering conformal dose to shallow tumors while sparing distal structures and surrounding tissues. Conventional systems for electron beam collimation are labor and time intensive in their construction and are therefore inadequate for use in the sequential delivery of multiple complex fields required by MERT. This study investigates two proposed methods of electron beam collimation: the use of existing photon multileaf collimators (MLC) in a helium atmosphere to reduce in-air electron scatter, and a MLC specifically designed for electron beam collimation. Monte Carlo simulations of a Varian Clinac 2100C were performed using the EGS4/BEAM system and dose calculations performed with the MCDOSE code. Dose penumbras from fields collimated by photon MLCs both with air and with helium at 6, 12, and 20 MeV at a range of SSDs from 70 to 90 cm were examined. Significant improvements were observed for the helium based system. Simulations were also performed on an electron specific MLC located at the level of the last scraper of a 25×25 cm² applicator. A number of leaf materials, thicknesses, end shapes, and widths were simulated to determine optimal construction parameters. The results demonstrated that tungsten leaves 15 mm thick and 5 mm wide with unfocused ends would provide sufficient collimation for MERT fields. A prototype electron MLC was constructed and comparisons between film measurements and simulation demonstrate the validity of the Monte Carlo model. Further simulations of dose penumbras demonstrate that such an electron MLC would provide improvements over the helium filled photon MLC at all energies, and improvements in the 90–10 penumbra of 12% to 45% at 20 MeV and 6 MeV, respectively. These improvements were also seen in isodose curves when a complex field shape was simulated. It is thus concluded that an MLC specific for electron beam collimation is required for MERT. © 2000 American Association of Physicists in Medicine. [S0094-2405(00)01612-6]

Key words: modulated electron radiation therapy (MERT), IMRT, EGS4 Monte Carlo, multileaf collimator (MLC)

I. INTRODUCTION

In recent years, intensity modulated radiation therapy (IMRT) with photon beams has been used to deliver highly conformal doses to target areas while sparing neighboring tissues. However, because of the need for electron buildup, photon fields provide low surface doses and are thus not well suited to the treatment of shallow tumors. Additionally, due to the highly penetrating nature of the photon beams, some scenarios present an unavoidable accompanying risk to distal structures during photon treatments. Therefore shallow tumors are often treated with megavoltage electron beams. The rapid depth-dose fall-off associated with electron beams allows delivery of therapeutic doses to the target areas while sparing distal tissues. This makes electron beam therapy ideal for treatment of the head and neck and the chest wall. However, presently electron beam techniques offer only limited conformity in the depth direction.

One proposed treatment modality that overcomes this limitation is modulated electron radiation therapy (MERT).^{1–7} In a MERT treatment, lateral dose conformity and uniformity may be achieved by intensity modulation,

while conformity in the depth direction may be improved through use of different energies. This technique may be extremely valuable for treatment of curved surfaces, such as irradiation of the intact breast, shallow head and neck tumors, and irradiation of targets located on the extremities.

However, before MERT can be used in a clinical setting, a new system of electron beam collimation must be developed. The present system of lead alloy (Cerrobend) cutouts and boluses are not practical for the rapid delivery of the intensity distributions required in MERT. As with photon IMRT, a multileaf collimator (MLC) may provide a solution to the field shaping and intensity modulation problem. It has been proposed that scanned beam systems, alone or in conjunction with existing photon MLCs can provide adequate collimation.⁸ In his work, Brahme further suggests that “fourth-generator” clinical accelerators may be filled with helium, thereby significantly reducing in-air electron scatter and making the photon MLC a practical system for electron beams. Indeed, a number of studies have been conducted utilizing scanned beam systems (MM50, Scanditronix Medical AB, Uppsala, Sweden) in a clinical setting to improve

dose distributions.^{3,5} Jansson *et al.* have demonstrated that a scattering foil accelerator (MM22, Scanditronix Medical AB, Uppsala, Sweden) and its intrinsic MLC can be used to generate matched photon and electron fields to improve dose distributions in breast cancer therapy.⁹

Despite these successes, the use of the photon MLC with electrons has key limitations. Experimental work by Klein *et al.* has shown that in a standard Varian Clinac 2100C (Varian Oncology Systems, Palo Alto, CA), a source-to-surface distance (SSD) of 70 cm is necessary to provide a clinically acceptable field when using the photon MLC.¹⁰ Indeed, beams collimated by a photon MLC were shown to be inferior to applicator fields in penumbra and uniformity and furthermore could not be adequately matched to photon fields. Monte Carlo simulations by Karlsson *et al.* have shown that for a 9 MeV beam from a Varian Clinac 2100C/D, a reduction of the 80–20 fluence penumbra from 18 mm to 11 mm could be achieved by replacing the treatment head air with helium (including the use of a helium filled balloon between the accelerator and patient) and/or moving the MLC at least 11 cm towards the patient.⁵ Thus, this work focuses on developing an electron specific MLC (eMLC) located at the same level as a Cerrobend cutout, typically 40 cm or more closer to the patient than the photon MLC. Such a system could have the additional benefit of being backwards-compatible with existing accelerators and also being more generally accessible than scanned beam systems.

In order to have an eMLC system that may be used for MERT, several issues must be considered. While any beamlet distribution may be used during inverse planning, dose conformity will improve if the field edges are sharpened. To this end, it is desirable to have a system that provides the smallest penumbra possible and be able to provide maximum ability to resolve narrow fields. Furthermore, as with photon IMRT, a larger number of monitor units must be delivered relative to conventional treatments, and so both photon and electron leakage must be reduced. It has been shown by Ma *et al.* that if such a system is developed, intensity-modulated electron fields may be delivered.⁷

This study utilizes a combination of Monte Carlo simulations and film measurements to compare a helium/photon MLC based system, an air/photon MLC based system, and an electron specific MLC located near the phantom surface. It has been demonstrated that traditional analytical dose calculation algorithms, such as the 3D pencil beam¹¹ are limited in their use with small irregular electron fields,^{12–14} and therefore Monte Carlo simulations were chosen for treatment head modeling and dose calculations. The EGS4/BEAM^{15,16} and MCDOSE¹⁷ systems were employed to simulate different MLC systems and calculate dose in homogeneous water phantoms. These simulations allowed comparisons of the proposed collimation systems. Recommendations with regard to eMLC design and construction are also presented on the basis of the Monte Carlo simulations.

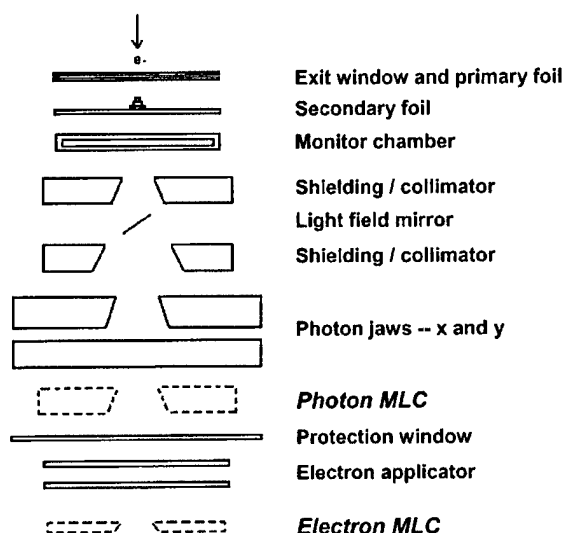


FIG. 1. Schematic of a Varian Clinac 2100C treatment head used in the BEAM simulation. Also shown are the two collimation systems proposed for electron beams.

II. MATERIALS AND METHODS

A. Monte Carlo simulation of the photon MLC

Electron beam simulations of a Varian Clinac 2100C (Varian Oncology Systems, Palo Alto, CA) were performed using the EGS4/BEAM code.^{15,16} Vendor supplied geometries were used in the component-wise simulation, and a schematic of the simulation model is displayed in Fig. 1. The simulation code and geometry employed have been previously shown to provide agreement with measured data of better than 2% in transverse profiles and depth dose curves for the three nominal energies simulated: 6, 12, and 20 MeV.¹⁸ Phase space files were obtained below the photon jaws. The photon jaws were set according to the manufacturer specifications for a 25×25 cm² applicator. These phase space files were then used as the sources for simulating various MLCs.

In the first set of simulations, the particles in the first phase space were transported through a photon MLC open to 10×10 cm² projected, the protective window and an appropriate thickness of air to the desired SSD. The photon MLC in this study was an idealized MLC with tungsten leaves of the same geometry as the Varian 52 leaf MLC (~7 cm thick, ~55 cm downstream of the target), with ends and sides always focused to the source regardless of leaf position (i.e., double focused). The MLC was set to project to an exact 10×10 cm² field at the SSD of interest (measured here from the photon target to the phantom surface). No attempt was made to simulate the number and width of the leaves of any existing accelerator. In all cases, interleaf leakage (i.e., tongue and groove effect) was ignored. Simulations were performed beginning with the aforementioned phase space source, through the photon MLC, the protective window, and through an appropriate thickness of air to the SSD of interest.

For each energy, two phase space files were generated, one in which the ambient atmosphere of the treatment head

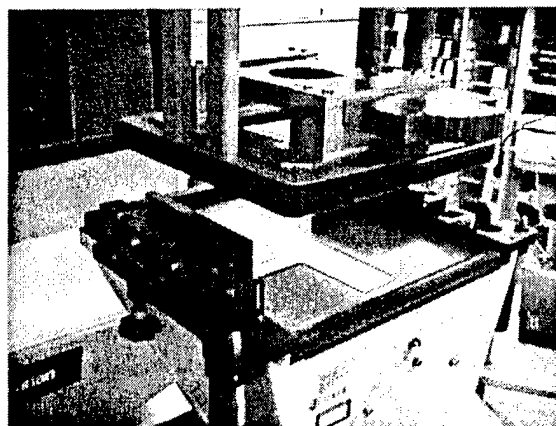


FIG. 2. Prototype electron MLC used for Monte Carlo simulations and film measurements. The MLC consists of 30 pairs of manually set steel leaves, and is designed to mount in the cutout position of a 25×25 cm² Varian applicator.

was air (density = $1.205 \times 10^{-3} \text{ g cm}^{-3}$), and one in which it was replaced with helium (density = $1.663 \times 10^{-4} \text{ g cm}^{-3}$). In the case of helium filled accelerators, the atmosphere of the air gap was also replaced with He, to simulated the use of helium bags. The walls of the bag were not simulated, as it was believed that $\sim 0.01 \text{ cm}$ Mylar would have a trivial impact on dose distributions. In all cases, phase space files were obtained at the SSD of interest (70, 75, 80, 85, 90 cm nominal SSD) and used for dose calculations.

This and all subsequent Monte Carlo simulations were performed on various elements of a suite of 22 Pentium Pro (200 MHz) CPUs and 10 Pentium III CPUs (450 MHz), all running EGS4, BEAM, and MCDOSE under the Linux operating system. In general, simulations were performed in parallel and the phase space files (or dose files) statistically combined to give improved performance. All simulations utilized an electron cutoff (ECUT) of 0.7 MeV total energy and a photon cutoff of 10 keV, below which all remaining energy was deposited on the spot. It has been documented that an ECUT of 0.7 MeV, corresponding to a residual continuous-slowing-down approximation range in water of $< 0.5 \text{ mm}$, is sufficient for most dosimetric purposes.¹⁶ PRESTA extensions were employed for step length calculations.¹⁹ The number of initial electron histories ranged from 150×10^6 for 6 MeV to 50×10^6 for 20 MeV.

Dose calculations were performed using the above generated phase space files using the EGS4/MCDOSE code.¹⁷ Homogeneous water phantoms were simulated with voxels 3 mm along the profiled axis, and 15 mm in the orthogonal in-plane direction, and 2 mm along the direction in axis. Statistical error was less than 1% (1σ) in all dose calculations.

B. Electron MLC design considerations

1. Material and leaf thickness

A number of different prototypes for eMLCs were simulated. First, under the assumption that a minimal distance

TABLE I. Simulated penumbras of a 10×10 cm² field collimated by different MLC systems. The 6 MeV beam penumbra was calculated at 0.75 cm depth, the 12 MeV beam at 2.0 cm, and the 20 MeV beam at 3.0 cm depth. The ideal MLC is built out of 1.5 cm thick tungsten located at the level of the last scraper, while the prototype MLC is 2.54 cm thick steel located 3.0 cm above the last scraper.

Energy	Gas	MLC	SSD	Dose penumbra			
				Absolute (mm)		Relative to ideal eMLC	
				80/20	90/10	80/20	90/10
6 MeV	air	photon	70	18.5	30.7	2.28	2.33
			75	23.9	38.7	2.95	2.93
			80	29.0	46.7	3.58	3.54
			85	33.2	52.3	4.10	3.96
			90	37.6	60.0	4.64	4.55
	He	photon	80	17.3	27.6	2.14	2.09
			85	19.8	32.5	2.44	2.46
			90	22.3	35.1	2.75	2.66
	air	ideal e-	100	8.1	13.2	1.00	1.00
	air	proto. e-	100	12.0	19.3	1.48	1.46
12 MeV	air	photon	70	10.9	18.8	1.31	1.38
			75	14.0	23.1	1.69	1.70
			80	16.5	26.0	1.99	1.91
			85	19.0	30.3	2.29	2.23
			90	22.0	35.0	2.65	2.57
	He	photon	80	11.3	18.6	1.36	1.37
			85	12.7	20.5	1.53	1.51
			90	13.9	22.8	1.67	1.68
	air	ideal e-	100	8.3	13.6	1.00	1.00
	air	proto. e-	100	9.8	17.1	1.18	1.26
20 MeV	air	photon	70	10.5	17.4	1.21	1.20
			75	11.7	18.9	1.34	1.30
			80	13.1	22.3	1.51	1.54
			85	14.2	23.1	1.63	1.59
			90	16.0	26.3	1.84	1.81
	He	photon	80	10.0	16.5	1.15	1.14
			85	10.7	17.5	1.23	1.21
			90	11.3	18.6	1.30	1.28
	air	ideal e-	100	8.7	14.5	1.00	1.00
	air	proto. e-	100	10.3	18.4	1.18	1.27

between the MLC and the treatment surface was optimal,^{8,12} simulations were performed with the MLCs completely replacing the last scraper of a 25×25 cm² applicator (i.e., with the back surface at approximately 95 cm from the photon target). Different materials and thicknesses were simulated, and phase space files obtained immediately at the back surface of the MLC. A total of five construction materials were considered in this investigation: zinc (density = 7.14 g cm^{-3}), steel (8.06 g cm^{-3}), copper (8.93 g cm^{-3}), lead (11.34 g cm^{-3}), and tungsten (19.30 g cm^{-3}). The copper, zinc, lead, and tungsten MLCs were limited to 1.5 cm in thickness, and the steel MLC was 2.0 cm in thickness. Analysis of phase space fluence and energy spectra was performed using the BEAMDP software.²⁰ Based on fluence leakage profiles, 1.5 cm tungsten was selected as the optimal leaf thickness and material and used in the following sections.

2. Leaf width

Simulations were performed to examine the optimal leaf width. The overall width of the MLC and the number of

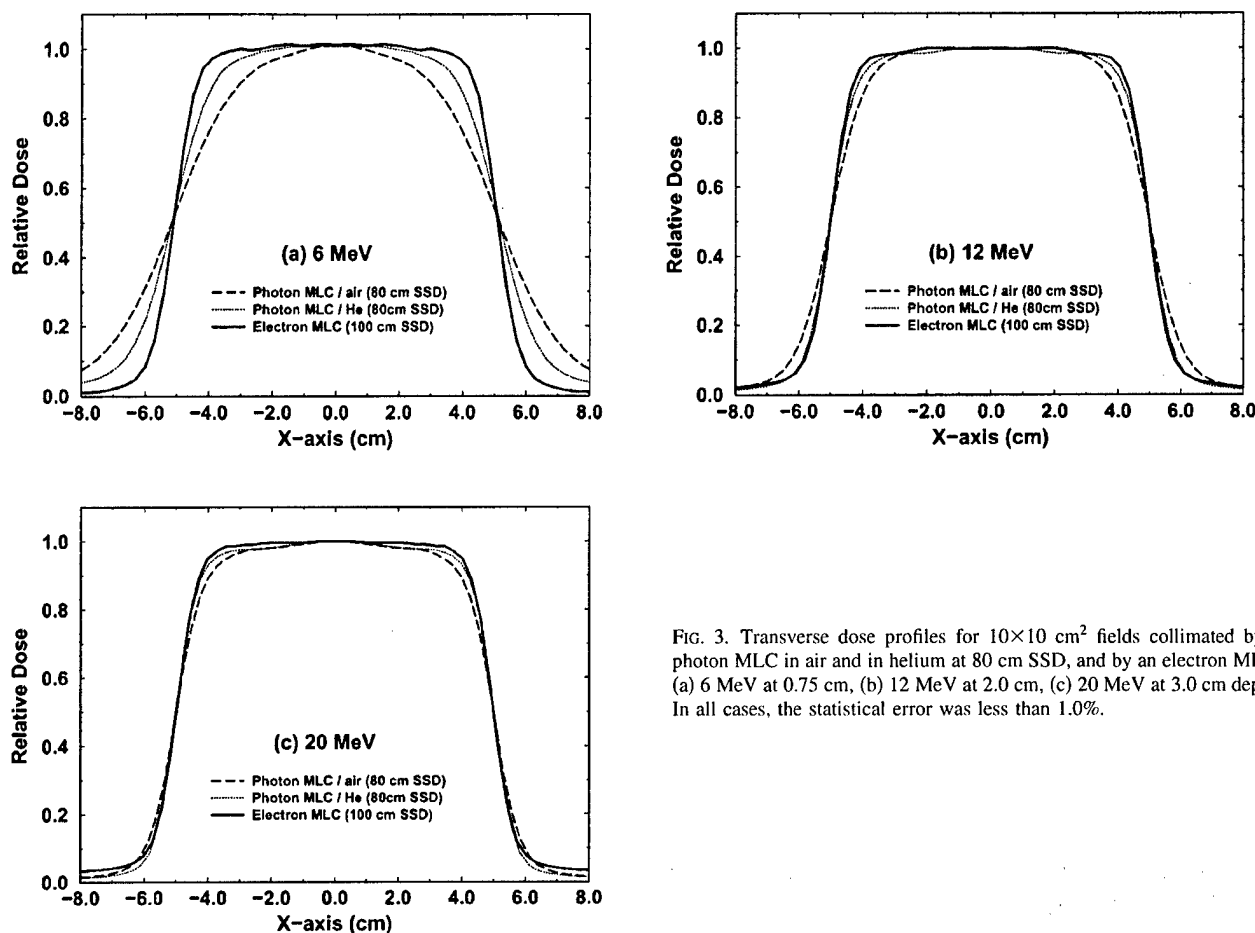


FIG. 3. Transverse dose profiles for 10×10 cm² fields collimated by a photon MLC in air and in helium at 80 cm SSD, and by an electron MLC. (a) 6 MeV at 0.75 cm, (b) 12 MeV at 2.0 cm, (c) 20 MeV at 3.0 cm depth. In all cases, the statistical error was less than 1.0%.

leaves and their positions were adjusted so that a single leaf of varying width was inserted in the first off-axis position of a 20×20 cm² field. Electron beams of 6 and 20 MeV electron beam were simulated through this collimator and the resulting phase space files were used for a dose calculation. The geometry for the dose calculation utilized $2 \times 40 \times 2$ mm³ in the region from $x = -3$ cm to 3 cm, and $5 \times 40 \times 2$ mm³ in the remaining in-field region. Additionally, the same single leaf simulation was performed for a photon MLC based on the dimensions of the intrinsic MLC in the Varian Clinac 2100C.

3. Leaf end shape

Additional BEAM simulations were performed to examine the effect of leaf shape of the eMLC. Two simulations were performed at each of two energies, 6 and 20 MeV. In one case, the leaf ends and sides were focused to the photon target, and in the second case, the ends and sides of the 1.5 cm thick tungsten leaves were parallel to the beam axis. The phase space at 100 cm SSD was analyzed using BEAMDP and used for dose calculations.

C. Prototype electron MLC

Based on the results of the theoretical study, a prototype of an eMLC was designed and built. A view of the prototype eMLC is shown in Fig. 2, and the design information is

summarized here. The MLC comprised two sets of 30 leaves, each leaf 2.54 cm (1") in thickness and 0.48 cm (3/16") in width. Both ends and sides were designed to be parallel with the beam axis, i.e., unfocused. Leaf positions could be set manually and allowed a maximum opening of 14.2×15.9 cm² with complete leaf over run allowed. The MLC was designed to fit into the cutout mounting frame in the last scraper of a 25×25 cm² applicator from a Varian Clinac 2100C linear accelerator.

The geometry of this prototype was simulated using the EGS4/BEAM simulation package and phase space files were obtained for a representative set of leaf positions shown in Fig. 11(d). A dose calculation was then performed using MCDOSE on a homogeneous water phantom composed of $3 \times 3 \times 2$ mm³ voxels.

The MLC was then installed onto the treatment head and film (Kodak X-omat V, Eastman Kodak Company, Rochester, NY) measurements were taken at the surface and at 2 cm depth in solid water. Measurements were taken at energies of 6, 12, 20 MeV at an SSD of 100 cm. The film was scanned using a Vidar scanning system and the RIT315 software package (Radiological Imaging Technology, Colorado Springs, CO) was then used to generate isodose distributions for comparison with the simulated dose results.

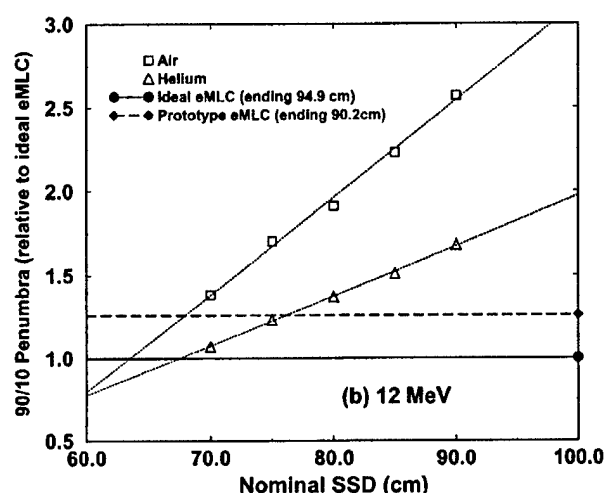
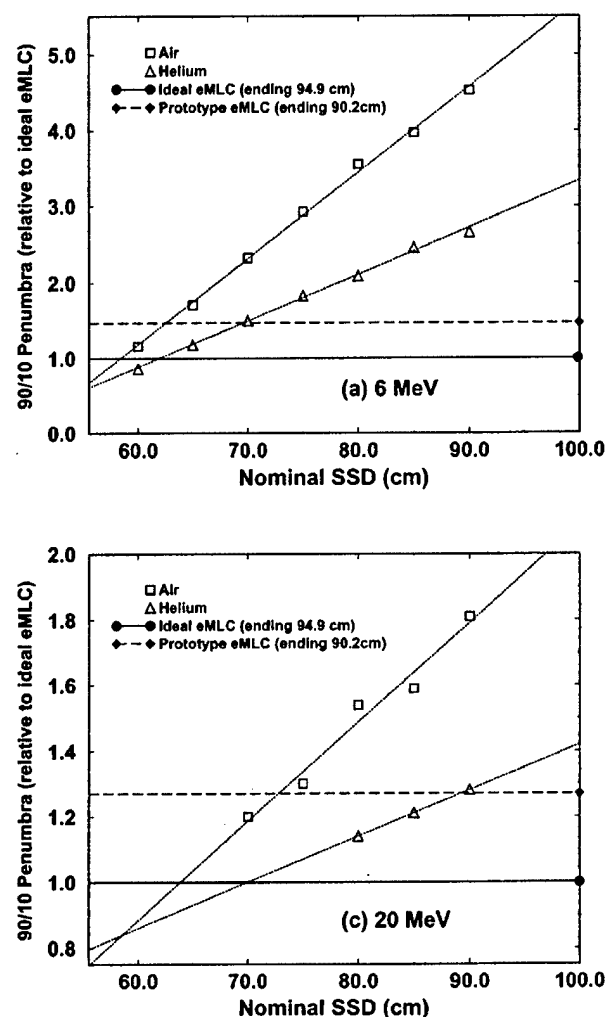


Fig. 4. Plot of 90–10 penumbra size as a function of SSD for $10 \times 10 \text{ cm}^2$ fields collimated by a photon MLC in air and in helium, the ideal electron MLC, and the prototype electron MLC. All data are normalized to the ideal electron MLC penumbra. (a) 6 MeV, (b) 12 MeV, (c) 20 MeV.

Additionally, a BEAM simulation and dose calculation were performed with the photon MLC in a helium atmosphere using these same leaf positions (projected).

III. RESULTS AND DISCUSSION

A. Electron beams collimated with the photon MLC

Collimation of electron beams with a photon MLC was simulated by using the standard BEAM component module for the MLC, and the resulting phase space files used to calculate dose in a homogeneous water phantom. The 80–20 and 90–10 penumbras, defined by the lateral distance between isodose curves along the major axes, were computed and are displayed in Table I. As expected, at all energies, there is a substantial difference in the penumbra width between the helium gas systems and the normal air-filled treatment heads. For a 6 MeV beam at 80 cm SSD and a depth of 0.75 cm, the improvement in the 90–10 penumbra was 40.9%. However, as a consequence of reduced in-air scatter of high energy electrons, the effect was much less pronounced at higher energies: for a 20 MeV beam at 3.0 cm depth and 80 cm SSD, the 90–10 penumbra was reduced by 26.0%. Similar results in both beam penumbra reduction and

energy dependence are seen for the 80–20 penumbras. Representative profiles at 80 cm SSD are shown in Fig. 3. The changes in 90–10 penumbras can be seen in Fig. 4.

B. Design considerations for an electron MLC

In order to compare the photon MLC and the eMLC, it was necessary to develop a model of an ideal eMLC. Three key design parameters were investigated:

- (i) leaf material and thickness;
- (ii) leaf width;
- (iii) leaf end shape (focusing).

The effect of these parameters on dose distributions and electron and photon transmission were examined through Monte Carlo simulations of the treatment head and MLC and dose distributions calculated in homogeneous water phantoms.

1. Leaf material and thickness

Preliminary studies were performed in which 20 MeV electrons were simulated through the treatment head and a $25 \times 25 \text{ cm}^2$ applicator, and incident upon proposed eMLC designs. The primary concern was leakage: though the leaves

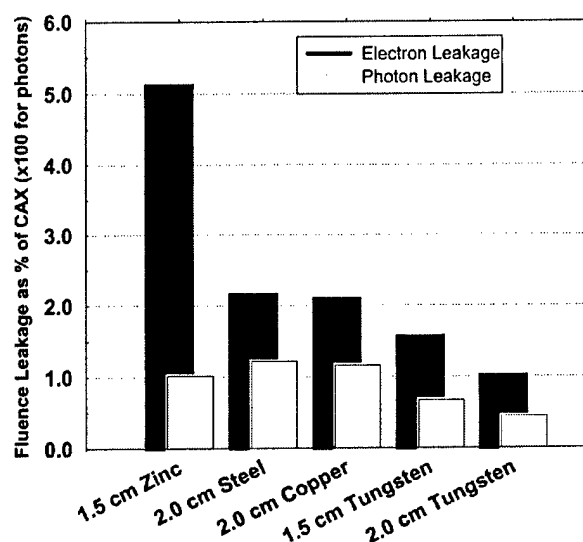


FIG. 5. Monte Carlo simulated fluence for electrons and photons for a 20 MeV electron field. Photon and electron leakage at a point 3 cm outside the field are shown, expressed as a percentage of central axis fluence. Note that for photons, the true value is the value shown $\times 100$.

themselves were thick enough to stop direct passage of all electrons, there was a concern regarding production of bremsstrahlung and secondary electrons, especially with regard to electrons interacting in the leaf ends and adding a contaminant dose in the penumbral region. To study this effect, the eMLC was set to define a 10×10 cm² field within the 25×25 cm² applicator and the electron and photon fluence studied using the BEAM system.

The electron leakage, scored 3 cm outside of the 10×10 cm² field, is shown in Fig. 5. The 1.5 cm thick tungsten MLC exhibited a background electron leakage of 1.5% of the central axis fluence, while both the steel and copper models exhibited greater than 2.0% leakage. Additionally, by examining the profiles at the field edge, it was observed that tungsten leaves resulted in a steeper drop at the field edge, corresponding to a reduction in the passage of large angle electrons through the leaf ends. While increasing the tungsten leaf thickness to 2.0 cm reduces background electron fluence to less than 1% of the central axis fluence, this modest improvement may not sufficiently offset the added weight and the associated cost.

The production of bremsstrahlung photons by the interaction of high energy electrons in the leaves was also considered. As seen in Fig. 5, as expected on the basis of the material bremsstrahlung production cross sections, tungsten again exhibits the best fluence profile, presenting less than half the photon leakage of the copper or steel MLCs. The conjecture that both photon and electron leakage is almost entirely due to bremsstrahlung and not direct leakage was supported by the use of the BEAM code "latch bit" settings to track particle interactions, as seen in Fig. 6. As expected, 1.5 cm tungsten is sufficient to stop most incident photons, and these direct photons account for only 15% of the total leakage. Also, in Fig. 7 it can be seen that the energy of the

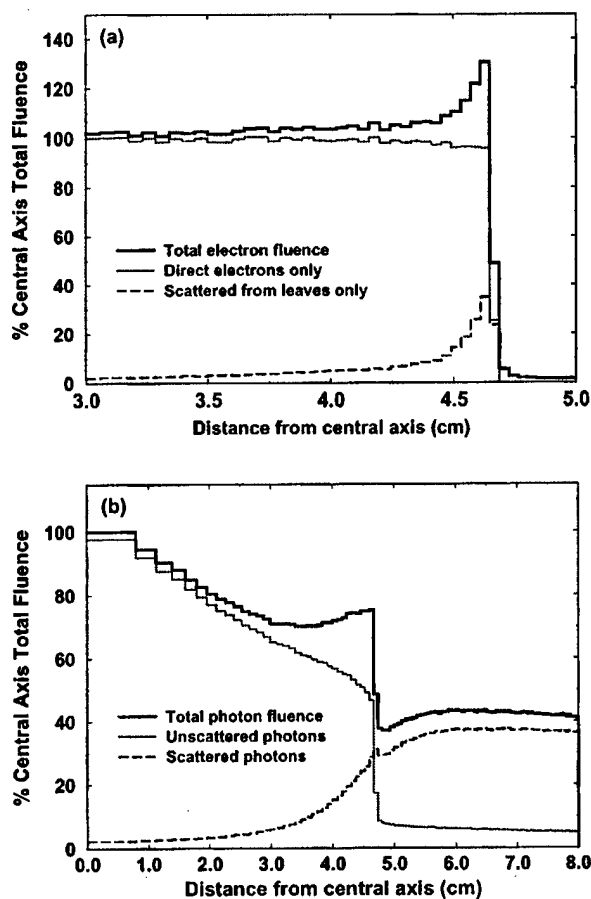


FIG. 6. Monte Carlo simulated (a) electron and (b) photon planar fluence at the edge of a 10×10 cm² field collimated by a 1.5 cm thick tungsten MLC, separated into particles that interacted in the leaves, and those that did not. The fluence was scored at the back surface of the eMLC.

photons escaping the tungsten leaves is higher than that of the photons from the copper or steel leaves (5.3 MeV versus 4.3 MeV). The ordering of the energies is as expected based on the ordering of the effective atomic numbers of the materials. However, even though the photons are more energetic, the overall photon energy fluence from the tungsten leaves remains significantly below that of the other materials. Furthermore, contaminant photon dose generally scales with the cube of the incident electron energy.²¹ As this simulation was performed with an initial electron energy of 20 MeV, it is expected that this photon dose effect will rapidly become trivial as the energy is reduced. Based on this information, the 1.5 cm thick tungsten leaf design was chosen as the model of what we hereafter refer to as the "ideal" eMLC.

2. Leaf width

Further Monte Carlo studies were performed to analyze the leaf width that provides the highest degree of resolution while optimizing the number of leaves so as to reduce inter-leaf leakage, mechanical complexity, and cost. A simulation was performed with a single leaf inserted into a 20×20 cm² field. The dose profile at d_{\max} was examined and the mini-

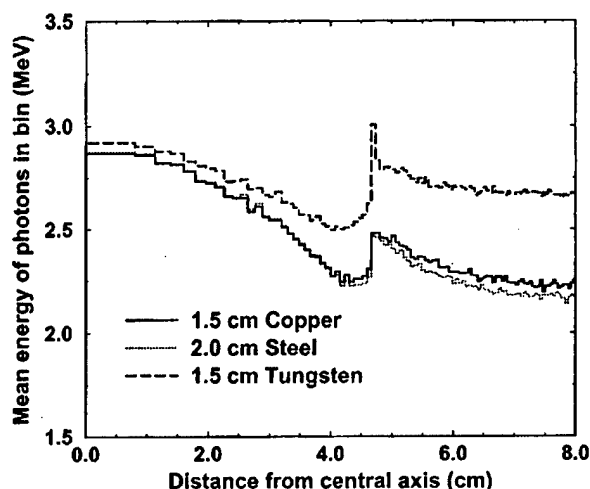


FIG. 7. Mean energy of photons in the presence of a copper, steel, and tungsten MLC set to a 10×10 cm² field with an incident electron energy of 20 MeV. The energy was scored at the back surface of the eMLC.

imum of the resulting dose "valley" was considered. As seen in Fig. 8 and Table II, the dose reduction as a function of leaf width can be well approximated by a decaying exponential. Using the "worst-case scenario," an energy of 6 MeV, it was found that a leaf width of 8.8 mm projected to 100 cm SSD, or 8.6 mm at the level of the MLC, would produce a dose reduction of 50%. As expected, the leaf width corresponding to a 50% reduction for the high energy 20 MeV beam was much smaller, and a dose reduction of 50% could be achieved by a leaf width of 4.9 mm projected, or 4.8 mm at the MLC.

Additionally, the full width of the region where the dose was less than 50% and the full width of the region where the dose was less than 75% are displayed in Table II. At 20

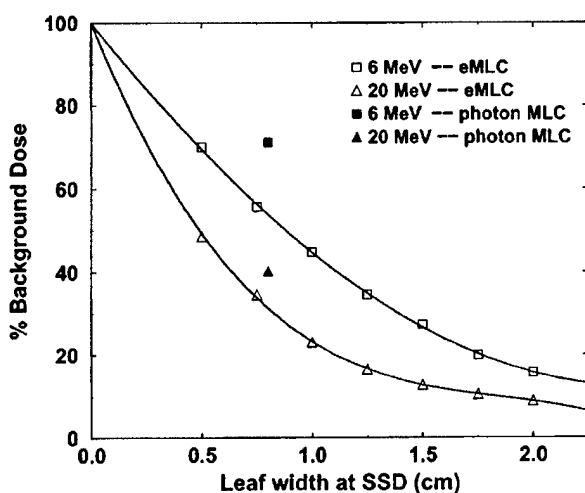


FIG. 8. Dose reduction as a function of leaf width. A Monte Carlo simulation was performed in which a single leaf was inserted a 20×20 cm² field and dose profiles computed. The plotted points represented the dose minimum as a percentage of background dose for various leaf widths. The two solid points represent the leaves of the intrinsic MLC of a Varian Clinac 2100C at 6 and 20 MeV at 80 cm SSD.

TABLE II. Achievable resolution for a (a) 6 MeV field at d_{\max} . Parameters from simulated single leaf dose profiles at d_{\max} . A single leaf of a given width was entered into a 20×20 cm² 6 MeV field generated by an idealized electron MLC. (b) Achievable resolution for a 20 MeV field at d_{\max} . * indicates that this dose was not passed, i.e., the dose reduction from a single leaf was less than 50% of the background dose.

		Width at % background dose	
Projected width at SSD (cm)	Dose at minimum (% background)	75% dose (cm)	50% dose (cm)
(a) 6 MeV			
0.50	70.0	0.77	*
0.75	55.7	1.49	*
1.00	44.8	1.88	0.60
1.25	34.5	2.08	1.16
1.50	27.3	2.48	1.45
1.75	19.9	2.81	1.81
2.00	15.7	3.02	2.04
Varian MLC 0.80 cm at 80 cm SSD (with He)	71.0	1.11	*
(b) 20 MeV			
0.50	48.6	0.87	0.08
0.75	34.5	1.22	0.67
1.00	23.1	1.50	0.96
1.25	16.5	1.75	1.19
1.50	12.8	2.05	1.52
1.75	10.5	2.31	1.79
2.00	8.9	2.54	2.04
Varian MLC 0.80 cm at 80 cm SSD (with He)	40.3	1.44	0.67

MeV, it is seen that at an eMLC leaf width of 1 cm, the 50% full width is approximately equal to the leaf width. A similar trend is noted beyond the 1.25 cm leaf width at 6 MeV.

Based on these findings, we conclude that a leaf width of less than 10 mm at 100 cm SSD is not useful for defining the shape of a low energy field, and leaves of less than 5 mm are not useful for defining the field shape at any energies. In order to provide maximum utility at both high and low energies, a 5 mm leaf width was chosen as the ideal leaf width for the eMLC. Individual leaves can then be used at high energies to provide maximum resolution, while multiple leaves may be moved together to define fields at lower energies.

For comparison, identical simulations were performed to simulate the leaves of a Varian 52-leaf multileaf collimator, with a leaf width projected at isocenter of 10 mm, using a helium filled accelerator (and air gap) at 80 cm nominal SSD. The results are also shown in Fig. 8 and Table II. It can be seen in Fig. 8 that at 20 MeV, the eMLC and photon MLC the difference in dose reduction for a projected leaf width of 8 mm is only 5%. However, at 6 MeV, a significant difference can be observed between the eMLC and Varian MLC systems, and it can be seen that for a given projected leaf width, the eMLC provides a superior level of resolution.

3. Leaf end shape

In contrast with observed results regarding photon MLC leaf shapes, simulations performed in this study demon-

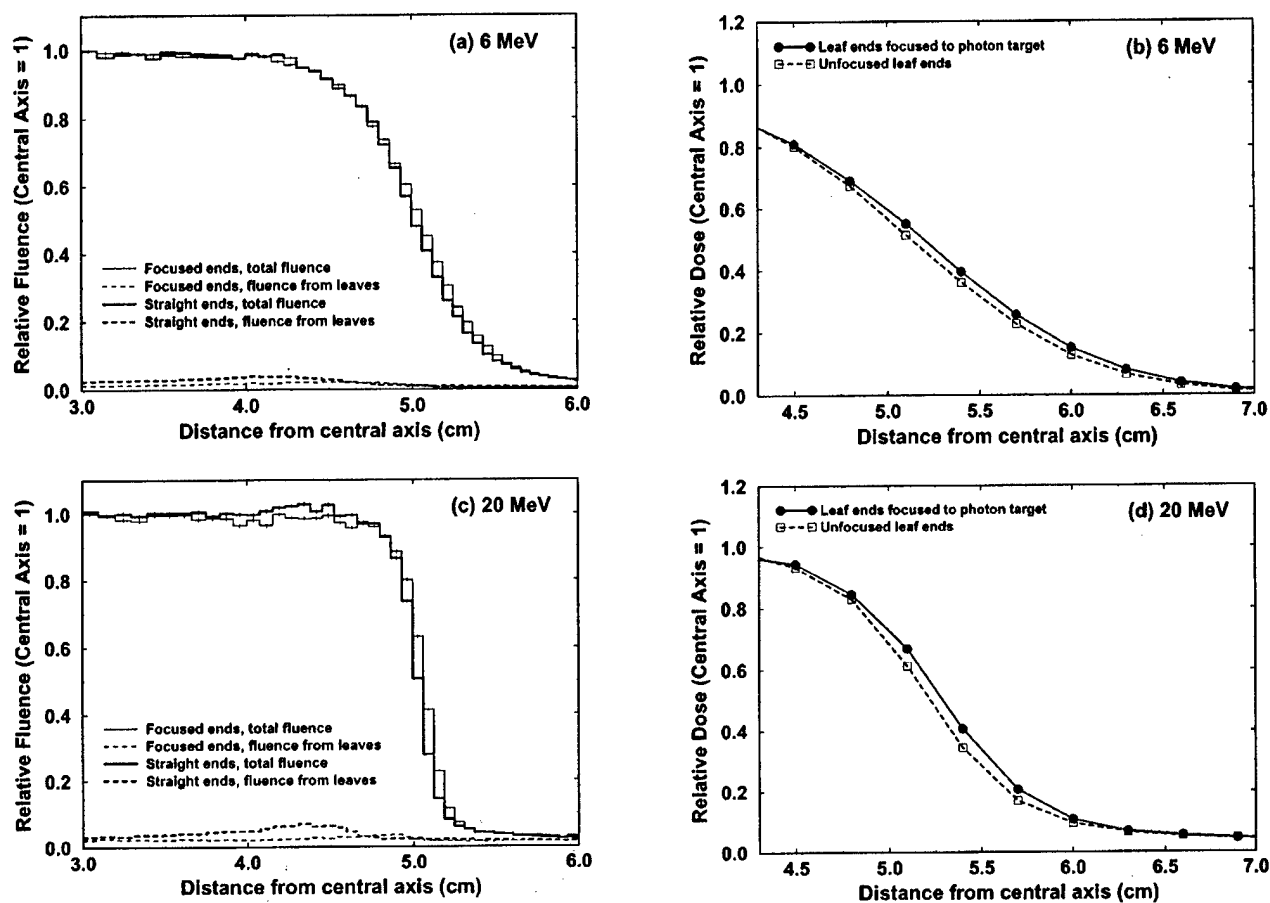


FIG. 9. Effect of leaf end shape on electron fluence and dose distribution. (a) 6 MeV fluence, (b) corresponding 6 MeV dose at 1 cm depth, (c) 20 MeV fluence, (d) corresponding 20 MeV dose at 3 cm depth. Latch bit settings were used to separate the 100 cm SSD fluence into the total fluence and fluence from electrons scattered from the leaves.

strated that focused leaf ends did not provide any benefit at all at either high or low energies. Indeed, unfocused leaf ends provided a "horn" effect at the edge of the fields which actually improved beam penumbras, as seen in Fig. 9. This eliminates the additional complexity required focusing, as well as the issue of choosing a focal point that would be useful for a range of electron energies.

C. Prototype electron MLC: Measurements and Monte Carlo simulations

Based on previous experiences, it was believed that Monte Carlo calculations could accurately calculate the dose distributions from the MLC, and that the Monte Carlo method could be used for MERT calculations. However, it was necessary to demonstrate that the Monte Carlo method remains valid for the more complex geometry of the eMLC. Monte Carlo simulations were used to generate isodose curves for fields collimated by the prototype eMLC and compared with film measurements taken using the actual prototype installed on an accelerator located at the Stanford University Medical Center. Isodose curves for the measured and Monte Carlo 20 MeV fields normalized to the in-plane maximum at 3 cm depth in solid water are displayed in Fig. 10. The agreement between the measured and simulated data is

excellent at all energies, with deviations falling within 2 mm at 3 cm depth for 12 and 20 MeV and 1.5 cm depth for 6 MeV. It is therefore concluded that the Monte Carlo method is capable of simulating the isodose distribution from an eMLC in homogeneous media.

D. Comparison of electron MLC and photon MLC

Having established a computer model of the eMLC and verified the validity of the model using film measurements and a prototype eMLC, it was possible to compare the dose distributions from the eMLC and the photon MLC.

1. Penumbra comparison

Calculations were performed to compare the dose penumbras from 10×10 cm² fields collimated by the eMLC to those from the photon MLC. As shown in Table I and Figs. 4 and 5, even when compared to a photon MLC in the presence of helium, using the ideal eMLC results in reductions in the 10×10 cm² 90–10 penumbra ranging from 12.1% at 20 MeV to as much as 44.6% at 6 MeV. However, the absolute change from 20 MeV was only 2 mm. Extrapolating from the existing data points, one can calculate the SSD required for the penumbra from the photon MLC to match the eMLC, as

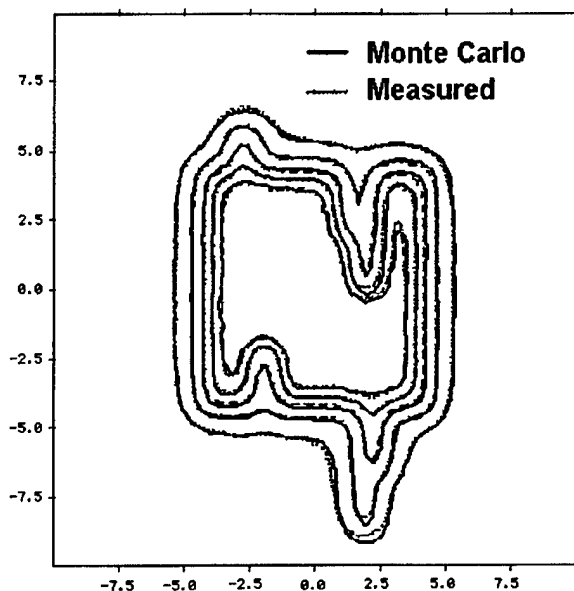


FIG. 10. Isodose curves for an arbitrary leaf pattern at 20 MeV, normalized to in-plane maximum. The plane displayed is orthogonal to the incident beam direction (beam eye view). The curves represent the 90%, 80%, 60%, 30%, and 10% isodose surfaces at a depth of 3 cm. The solid line represents the Monte Carlo results while the broken line represents the film measurements. With only a few small regions as exceptions, the two sets of curves are indistinguishable.

shown in Table III. It was determined that the required SSDs to match at 90–10 for 6, 12, and 20 MeV are, respectively, 65.5, 68.0, 69.8 cm. In a standard air atmosphere, the required SSDs are all less than 65 cm, which is clearly unachievable in any practical system. However, it was observed that at 80 cm SSD in the presence of helium, the photon MLC provided a sharper penumbra than the prototype eMLC at 20 MeV. Extrapolating from the helium penumbra data, it can be seen that at 6, 12, and 20 MeV, the required SSD to match the *prototype* eMLC are 68.5, 76.6, and 89.3 cm.

When comparing the photon and eMLC, it is crucial to note the difference in leakage dose. From Figs. 3(a), 3(b), and 3(c), it can be seen that at 6 and 12 MeV, the two MLCs provide comparable background doses, with the difference at 12 MeV representing less than 1% of the central axis dose.

TABLE III. SSDs required for a photon MLC to match the ideal electron MLC and the prototype electron MLC. These calculations are based on a linear interpolation of the penumbra data shown in Table I and Fig. 4.

Energy (MeV)	eMLC	SSD required for photon MLC to match electron MLC penumbras (cm)			
		Air		Helium	
		80/20	90/10	80/20	90/10
6	ideal	59	58	61	61
	prototype	63	62	69	69
12	ideal	65	64	68	68
	prototype	68	68	74	77
20	ideal	64	64	70	70
	prototype	70	73	82	89

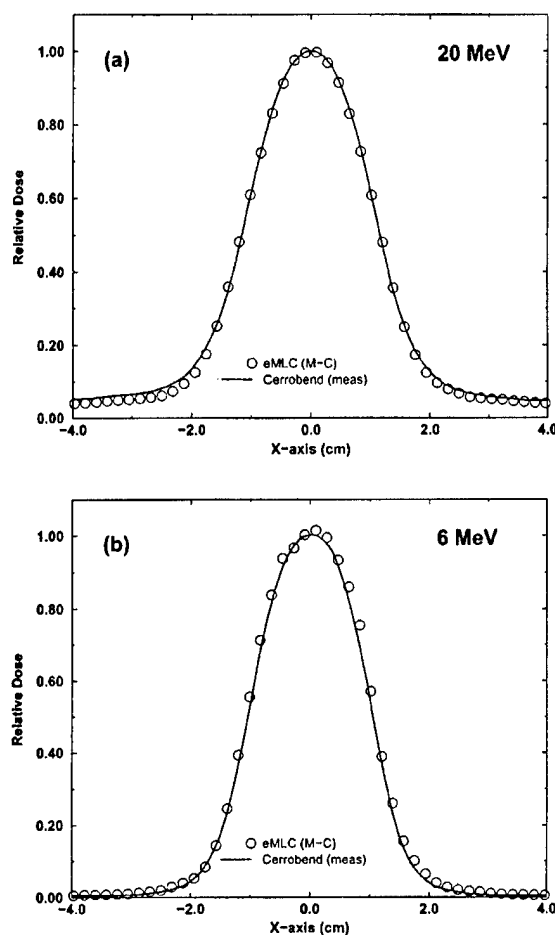


FIG. 11. Profiles obtained for 2×2 cm² fields defined by Cerrobend cutouts and by the electron MLC. (a) 20 MeV at 4 cm depth, (b) 6 MeV at 1 cm depth.

However, at 20 MeV, the leakage from the significantly thinner eMLC is more than twice that from the photon MLC (approximately 2%). This leakage dose still compares favorably to the 5% leakage seen at 20 MeV with 1.5 cm of Cerrobend cutout mounted in the 25×25 cm² scraper. However, it is imperative that any MERT treatment planning system using an eMLC account for this leakage dose and reduce the number of monitor units to be delivered.

For comparison with a well-understood system, simulations of a 2×2 cm² field defined by the ideal eMLC were performed and the dose distributions compared with measured profiles for a 2×2 cm² Cerrobend field in a 6×6 cm² applicator. Because the collimators are positioned identically with respect to the phantom surface, the penumbras were identical, as seen in Fig. 11. The leakage at 6 MeV was negligible in both the cutout and the eMLC, while the leakage at 20 MeV was greater in the case of the cutout. The same result was found for other field sizes, and similarly, using the photon MLC to define electron fields compares equally unfavorably with both cutouts and the electron specific MLC.

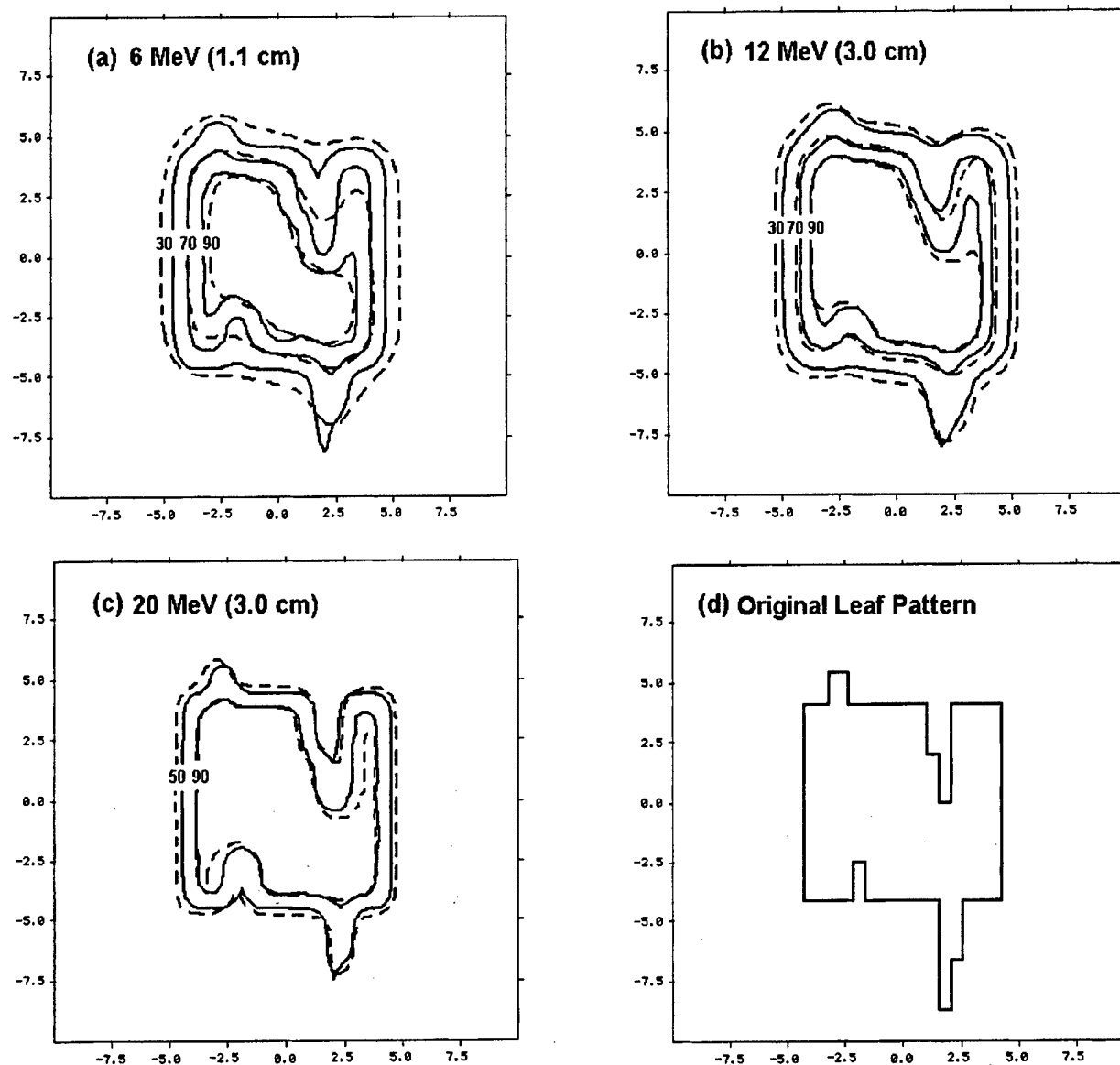


FIG. 12. Isodose curves for an arbitrary leaf pattern. Solid lines represent a 1.5 cm thick tungsten electron MLC at the last scraper level and dashed lines represent a photon MLC in the presence of helium at 80 cm SSD. (a) 6 MeV at 1.1 cm, (b) 12 MeV at 3.0 cm, (c) 20 MeV at 3.0 cm, (d) original leaf pattern, projected to the phantom surface.

2. Isodose curve comparison

In Fig. 12, the Monte Carlo simulated isodose curves for an electron field collimated by an idealized eMLC and an equivalent field collimated by a photon MLC with He are shown. The original leaf pattern is displayed in Fig. 12(d). In all cases, the fields were normalized such that the 90% isodose curves coincided for the open field portion ($y = -1.0$ cm), effectively "prescribing dose to an isodose curve." In all cases, the penumbras differed according to the trends described earlier: in particular, when 90% isodose curves are matched, the photon MLC collimated field exhibited 30% and 70% dose regions that were uniformly larger than those from the eMLC. More significant, however, is the ability to resolve narrow fields. In particular, focusing on the upper right portion of the fields, as displayed, it can be seen

that at both 6 and 12 MeV, the photon MLC is unable to fully resolve either the partially closed leaves or the open leaves at upper-right most corner. A much smaller but visible effect is observed at 20 MeV.

Based on these results, it is therefore concluded that at all energies, the eMLC is more faithful to the original leaf pattern than the photon MLC. However, as predicted by the leaf width simulations, even with the eMLC, leaf widths of less than 1 cm do not result in any appreciable improvement in resolution, especially at low energies.

Simulations were also performed with the photon MLC in air, and with the prototype eMLC. In all cases, the photon MLC in air performed worse in terms of resolution and penumbra when compared to the helium MLC, and likewise with the prototype when compared to the idealized eMLC.

IV. CONCLUSIONS

It has been demonstrated through the use of Monte Carlo simulations that the in-air scattering of the electron beam makes the photon MLC a poor choice for generating complex shapes needed for intensity modulated electron therapy. This is partially ameliorated by filling the treatment head with helium and placing a helium filled balloon between the patient surface and the treatment head. Indeed, for such a system, at 12 and 20 MeV at an SSD of 80 cm, the isodose curves are within 3 mm of the equivalent eMLC field. If accurate commissioning data is available for these helium-filled accelerator and accurate dose calculation algorithms are employed, it is believed that highly accurate MERT plans can be delivered and the quality of treatment will not differ significantly from an eMLC delivered plan. However, at 6 MeV the isodose curves are no longer comparable, and adding helium to the beam axis atmosphere does not improve the situation.

An electron specific multileaf collimator placed at the cut-out level of an electron applicator was then studied. Monte Carlo simulations were used to investigate construction and design considerations and on the basis of these simulations, it was concluded that an eMLC constructed of tungsten leaves of 15 mm thickness and 5 mm width, would be minimally sufficient for use in intensity modulated electron beam therapy. This MLC would optimally be part of a specially designed electron applicator, although experiments have indicated that an MLC designed as an applicator accessory also provides significant improvement in dose penumbras and field resolution when compared to the photon MLC. Additionally, it has been demonstrated that Monte Carlo simulations provide an accurate means of calculating dose distributions from such a collimation system.

ACKNOWLEDGMENTS

We thank our colleagues at Stanford: Art Boyer, Gary Luxton, Todd Pawlicki, Jun Deng, and Jinsheng Li, for helpful discussions of this work, and Professor Byong-yong Yi of Asan Medical Center, University of Ulsan, College of Medicine in Seoul, Korea for discussions regarding the prototype electron MLC. This work was supported in part by Grants Nos. BC971292 and BC990213 from the US Department of Defense, CA 78331 from the NIH, and the NIH Training Grant No. 5T32GM08294-11.

^{a)} Author to whom correspondence should be addressed: Department of Radiation Oncology, 300 Pasteur Drive, Stanford, CA 94305-5304. Electronic mail: mclee@reyes.stanford.edu

¹ E. P. Lief, A. Larsson, and J. L. Humm, "Electron dose profile shaping by modulation of a scanning elementary beam," *Med. Phys.* **23**, 33-44 (1996).

² S. Hyödynmaa, A. Gustafsson, and A. Brahme, "Optimization of conformal electron beam therapy using energy- and fluence-modulated beams," *Med. Phys.* **23**, 659-666 (1996).

³ B. Zackrisson and M. Karlsson, "Matching of electron beams for con-

formal therapy of target volumes at moderate depths," *Radiother. Oncol.* **39**, 261-270 (1996).

⁴ M. Asel, S. Hyödynmaa, A. Gustafsson, and A. Brahme, "Optimization of 3D conformal electron beam therapy in inhomogeneous media by concomitant fluence and energy modulation," *Phys. Med. Biol.* **42**, 2083-2100 (1997).

⁵ M. K. Karlsson, M. G. Karlsson, and B. Zackrisson, "Intensity modulation with electrons: calculations, measurements and clinical applications," *Phys. Med. Biol.* **43**, 1159-1169 (1998).

⁶ M. G. Karlsson, M. K. Karlsson, and C.-M. Ma, "Treatment head design for multileaf collimated high-energy electrons," *Med. Phys.* **26**, 2125-2132 (1999).

⁷ C.-M. Ma, T. Pawlicki, M. C. Lee, S. B. Jiang, J. Li, J. Deng, B. Yi, E. Mok, G. Luxton, and A. L. Boyer, "Energy- and intensity-modulated electron beams for radiotherapy," *Phys. Med. Biol.* **45**, 2293-2311 (2000).

⁸ A. Brahme, "Design principles and clinical possibilities with a new generation of radiation therapy equipment," *Acta Oncol.* **26**, 403-412 (1987).

⁹ T. Jansson, H. Lindman, K. Nygård, C. V. Dahlgren, A. Montelius, S. Öberg-Kreuger, S. Asplund, and J. Berg, "Radiotherapy of breast cancer after breast-conserving surgery: an improved technique using mixed electron-photon beams with a multileaf collimator," *Radiother. Oncol.* **46**, 83-89 (1997).

¹⁰ E. E. Klein, Z. Li, and D. A. Low, "Feasibility study of multileaf collimated electrons with a scattering foil based accelerator," *Radiother. Oncol.* **46**, 189-196 (1996).

¹¹ K. R. Hogstrom, M. D. Mills, and P. R. Almond, "Electron beam dose calculations," *Phys. Med. Biol.* **26**, 445-459 (1981).

¹² A. F. Bielajew, D. W. O. Rogers, J. Cygler, and J. J. Battista, "A comparison of electron pencil beam and Monte Carlo calculational methods," in *The Use of Computers in Radiation Therapy*, edited by I. A. D. Bruinvis *et al.* (Elsevier Science, New York, 1987), pp. 65-68.

¹³ T. R. Mackie, P. J. Reckwerdt, C. M. Wells, J. N. Yang, J. O. Deasy, M. Podgorsak, M. A. Holmes, D. W. O. Rogers, G. X. Ding, B. A. Faddegon, C.-M. Ma, A. F. Bielajew, and J. Cygler, "The OMEGA project: comparison among EGS4 electron beam simulations, 3D Fermi-Eyges calculations, and dose measurements," *Proceedings of the XIth International Conference on the use of Computers in Radiation Therapy, Manchester, UK* (Medical Physics Publishing, Madison, 1994), pp. 152 and 153.

¹⁴ C.-M. Ma, E. Mok, A. Kapur, T. Pawlicki, D. Findley, S. Brain, K. Forster, and A. L. Boyer, "Clinical implementation of a Monte Carlo treatment planning system for radiotherapy," *Med. Phys.* **26**, 2133-2143 (1999).

¹⁵ W. R. Nelson, H. Hirayama, and D. W. O. Rogers, "The EGS4 Code System," SLAC-Report-265, Stanford Linear Accelerator Center, 1985.

¹⁶ D. W. O. Rogers, B. A. Faddegon, G. X. Ding, C.-M. Ma, J. Wei, and T. R. Mackie, "BEAM: A Monte Carlo code to simulated radiotherapy treatment units," *Med. Phys.* **22**, 503-524 (1995).

¹⁷ C.-M. Ma, J. S. Li, T. Pawlicki, S. B. Jiang, and J. Deng, "MCDOSE—A Monte Carlo dose calculation tool for radiation therapy treatment planning," *Proceedings of the XIII International Conference on the Use of Computers in Radiotherapy*, edited by W. Schlegel and T. Bortfeld (Springer, Heidelberg, Germany), pp. 123-125.

¹⁸ A. Kapur, C.-M. Ma, E. Mok, D. Findley, and A. L. Boyer, "Monte Carlo calculations of clinical electron beam output factors," *Phys. Med. Biol.* **44**, 3479-3494 (1998).

¹⁹ A. Bielajew and D. W. O. Rogers, "PRESTA—the parameter reduced electron step algorithm for electron Monte Carlo transport," *Nucl. Instrum. Methods Phys. Res. B* **18**, 165-181 (1987).

²⁰ C.-M. Ma and D. W. O. Rogers, "BEAMDP Users Manual," National Research Council Report No. PIRS-0509(C), NRC, Ottawa, Canada 1995.

²¹ ICRU Report No. 35, "Radiation dosimetry: Electron beams with energies between 1 and 50 MeV," Bethesda, 1984.

Electron beam modeling and commissioning for Monte Carlo treatment planning

Steve B. Jiang,^{a)} Ajay Kapur, and C.-M. Ma

Department of Radiation Oncology, Stanford University School of Medicine, 300 Pasteur Drive, Stanford, California 94305-5304

(Received 19 April 1999; accepted for publication 22 October 1999)

A hybrid approach for commissioning electron beam Monte Carlo treatment planning systems has been studied. The approach is based on the assumption that accelerators of the same type have very similar electron beam characteristics and the major difference comes from the on-site tuning of the electron incident energy at the exit window. For one type of accelerator, a reference machine can be selected and simulated with the Monte Carlo method. A multiple source model can be built on the full Monte Carlo simulation of the reference beam. When commissioning electron beams from other accelerators of the same type, the energy spectra in the source model are tuned to match the measured dose distributions. A Varian Clinac 2100C accelerator was chosen as the reference machine and a four-source beam model was established based on the Monte Carlo simulations. This simplified beam model can be used to generate Monte Carlo dose distributions accurately (within 2%/2 mm compared to those calculated with full phase space data) for electron beams from the reference machine with various nominal energies, applicator sizes, and SSDs. Three electron beams were commissioned by adjusting the energy spectra in the source model. The dose distributions calculated with the adjusted source model were compared with the dose distributions calculated using the phase space data for these beams. The agreement is within 1% in most of cases and 2% in all situations. This preliminary study has shown the capability of the commissioning approach for handling large variation in the electron incident energy. The possibility of making the approach more versatile is also discussed. © 2000 American Association of Physicists in Medicine.[S0094-2405(00)03401-5]

Key words: electron beam, treatment planning, Monte Carlo simulation, beam commissioning, source modeling

I. INTRODUCTION

Electron beam radiation therapy is used extensively to treat head and neck cancers to avoid the irradiation of the spinal cord, and to treat chest walls to limit the irradiated volume of lung. The currently available commercial systems for electron treatment planning mostly utilize the Hogstrom algorithm as the dose calculation engine,¹ which is based on Fermi-Eyges theory.^{2,3} Due to the inappropriate treatment of electron transport in inhomogeneous phantoms, large discrepancies (10% or more) in the dose distributions have been observed between the current analytical algorithms and measurements or Monte Carlo simulations in some clinical situations where the treatment volumes encompass air cavities and bone.⁴⁻⁷ Accurate dose calculation is an important factor for the widespread clinical use of electron therapy and the development of new electron therapy techniques, such as electron beam or mixed electron/photon beam intensity modulated therapy, which are expected to improve the conformality of the delivered dose distribution to the target volume for some disease sites.⁸⁻¹⁰

The Monte Carlo method is generally considered to be the most accurate approach for electron dose calculation under all circumstances.¹¹⁻¹⁶ In particular, Monte Carlo simulation can handle electron multiple scattering in the presence of inhomogeneities (such as bone and air cavity) much more

accurately than any existing analytical dose models. The necessity of accurate electron dose calculation has motivated many efforts to develop Monte Carlo electron beam treatment planning systems.^{6,7,17-22} Due to the rapid development of computer technology and the employment of innovative variance reduction techniques, it is expected that treatment planning systems utilizing a Monte Carlo dose engine will begin to serve in routine clinical practice in the next few years.^{6,7,20-29}

The commissioning procedure for a Monte Carlo treatment planning system can be different from that for a conventional planning system, since it requires more detailed and accurate clinical beam data.²² For example, the phase space information (position, direction and energy) is needed to represent particles coming out of the accelerator treatment head. This information is extremely difficult, if not impossible, to acquire experimentally, mainly due to the very high intensity of the therapeutic electron beam.³⁰ Some researchers tried to extract the phase space information from the limited set of measured dose data (such as depth dose curves and dose profiles) by using a simple beam model.³¹ Although the approach may have great potential, at least currently it uses many approximations and the accuracy of the reconstructed phase space cannot be guaranteed. The only method to obtain the accurate electron beam phase space

information is to simulate the accelerator treatment head using the Monte Carlo method.³²⁻³⁴ An EGS4 Monte Carlo user code, OMEGA BEAM, was developed specifically for this purpose.³⁴ Using the BEAM code, the accelerator treatment head and electron applicator can be simulated to yield a data file containing the phase space information for tens of millions of particles exiting the treatment head. The phase space data can then be used as input to calculate dose distributions in a patient's CT phantom.³⁴

However, direct simulation of the accelerator treatment head using the Monte Carlo method is not a viable commissioning approach for Monte Carlo treatment planning. The beam characteristics are usually different due to variation in accelerator designs and on-site beam tuning. The simulated electron beam phase space for one accelerator may not be used directly for another. It is necessary to simulate each accelerator individually to obtain the phase space information. This fact presents three problems for the clinical acceptance of Monte Carlo treatment planning systems. First, the simulation of the accelerator treatment head for every energy/applicator combination takes much more time than the commissioning of a conventional electron planning system. As estimated by Faddegon *et al.*,²² even for users with Monte Carlo simulation experience, it takes about two months of CPU time to generate a complete set of beam data for a single accelerator. Second, the storage of the phase space information requires a lot of computer disk space. For each energy/applicator combination, a phase space file is usually pre-calculated and stored in the treatment planning computer. For accurate treatment planning, a phase space file occupies hundreds of megabytes of disk space. This is certainly a substantial burden for the computer resources at most clinical centers. Third, the generation and quality assurance of the phase space data files by simulating the treatment head requires Monte Carlo simulation experience. Therefore, it is a prohibitive task for general users to perform Monte Carlo simulations for their own accelerators.

In this paper, a hybrid approach for commissioning electron beam Monte Carlo treatment planning systems is proposed. This method combines the advantages of the full Monte Carlo simulation and the method of Janssen *et al.*³¹ It is based on the assumption that accelerators of the same type have very similar electron beam characteristics and the major difference is the electron incident energy at the exit window due to beam tuning during linac acceptance. By simulating a reference accelerator for a particular type of accelerator using the Monte Carlo BEAM code,³⁴ a beam model is constructed using the resultant phase space information. The beam model is a simplified implementation of a previously developed multiple source model which can compress the Monte Carlo phase space data by a factor of 1000 or more.³⁵⁻³⁷ When commissioning another accelerator of the same type, the energy spectra in the beam model are tuned to match standard measured data such as depth doses and dose profiles. Using this approach, we do not have to simulate every accelerator individually. Only one reference accelerator needs to be simulated for a type of accelerator, and this can be done carefully by someone with Monte Carlo exper-

tise. In this paper, a Varian Clinac 2100C accelerator is chosen as the reference machine. The machine is simulated using the BEAM code³⁴ and a four-source beam model is established based on the simulated beam phase space information. The accuracy of the Monte Carlo dose distributions calculated with the model is verified. Then, the model based on the reference beam is used to commission three other electron beams. Two beams are also from the reference machine but with incident energies significantly different from that of the reference beam. The third beam is from another Clinac 2100C machine at a different institution.³⁸ The validity of the proposed commissioning approach is demonstrated by commissioning these three beams.

II. METHODS AND MATERIAL

A. Beam modeling

1. General considerations

Beam modeling is the first step in our hybrid commissioning procedure for a Monte Carlo treatment planning system. A beam model for a type of accelerator is established using the Monte Carlo simulated phase space information for the reference beam. The beam data are modeled using the multiple source model developed by Ma *et al.*,³⁵⁻³⁷ which is modified in the current work for use in the commissioning procedure. The major modifications of the model are discussed here.

The multiple source model is based on the observation that particles from different components of an accelerator have significantly different energy, angular, and spatial distributions, while the particles from the same component have very similar characteristics.³⁵⁻³⁷ Therefore, the particles from different components of an accelerator can be treated as they are from different sub-sources. Each sub-source represents a critical component in the treatment head and its geometrical dimensions are determined by the component dimensions. Each sub-source has its own energy spectrum and planar fluence distribution derived from the simulated phase space data. When the model is used for dose calculation, the incident energy and position of a particle are sampled from the corresponding stored energy spectrum and planar fluence distribution. The incident direction of the particle is reconstructed by sampling the position of the particle on the sub-source and on the phantom surface. The correlation between the particle position and incident angle is naturally retained.

A primary reason to develop the multiple source model was to find a concise way to replace the huge phase space data files generated from Monte Carlo simulations.^{35,36} The emphasis of the current work is to develop a clinically practical commissioning procedure for Monte Carlo treatment planning. The multiple source model is simplified to make the commissioning procedure as simple as possible while trying to maintain dose calculation accuracy under all circumstances of clinical relevance. The number of sub-sources in the model is minimized and only those sub-sources of dosimetric significance are retained. The dependence of the model on the detailed information of accelerators is reduced. Sub-sources are represented by dimensionless geometric ob-

jects, such as points and lines, instead of the actual geometrical shapes and sizes of the treatment head components as used previously.^{35,36}

Ma *et al.* established their multiple source model from the Monte Carlo simulated phase space data on the patient surface (at 100 cm SSD) and the last scraper of the electron applicator was included in the model as a sub-source.^{35,36} In this work, the treatment head is simulated using the BEAM code down to just above the last scraper of the electron applicator,³⁴ where the patient specific cutout is inserted. The last scraper, as well as the field-defining cutout, are simulated together with the patient CT phantom when performing Monte Carlo treatment planning dose calculations. The advantage of this method is that the beam model is patient independent. However, this approach, compared to that of Ma *et al.*,^{35,36} requires more careful beam modeling since an air gap between the last scraper and patient surface is not included in the original BEAM simulation.

In the present paper, the beam modeling approach is applied to a Varian Clinac 2100C machine at Stanford Medical Center, which is chosen as the reference machine to build beam models. At first, a very detailed model for each beam is used as the starting point. All the critical components of the treatment head are modeled as sub-sources. With this model, the phase space information of the electron beam can be precisely reconstructed and the dose distribution in a water phantom can be accurately calculated. Then, the number of sub-sources is gradually reduced while maintaining the accuracy in dose distribution calculation. We find that a point electron source with the energy spectrum obtained from the Monte Carlo simulation is able to give a reasonably accurate depth-dose curve, which is consistent with the previous observation.³⁶ By adding another point photon source, the bremsstrahlung tail in the depth dose distribution can be reproduced accurately. However, it is found that the penumbra at the phantom surface generated with this two point source model is sharper compared to that generated with the full phase space data. In order to get the dose profiles correct, we find that, in addition to the two point sources, two square ring electron sources (which emit electrons isotropically) are needed to represent electrons scattered from the applicator scrapers. (The term *square ring* is used here to represent the edge of a square.) Therefore, the beam model should include four sub-sources: a point electron source for direct electrons (which do not interact with the beam defining system) and electrons scattered from the primary collimator, movable jaws and shieldings, a point photon source for all contaminant photons, and two square ring electron sources for electrons scattered from the first two scrapers of the electron applicator (the third also last scraper is not included in the model).

As described previously, beam modeling consists of two steps, namely, beam representation and beam reconstruction.^{35,36} In beam representation, parameters in the model are extracted from the simulated phase space file. In the current simplified model, these parameters include the positions and relative intensities of the sub-sources, the energy spectra for particles inside and outside the field for each

sub-source, and the planar fluence distributions on the scoring plane (directly above the last scraper) for each sub-source. Beam reconstruction is performed when using the model for dose calculations. The phase space information for each particle, including the energy, position and direction, is reconstructed from the scored source parameters.

2. Beam representation

The positions of the virtual electron and photon point sources can be determined using a method described in Ref. 36, which is analogous to the pinhole method.³⁹ A thin annular aperture is selected on the scoring plane and phase space particles are allowed to pass through the aperture and form an image at a distance below the scoring plane. Ray lines drawn through the center of the aperture and the peak of the aperture image form a virtual focal spot, which is adopted as the position of the point source. This pinhole method is very effective for the photon point source. However, we find that for electrons, this method is only applicable to high energy beams. For lower energy beams, e.g., 6 MeV, the virtual SSD determined with this method is greatly overestimated and dependent on the radius of the thin annular aperture on the scoring plane. This is due to the fact that the in-air multiple scattering of low energy electrons is significant. To overcome this problem we performed another Monte Carlo simulation of the accelerator treatment head by replacing the intervening air with vacuum. Then, based on the new phase space data, this pinhole method can be used to generate the correct position for the virtual electron point source, which is independent of the sampling radius. The effect of in-air multiple scattering is taken into account during beam reconstruction by adding a perturbation to the electron incident direction, as discussed later.

Two square ring sources of electrons are located at the corresponding positions of the two applicator scrapers. The sides of the square rings correspond to the actual openings of the scrapers.

The energy spectrum for each sub-source is derived from the simulated phase space data. It was found that the mean energy of the electrons is relatively uniform inside the field as well as outside the field. The change of mean energy with the distance from the central axis is more like a step function.³⁶ Therefore, in the current model, each sub-source has two different energy spectra, one for electrons inside and the other for electrons outside the treatment field. Parameters stored in the model are the minimum and maximum energies, number of energy bins as well as the relative fluence for each energy bin. The minimum and maximum energies correspond to the cutoff energies (ECUT or PCUT) and the incident energy used in the accelerator simulation. The number of bins is determined by the desired resolution. For example, if we want the uncertainty in the calculated depth of 50% dose, R_{50} , to be less than 1%, the uncertainty in the peak position of the energy spectrum should be within 1% and therefore the bin width should be smaller than 1% of the peak energy. For the 12 MeV beam, we used 128 bins and then the bin width is less than 0.1 MeV. This bin width is

also found to be small enough to represent the peak width of the energy spectrum, which has a significant effect on the slope of the depth dose fall-off.

The planar fluence distribution for each sub-source is also derived from the simulated phase space data and recorded on the scoring plane using a grid scheme. Within each pixel of the grid, the planar fluence is assumed to be uniform. The dimension of a pixel is dependent on field size, usually from 1 to 3 mm. Parameters used to represent the planar fluence distribution include the treatment field dimension, the number of pixels and the relative intensity of each pixel, for each sub-source. It has been found that in general, the mean energy varied from position to position in the treatment field by less than 10% for a given sub-source.³⁶ Thus, it is reasonable to store and then sample the particle energy and position independently.

The angular distributions are not scored explicitly. They are reconstructed during the dose calculation, as described in the next section.

Finally, the simulated phase space information is represented with a set of parameters for each sub-source. The resultant source parameter file is much smaller (about 100 kilobytes) than the original phase space file (>100 megabytes).

3. Beam reconstruction

When performing dose calculation in a patient's CT phantom, the source parameter file is used to reconstruct the phase space information (energy, position and direction) of every incident particle. The beam reconstruction process consists of the following steps:

- (1) Determine from which particular sub-source a particle originates by sampling from the relative source intensity of each sub-source.
- (2) Determine the position on the sub-source (excluding point sources) where the particle is emitted.
- (3) Sample the particle position on the scoring plane from the fluence pattern for the sub-source.
- (4) Sample the particle energy from the energy spectrum for the given sub-source based on the particle position (inside or outside the treatment field).
- (5) Determine the particle incident angle by connecting the position on the sub-source from where the particle is emitted and the position of the particle on the scoring plane.
- (6) Add in-air perturbation on the particle direction if it is an electron.

The sampling from the relative source intensity distribution is done by a table-look-up method.³⁵ All the sub-sources are in turn numbered from 1 to N (here $N=4$ for accelerators with designs similar to the Varian Clinac 2100C machine) and the relative intensity of the i th sub-source is p_i ($i=1, \dots, N$). The accumulative source intensity for the i th sub-source, $P_i = (\sum_{j=1}^i p_j)$, is multiplied by a large integer M . The value of M is determined according to the desired sampling precision of the relative source intensity. For ex-

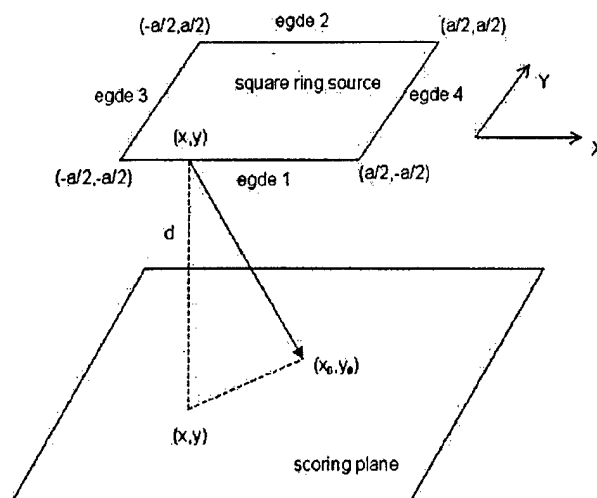


FIG. 1. A diagram for illustrating the sampling algorithm from a square ring source. The origin of the coordinate system is at the center of the square ring.

ample, $M=1000$ corresponds to the precision of 0.1% in sampling from the relative source intensity distribution. Then, a one dimensional array of M elements is prepared by assigning value i to array elements from $INT(MP_{i-1})$ to $INT(MP_i)$, where the operator INT returns the integer part of a real number. During the beam reconstruction, a random integer number K between 1 and M is generated and the value of the K th array element is the sub-source number where the particle is emitted. Such a table-look-up method is of very high sampling speed and efficiency. Its speed is also independent of the number of sub-sources. The sampling precision is usually adequate as long as an large enough array is used.

According to the energy spectra on the scoring plane, the bin number in which the particle energy falls is also sampled using the table-look-up method. An additional uniform sampling is done within the given energy bin to make the particle energy continuous.

The same table-look-up method is also used to sample the pixel number corresponding to a particle position on the scoring plane. Another sampling is performed uniformly to determine the particle's coordinates within the chosen pixel.

For the point sources, the incident angle of the particle is determined by constructing a ray line from the point source to the position of the particle on the scoring plane. For the square ring electron sources, we need to determine where the electron comes from on the ring. This is done in two steps. First, we determine from which edge of the square ring the electron is emitted. Second, we determine from where on the chosen edge the electron comes.

As illustrated in Fig. 1, a square ring of size $a \times a$ is located above the scoring plane at a distance d . We assume that the square ring edge emits electrons uniformly and isotropically. Under this approximation, the probability for an electron on the scoring plane to come from a point on the ring is proportional to the inverse square of the distance be-

tween the points on the ring and plane. This approximation greatly simplifies the sampling process. It is found that the angular distribution of the scattered electrons reconstructed based on the fluence distribution on the scoring plane and the emitting position on the square ring source is reasonably accurate, although electrons scattered from the applicator scraper mainly correspond to electrons incident on the vertical face of the scraper and are dominantly forward directed.⁴⁰ Furthermore, the dose profile at the patient surface is greatly influenced by electrons scattered from the last scraper or cut-outs, which are not included in the source model but will be accurately simulated with the patient CT phantom.

For an electron at position (x_0, y_0) on the scoring plane (see Fig. 1), the probability for it to have come from the i th edge is given as

$$p'_i(x_0, y_0) \sim \frac{1}{C_i} \left[\arctan\left(\frac{x_0 + a/2}{C_i}\right) - \arctan\left(\frac{x_0 - a/2}{C_i}\right) \right] \text{ for } i=1,2, \quad (1)$$

$$p'_i(x_0, y_0) \sim \frac{1}{C_i} \left[\arctan\left(\frac{y_0 + a/2}{C_i}\right) - \arctan\left(\frac{y_0 - a/2}{C_i}\right) \right] \text{ for } i=3,4, \quad (2)$$

where

$$C_1 = \sqrt{(y_0 + a/2)^2 + d^2}, \quad (3)$$

$$C_2 = \sqrt{(y_0 - a/2)^2 + d^2}, \quad (4)$$

$$C_3 = \sqrt{(x_0 + a/2)^2 + d^2}, \quad (5)$$

$$C_4 = \sqrt{(x_0 - a/2)^2 + d^2}. \quad (6)$$

Using the probabilities given above, the edge from which the electron has come can be sampled. Then, the position (x, y) on the chosen edge is further sampled. For edges 1 and 2,

$$x = x_0 - C_i \cdot \tan \left[(1 - \xi) \cdot \arctan\left(\frac{x_0 + a/2}{C_i}\right) + \xi \cdot \arctan\left(\frac{x_0 - a/2}{C_i}\right) \right] \quad i=1,2, \quad (7)$$

$$y = \begin{cases} -a/2 & \text{for } i=1 \\ a/2 & \text{for } i=2 \end{cases}, \quad (8)$$

and for edges 3 and 4,

$$x = \begin{cases} -a/2 & \text{for } i=3 \\ a/2 & \text{for } i=4 \end{cases} \quad (9)$$

$$y = y_0 - C_i \cdot \tan \left[(1 - \xi) \cdot \arctan\left(\frac{y_0 + a/2}{C_i}\right) + \xi \cdot \arctan\left(\frac{y_0 - a/2}{C_i}\right) \right] \quad i=3,4, \quad (10)$$

where ξ is a random number uniformly distributed from 0 to 1.

After the electron position on the square ring is determined, the connection of this position to the position on the scoring plane gives the electron's incident direction, which needs to be additionally perturbed to address the in-air multiple scattering.

In a previous implementation of this model, the effect of electron multiple scattering in air as well as other materials on its path to the scoring plane was taken into account by sampling the electron perturbation angle from a Monte Carlo simulated angular distribution.³⁶ This angular distribution was stored while performing the Monte Carlo simulation for the accelerator and only included electrons falling into a small region (e.g., of 1 cm radius) around beam central axis. In the current work, the effect of in-air multiple scattering is considered more accurately using the Fermi-Eyges theory.^{2,3} The effect of other materials is considered by adding a parameter to the standard deviation of the angular distribution. The Fermi-Eyges theory is a well-known small-angle theory and can predict the multiple scattering effect of megavoltage electrons in air or other heavier materials as long as the electron effective pathlengths are small.^{41,42}

Assume that an electron initially travels along the z axis. According to the Fermi-Eyges theory, the distributions for the projections of the polar angle, θ , on the $x-z$ plane, θ_x and on the $y-z$ plane, θ_y , are both Gaussian after electrons travel a distance, and are given as^{3,42}

$$f(\theta_x) = \frac{1}{\sqrt{2\pi}\sigma_{\theta_x}} \exp\left(-\frac{\theta_x^2}{2\sigma_{\theta_x}^2}\right), \quad (11)$$

$$f(\theta_y) = \frac{1}{\sqrt{2\pi}\sigma_{\theta_y}} \exp\left(-\frac{\theta_y^2}{2\sigma_{\theta_y}^2}\right), \quad (12)$$

where σ_{θ_x} and σ_{θ_y} are the standard deviations for each Gaussian distribution, respectively. In a homogeneous material, and without the presence of an electromagnetic field, both standard deviations should be the same, so we let $\sigma = \sigma_{\theta_x} = \sigma_{\theta_y}$. Under the small-angle approximation

$$\theta^2 = \theta_x^2 + \theta_y^2, \quad (13)$$

therefore the polar angle θ obeys a radial Gaussian distribution while the azimuthal angle ϕ is uniformly distributed in $[0, 2\pi]$. Hence the sampling method for these two angles is given as follows:

$$\theta = \sigma \sqrt{-2 \ln \xi_1}, \quad (14)$$

$$\phi = 2\pi \xi_2, \quad (15)$$

where ξ_1 and ξ_2 are random numbers uniformly distributed in $[0, 1]$.

According to the Fermi-Eyges theory, σ can be calculated as^{3,42}

$$\sigma^2 = A_0 - A_1^2/A_2, \quad (16)$$

where

$$A_i = \frac{1}{2} \int_0^l K(l-t)^i dt, \quad i=0,1,2. \quad (17)$$

Here, K is the electron linear scattering power and l is the distance at which electrons travel. The electron linear scattering power can be fitted well using a simple formula proposed by Werner *et al.*:⁴³

$$K(E) = \alpha E^{-\beta}. \quad (18)$$

Using this formula we fitted the linear scattering power data in air supplied by ICRU Report 35⁴⁴ and found that $\alpha = 3.329 \times 10^{-3} \text{ rad}^2/\text{cm}$ and $\beta = 1.638$. E is the electron energy in MeV and sampled from the energy spectrum at the scoring plane. The energy loss of electrons in air is usually very small and can be ignored when they travel from the virtual source to the scoring plane. The mean energy loss of 6 MeV electrons after traveling 100 cm in air is about 4% of its initial energy (estimated using the stopping power) and it is about 2% for 20 MeV electrons. Therefore σ can be given as

$$\sigma^2 = \frac{1}{8} K(E)l, \quad (19)$$

which is a function of electron energy and the distance between the virtual source and the position on scoring plane. During beam reconstruction, according to the sampled electron energy, positions on the scoring plane and on the virtual source, σ can be calculated. Then using Eqs. (14) and (15) θ and ϕ are sampled and a perturbation is added to the electron's incident direction.

The perturbation caused by in-air multiple scattering can be directly calculated using Eq. (19) for electrons from the squaring ring sources. For direct electrons, there are other accelerator components in their paths from the virtual point source to the scoring plane in addition to the intervening air, such as the exit window, scattering foil, monitor chamber, mirror and protection window. The effect of these materials on electron angular distribution has been mainly included in the determination of the virtual electron point source position. We also need to take into account the angular perturbation caused by these materials. If we know precisely the material and thickness of these parts, we can calculate their effect on σ , as done by Keall and Hoban.⁴¹ However, it is usually difficult for users to know this information about their accelerator when commissioning a Monte Carlo treatment planning system. Therefore, we introduce a factor k to account for the effect of these materials. For direct electrons, σ is then given as

$$\sigma^2 = \frac{1}{8} K(E)lk. \quad (20)$$

The factor k is determined by fitting the angular distribution calculated using Fermi-Eyes theory to that simulated with the Monte Carlo method for direct electrons. The introduction of k factor provides a potentially tunable parameter in the source model.

4. Model verification

The four-source model is verified dosimetrically by comparing the dose distributions in a water phantom calculated

using the model with those calculated using the full phase space data. Dose distributions are calculated for various combinations of three electron energies (6, 12, and 20 MeV), three applicator sizes (6×6 , 10×10 , and $20 \times 20 \text{ cm}^2$), and two SSDs (100 cm and 120 cm).

The measurement of electron beam applicator factors (defined as the ratio of the open field dose in water at d_{\max} for a given applicator to that of the reference applicator, typically the 10×10 or $15 \times 15 \text{ cm}^2$, for the same beam energy) is done during accelerator commissioning for all energy/cone combinations. Therefore, the applicator factors will be supplied by the user when performing the model commissioning. Cutout factors (defined as the ratio of the dose in water at d_{\max} for a blocked field to that of the open field for the same applicator and beam energy) are patient specific and not always easy to measure accurately for all clinical situations. Therefore, the model should be able to calculate cutout factors. To demonstrate this, we compare the model calculated cutout factors with those measured and calculated by Kapur *et al.* using a full Monte Carlo simulation.⁴⁵

B. Beam commissioning

The four-source model which is built using a Varian Clinac 2100C accelerator as the reference machine can be used to reconstruct electron beams from other Clinac 2100C accelerators by tuning the energy spectra in the model.

For accelerators with exactly the same design, the major different is the electron incident energy due to the on-site tuning to suit the user. This energy approximately corresponds to the maximum energy of all the stored energy spectra in the source model. It is found that the energy spectra for all sub-sources are very similar for different accelerators of the same type. When the incident energy is changed, the energy spectra can be approximated as stretched or compressed along the energy axis accordingly. The depth dose curve is very sensitive to the electron incident energy and therefore used to adjust the maximum energy, E_{\max} , in the model. The relationship between the incident energy, E_{in} , and R_{50} has been studied by simulating the reference accelerator using a $10 \times 10 \text{ cm}^2$ cone and 100 cm SSD with various incident energies. Then, the variation of E_{in} as a function of the variation of R_{50} is established for this type of accelerator. This relationship is used as a guide to tune the maximum energy in the model to commission a clinical beam.

The proposed commissioning approach can be summarized as follows:

- (1) Chose an accelerator as the reference machine for all other accelerators of the same design, and carefully perform full Monte Carlo simulations for the electron beams of various nominal energies from the reference machine with $10 \times 10 \text{ cm}^2$ applicator.
- (2) Build the source models for the simulated beams based on the Monte Carlo phase space data, perform Monte Carlo dose calculation in water for 100 cm SSD, and record the maximum energy, $E_{\max}^{(\text{ref})}$, in the model and the $R_{50}^{(\text{ref})}$ value for each beam.

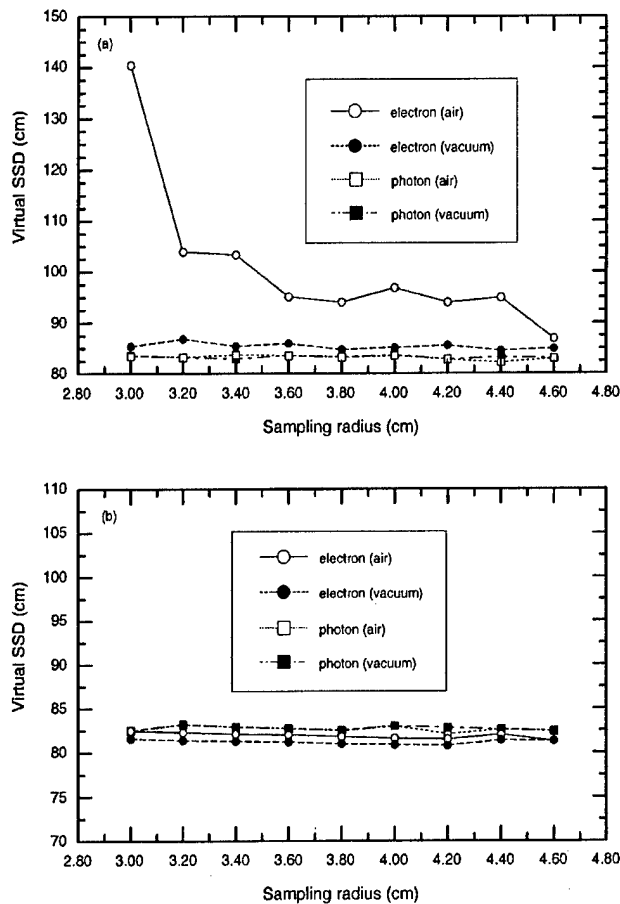


FIG. 2. Effects of intervening air and sampling radius on virtual SSD (defined here as the distance from the point source to the scoring plane) for the electron point source determined with the pinhole method. (a) 6 MeV; (b) 20 MeV.

- (3) For the beam to be commissioned, find the $R_{50}^{(mea)}$ value of the measured depth-dose curve in water for $10 \times 10 \text{ cm}^2$ applicator and 100 cm SSD.
- (4) Select the reference beam which has the same or closest nominal energy as the commissioning beam. Let $i=0$, $E_{\max}^{(i)} = E_{\max}^{(ref)}$, and $R_{50}^{(i)} = R_{50}^{(ref)}$.
- (5) Calculate $\Delta R_{50}^{(i)} = R_{50}^{(i)} - R_{50}^{(mea)}$. If $\Delta R_{50}^{(i)} \leq \epsilon$, where ϵ is the pre-set convergence tolerance, stop iteration and use $E_{\max}^{(i)}$ as the maximum energy in the source model for the commissioning beam; otherwise, go to the next step.
- (6) According to the relationship between ΔE_{in} and ΔR_{50} , calculate $\Delta E^{(i)}$ using $\Delta R_{50}^{(i)}$ and then calculate $E_{\max}^{(i+1)} = E_{\max}^{(i)} - \Delta E^{(i)}$.
- (7) Calculate the dose distribution using the source model with $E_{\max}^{(i+1)}$ and find the corresponding $R_{50}^{(i+1)}$.
- (8) Let $i \leftarrow i+1$; go back to step 5.

The first two steps only need to be done once for all accelerators of the same design. The convergence tolerance, ϵ , is set by the user, usually according to the estimated measurement error in R_{50} . For example, $\epsilon=1 \text{ mm}$ is good enough in most

clinical situations. The iteration process converges very fast; usually only two or three iterations are needed even for ϵ much smaller than 1 mm.

The commissioning approach has been applied to three electron beams, A, B, and C. The reference beam is the same for all three beams, which is from the reference Clinac 2100C accelerator with $E_{\text{in}}=12.0 \text{ MeV}$. Beam A and beam B are also from the reference machine but with E_{in} as 9.0 MeV and 15.0 MeV, respectively. These two beams are used to mimic two clinical beams of the same nominal energy as the reference beam but with significantly different incident energies. Of course, in reality, the electron incident energy will not be tuned so much ($\pm 3 \text{ MeV}$). These two beams are used as extreme cases to test the commissioning approach. Beam C is a 9 MeV electron beam from another Clinac 2100C accelerator. The dose distributions for beam C are taken from the published data.³⁸

III. RESULTS AND DISCUSSION

Figure 2 shows the effects of intervening air and sampling radius on the electron and photon virtual SSD determined with the pinhole method for 6 MeV and 20 MeV beams. It can be seen that for photons and high energy electrons (20 MeV) effects of intervening air and sampling radius on the positions of virtual point sources are negligible. However, for low energy electrons (6 MeV), these effects are significant. Therefore, to obtain the accurate virtual electron point source position for low energy beams, the phase space simulated without intervening air should be used.

Figure 3 shows the comparison between the angular distributions for direct electrons in 6, 12 and 20 MeV beams calculated with the Fermi-Eyges theory and the Monte Carlo method. We can see that, in general, the fitted angular distributions based on the Fermi-Eyges theory match well with those calculated with the Monte Carlo simulation. We also notice that at large angles the Fermi-Eyges theory slightly

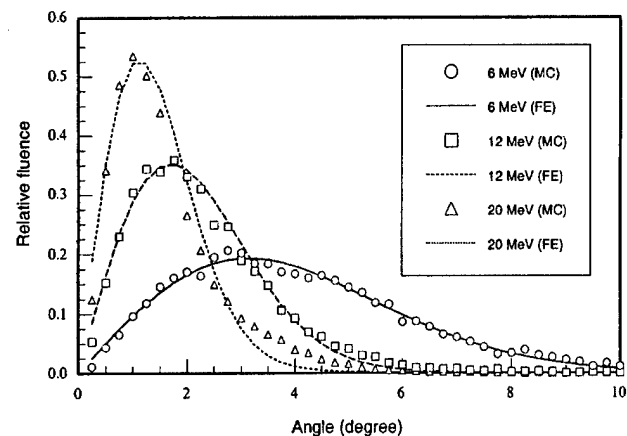


FIG. 3. Angular distributions for direct electrons calculated using the Fermi-Eyges theory and the Monte Carlo method. Beam energies are 6 MeV, 12 MeV and 20 MeV. The fitted k factor is 1.540 for 6 MeV, 1.501 for 12 MeV and 1.571 for 20 MeV. Each distribution is normalized to have unit area under the curve.

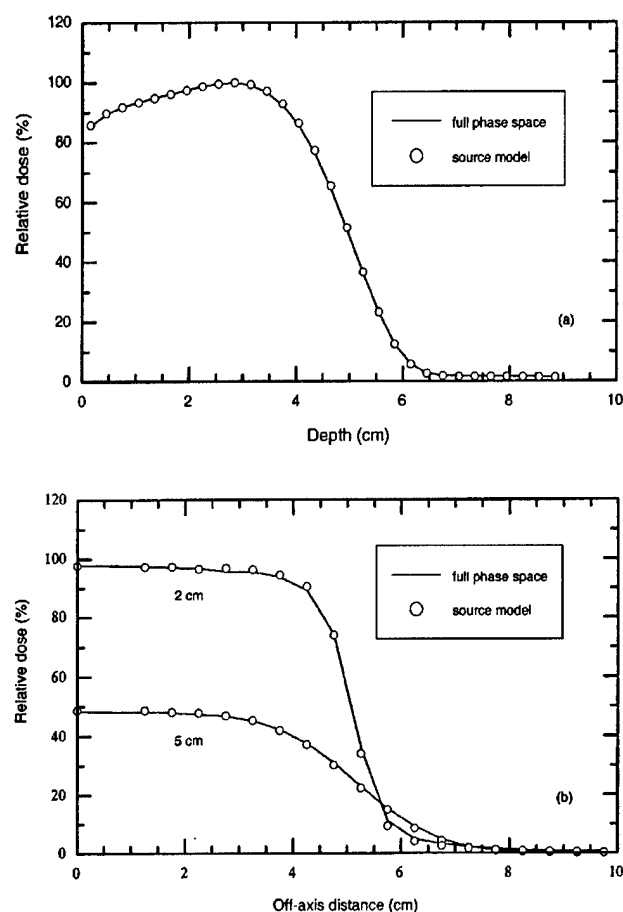


FIG. 4. Dose distributions in water for 12 MeV electron beam with $10 \times 10 \text{ cm}^2$ applicator at 100 cm SSD, calculated with full phase space data and source model: (a) Depth-dose distributions; (b) dose profiles at depths of 2 cm and 5 cm. Curves are normalized to the dose at d_{max} .

underestimates electron fluence due to the fact that it is a small-angle theory. We found that the small discrepancy does not have any significant effect on the final dose distributions. Therefore, the Fermi-Eyges theory with the fitted k factor can be used to account for the angular perturbations of electrons on their way from the source to the scoring plane.

The four-source model was tested by comparing the dose distributions calculated by the model with those calculated by full phase space data for various combinations of three electron energies (6, 12, and 20 MeV), three applicator sizes (6×6 , 10×10 , and $20 \times 20 \text{ cm}^2$), and two SSDs (100 cm and 120 cm). For all the cases tested, the agreement of 1%–2%/1–2 mm has been achieved. Figure 4 shows the comparison for a 12 MeV beam with a $10 \times 10 \text{ cm}^2$ cone at 100 cm SSD. Figure 5 gives the depth-dose curves and dose profiles for 20 MeV beam with $6 \times 6 \text{ cm}^2$ cone at 120 cm SSD, calculated with both the source model and full phase space data. All the curves in Figs. 4 and 5 are normalized to the doses at d_{max} . The Monte Carlo uncertainty is always less than 0.5% and therefore not shown on the curves. In both figures the agreement between the full Monte Carlo simulations and the source model calculations is better than 1%/1 mm. Keep in

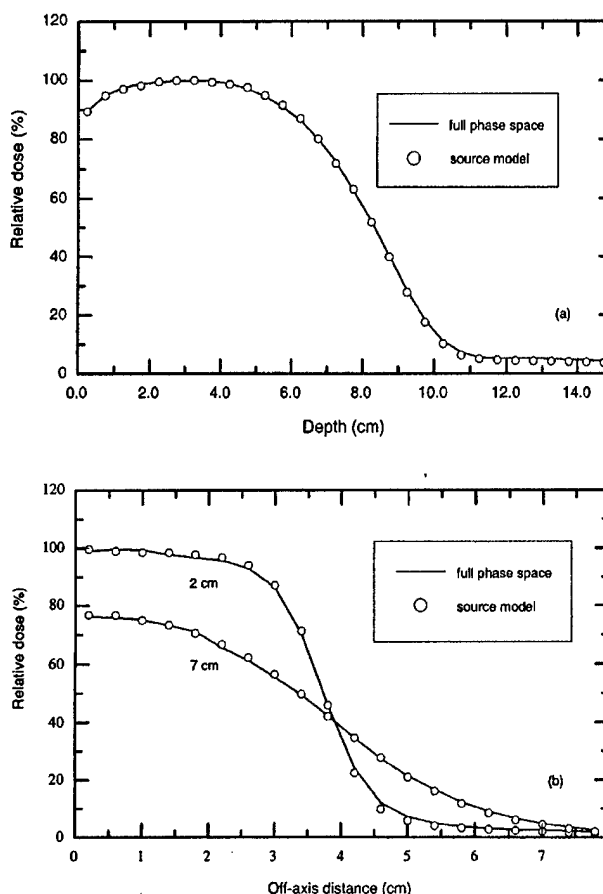


FIG. 5. Dose distributions in water for 20 MeV electron beam with $6 \times 6 \text{ cm}^2$ applicator at 120 cm SSD, calculated with full phase space data and source model: (a) Depth-dose distributions; (b) dose profiles at depths of 2 cm and 7 cm. Curves are normalized to the dose at d_{max} .

mind that 20 cm air gap is rarely used in actual clinical situations. Therefore, we have demonstrated that the simplified four-source model can be used for accurate dose calculations even for extreme cases (such as very large extended SSDs).

The capability of the model for calculating the relative beam output was also tested. Table I shows cutout factors for various square inserts in a $10 \times 10 \text{ cm}^2$ applicator for 6, 12 and 20 MeV electron beams. It is found that the cutout factors calculated with the four-source model are within about $\pm 2\%$ compared to the measured values except for one case where we see 2.5% difference. This is at about the same accuracy level as the full Monte Carlo simulation and considered to be acceptable for clinical use.

The relationship between E_{in} and R_{50} for the reference accelerator with a $10 \times 10 \text{ cm}^2$ cone and 100 cm SSD is shown in Fig. 6. A linear relationship was found and fitted as

$$E_{\text{in}} = 2.597R_{50} + 0.633. \quad (21)$$

It gives the relationship between the variation in the incident energy and the variation in R_{50} as

$$\Delta E_{\text{in}} = 2.597\Delta R_{50}. \quad (22)$$

TABLE I. The electron cutout factors for various square inserts in $10 \times 10 \text{ cm}^2$ applicator for 6, 12, and 20 MeV beams calculated with the source model and the full phase space data and compared with the measurement of Kapur *et al.* (Ref. 45). The values in parenthesis indicate the difference of the data calculated with the source model or the full phase space from the measured data.

Energy (MeV)	Insert (cm^2)	Cutout factor		
		Source model	Full phase space	Measurement
6	2×2	0.803 (2.5%)	0.765 (-1.3%)	0.778
	3×3	0.930 (0.3%)	0.923 (-0.4%)	0.927
	4×4	0.970 (-1.8%)	0.982 (-0.6%)	0.988
	8×8	1.002 (-0.1%)	1.005 (-0.2%)	1.003
12	2×2	0.881 (-0.8%)	0.861 (-2.8%)	0.889
	3×3	0.908 (-2.0%)	0.930 (0.2%)	0.928
	4×4	0.942 (-2.1%)	0.956 (-0.7%)	0.963
	8×8	0.999 (0.8%)	1.002 (1.1%)	0.991
20	2×2	0.963 (-1.1%)	0.957 (-1.9%)	0.976
	3×3	0.989 (-0.4%)	0.968 (-2.5%)	0.993
	4×4	0.993 (-1.8%)	0.993 (-1.8%)	1.011
	8×8	0.999 (-0.5%)	0.993 (-1.1%)	1.004

Equation (22) is used for tuning the maximum energy in the source model to match the measured depth dose curves when commissioning a clinical beam.

Figure 7 shows the dose distributions for the reference beam, beam A, and beam B with the applicator size of $10 \times 10 \text{ cm}^2$ and SSD of 100 cm. All the curves are normalized to the dose at d_{max} . The statistical uncertainty (1σ) in all the Monte Carlo dose calculations was kept to be smaller than 0.5%, therefore, the error bars are smaller than the symbol size and not shown on the curves. The maximum energy in the source model was adjusted to 8.87 MeV to match the dose distributions of the beam A ($E_{\text{in}}=9.0 \text{ MeV}$) and to 15.17 MeV to match the dose distributions of the beam B ($E_{\text{in}}=15.0 \text{ MeV}$). The difference between the depth-dose curves calculated by the adjusted models and the full Monte Carlo simulation is always less than 0.5% for both beam A and beam B. For dose profiles, the difference is usually less than 1% except that in the shoulder region for beam B the difference is about 2%.

Figure 8 shows the dose distributions for the reference beam and beam C with the applicator size of $10 \times 10 \text{ cm}^2$ and SSD of 100 cm. Again, the curves are normalized to the dose at d_{max} and the Monte Carlo uncertainty is lower than 0.5%. In this case, the maximum energy in the source model was adjusted to 11.25 MeV. The dose distributions calculated by the source model with the adjusted maximum energy agree very well (1%/1 mm) with the published data.³⁸

Table II gives E_{in} and R_{50} for the reference and Monte Carlo simulated beams, and E_{max} and R_{50} for the adjusted source models. For the reference beam, E_{max} was directly obtained from the full Monte Carlo simulation. For beam C, E_{in} is unknown. In this study, we set $\epsilon=0.01 \text{ cm}$. Therefore, the R_{50} 's calculated using the adjusted source model match with the full Monte Carlo simulation to within 0.01 cm. Of course, we will not use such a small ϵ in real clinical applications since it is much smaller than the measurement uncertainty in R_{50} . Here, we just want to demonstrate the capa-

bility of the method to reproduce R_{50} accurately.

We have applied the commissioning approach to electron beams from a Clinac 2300C/D accelerator in our institution. The reference machine is still the same Clinac 2100C accelerator. These two machines are sufficiently similar to each other in treatment head geometry. Their dosimetric characteristics are very close to each other due to the beam tuning during linac acceptance. Therefore, it is not surprising to see that the dose distributions calculated with the adjusted source model agree well (within 1%–2% or 1–2 mm) with the measured data.

These preliminary results have shown that the proposed hybrid commissioning approach can be used for accelerators of the same design to account for the dosimetric variations mainly caused by the on-site tuning of the electron incident energy. The capability of the approach to handle large variation in the electron incident energy has been demonstrated. It is believed that for most clinical accelerators of the same type, their treatment head designs are exactly the same or at least very similar, therefore the dosimetric difference can usually be traced back to the difference in the electron incident energy. Therefore, the current approach should be applicable in most clinical situations. In the future work, the method will be evaluated under more critical conditions, such as small field sizes, extended SSD, and heterogeneous phantoms.

The general idea proposed here should also work for other types of accelerators, although we have selected the Varian Clinac 2100C accelerators in the current study. For each type of accelerator, a reference machine should be carefully simulated using the Monte Carlo method. A source model, which may consist of a different number of sub-sources, can be established based on the simulated data. Then, the maximum energy in the model can be adjusted to commission electron beams from other accelerators of the same type.

In some situations, the proposed commissioning approach may not be directly applicable. For example, the measured

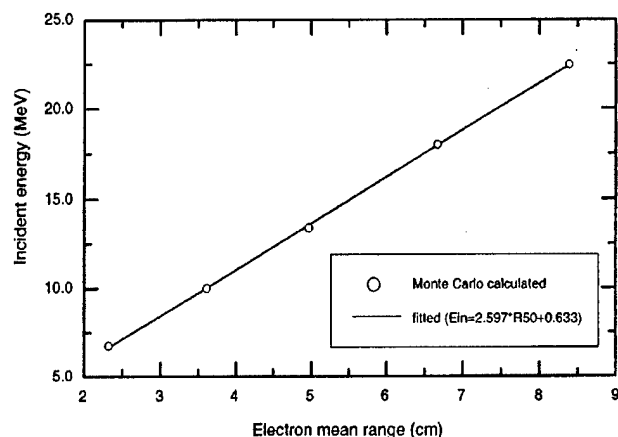


FIG. 6. The relationship between electron incident energy at accelerator exit window (E_{in}) and the depth of 50% dose (R_{50}) for electron beams from the reference accelerator with 10×10 cm² applicator and 100 cm SSD. Symbols are calculated with Monte Carlo simulation of the accelerator treatment head. Solid line is the fitted result with formula $E_{in} = 2.597 R_{50} + 0.633$.

dose distributions used for commissioning more or less contain measurement errors, depending on the measurement techniques and the experience of the person who performs the measurements. Since only the maximum energy is the adjustable parameter in the current source model, our approach may not be able to exactly match the measured data. Occasionally, an accelerator used in the clinic may differ from its original design in addition to the electron incident energy. Some parts in the accelerator treatment head may be replaced with nonstandard ones. In this case, we can always perform a full Monte Carlo simulation for this unique accelerator and build its own source model. Alternatively, we can make the present approach more versatile to handle those situations. More parameters in the source model other than the maximum energy, such as the relative intensity of each sub-source, the k factor for in-air perturbation for the direct electrons, and the field size, can be adjusted to match the measured dose distributions. For example, the adjustment of the relative intensity of the photon source will ensure a good match to the bremsstrahlung tail in the depth-dose curve. If some of the materials in the paths of direct electrons, such as the scattering foil, monitor chamber or mirror, are different from those used in the reference accelerator, the adjustment of the k factor can yield a better estimation of the electron angular perturbation. The adjustment of the field size in the source model should recover the measurement error in the width of the dose profiles (e.g., errors of the order of about 1 mm are not rare in a clinical situation). In summary, the introduction of more adjustable parameters in the source model will make the current commissioning approach more powerful. This possibility will be investigated in our future study.

IV. CONCLUSIONS

A hybrid commissioning approach based on a multiple source model has been proposed for Monte Carlo treatment planning. It has been demonstrated that a simplified four-

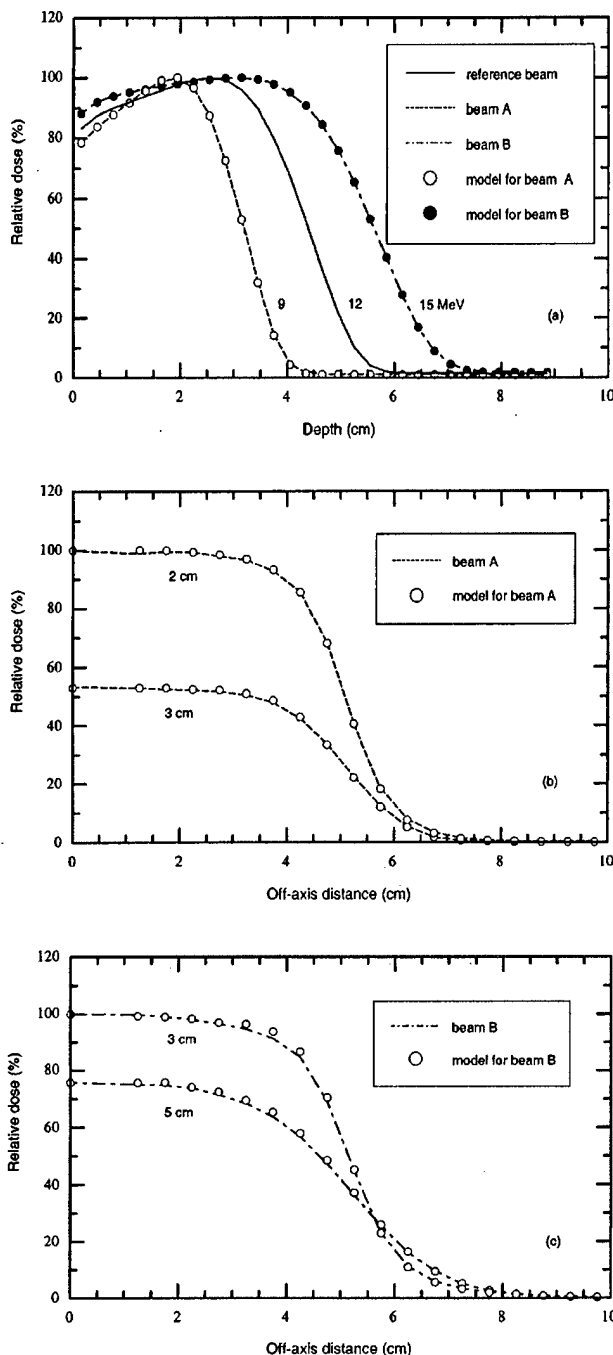


FIG. 7. Dose distributions in water for electron beams from the reference accelerator with 10×10 cm² applicator and at 100 cm SSD. The reference beam has the electron incident energy of 12.0 MeV. A source model was built based on the Monte Carlo simulation of the reference beam. The maximum energy of the energy spectra in the model was adjusted to 8.87 MeV to match the beam A (with $E_{in} = 9.0$ MeV) and 15.17 MeV to match the beam B (with $E_{in} = 15.0$ MeV). Lines are dose distributions from the full Monte Carlo simulations. Symbols are data calculated by the source model with adjusted maximum energies. All data are normalized to the doses at d_{max} . (a) Depth-dose distributions; (b) dose profiles at depths of 2 cm and 3 cm for beam A; (c) dose profiles at depths of 3 cm and 5 cm for beam B.

source model can be used to generate accurate Monte Carlo dose distributions for electron beams from Varian Clinac 2100C accelerators. The model includes a point electron source for direct electrons and electrons scattered from pri-

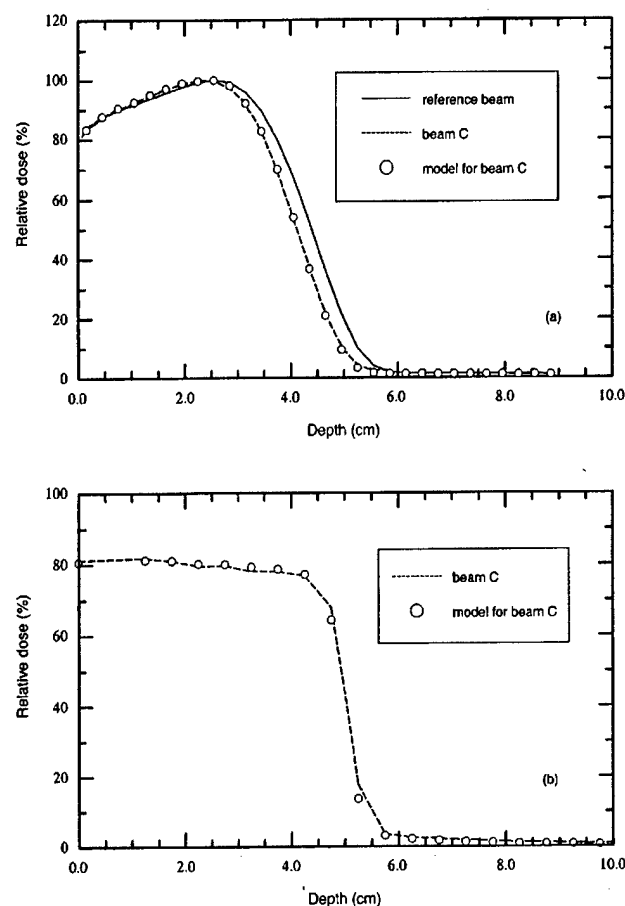


FIG. 8. Dose distributions in water for electron beams with $10 \times 10 \text{ cm}^2$ applicator and at 100 cm SSD. The reference beam (solid line) is from a Clinac 2100C accelerator with $E_{in} = 12.0 \text{ MeV}$. The dose distributions for beam C (dashed lines) is taken from the published data for a 9 MeV beam from another Clinac 2100C accelerator with type III applicator (Ref. 38). A source model built based on the Monte Carlo simulation of the reference beam is used to match beam C by adjusting the maximum energy to 11.25 MeV (open circles). All data are normalized to the dose at d_{max} . (a) Depth-dose distributions; (b) dose profiles at depth of 0.1 cm.

mary collimator and jaws, a point photon source for all contaminant bremsstrahlung photons, and two square ring electron sources representing electrons scattered from two scrapers (other than the last scraper) of the Varian electron applicator (type III). It was found that the position of the virtual point source can be determined accurately using the pinhole method for photons in all cases and electrons in high energy beams. For low energy beams, we should use the Monte Carlo phase space data which are obtained by simulating the treatment head with the intervening air replaced by vacuum. We also found that the in-air perturbation on the electron incident direction can be properly accounted for using the Fermi-Eyges model. The source model which was built based on the simulated phase space data for the reference accelerator can be used for other accelerators of the same type, by simply adjusting the energy spectra in the model. The capability of this commissioning approach for handling large variation in the electron incident energy has been demonstrated.

TABLE II. Some parameters for the full Monte Carlo simulations and the adjusted source models. E_{in} is the electron incident energy at the exit window in the simulation. E_{max} is the maximum energy in the source model. R_{50} is the depth of 50% dose of the depth dose curve in water for $10 \times 10 \text{ cm}^2$ applicator and 100 cm SSD. A source model was built based on the full Monte Carlo simulation of the reference beam. For beams to be commissioned (A, B, and C), E_{max} in the model was adjusted to match the corresponding R_{50} from the Monte Carlo simulation.

Beam tested	MC simulation		Source model	
	E_{in} (MeV)	R_{50} (cm)	E_{max} (MeV)	R_{50} (cm)
Reference	12.0	4.397	12.00	4.397
Beam A	9.0	3.197	8.87	3.192
Beam B	15.0	5.622	15.17	5.624
Beam C	unknown	4.116	11.25	4.119

ACKNOWLEDGMENTS

The authors are grateful to the referees, Drs. Art Boyer, Alan Nahum, Alex Bielajew, David Findley, Gary Luxton, Ed Mok, Todd Pawlicki, and Frank Verhaegen for useful comments on the manuscript. The authors would also like to thank Dr. Sam Brain, Todd Koumian, and Behrooz Tofigh-rad for computer support, Dr. Dave Rogers and his OMEGA/BEAM team at the National Research Council of Canada for the Monte Carlo simulation system, and Eva Papiez for supplying some measured data. The work was supported in part by the U.S. Army breast cancer research program (BC971292), NCI Grant No. CA78331 and a consortium agreement with the Numerix Cooperation.

^aCorresponding author. Tel: (650)498-4074, Fax: (419)498-4015, E-mail: stevej@reyes.stanford.edu

¹K. R. Hogstrom, M. D. Mills, and P. R. Almond, "Electron beam dose calculations," *Phys. Med. Biol.* **26**, 445-459 (1981).

²E. Fermi, in B. Rossi and K. Greisen, "Cosmic-ray theory," *Rev. Mod. Phys.* **13**, 265-268 (1941).

³L. Eyges, "Multiple scattering with energy loss," *Phys. Rev.* **74**, 1534-1535 (1948).

⁴J. Cygler, J. J. Battista, J. W. Scrimger, E. Mah, and J. Antolak, "Electron dose distributions in experimental phantoms: A comparison with 2D pencil beam calculations," *Phys. Med. Biol.* **32**, 1073-1086 (1987).

⁵E. Mah, J. Antolak, J. W. Scrimger, and J. J. Battista, "Experimental evaluation of a 2D and a 3D electron pencil beam algorithm," *Phys. Med. Biol.* **34**, 1179-1194 (1989).

⁶I. Kawrakow, M. Fippel, and K. Friedrich, "3D electron dose calculation using a voxel based Monte Carlo algorithm (VMC)," *Med. Phys.* **23**, 445-457 (1996).

⁷C. M. Ma, E. C. Mok, A. Kapur, T. Pawlicki, D. O. Findley, S. Brain, K. Forster, and A. L. Boyer, "Clinical implementation of a Monte Carlo treatment planning system," *Med. Phys.* **26**, 2133-2143 (1999).

⁸M. A. Ebert and P. W. Hoban, "Possibilities for tailoring dose distributions through the manipulation of electron beam characteristics," *Phys. Med. Biol.* **42**, 2065-2081 (1997).

⁹M. G. Karlsson, M. Karlsson, and B. Zackrisson, "Intensity modulation with electrons: calculations, measurements and clinical applications," *Phys. Med. Biol.* **43**, 1159-1169 (1998).

¹⁰M. Åsell, S. Hyödynmaa, S. Söderström, and A. Brahme, "Optimal electron and combined electron and photon therapy in the phase space of complication-free cure," *Phys. Med. Biol.* **44**, 235-252 (1999).

- ¹¹ A. E. Nahum, "Monte Carlo electron transport simulation II: Application to dose planning," in *The Computation of Dose Distributions in Electron Beam Radiotherapy*, edited by A. E. Nahum (Umeå University, Umeå, Sweden, 1985), pp. 319–340.
- ¹² T. M. Jenkins, W. R. Nelson, A. Rindi, A. E. Nahum, and D. W. O. Rogers, *Monte Carlo Transport of Electrons and Photons* (Plenum, New York, 1988).
- ¹³ T. R. Mackie, "Applications of the Monte Carlo method in radiotherapy," in *Vol. III of Dosimetry of Ionizing Radiation*, edited by K. Kase, B. Bjärngard, and F. H. Attix (Academic, New York, 1990), 541–620.
- ¹⁴ D. W. O. Rogers and A. F. Bielajew, "Monte Carlo techniques of electron and photon transport for radiation dosimetry," in *Vol. III of The Dosimetry of Ionizing Radiation*, edited by K. R. Case, B. E. Bjärngard, and F. H. Attix (Academic, New York, 1990), pp. 427–539.
- ¹⁵ D. W. O. Rogers, "The role of Monte Carlo simulation of electron transport in radiation dosimetry," *Int. J. Appl. Radiat. Isot.* **42**, 965–974 (1991).
- ¹⁶ P. Andreo, "Monte Carlo techniques in medical radiation physics," *Phys. Med. Biol.* **36**, 861–920 (1991).
- ¹⁷ C. Manfredotti, U. Nastasi, R. Ragona, and S. Anglesio, "Comparison of three dimensional Monte Carlo simulation and the pencil beam algorithm for an electron beam from a linear accelerator," *Nucl. Instrum. Methods Phys. Res. A* **255**, 355–359 (1987).
- ¹⁸ C. Manfredotti, U. Nastasi, R. Marchisio, C. Ongaro, G. Gervino, R. Ragona, S. Anglesio, and G. Sannazzari, "Monte Carlo simulation of dose distribution in electron beam radiotherapy treatment planning," *Nucl. Instrum. Methods Phys. Res. A* **291**, 646–654 (1990).
- ¹⁹ A. A. al-Beteri and D. E. Raeside, "Optimal electron-beam treatment planning for retinoblastoma using a new three-dimensional Monte Carlo-based treatment planning system," *Med. Phys.* **19**, 125–135 (1992).
- ²⁰ H. Neuenschwander, T. R. Mackie, and P. J. Reckwerdt, "MMC—A high-performance Monte Carlo code for electron beam treatment planning," *Phys. Med. Biol.* **40**, 543–574 (1995).
- ²¹ P. J. Keall and P. W. Hoban, "Super-Monte Carlo: A 3-D electron beam dose calculation algorithm," *Med. Phys.* **23**, 2023–2034 (1996).
- ²² B. Faddegon, J. Balogh, R. Mackenzie, and D. Scora, "Clinical considerations of Monte Carlo for electron radiotherapy treatment planning," *Radiat. Phys. Chem.* **53**, 217–227 (1998).
- ²³ C. M. Ma and A. E. Nahum, "Calculation of absorbed dose ratios using correlated Monte Carlo sampling," *Med. Phys.* **20**, 1189–1199 (1993).
- ²⁴ M. A. Holmes, T. R. Mackie, W. Sohn, P. J. Reckwerdt, T. J. Kinsella, A. F. Bielajew, and D. W. O. Rogers, "The application of correlated sampling to the computation of electron beam dose distributions in heterogeneous phantoms using the Monte Carlo method," *Phys. Med. Biol.* **38**, 675–688 (1993).
- ²⁵ A. F. Bielajew, "Monte Carlo modeling in external electron-beam radiotherapy—Why leave it to chance?," in *Proceedings of The 11th International Conference on The Use of Computers in Radiation Therapy*, edited by A. R. Hounsell, J. M. Wilkinson, and P. C. Williams (Manchester, UK, 1994), pp. 2–5. North Western Medical Physics Department, Christie Hospital NHS Trust.
- ²⁶ R. Mohan, "Why Monte Carlo?" in *Proceedings of The 12th International Conference on The Use of Computers in Radiation Therapy*, edited by D. D. Leavitt and G. Starkschall, Salt Lake City, Utah (Medical Physics Publishing, Madison, 1997), pp. 16–18.
- ²⁷ C. L. Hartmann-Siantar, P. M. Bergstrom, W. P. Chansler, L. Chase, L. J. Cox, T. P. Daly, D. Garrett, S. M. Hornstein, R. K. House, E. I. Moses, R. W. Patterson, J. A. Rathkopf, and A. S. von Wittenau, "Lawrence Livermore National Laboratory's PEREGRINE project," in *Proceedings of the 12th International Conference on The Use of Computers in Radiation Therapy*, edited by D. D. Leavitt and G. Starkschall, Salt Lake City, Utah (Medical Physics Publishing, Madison, 1997), pp. 19–22.
- ²⁸ J. J. DeMarco, T. D. Solberg, and J. B. Smathers, "A CT-based Monte Carlo simulation tool for dosimetry planning and analysis," *Med. Phys.* **25**, 1–11 (1998).
- ²⁹ L. Wang, C. S. Chui, and M. Lovelock, "A patient-specific Monte Carlo dose-calculation method for photon beams," *Med. Phys.* **25**, 867–878 (1998).
- ³⁰ J. O. Deasy, P. R. Almond, and M. T. McEllistrem, "Measured electron energy and angular distributions from clinical accelerators," *Med. Phys.* **23**, 675–684 (1996).
- ³¹ J. J. Janssen, E. W. Korevaar, L. J. van Battum, P. R. M. Storchi, and H. Huizenga, "Clinical electron beam dose calculations with the Phase Space Evolution model," in *Proceedings of the 12th International Conference on The Use of Computers in Radiation Therapy*, edited by D. D. Leavitt and G. Starkschall, Salt Lake City, Utah (Medical Physics Publishing, Madison, 1997), pp. 195–196.
- ³² M. Udale, "A Monte Carlo investigation of surface doses for broad electron beams," *Phys. Med. Biol.* **33**, 939–954 (1988).
- ³³ M. Udale-Smith, "Monte Carlo calculations of electron beam parameters for three Philips linear accelerators," *Phys. Med. Biol.* **37**, 85–105 (1992).
- ³⁴ D. W. O. Rogers, B. A. Faddegon, G. X. Ding, C. M. Ma, J. We, and T. R. Mackie, "BEAM: A Monte Carlo code to simulate radiotherapy treatment units," *Med. Phys.* **22**, 503–524 (1995).
- ³⁵ C. M. Ma and D. W. O. Rogers, "Beam characterization: a multiple-source model," Technical Report PIRS 509d, National Research Council of Canada, Ottawa, Canada, 1995.
- ³⁶ C. M. Ma, B. A. Faddegon, D. W. O. Rogers, and T. R. Mackie, "Accurate characterization of Monte Carlo calculated electron beams for radiotherapy," *Med. Phys.* **24**, 401–416 (1997).
- ³⁷ C. M. Ma, "Characterization of computer simulated radiotherapy beams for Monte-Carlo treatment planning," *Radiat. Phys. Chem.* **53**, 329–344 (1998).
- ³⁸ G. X. Ding and D. W. O. Rogers, "Energy spectra, angular spread and dose distributions of electron beams from various accelerators used in radiotherapy," Technical Report PIRS 0439, National Research Council of Canada, Ottawa, Canada, 1995.
- ³⁹ AAPM TG-25, "Clinical electron beam dosimetry: Report of AAPM Radiation Therapy Committee Task Group No. 25," *Med. Phys.* **18**, 73–109 (1991).
- ⁴⁰ M. A. Ebert and P. W. Hoban, "A Monte Carlo investigation of electron-beam applicator scatter," *Med. Phys.* **22**, 1431–1435 (1995).
- ⁴¹ P. J. Keall and P. W. Hoban, "Calculating the angular standard deviation of electron beams using Fermi-Eyges theory," *Phys. Med. Biol.* **41**, 1511–1515 (1996).
- ⁴² S. B. Jiang, Z. M. Luo, and K. M. Ayyangar, "Incorporation of the electron energy-loss straggling into the Fermi-Eyges equation," *Radiat. Phys. Chem.* **53**, 477–482 (1998).
- ⁴³ B. L. Werner, F. M. Khan, and F. C. Deibel, "A model for calculating electron beam scattering in treatment planning," *Med. Phys.* **9**, 180–187 (1982).
- ⁴⁴ ICRU 35, "Radiation Dosimetry: Electron Beams with Energies Between 1 and 50 MeV," International Commission on Radiation Units and Measurements, Bethesda, MA, 1984.
- ⁴⁵ A. Kapur, C. M. Ma, E. C. Mok, D. O. Findly, and A. L. Boyer, "Monte Carlo calculations of electron beam output factors for a medical linear accelerator," *Phys. Med. Biol.* **43**, 3479–3494 (1998).

Concurrent Boost Using Forward Multiple-Segment Planning and Step-and-Shoot Delivery: A Novel Technique of Breast-Conserving Radiation Therapy

Yulin Song, Penny Peng, Arthur L. Boyer, and Lei. Xing

Department of Radiation Oncology, Stanford University School of Medicine,
Stanford, California 94305-5304

Purpose: Currently, most-widely used breast radiation therapy employs two opposed tangential photon beams with either uniform or wedge-shaped intensity profiles, followed by an electron boost field. Since plans created using this technique are not optimized, a certain portion of the ipsilateral lung and, in the case of the left breast treatment, a small volume of the heart is inevitably included in the treatment fields, resulting in high radiation doses to these areas. Recently, tangential field treatment using intensity-modulated fields has shed some light on breast cancer treatment. Although the dosimetric advantage of IMRT with opposed tangential beam configuration is obvious, its wide clinical application has not been realized. This is, in part, due to the fact the current IMRT planning and treatment procedure deviate significantly from the conventional approach and require additional steps in planning, delivery, quality assurance, and intensive personnel training. The goal of this study was to establish a variant of IMRT, multiple segment radiation therapy (MSRT), for concurrent breast boost treatment using forward planning and step-and-shoot delivery and address several untouched clinical issues related to the technique.

Materials and Methods: Five right-sided and five left-sided breast cancer patients, who had previously undergone lumpectomy, were selected for the study. The patients were CT scanned in the conventional treatment position supported by an Alpha Cradle immobilization device. Radiopaque markers were placed on the patients' chest to indicate the medial and lateral borders of the palpable breast tissue and the location of the lumpectomy scar. The critical structures, including the left and right lungs, the heart, and the contralateral breast, were delineated by a radiation oncologist. It is, however, not required to outline the structures in general MSRT concurrent boost planning. Treatment planning was performed using a 3D treatment planning

system. A uniform dose of 4,500 cGy or 5,040 cGy was prescribed to the entire target volume and a concurrent boost dose of 1,800 cGy was prescribed to the surgical region of the target volume. All plans were delivered in 180-cGy fractions. For comparison, three plans were created for each patient. One was the standard opposed tangential field (OTF) plan and the other two were the MSRT concurrent boost plans with different constraints. The standard plans employed a medial and a lateral tangential field with 6 or 15 MV photon energy. A wedge filter was used in the lateral beam. The MSRT concurrent boost planning started with a standard OTF plan. After the initial wedged plan was obtained, an additional MLC field segment was added to one or both beam directions to boost the surgical region under the guidance of dose distributions and DVH. If necessary, more segments were added to boost the "cold" or to remove the "hot" regions in the target. A segment may also be needed to reduce the dose to the ipsilateral lung and the heart. Once the plan was completed, the static MLC files were exported and concatenated to form a step-and-shoot delivery file. The intensity map, MU, and the maximum boundary of the MLC were independently checked prior to the first treatment.

Results: Compared with the OTF plans, the MSRT concurrent boost plans showed a much better dose uniformity in the target and a significant dose reduction in the ipsilateral lung and heart. In addition, the target volume receiving high dose irradiation was significantly reduced. Furthermore, it was found that the overall planning, treatment, and delivery overhead was insignificant and was more time efficient than the current conventional IMRT planning.

Conclusions: A clinical challenge in IMRT breast treatment is how to modulate breast irradiation without increasing the treatment complexity. In this study, we investigated MSRT concurrent breast boost treatment and demonstrated its clinical utility. When dose conformity can be realized using MLC beam shaping devices, the addition of a few extra segments could often improve the dose distribution significantly. The manual forward planning technique is a competitive approach compared with computerized inverse planning. MSRT is particularly efficient in incorporating prior and posterior knowledge and physical constraints into the treatment planning process. It is thus a more natural way to evolve from the conventional radiation therapy to the more sophisticated IMRT treatment. MSRT is likely to be beneficial for any radiation treatment where a simple beam configuration is used and where it is difficult to achieve a desired dose distribution within the target volume.

This study was supported in part by grant DAMD17-00-1-0443 from the US Department of Defense

Combining IMRT and MERT for Breast-Conserving Radiation Therapy

Anthony Lo, Yulin Song, Arthur L. Boyer, Todd Pawlicki, and Lei. Xing

Department of Radiation Oncology, Stanford University School of Medicine,
Stanford, California 94305-5304

Purpose: The conventional opposed tangential photon beam treatment for breast cancer has two major limitations. Firstly, part of the lung and heart (in the case of the left breast treatment) may be exposed to a high radiation dose. Secondly, the contralateral breast may receive a significant amount of scatter dose. To reduce radiation side effects, we have investigated the strategy of treating breast cancer by combining intensity modulated radiation therapy (IMRT) and modulated electron radiation therapy (MERT). The objective of this study was to fully utilize the desirable characteristics of electron beams and intensity-modulated photon beams to achieve an optimal dose distribution in the target and minimize the exit and scatter doses to the critical structures.

Materials and Methods: Five early-stage breast cancer patients, who had previously undergone lumpectomy, were chosen for this combined-modality study. The patients were CT scanned in the conventional treatment position supported by an Alpha Cradle immobilization device. Radiopaque markers were placed on the patients' chest to indicate the medial and lateral borders of the palpable breast tissue and the location of the lumpectomy scar. The clinical target volume (CTV) and critical structures, including the left and right lungs, the heart, and the contralateral breast, were delineated on the axial CT images by a radiation oncologist. The PTV was obtained by adding a 1.0 cm margin uniformly to the CTV to account for patient setup uncertainty and organ shift. A uniform dose of 50.4 Gy was prescribed to the PTV in 1.8-Gy fractions. For comparison, two plans were computed for each patient. One was the standard opposed-tangential-field plan and the other the composite plan using the combined IMRT and MERT technique. The standard plan consisted of a medial and a lateral tangential field treated with a 6 MV photon beam. A 45° wedge was used in the lateral beam to obtain the desired dose distribution. The combined IMRT and MERT plan was computed using modified

EGS4/MCDOSE code. It was composed of five coplanar fields: two medial and two lateral IMRT fields (6 MV) and one perpendicular MERT field ($\sim 20^\circ$ from the anterior-posterior direction). The MERT field was treated with three nominal electron energies (6, 12, and 20 MeV). To deliver the MERT field effectively, we designed and manufactured a prototype electron MLC based on the results of Monte Carlo simulations and a conventional Varian 25 x 25 cm² electron applicator. The intensities of each electron energy were determined by the optimizer. Each of the photon and electron fields was divided into 1.0×1.0 cm² beamlets for the purpose of intensity optimization. The prescribed dose to the target was 50.4 Gy in 1.8 Gy fractions. For comparison, isodose lines were normalized to 50.0 Gy for all plans.

Results: The dose coverage to the PTV was similar for both techniques. However, the combined IMRT and MERT plans showed a much better dose homogeneity than the conventional opposed-tangential-field plans, which often exhibited extensive “hot” spots in the superior and inferior regions of the target. The dose to the ipsilateral lung, the heart, and, particularly, the contralateral breast was significantly reduced. In addition, the volume of normal tissue receiving low dose irradiation was significantly reduced.

Conclusions: Based on the results of this comparative dosimetric study, it seems that the combined IMRT and MERT technique offered a viable treatment option for breast cancer therapy. It is especially suitable to patients with large breasts, where a homogeneous dose distribution is difficult to achieve using the conventional opposed-tangential-field technique. As the IMRT treatment planning systems become more easily available and the development of the computer-controlled electron MLC is underway, we believe that the widespread routine implementation of this technique for breast cancer treatment should be investigated thoroughly.

This study was supported in part by grant DAMD17-01-1-0635 (Lei Xing) from the US Department of Defense.

Dose Matching of Two IMRT Plans or an IMRT and a 3D Conformal Treatment plan

L Xing, Z. Shou, J.G. Li, Y. Song, T. Pawlicki, A.L. Boyer, Q.-T. Le,

Purpose: IMRT is being increasingly adopted in radiation therapy community as a viable modality for radiation therapy of various cancers. One of the important problems related to its clinical application is the matching of an IMRT dose distribution for the treatment of part of the target volume(s) with a conventional 3D or another IMRT dose distribution for the treatment of the other portion of target volume(s). The purpose of this work is to develop an effective method for optimally matching the two sets of dose distributions and to demonstrate its clinical utility.

Methods and Materials: The two plans that need to be matched are dealt sequentially. First, the 3D conformal radiation therapy plan or the 1st IMRT plan used for treating part of the tumor volume(s) is obtained. To reduce the sensitivity of the final matching to the potential setup errors, attempt needs to be made to "blur" the penumbra or dose gradient in the direction perpendicular to the general matchline. Specifically, instead of having a sharp dose gradient, we let the dose to extend by additional 1.5~5cm in the direction perpendicular to the matchline and in this transition region, the dose is forced to fall-off linearly. The overlap is generally determined by the desired sensitivity against the setup error. After the first plan is done with the extended transitional dose gradient region, we proceed to optimize the 2nd IMRT plan with consideration of the existing doses of the first treatment plan. The goal of the 2nd dose optimization is to obtain an IMRT that yields a uniform composite dose distribution in the target volume(s) and (including the transitional regions) while sparing the sensitive structures. The technique is applied to the treatment of head and neck cancer, where matching of a conventional supraclavicular field for the irradiation of supraclavicular lymph nodes and an IMRT plan for the irradiation of the nasopharynx tumor and cervical lymph nodes is required. The matching between breast IMRT treatment and the supraclavicular field is also investigated. Finally, the method is demonstrated by the combining radiotherapy of intensity modulated photon and electron beams.

Results: To test the technique, the matching of two pairs of parallel opposed fields is first performed on a cubic phantom. A comparison with conventional approach shows significant improvement in target dose homogeneity and the sensitivity against a few intentionally introduced errors. A similar phantom test based on the matching of an intensity modulated photon beam and an electron beam also shows more dramatic improvement. Without intensity modulating the photon beam, overdosing/underdosing on the electron/photon side of the matchline was found to be +19% and -16%, respectively. The dose becomes almost perfectly uniform at the target region with the help of intensity modulation. The hybrid dose distribution also shows a ~50% reduction in the sensitivity with respect to the setup error. For each of the clinical cases investigated here, satisfactory matching between the different treatment regimes is found. Most importantly, with the implementation of the composite dose optimization technique, the matching becomes much controllable and transparent to the clinicians.

Conclusion: A general method for matching an IMRT dose distribution with a 3D conformal or another IMRT treatment is proposed. The approach takes advantage of the state-of-the-art intensity modulation and dose optimization techniques and provides an effective solution to the timely clinical problem of IMRT dose matching. In addition to better dose uniformity in the target volumes in the matchline region, we found that the sensitivity of the doses in the matchline region is significantly improved.

SU-EE-PDS-48**Incorporating Target Motion in IMRT Plans**

A Sethi*, L Leybovich, N Dogan, Loyola University Medical Center, Maywood, IL

Organ motion presents a significant challenge in IMRT. Due to lung motion, free-breathing CT scans may not be reliable in outlining CTV. Due to uncertainties associated with organ motion, internal target volumes, ITV (CTV + margin for target motion) may not be accurate. In this work, we present a novel method of tracking tumor motion. Depending on time spent at different locations, a target cloud with varying probability densities was generated around the CTV. Rectangular, spherical and oval shaped objects embedded in a cork phantom were CT scanned using abutting 2mm thick slices. Slice acquisition time varied from 1 to 5 sec. The objects moved in axial and sagittal planes with 2cm amplitude and 1 to 10 sec time periods. Correlation between target electron density on CT scans and temporal probability of various target locations was studied. CTV and ITV were outlined using mediastinum and lung windows respectively. As scan speed increased and/or target speed decreased, target was not detected on some CT slices. To obtain complete target information, the slice acquisition time needed to be greater than the period of target motion. Target electron density showed strong correlation with the percentage of time occupied by the target at different locations. IMRT plans were generated for ITV based PTV. Areas always occupied by the target were prescribed full dose, whereas doses to areas partially occupied by the target were reduced. Compared to conventional IMRT plans, plans developed using a modified prescription resulted in reduced dose to lung tissue.

SU-EE-PDS-49**The Dose Sensitivity to Lung Motion in Optimized Plan for IMPT, VHEET and IMXT**

TK Lee and G Sandison*, Purdue University, West Lafayette, IN

A mathematical homogeneous phantom was defined to simulate the motion of a target as lung size changes during the breathing cycle from full inspiration to full expiration. The dependence of dose sensitivity for the target and lung was studied for intensity modulated proton therapy (IMPT), intensity modulated very high-energy electron therapy (VHEET) and intensity modulated x-ray therapy (IMXT) during lung motion. Other parameters studied were beam number and beam direction. It was assumed that the plan was optimized for the lung size and target position at full inspiration. Of the three radiation types studied the results show that IMPT is the most sensitive to the lung motion. For importance factors of $I_{\text{target}}=500$ and $I_{\text{lung}}=10$, we calculated the relative dose error due to breathing as the mean doses at full inspiration to that at full expiration. Relative dose errors were 42 % (target) and 160 % (OAR) for IMPT, 23 % (target) and 47 % (OAR) for VHEET and 21 % (target) and 36 % (OAR) for IMXT. VHEET was found to be more dose sensitive than IMXT. Sensitivity to the organ motion depends upon the physical ability to localize the radiation on the assumed static position of the target.

SU-EE-PDS-50**Quantitative Fluoroscopy of Respiration-Induced Abdominal Tumor Motion and the Impact of Motion On IMRT Dose Distributions**

D Gierga^{*1}, G Chen¹, J Kung¹, M Betke², J Lombardi², C Willett¹, (1) Massachusetts General Hospital and Harvard Medical School, Boston, MA, (2) Boston University, Boston, MA

The treatment of moving targets with Intensity Modulated Radiation Therapy (IMRT) may introduce errors in dose delivery. The motion of tumors in the abdomen was studied using quantitative fluoroscopic analysis, and the effect on dose delivery to the target was studied. Fluoroscopy sessions for seven patients with pancreas or liver tumors were recorded, converted to digital format, and analyzed to quantify the characteristics of tumor motion. Clip motion was quantified by analyzing each patient's fluoroscopy session, using image processing and recursive filtering techniques to track the motion of the tumor clips. For three patients (a total of five plans), IMRT treatment plans were generated, and the DVH for the target volume was compared for plans with and without tumor motion. The average magnitude of peak-to-peak motion for the seven patients in the cranio-caudal and anterior-posterior directions was 7.4 mm and 3.8 mm, respectively. The clip motion varied widely, as the maximum clip excursions were about 47% greater than the average clip excursions for each patient. The inclusion of tumor motion did not lead to

a significant degradation in the target DVH for 4 of 5 treatment plans studied. The amount of tumor motion for most patients in this study is not large, but can in some instances significantly degrade the planned target DVH. For some patients, therefore, motion mitigation or intervention during treatment may be necessary.

SU-EE-PDS-51**Effect of the Number of Treatment Fields On Respiration-Induced Dose Errors in Single and Multi-Fraction IMRT Delivery**

J Duan*, S Shen, R Popple, S Ye, P Pareek, I Brezovich, University Alabama Birmingham, Birmingham, AL

Radiation doses are subject to errors when delivered with IMRT to sites affected by respiratory motion. We have previously shown that motion-induced errors tend to cancel after multiple fractions. In the present study we investigated the effect of increased number of treatment fields on dose errors. A polystyrene phantom with simulated target and organs at risk was used for treatment planning and delivery. IMRT plans involving five, seven, nine and ten non-opposing fields were prepared on a commercial treatment planning system, using identical dose constraints. All plans were delivered for five fractions, and the dose at isocenter was measured using a 0.125cm³ ion chamber. The phantom was moved sinusoidally at 0.75cm amplitude (1.5cm motion range) to simulate respiratory motion. Errors were calculated by comparing doses delivered to the same point in moving and in stationary phantoms. Single fraction dose errors for individual fields ranged -4.0% to 8.6%, -5.7% to 47.8%, -7.5% to 20.1%, and -11.7% to 12.1% for the five-, seven-, nine-, and ten- field plans, respectively. Single fraction error of total dose ranged -1.1% to 1.2%, -0.8% to 0.8%, -1.7% to 2.8, and -0.5% to 3.5%, respectively. Although dose errors of individual fields tended to cancel, resulting in substantially smaller errors in total doses, increasing the number of fields does not necessarily reduce dose errors. No direct correlation between dose errors and the number of treatment fields in the IMRT plan was observed.

SU-EE-PDS-52**IMRT Using Audio and Optical Respiration Gating**

A. Boyer*, T. Pawlicki, C. Cardenas, Y. Song, Stanford University School of Medicine, Stanford, CA

We report on an investigation of beam gating to compensate for respiration. We have studied audio coaching synchronized to a gating signal to the linear accelerator as the primary timing method while using a secondary respiration monitor to confirm that the patient (subject) is complying with the audio coaching. We asked whether this approach provides a more regular gating pattern for the linear accelerator and therefore a more consistent daily treatment than physical measures of the subject respiration. We studied optical observation of the subject with a video camera as a respiration monitor. A fixed field of view centered on the treatment isocenter was established for two cameras viewing the patient from the right and left lateral directions. The video signals produced by the cameras were digitized by an image processing board in a personal computer (Sony XC-73 camera, Matrox Meteor-II/Multi-Channel video board, Pentium III CPU, 864MHz, 256M RAM, Microsoft Windows 2000, Matrox Imaging Library). Respiration was monitored by the correlation of a region-of-interest within the field of view that was acquired and correlated once every 200 milliseconds. The correlation value yielded an adequate measure of chest wall motion and served as a respiration phase parameter. A means was sought to use this time-dependent correlation value as a measure of subject compliance with the audio coaching. A two-standard deviation, phase-dependent threshold was tested using a gating pattern that was found to be adequate for compensating for lung or kidney motion.

SU-EE-PDS-53**Comparison of Two Breathing Levels for Gated Intensity Modulated Radiation Therapy (IMRT) of Lung Cancer**

C Della Bianca^{*1}, E Yorke¹, G Mageras¹, P Giraud², K Rosenzweig¹, H Amols¹, C Ling¹, (1)Memorial Sloan-Kettering Cancer Center, New York, NY, (2)Institut Curie, Department of Radiation Oncology, Paris, France

Gated delivery of radiation during part of the breathing cycle may improve the precision of lung cancer IMRT. End-expiration (EE) is more stable but end-inspiration (EI) increases lung volume. We compare the relative merit of using EI and EE in gated IMRT for sparing normal lung tissue.

PO-T-267**Automated Monte Carlo Commissioning for Photons Using the NXEGS Software**

T Pawlicki¹, Y Song¹, G Zhang², T Guerrero², K Prado², N Tolani², JA Both¹, AL Boyer¹, (1) Stanford University School of Medicine, Stanford, CA, (2) MD Anderson Cancer Center, Houston, TX

Commissioning a Radiotherapy Linear Accelerator for clinical dose calculation is a time consuming process. The aim of this work is to present a new Monte Carlo software package (NXEGS version 1.0.10.0, Numerix LLC.) that provides a fully automated commissioning process based on measured data. Physical data about the linear accelerator (eg. source-to-flattening filter distance) and measured data are required for the commissioning process. The measured data includes central axis depth-doses, beam profiles (inplane and/or crossplane, and at least one diagonal), and output factors. These data are presented in a single XML formatted file for the NXEGS software. We have commissioned NXEGS for 4MV, 6MV, 15MV, and 18MV photon beams across two institutions (MDACC and Stanford). Varian Clinac C-series linear accelerators were used. The output of the commissioning procedure is a source model file. Individual source models are created for each beam energy. NXEGS was able to reproduce the input data for all energies studied. The commissioning process will be described. We have begun some initial verification of the commissioned energies using asymmetric jaws and MLCs in homogeneous phantoms. We found that the source model generated by NXEGS was able to reproduce the beam penumbra for the jaws and the rippled isodose curves from the MLC. Results of dose measurements using film are within the 2% or 2mm criteria as recommended by the AAPM Task Group 40.

This work was partly supported by NX Medical Software, LLC and a 2001-2002 Stanford University OTL Research Incentive Fund Award.

PO-T-268**Monte Carlo Commissioning of Low Energy Electron Beams Using NXEGS Software**

JA Both*, T Pawlicki, Stanford University School of Medicine, Stanford, CA

This work is a report on the commissioning of low energy electron beams for Monte Carlo dose calculation using NXEGS software (NXEGS version 1.0.10.0, Numerix, LLC). As an electron beam commissioning tool, NXEGS uses both analytic and Monte Carlo methods to generate a beam source model from dose data collected in a water phantom. This study used NXEGS to commission 6-, 9-, and 12- MeV electron beams of a Varian Clinac 2100C at three open field sizes. Central axis depth-dose, primary axis and diagonal beam profiles, and output factors are the measurements necessary for commissioning. We present a comparison of the measured dose data with the results generated by NXEGS. The Monte Carlo results are typically accurate to within 2% of D_{max} or 2 mm of the measured data. As a quality assurance step, we have used the beam models resulting from commissioning to generate data for cases in which cutouts are placed in the applicator. We find that such results compare to measurement with a similar accuracy. We also attempt a preliminary determination of the "minimum" data set necessary for successful electron beam commissioning with NXEGS.

This work was partly supported by NX Medical Software, LLC and by a 2001-2002 Stanford University OTL Research Incentive Fund Award.

PO-T-269**Performance of Lattice- and Mesh-Based Tallies in MCNP and MCNPX Monte Carlo Codes**

M Kowalok*, R Jeraj, T Bohm, T Mackie, D Henderson, University of Wisconsin-Madison, Madison, WI

The MCNP Monte Carlo transport code is widely used in radiotherapy applications. A major drawback for its use in dose calculations, however, is a significant increase in run times for simulations requiring more than 10^3 scoring voxels. MCNPX is an extended version of MCNP that offers a mesh-based tally in addition to standard MCNP tallies. The mesh tally is independent of the problem geometry and provides several scoring options within uniform or non-uniformly-spaced grids. The aim of this work was to compare the MCNPX 2.4 mesh tally with the standard lattice tallies in

MCNP4c3. The test geometry consisted of a 5×5 cm² monodirectional 10MeV photon source centered above $20 \times 20 \times 20$ cm³ homogeneous and heterogeneous phantoms. To vary the size and number of scoring cells, the phantoms were segmented into different numbers of geometry and scoring voxels ranging from 1 to 10^6 . For this geometry, MCNP and MCNPX had similar performance for lattice-based tallies. The MCNPX mesh tally outperformed the lattice tally by factors of 10 and 1000 for 10^3 and 10^5 scoring cells, respectively. In addition, 10^6 voxels was found to be prohibitively large for lattice-type, but not for mesh-type tallies. Lattice-based and mesh-based energy deposition tallies closely matched. The level of agreement between lattice based kerma tallies and track-averaged dose deposition mesh tallies depended on the conversion factors used. In conclusion, the new MCNPX mesh tally enables efficient and accurate dose calculation in simulations requiring up to 10^5 scoring voxels.

PO-T-270**A Robust Instantiation Method for the Commissioning Process of the PEREGRINE Code**

Daryoush Sheikh-Bagheri*, NOMOS Corporation, Cranberry Twp., PA

The commissioning process of a MC code typically involves derivation of some simulation parameters from dose measurements. The PEREGRINE code¹ matches the individual energy of a specific linac by using a measured depth dose through a simple instantiation process. The pre-made PEREGRINE model of the linac, used in the instantiation, consists of a set of correlated histograms for a series of energies (e.g., 5.0, 5.5, 6.0, 6.5, 7.0 for a 6 MV model) calculated by a detailed modeling of the fixed components of the linac. For each set a depth dose is calculated for a 10×10 field and the fall-off region parametrized using an exponential fit with an S3 fit parameter. The incident electron energy is derived by comparison of the S3 value of the measured depth dose to those corresponding to the set. In this work we propose an alternative to the S3 instantiation method, called the ratio method, where the calculated depth dose curves for each of the energies are divided by the one corresponding to the median energy and the slope of the linear portion used for instantiation. We compare the instantiated energies of the ratio method to the S3 method for a variety of energies and linacs and discuss the robustness of the ratio method.

Supported by NOMOS Corporation, www.nomos.com

¹ "Description and dosimetric verification of the PEREGRINE Monte Carlo dose calculation system for photon beams incident on a water phantom" C. L. Hartmann Siantar, et al., Med. Phys. 28 (7), July 2001

PO-T-271**Calculation of the Depth Dose Curves and Output Factors for Small Electron Fields**

S J Weston*, J Smith*, W G Pitchford *, N MacDougall*, (1) Yorkshire Centre for Clinical Oncology, Leeds Teaching Hospitals Trust, Leeds UK, (2) Lincoln County Hospital, Lincoln, UK, (3) Guys and St. Thomas's Hospital, London, UK

The multiple scattering of electrons in tissue complicates the dosimetry of high-energy electron beams. There are no algorithms available that can calculate an electron dose distribution accurately and efficiently. In order to use electron beams clinically it is necessary to determine the central axis percentage depth dose (CAPDD) and the output factor (EOF) relative to a reference field size. The shape of the CAPDD curve and the EOF are highly dependent upon the beam energy and the electron field size. The EOF and CAPDD for common field sizes are measured during the linac commissioning process, however irregular field shapes require the measurement of the CAPDD and the EOF before the treatment can be prescribed.

A model based upon the lateral build-up ratio (LBR) of the electron pencil beam kernel has been proposed (Khan et al, PMB 1998 Oct;43(10):2741-54.) and evaluated for a Varian Clinac. In this work the LBR method and a normalized depth dose sector integration (NDDSI) method of determining the EOF and CAPDD for an arbitrary electron field shape are evaluated for an Elekta Precise linac.

setting. No acute radiation-induced toxicity or new neurological deficits occurred during the follow-up period. Pain improved in all patients who were symptomatic prior to treatment. End-to-end tests have shown that the planned dose never deviated more than 5% from the measured dose. Film dose measurements in a phantom also demonstrated excellent agreement between the planned and measured isodose lines.

PO-T-292

Partial Blocking of Cones in Stereotactic Arc Therapy for Treatment of Small (about 1 Cm) Intra-Cranial Lesions; Dosimetric and Planning Aspects

J de Pooter*, M Essers, P Nowak, C de Pan, B Heijmen, P Levendag, ErasmusMC-Daniel, Rotterdam, NL

Stereotactic arc treatment of small intra-cranial lesions is usually performed with circular collimators (cones), resulting in spherically shaped treatment volumes, while often the target volume is non-spherical. Multiple isocenters improve dose conformation to the tumor, but also lead to large dose inhomogeneities. Therefore, using Radionics equipment, cones > 2cm can be partially blocked with the linac jaws, resulting in more homogeneous target doses. Partial blocking would also be advantageous for smaller lesions, irradiated with cones having a diameter of 1 cm or larger, with block positions from 0.3 cm from the central beam axis. A crucial prerequisite for using such small field sizes is the reproducibility in jaw positioning, which turned out to be 0.3 mm (1 SD) for our Varian Clinac 2300 C/D machine, resulting in a dose delivery reproducibility on the central beam axis within 0.8 % (1 SD). Furthermore, an accurate dose calculation algorithm is required. It turned out that the Radionics XKnife algorithm is critically dependent on the used penumbra fit. The agreement could be improved from a maximum deviation of 12% to 3% for all situations by using a deconvolved penumbra. Planning studies have shown that partial cone blocking indeed results in improved dose distributions for small elongated tumor sizes, such as schwannomas and uveal melanomas. The dose to critical structures such as the chiasm and brain stem (schwannomas) and the lacrimal gland (uveal melanoma) could be reduced considerably.

PO-T-293

Absolute Dosimetric Verification of 3d Dose Distributions in Radiosurgery Using Bang Gel

S Scheib*, Y Schenkels, S Gianolini¹, (1) Klinik Im Park, Zurich, Switzerland, (2) Federal Institute of Technology, Zurich, Switzerland

For absolute dosimetric 3D dose verifications in radiosurgery using the Gamma Knife B commercially available BANG Gels (BANG 25 Gy and BANG 3 Gy) have been chosen. For these two polymer gels the linear dose - R2 relation ship has been measured using a clinical 1.5 MR scanner. The imaging parameter of the Hahn spin echo pulse sequence used (TR, TE, NEX, slice thickness, in plane resolution) have been varied in order to maximize the signal to noise ratio and therefore minimize the statistical uncertainty in the measured R2 values, for the purpose of a about 1 mm isotropic resolution in 3d. The influence of dose rate, ambient light exposure, fractionated irradiation, scan temperature and aging has been studied for both gel types. The linear dose - R2 relation ship varies strongly with gel temperature during scanning. The dose response curve gets steeper with decreasing temperature. It gets also steeper when analyzed at an increasing time delay after irradiation. In order to compare measured and calculated dose distributions, systematic errors due to susceptibility artifacts and statistical errors in the measured R2-values have been taken into account. Dose profiles (1D), isodose plots (2D), differential dose volume histograms (3D) and correlation values between measured and calculated dose distributions in radiosurgery are used to quantify the conformity. Using appropriate imaging parameter and experimental procedure, a dose uncertainty of 5 % (1 standard deviation) can be obtained together with an isotropic geometrical resolution of about 1 mm.

PO-T-294

Polymer Gels for NMR Imaging Manufactured in Normal Atmosphere

S Scheib*, W Vogelsanger², (1) Klinik Im Park, Zurich, Switzerland, (2) Kantonsschule Schaffhausen, Schaffhausen, Switzerland

Polymer based dosimetry gels, which change their NMR properties when irradiated, usually have to be manufactured in hypoxic conditions.

Recently, the formulation for a new polymer gel, which is made under normal atmospheric conditions, has been published. We produced and characterized this new gel. The gel, named MAGIC, is made of water, hydroquinone (18 mM), Methacrylic (9 %) and Ascorbic (2 mM) acid in Gelatin (8 %), Initiated by Copper ($\text{CuSO}_4 \cdot 5\text{H}_2\text{O}$, $8 \cdot 10^{-2}$ mM). Several gel batches have been produced with different amounts of methacrylic acid, ascorbic acid, $\text{CuSO}_4 \cdot 5\text{H}_2\text{O}$ and hydroquinone and dose response curves were measured. The relaxation rate R_2 varies linearly with absorbed dose and is calculated using spin echo ($\text{TR} = 1000$ ms, $\text{TE} = 10$ to 100 ms) images on a clinical 1.5 T MR scanner. Additionally the temperature dependence of the measured R_2 values and aging effects of the gel has been studied. Finally a 3D dose verification in radiosurgery using the Gamma Knife B was accomplished. Dependent on the chemical composition, the dose response curves were linear up to a dose of 50 Gy. The error (5 %) in R_2 (range: $3 - 55 \text{ s}^{-1}$) increases with increasing dose. The slope of the curves varies between 0.79 and $0.95 (\text{Gy s})^{-1}$, the intercept between 3 and 4 s^{-1} . Like other polymer gels, the measured R_2 values are strongly temperature dependent. In order to use these gels for absolute dose verifications the post irradiation changes of the R_2 values have to be considered.

PO-T-295

Quality Assurance in Stereotactic Radiosurgery (QUASIR)

A Mack¹, S Scheib*, D Weltz¹, H Czempel¹, H-J Kreiner¹, G Mack³, (1) Gamma Knife Zentrum Frankfurt, Frankfurt, Germany, (2) Klinik Im Park, Zurich, Switzerland, (3) PTGR GmbH, Tübingen, Germany

A quality assurance system has been developed for stereotactic radiosurgery and radiotherapy, to fulfill three goals: First to evaluate the geometrical error within imaging, second to simulate the complete chain of a treatment beginning with the imaging and ending with the application of dose and third to verify calculated dose distributions in three dimensions with high spatial resolution and accuracy. A water filled cylindrical imaging phantom has been manufactured in which equally spaced rods are placed. It can be mounted in a stereotactic frame in different orientations to be imaged using CT and MRI. The distances of the rod positions are analyzed and a reference grid can be positioned in order to calculate displacement vectors. To measure 2D dose distributions a drum scanner has been investigated and modified. The spectral emission of the light and the filters together with the efficiency of the red CCD channel were matched and balanced with the absorption spectra of the radiochromic film used. Software has been designed for evaluating the film data, for calibration, and for correction of temperature and darkening. A stack of films can be used to verify calculated dose distributions within an accuracy of up to 3 % (double irradiation technique) and resolutions down to $\sim 1/100$ mm in film plane. A spherical phantom with shells of different tissue equivalent materials and inserts for measurements using different detectors has been developed to simulate complex treatment situations within the human skull, which allows the complete simulation of the patient's treatment.

PO-T-296

A Comparative Dosimetric Study of CyberKnife Stereotactic Radiosurgery System and Intensity Modulated Radiation Therapy (IMRT) for Localized Cancers in the Head and Neck

Y Song*, A Ho, T Pawlicki, A Lo, Stanford University School of Medicine, Stanford, CA

Radiotherapy is one of the major treatment modalities for head and neck tumors. Unfortunately, because of the target's proximity to many critical structures, such as the brainstem, auditory apparatus, spinal cord, optical nerves, and the lenses of the eyes, conventional external beam radiotherapy is not able to deliver sufficiently high doses to the targets. In this study, we investigated treating head and neck tumors using CyberKnife Stereotactic Radiosurgery System and compared CyberKnife plans with corresponding IMRT plans in terms of target dose coverage and normal tissue sparing.

CyberKnife plans were created using CyberKnife On-Target Treatment Planning System (Accuray Inc., Sunnyvale, California). All CyberKnife plans employed the non-isocentric technique and were optimized using a linear programming technique. Each plan was treated with a 6 MV photon beam and a 15 mm diameter collimator and delivered in a step-and-shoot fashion with an image-guided system. The corresponding IMRT plans using eight coplanar beams (15° , 30° , 60° , 148° , 180° , 230° , 255° , and 345°) and 1 cm MLC leaves were computed using CORVUS treatment planning

system (NOMOS Corp, Sewickley, Pennsylvania). For both CyberKnife and IMRT plans, the target and the maximum doses were 20.00 and 26.32 Gy, respectively. All isodose plans were normalized to 76% of the maximum dose. Our data showed that CyberKnife plans provided a better target dose coverage compared with corresponding photon beam IMRT plans. It offered a similar protection to the critical structures. Additionally, because of highly collimated beams used, CyberKnife plans showed a better normal tissue sparing capability.

PO-T-297

An Analytical Approach to Prevent Gantry-Couch Collision for Linac-Based Radiosurgery

C Hua*, J Chang, K Yenice, H Amols, Memorial Sloan-Kettering Cancer Center, New York, NY

Gantry-couch collision is a serious concern for the treatment planning of the linac-based stereotactic radiosurgery (SRS). The ability to detect collision at the planning time removes the need for backup plans and preserves the useful beam angles that would be deemed unsafe and discarded otherwise. Most collision-detection schemes guard only against the most apparent collisions. A fool-proof collision-map requires detailed measurement of machine geometry and complex graphic operations. In this study, we propose a simple analytical method for collision detection using machine-specific data. Gantry and couch parts are modeled as cubic or cylindrical objects, which are geometrically defined by the coordinates of eight corners for cubic objects, and by five parameters for cylindrical objects. The collision problem is mathematically solved by determining whether any physical dimensions of the couch and gantry approach each other closer than an allowed limit. A computer code was implemented and tested on a Varian Clinac 600C linac equipped with a BrainLab micro-MLC. The coordinates of couch and collimator objects were first measured at the origin of the patient BRW coordinate system. They were subsequently translated and rotated to study the clearance of various beam arrangements. The predicted collision schemes were verified at the machine. Our method correctly predicted the collision map for a retrospective study of ten previously-treated SRS plans. It also accurately predicted the collisions for all five artificially created setup conditions. In conclusion, we have developed an analytical method for SRS collision detection that is easy to implement, computationally inexpensive, and accurate.

Energy and Intensity Modulated Electron Radiotherapy: A Comparative Dosimetric Study of MERT and IMRT for Head & Neck Cancer

Y. Song, M. C. Lee, and A. L. Boyer

Department of Radiation Oncology, Stanford University School of Medicine, Stanford, CA

In this study, we investigated treating head and neck cancers using modulated electron radiation therapy (MERT) by comparing MERT plans with x-ray intensity-modulated radiation therapy (IMRT) plans in terms of target coverage and normal tissue sparing.

An experimental electron multi-leaf collimator was fabricated by modifying a conventional electron cone (Varian Medical Systems, Palo Alto, CA). Electron beams produced by a medical linear accelerator (Clinac 2100C, Varian Medical Systems) and collimated by this electron MLC were simulated using the EGS4/BEAM code. The simulations were based on the manufacturer's specifications of the beam production system and the electron cone design. The MERT plans with three coplanar beams (205^0 , 235^0 , and 255^0) and five nominal energies (6, 9, 12, 16, 20 MeV) were created using a modified EGS4/MCDOSE system. The doses were checked against another Monte Carlo simulation (NXEGS, Numerix, New York, New York) and measurements. The IMRT plans with five coplanar beams (0^0 , 205^0 , 235^0 , 270^0 , and 320^0) were computed using a commercial treatment planning system (CORVUS, NOMOS Corp, Sewickley, Pennsylvania). In both cases, the prescribed dose to the target was 50 Gy.

Our preliminary data indicated that MERT is able to provide similar target dose coverage compared with photon beam IMRT. However, MERT can significantly reduce the dose to the critical structures. In the cases we studied, the maximum dose to the orbits, brainstem, optic chiasm, and spinal cord were reduced by 3.0, 16.2, 11.5, and 19.6 Gy, respectively, suggesting a distinct normal tissue sparing advantage for MERT.

Energy and Intensity Modulated Electron Radiotherapy: A Comparative Dosimetric Study of MERT and IMRT for Head & Neck Cancer

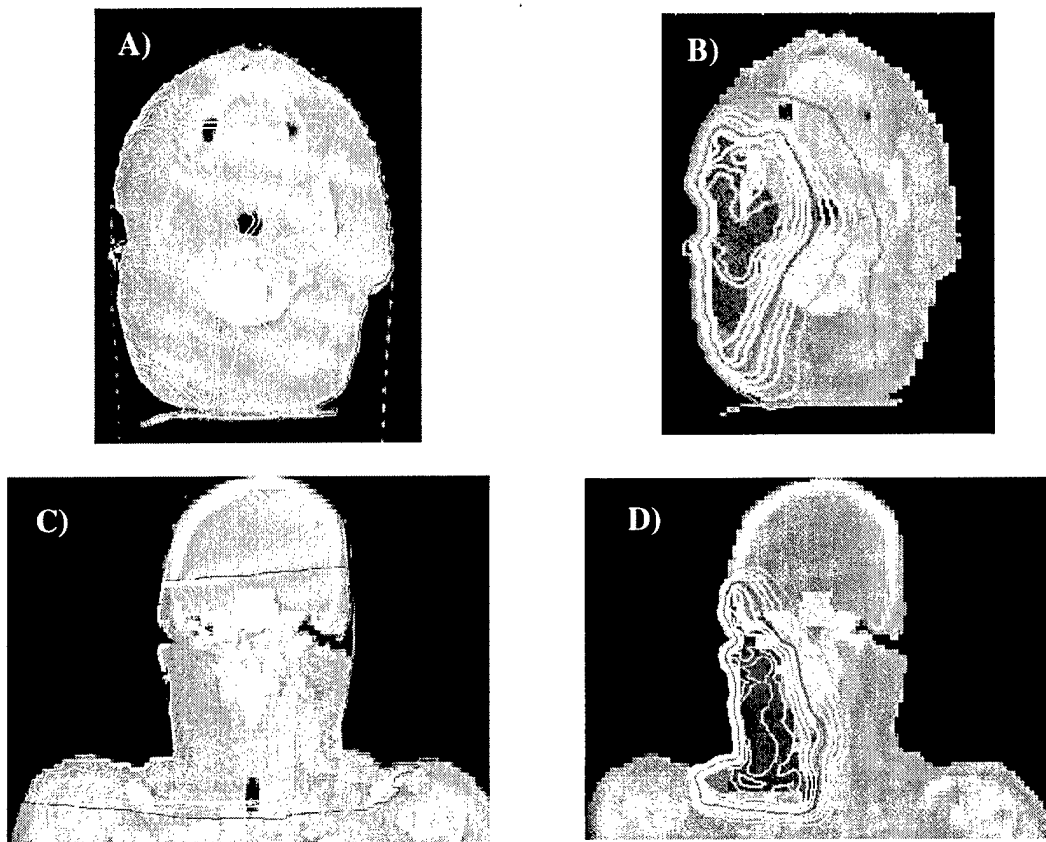
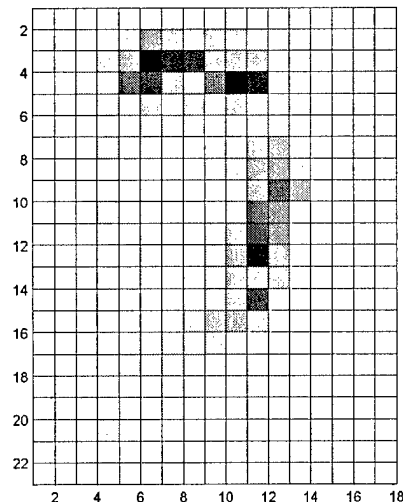


Figure 1. Comparison of dose distributions between the x-ray IMRT plan (A, C) and the MERT plan (B, D). The IMRT plan was computed using NOMOS CORVUS treatment planning system with five coplanar 4 MV beams. The MERT plan was computed using the modified EGS4/MCDOSE system with three coplanar beams (205° , 235° , and 255°), with each beam being energy and intensity modulated. The final MERT dose distribution was computed based on 15 intensity maps reconstructed from corresponding 15 leaf sequences. The beamlet size is 1x1 cm for both plans. The isodose curves, normalized to 55 Gy, represent 10, 20, 30, 40, 50, 60, 70, 80, 90, and 100%, respectively. As shown here, the MERT plan offers at least similar or better target dose coverage and uniformity.

Figure 2. A representative MERT intensity map. The intensity map was generated with a 205° gantry angle and a 20 MeV electron beam. For this particular map, five different intensity levels were used, with darker beamlets indicating a higher intensity level.



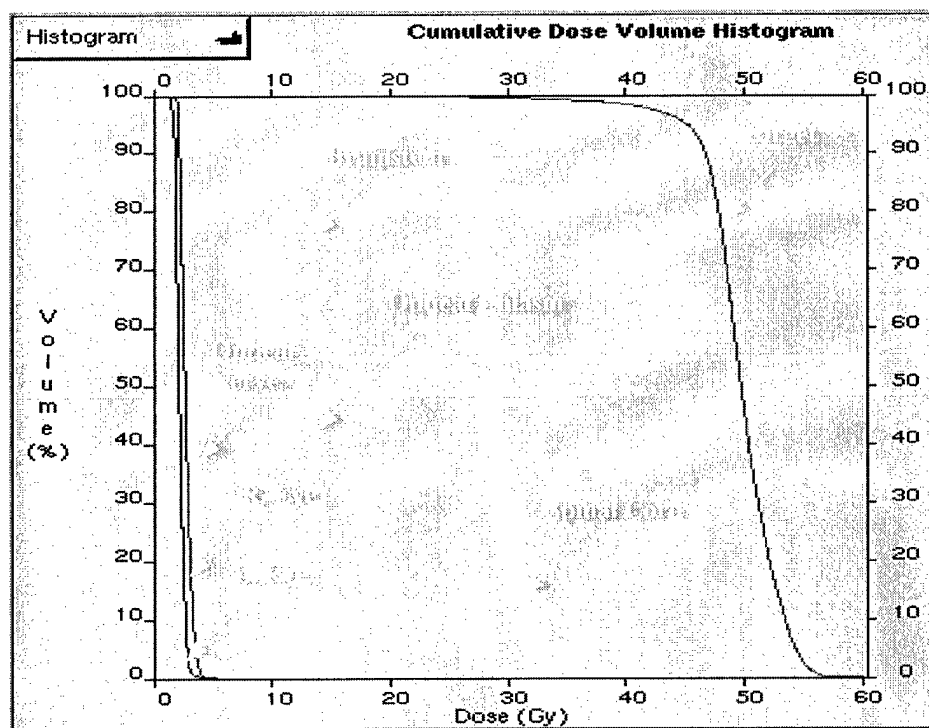
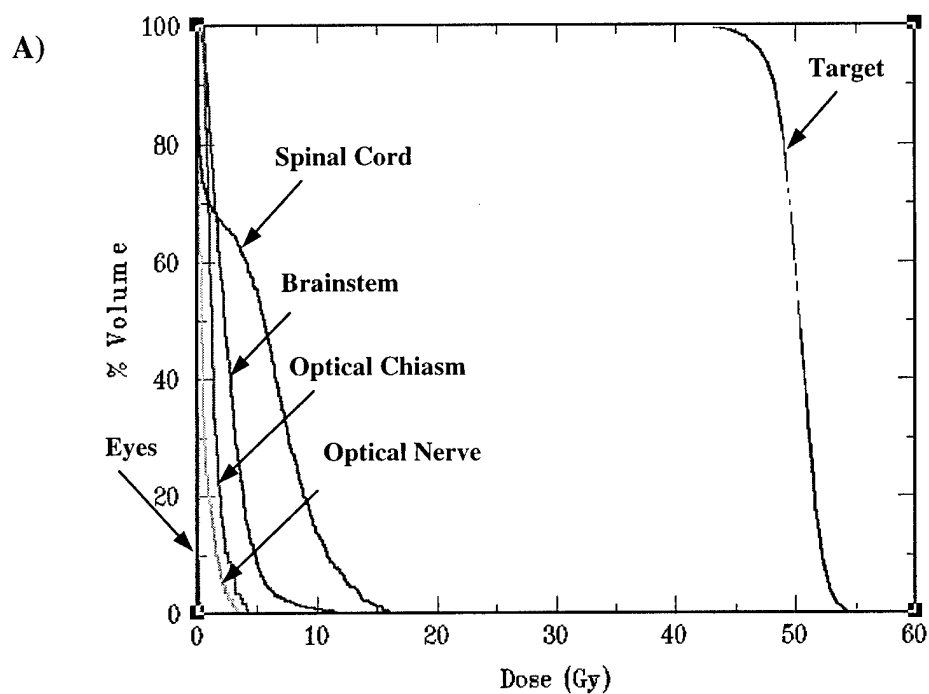


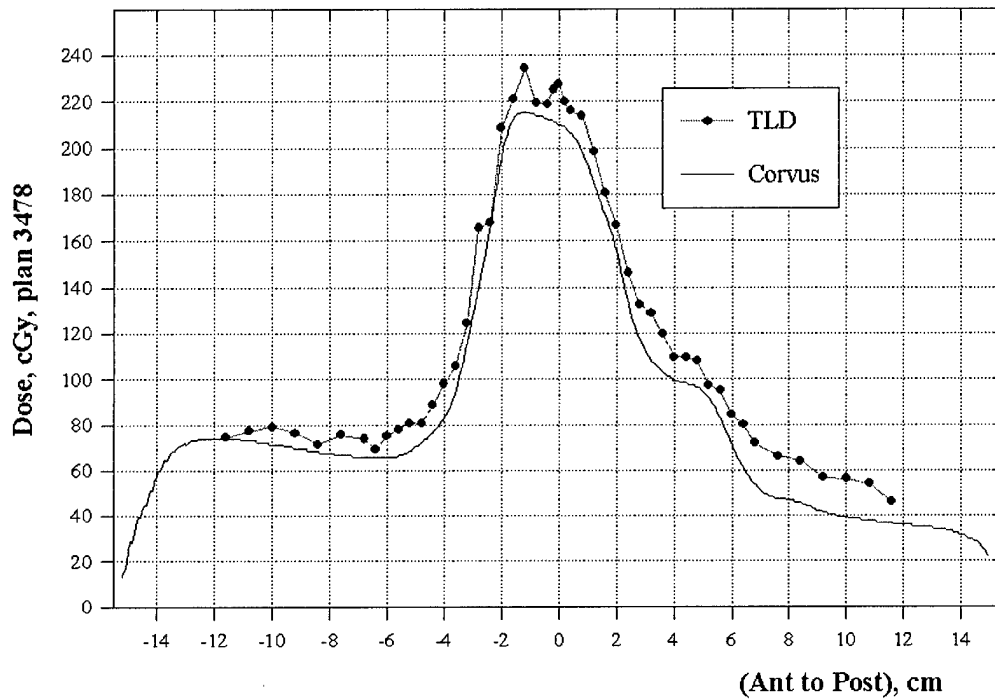
Figure 3. Comparison of dose volume histograms (DVH) for a representative head and neck case. **A)** DVH of the MERT plan. **B)** DVH of the corresponding IMRT plan. Clearly, the MERT plan shows superior normal tissue sparing.

AbstractID: 8116 Title: TLD measurement system for comprehensive dosimetric quality assurance in IMRT

TLD measurement system for comprehensive dosimetric quality assurance in IMRT

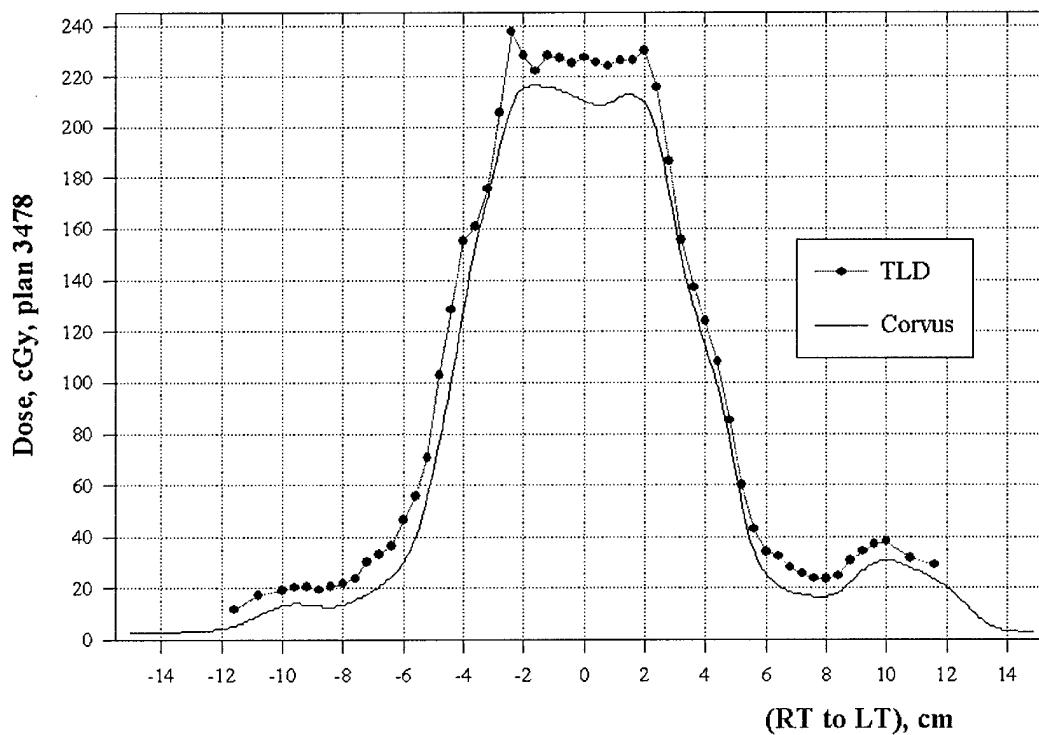
Intensity-modulated radiotherapy (IMRT) provides a technique for improving dose distributions by using inverse planning computer treatment plan optimization and computer-controlled dynamic delivery of complex planned intensity distributions. IMRT places unique demands on capabilities of treatment planning and delivery systems, strongly suggesting a need for a method of systematic quality assurance that includes detailed testing and verification of dose delivery. A multi-slab Plastic Water™ phantom was constructed to accommodate measurement in different planes of 2-D dose distributions from complete IMRT treatment plans with millimeter resolution, using 1-mm thermoluminescent dosimeter (TLD) cubes. The phantom can accommodate single-point ionization chamber measurement as well. The 30 x 30 cm axial cross section phantom was imaged with 1.5-mm spacing between CT slices, and the data set exported to a commercial IMRT treatment planning system (Corvus™) with an accompanying DICOM structure of idealized 30 x 30 axial contours to represent idealized surface anatomy. The planning system assigned the phantom a bulk density of that of water. Using Corvus utilities, clinical patient treatment plans were calculated as though they were applied to the slab phantom unchanged. Numerical data was extracted in matrix form from axial plane dose computation files by following a procedure documented by the manufacturer to convert dose images to 'tif' format, and a utility available within MATLAB™ software to interpret these files. Results were compared with TLD measurements. Initial data show general agreement of the shape of the calculated dose distributions, but with systematic relative deviations appearing in the lower-dose regions.

Dose profile: TLD vs. corvus, 15X, A-P, (avg 2 meas.)



Small-field plan, 15X

Dose profile: TLD vs. corvus, 15X, RT-LT.(avg 2 meas.)



Sweeping Window Arc Therapy (SWAT)

Arthur L. Boyer, Yulin Song, David Yong, Lei Xing
Stanford University
Stanford, California

Abstract

A novel variant of intensity-modulated radiation therapy is proposed in which the dose distribution is delivered with a single rotation of the accelerator gantry while multi-leaf collimator leaves modulate the x-ray beam. The leaves move along horizontal leaf tracks parallel to the axis of rotation of the gantry. The leaf sequence is derived from an initial leaf sequence produced by sweeping windows that lead to all voxels in the target volume being alternately irradiated at some gantry angles and then shielded from the parallel-opposed gantry angles. The result is a uniform irradiation of the target volume identical to that delivered by the classical Takahashi arc, but employing twice as many monitor units. This sequence was used to initiate an optimization algorithm that sought to minimize a traditional cost function by testing variations from the initial sweeping window sequence. An overshoot of a leaf beyond the initial window boundary can be used to produce regions where dose is reduced to spare a structure. An undershoot of a leaf back from the initial window boundary can be used to produce a region of additional dose to compensate for the target dose inhomogeneity produced by shielding. Prototype optimization codes were used to test the procedure for three-dimensional target volumes and adjacent organs-at-risk structures. The results with these simple preliminary tests approached the results of more sophisticated fixed-gantry intensity-modulated radiation therapy calculations. The delivery sequences have been verified by film dosimetry using a computer-controlled linear accelerator equipped with a multi-leaf collimator.

Comparison of Takahashi arcs with current IMRT techniques.

Arcs with a micro-MLC.

Experience with commercially available treatment planning systems indicates that continuous arcs with intensity modulation should be investigated further. Implementation of the Takahashi arc technique has been promising. Quite excellent results can be achieved with commercially available MLCs. The example in Figure 1 was delivered with a MLC with leaves that project to 3mm at isocenter (Xia et.al., 1999). The conformation of the isodose curves to the butterfly-shaped Gadolinium enhanced lesion can be appreciated. This case was treated using a computer-controlled MLC (MM3, Brainlab GbH, Munich, Germany). An "inverse treatment planning" algorithm is available with this commercial system that provides some normal structure sparing over the arc. We compared the results of the Brainlab inverse planning algorithm with stereotactic treatments planned with circularly collimated fields produced by cones on a robotic linear accelerator (Cyberknife, Accuray Inc., Sunnyvale, California). We used three clinical cases that had been treated with the Cyberknife and recomputed the treatment plans using the Brainlab inverse planning software. The stereotactic technique used three to five coronal arcs delivered in a step-and-shoot fashion by the Cyberknife robotic delivery system. Continuous arcs were mimicked by the use of 100-200 individual beams all using the same circular collimation. The MLC treatments were not delivered, but were only calculated for purposes of comparison. Four cases were studied. The MLC-collimated strategy were found to be superior to the circularly collimated strategy. In this study we found that IMRT was more conformal in 3 of the 4 cases



Figure 1. Sagittal view of brain tumor treated with Takahashi arcs implemented with a mini-MLC.

studied - depending on the priority given to normal structures. In addition, IMRT plans achieved superior sparing of organs at risk in 5 of 7 structures that were analyzed in the study. The MLC inverse planning in the Brainlab system is heuristic and attempts to minimize the dose to normal structures by shielding the normal structure projections over portions of the arcs. The algorithm allows the user to weight the amount of shielding to either fully protect the normal structure (similar to shielding the central structure in the Figure 1) or to maximizing the dose uniformity to the target volume. The results suggest that some extension of the Takahashi arc technique to intensity modulation during the arc can produce dose distributions superior to arcing alone. The problem is to determine the sequence of leaf settings over the course of the arc that will provide for the most uniform treatment of the tumor volume while achieving acceptable sparing of the normal structure. The selection of these leaf settings must be such that it can be done automatically by a computer in one to ten minutes for a particular case with a minimum of selection of parameters by the operator.

Comparisons of Takahashi arcs with current IMRT

We have studied the selection of the leaf settings manually using a conventional three-dimensional treatment planning system (Focus, Computerized Medical Systems, St. Louis, Missouri). We used prostate treatments that were currently being planned by another commercial IMRT treatment planning system (Corvus, NOMOS Corporation, Sewickley, Pennsylvania). These cases were chosen because a large volume of bowel was included in the plan. Continuous arcs were computed with the MLC field shapes selected manually to optimize the DVHs by trial and error. This was a relatively labor-intensive exercise, but it yielded interesting results. A characteristic example is shown as a DVH in Figure 2 to the right. The DVH curves for the prostate are nearly identical. The arc DVH for the bladder is significantly lower than the IMRT DVH curve for the same maximum dose, but the modified Takahashi arc curve is always significantly lower than the IMRT curve. The same pattern is observed for the bowel curve. If these results can be obtained with intuitive guesses of leaf trajectories and aperture patterns, then there is strong reason to expect that there are algorithmic processes that can lead to similar and superior results.

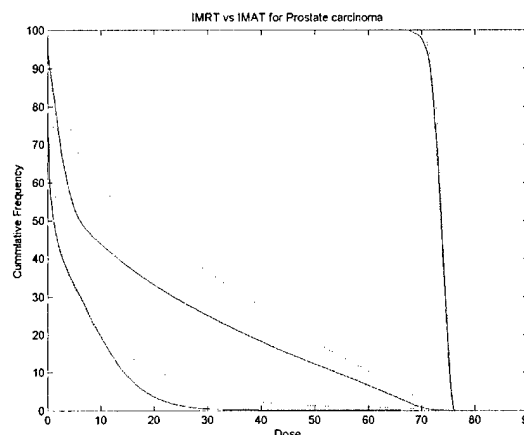


Figure 2. Comparison of a plan using manual quasi-Takahashi cone-beam arcs with fixed-gantry IMRT treatment plans. The arced plan is plotted with thick lines, and IMRT plan is plotted with thin lines.

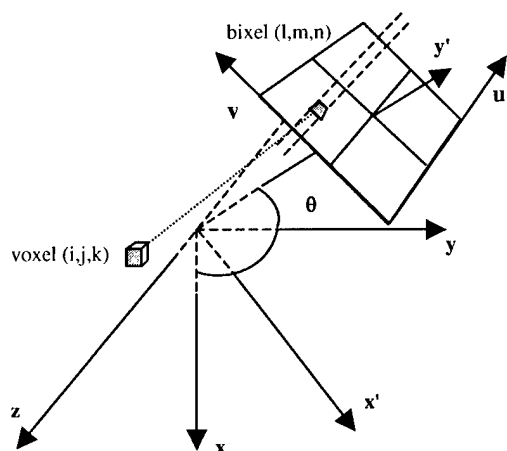


Figure 3. Illustration of the orientation of the MLC leaves and the coordinate system used in this discussion. Parallel dashed lines indicate a leaf track.

Arc therapy with a dynamic MLC.

Technical potentials.

There are installed software packages and hardware components capable of delivering exposures with a computer-controlled linear accelerator during gantry rotation while moving the MLC leaves in a prescribed fashion. The MLC leaf positions are specified in a computer file written in an ASCII format. The control system reliably interprets the file and moves the gantry and leaves accordingly. Software is available to simulate the sequence on a PC before applying it on the linear accelerator. The files consist of a series of aperture specifications at sequential gantry angles. The motion of the leaves is linear between aperture specifications at the selected number of gantry angles. The number of gantry angles used can easily be set to specify apertures every 5° to every 10°. We have developed algorithms to write the leaf-sequence files required by the control system and have demonstrated that our

specifications are delivered. We can fix the collimator such that either the leaves move in a direction parallel to the direction of rotation (between x-y planes in Figure 3) or in a direction parallel to the axis of rotation (parallel to the z-axis in Figure 3). The gantry can rotate slowly as the sequence is delivered providing for delivery times of one to five minutes. The maximum size of the leaf sequence is not a practical technical limitation. The

leaves move at a maximum velocity of 2cm/sec. This technical capability has not been investigated intensely as a means of delivering IMRT with multiple fixed gantry fields.

At a given gantry angle θ the MLC will form a window using a series of gaps between the opposing leaves along each track. A track centered at coordinate v in Figure 4 creates a gap from position u_m^A for what will be the a-leaf extending into the field from the patient's inferior to position u_m^B for the b-leaf extending into the field from the patient's superior. This forms a single gap of width $W_m(\theta)$ centered about a point at $u = M_m(\theta)$ as depicted in Figure 4. The bixel at (l,m) in Figure 3 either passes full fluence to voxels in the treatment field, such as the voxel (i,j,k) in Figure 3, or the fluence is attenuated by the leaf depending on whether the bixel falls within the gap.

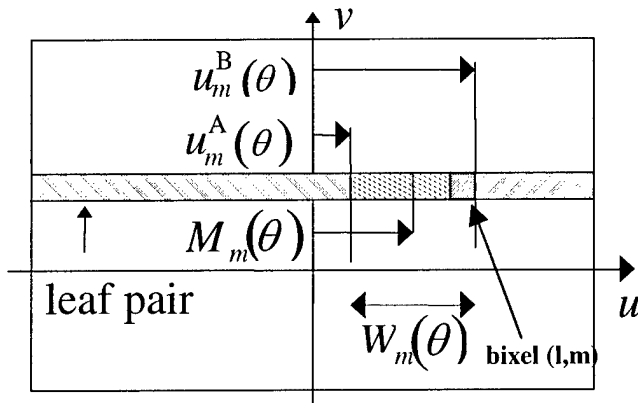


Figure 4. Representation of a single gap between opposed MLC leaves $W_m(\theta)$ is the width of the gap.

Sweeping arc.

We investigated leaf sequence optimizations that began with a leaf sequence that delivered dose to a volume while the leaves formed a window that swept across the target volume as the gantry rotated. A Takahasi arc sets the leaves to conform to the projection of the target volume throughout the rotation. For a spherical target volume centered on the axis of rotation, the Takahasi arc technique would set the leaves to a fixed circle throughout the entire arc. The results of a Takahasi arc are a nearly uniform dose in the circle and a cylindrically symmetric skirt of dose outside the target.

However, one can also achieve a uniform dose to the target volume using a sweeping window that can be described with the aid of Figure 5. This figure represents schematically the positions of complimentary leaf tracks as a function of gantry angle. The position for some leaf track centered a distance $v(m)$ from the aperture center is given on the left panel for gantry angles from 0° to 180° . The positions for the complimentary leaf track at $v(m_c)$ is shown in the right panel for the parallel-opposed gantry angles between 180° and 360° . The index of the complimentary leaf track is calculated by $m_c = m_{max} - m + 1$ where m_{max} is the maximum number of leaf tracks. In the left panel the right most leaf (let us assume it is the superior leaf of a pair) tracks the superior projection of

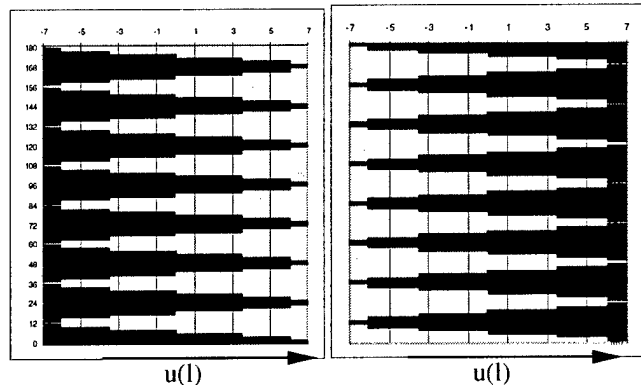


Figure 5. Dark areas represent relative extension of the leaves between the superior and inferior margins of the target volume. Left column represents gantry angles between 0° (bottom) and 180° (top). Right column represents the parallel opposed angles.

the target volume for the first 180° of gantry rotation (note that 0° is at the bottom of the column and 180° is at the top). This is depicted as a straight line running along the right side of the left column in Figure 5. The left leaf (let us assume it is the inferior leaf of the same pair) starts extended entirely across the target volume. As the gantry rotates, the inferior leaf retracts to the inferior projection of the target volume and then sweeps back to meet the superior leaf at the superior projection. This pattern is repeated (seven and one-half times in Figure 5) until the gantry reaches the 180° angle where the sweeping leaf in is the retracted state. For the next 180° of

gantry rotation, the inferior leaf tracks the inferior projection of the target (depicted as the left straight vertical side of the right column in Figure 5) while the superior leaf executes the sweeping pattern, arriving at a fully extended condition at 360° . Inspection of the patterns in Figure 5 shows that the patterns complement one another. Attenuation of a voxel from one side is complemented by irradiation from the other. The result is a sum-zero deviation from uniform irradiation of the target volume. The total irradiation is reduced by one-half that of an open, unswept field delivered with the same number of monitor units. The advantage of this strategy is that it provides opportunities for the leaves to deviate from the sum-zero sweep in order to modulate the dose delivery over the arc. By deviating from the sum-zero pattern, the relative dose to portions of the target volume (or adjacent structures) can be increased or decreased.

Figure 6 contains the axial and sagittal plane films exposed by such a sweeping arc pattern. The circular target volume was uniformly irradiated while the leaves moved continuously during the arc in the manner of the

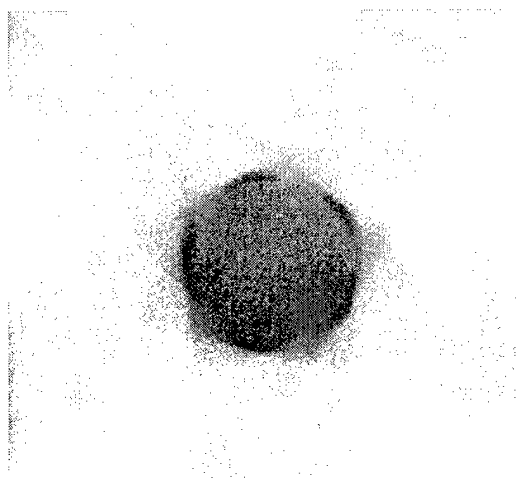


Figure 6a. Dose delivered by MLC leaves producing sweeping window in 360° arc in axial plane measured with film.

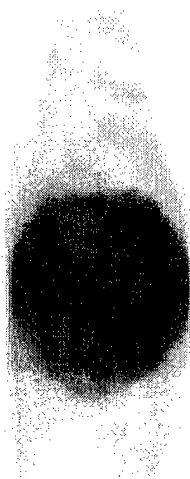


Figure 6b. Dose delivered by MLC leaves producing sweeping window in 360° arc in sagittal plane measured with film.

The transit dose outside the target volume is not uniform as is the case for a pure Takahashi arc, but contains a heterogeneous pattern with a number of arms determined by the frequency of the sweeping pattern over the gantry rotation (in this case five total sweeps). The sweeping window is proposed as the starting condition for the optimization process described in the next section.

Fast calculations using pointer arrays.

Pointer arrays for optimization. Preliminary investigations of optimization of continuous sweeping window arcs have used a calculation schema illustrated in Figure 7. The prototype calculations were based on a dose score array consisting of voxels, and a sequence of MLC windows as a function of gantry angle consisting of bixels. A voxels were defined as cubic volumes centered around the regularly-spaced calculation points. The voxels used in the prototype calculations were 5mm on a side. The bixels were defined as square areas bounded in one dimension by the leaf widths and bounded in the direction of travel of the leaves by an arbitrary step size. The calculations and measurements were carried using 5mm wide leaves and 5mm step sizes for 5mmx5mm bixels. The pointer arrays were a fast method of pointing between bixels and voxels. For a given gantry angle, each voxel was assigned one bixel by determining the bixel center most closely approached by the ray line from the voxel center to the radiation source. In the cases in which ray lines intersected bixel boundaries, a single bixel was arbitrarily

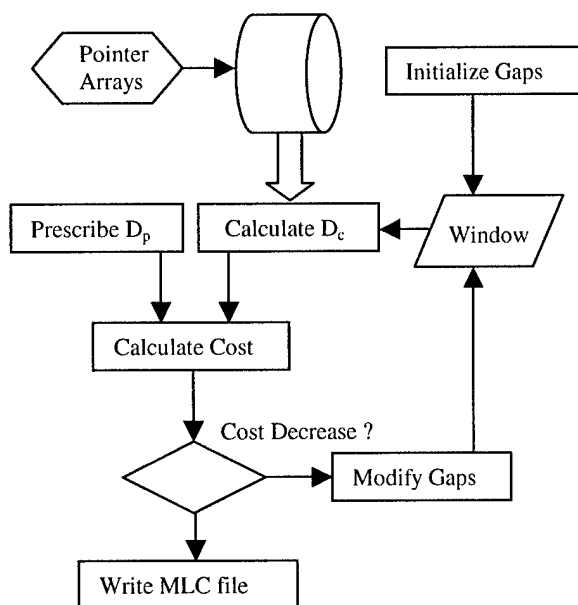


Figure 7. Diagram depicting modification of leaf sequence in Figure 5 by optimization using cost function.

assigned. The voxel-to-bixel integer pointers were computed once for the chosen array geometry and saved as a file. The size of the array was determined by the size of the calculation array (in these tests, a 32x32x32 element array representing a cube 16cm on a side), the maximum size of the MLC aperture considered (in these tests, a 46x46 element array representing a maximum window size of 23cmx23cm) and the number of gantry angles chosen (in these tests 36 gantry angles at every 10° of gantry angle). The voxel-to-bixel test array used for the preliminary tests required 6.87 MB of storage. The ray line passing through the center of a single bixel within the MLC space at a given gantry angle passes through a sequence of voxels. The previously defined voxel-to-bixel array was used to determine the sequence of voxels projected to the selected bixel. The number of voxels determined in this manner is maximal along a ray passing obliquely through the calculation matrix. This dimension of the bixel-to-voxel array was set at one and one-half times the dimension of the calculation array. The bixel-to-voxel array was computed for the geometry selected for the tests and saved as a 31.8 MB file. These array sizes are not a practical limitation for dose calculations. The three-dimensional dose and fluence arrays can themselves be represented as long vectors. This operation on the fluence is usually represented by the matrix symbolism as

$$\bar{D}_c = \bar{F} \cdot |H|$$

where $|H|$ is the matrix whose elements are zero if a bixel element does not contribute to the dose in the voxel element, and some ratio if the ray in \bar{F} strikes the voxel in the vector \bar{D}_c . The general form of the optimization scheme used in the initial tests is given in Figure xx. A prescribed dose distribution was determined for a target volume and limiting structures, represented by D_p in the schematic in Figure 7. An initial sequence of windows or apertures, defined by the MLC leaves, was selected, using the sweeping window approach. This is indicated by the "Initialize Gaps" box in Figure 7. Unattenuated fluence reaching the voxels was the zero-order surrogate for dose in these initial tests. A more accurate dose calculation is proposed for the investigations to be conducted during the funded research using Monte Carlo computations to determine the exact fluence-to-dose ratios that are the nonzero matrix elements of $|H|$. The computed surrogate dose, D_c in Figure 7, was used with the prescribed dose, D_p , to compute a least-squares cost value, $C = \sum_x \sum_y \sum_z |D_p(x, y, z) - D_c(x, y, z)|^2$. The

initial sweeping window gaps composing the elements of \bar{F} were then modified such that the cost value was reduced. Two strategies were tested in the preliminary tests to modify the gaps in the window sequence. One strategy was an *ad hoc* intuitive selection of gap changes. The other was an application of the Simplex technique. Once modified, the dose distribution and associated cost were recomputed to determine whether the modified windows produced a reduced cost. If the cost decreased, the modifications were accepted. Otherwise they were rejected and another set of modifications was chosen to be tested. Modifications for single gaps along each leaf track intersecting the projection of the target volume were tested in each cycle through this loop. Thus the dose was recalculated repeatedly, and required a fast assessment of the consequence of the gap modifications.

Test cases with *ad hoc* search. The results of this prototype calculation produced by the intuitive gap modification strategy are given in the following paragraph. Tests were carried out using artificial target structures and organ-at-risk structures. In the example given here the target volume was a 12-cm diameter sphere with a 5-cm diameter cylindrical structure embedded in its periphery. The initial zero-sum swept window pattern was modified to account for a sensitive structure by initially keeping it always shielded from every angle. Two strategies were tested in the preliminary tests to modify the gaps in the window sequence. One strategy was an *ad hoc* intuitive selection of gap changes tested within 7 bixels of the window track. The other was an application of the Simplex technique. Once modified, the fluence distribution and associated cost were recomputed to determine whether the modified windows produced a reduced cost. If the cost decreased, the modifications were accepted. Otherwise they were rejected and another set of modifications was tested.

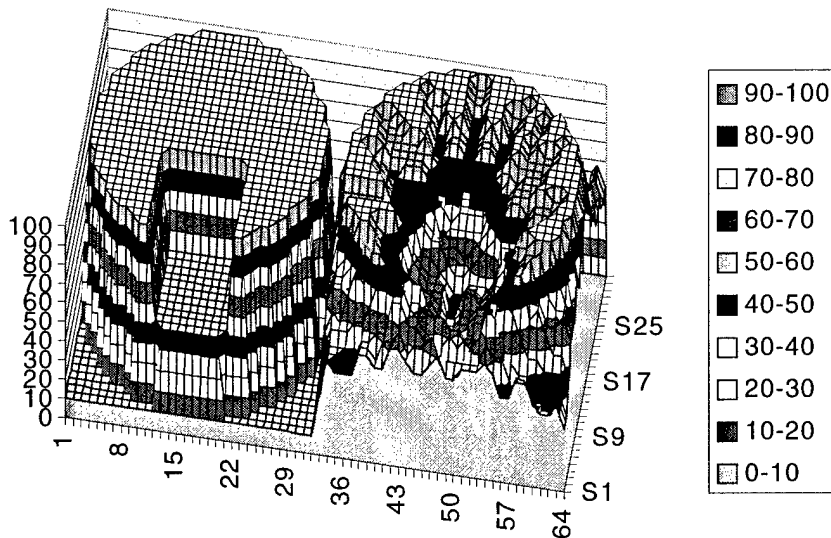


Figure 8. Comparison of the prescribed fluence (left) with the computed SWAT fluence (right).

The results of this prototype calculation produced by the intuitive gap modification strategy are given in Figure 8. The prescribed dose on the left consisted of a 12-cm diameter spherical target structures with a 5-cm diameter cylindrical critical structure embedded in its periphery. The dose constraint to the critical structure was 50%. An isometric three-dimensional plot of the final computed fluence in the central axial plane of the target volume is given the right side in Figure 8. The target volume had about 20% inhomogeneity, similar to what is achieved with fixed-gantry IMRT. The computed distribution was verified with film measurements.

SWAT Implementation

The goal of the investigation is to determine the best algorithm for computing the set of MLC leaf trajectories,

$$\begin{aligned} W_m(\theta) \quad m = 1, 2, \dots, m_{\max} \\ M_m(\theta) \end{aligned}$$

(see Figure 4) for a multileaf collimator with m_{\max} leaves as a function of the gantry angle θ in order to deliver a conformal radiation dose. These trajectories are to produce dose distributions that are equal to or superior to those that can be obtained by presently available commercial systems that use multiple fixed-gantry cone beam IMRT implemented with dynamic and step-and-shoot delivery techniques. The algorithms would be considered to be superior if dose distributions can be achieved that are equivalent to the fixed-gantry sweeping window approaches, but with a significantly shorter delivery time and a simplified planning process. A key element of this investigation is on the use of a sweeping window arc as the starting point of iterative searches. The motivation for this focus is the notion that such a sweeping window will achieve intensity modulation over the course of a single arc. The technique will therefore be referred to as a sweeping window arc therapy or SWAT. Preliminary investigations indicate that the approach has considerable potential, but the investigations detailed here are needed to clarify the practicality of implementation.

Refine computation of dose in the spatial domain using pointers.

Application of Monte Carlo techniques to dose calculation matrix. The computation of the three-dimensional dose distribution due to an arc pattern must be fast, but it must also be accurate. The symbolic representation of the dose calculation from the swept window sequence is

$$\bar{D}_c = \bar{F} \cdot |H|$$

where H is the matrix of ratios of dose to a voxel per fluence in a bixel. In the preliminary work, these elements were crudely approximated using a parallel ray approximation and neglecting both attenuation and scatter. The parallel-ray approximation can be easily removed by tracing rays along the slant lines given by

$$v = \frac{SAD(y \cos \theta - z \sin \theta)}{SAD - z \cos \theta - y \sin \theta}$$

$$u = \frac{xSAD}{SAD - z \cos \theta - y \sin \theta}$$

In addition, a number of better approximations can be made to improve the dosimetric accuracy of the computation. We propose to use Monte Carlo methods to compute the nonzero elements of the H matrix. Monte Carlo code has been developed at Stanford that can be easily adapted to carry out this part of the project. For a particular patient, the CT data of the patient in treatment position will be used to compute the matrix



Figure 9. Dose along the track of a single bixel ray computed by a Monte Carlo simulation illustrating accounting for both bone and air heterogeneities.

elements taking into account the attenuation up to each voxel and electron transport and scatter from the upstream voxels along the ray path from the bixel to the voxel. All voxels that receive a significant amount of scatter will be added to the list of voxels to which the pointer points. An example of this type of pencil beam Monte Carlo calculation is given in Figure 9. The time required to compute these matrix elements may seem excessive, but in fact it is not. Each element need only be calculated to a precision sufficient to give a cumulative precision when all elements are used in the summation. For example, a given voxel may require 2.5 million Monte Carlo histories to achieve a standard deviation of 2%. It would take an inordinately long time to run this many histories for each bixel in a sequence of 20 gantry angles. However, at each gantry angle, the voxel will be struck, so the number of histories required for each bixel is only about 250,000. The calculations will be carried out using a network of 20 dedicated Pentium PC computers at Stanford. The calculation will be run

in parallel on this cluster of computers such that the total calculation time will be further reduced by another order of magnitude. However, if a given bixel is struck only a few times, this line of reasoning does not apply and the accuracy may be compromised. It is difficult to predict without a systematic investigation of the process how difficult it will be to compute sufficiently accurate H -matrix elements.

Cost computation acceleration using limited spatial domain techniques.

We propose to accelerate the *dose* computation by using bixel-to-voxel pointers. As described in the Preliminary Studies section, bixel-to-voxel pointers are look-up tables that point from a given bixel within the aperture of the MLC at a given gantry angle to the voxels that lie on the ray line passing from the target, through the bixel, and on through the calculation array. The bixel-to-voxel pointer allows the effect of opening or closing a voxel to be propagated rapidly through the dose distribution. The time required to compute the *cost* can be reduced further with additional applications of the bixel-to-voxel pointers. The procedure is applied during the recalculation of the dose in the optimization iterations. This allows one to consider only those voxels in the dose array, D_c , that change because of a test modification of one segment of the window sequence. Using the bixel-to-voxel pointers, changes in a set of bixels in the sweeping window sequence will be related to a set of voxels $(i, j, k) \in \delta$. The cost function before making the change in window sequence will be calculated by

$$\text{cost}_{old} = \sum_{i,j,k \notin \delta} (D_p - D_c)^2 + \Delta_{old}(\delta)$$

where $\Delta_{old}(\delta) = \sum_{\delta} (D_p - D_{c-old})^2$. The second term can be separated from the summation as a consequence of the cost function being a simple linear summation of terms of cost, each term arising from an individual voxel. The cost after the trial change in the window sequence will be computed by

$$\text{cost}_{new} = \sum_{i,j,k \notin \delta} (D_p - D_c)^2 + \Delta_{new}(\delta)$$

where $\Delta_{new}(\delta) = \sum_{\delta} (D_p - D_{c-new})^2$. The majority of the terms in the overall cost are common to both calculations and need not be recomputed for each trial. The change in cost function can be computed directly as

$$\Delta \text{cost} = \text{cost}_{new} - \text{cost}_{old} = \Delta_{new}(\delta) - \Delta_{old}(\delta)$$

using only the computation of dose on those voxels in the set δ identified by the bixel-to-voxel pointer. In those iterations in which a change is accepted, the dose calculation array, D_c , will also need to be up-dated with the changes in dose due to the bixels in the set δ . This strategy will result in a considerable time-savings. However, the addition of scatter to the H-matrix may reduce this time-savings to an extent that is hard to predict without carrying out a thorough investigation. More importantly, the use of pointer arrays uses a considerable amount of memory. Unless the pointer arrays as well as the two dose arrays, D_p and D_c , are held in directly accessible memory, the calculation will not be as fast as possible. For example, if the operating system is allowed to start disk swapping the arrays during the calculation, the acceleration will be lost. These and other details of the implementation will need to be tested during the course of the investigation.

Develop and verify computation of dose using analytic functions in the frequency domain.

Another approach to increasing the speed of the dose calculation of arced fields is to use mathematical tools borrowed in part from imaging theory. This theory allows the representation of the dose distribution in the Fourier frequency domain. The representation of dose in the frequency domain is intimately related to the theory of image formation developed for CT, PET, and SPECT reconstruction algorithms. In what follows we outline the theory.

Theory of dose calculation using central slice theory.

Dose is related to incident fluence by the relation $D = (\mu_{en}/\rho) \Psi$ where (μ_{en}/ρ) is the energy absorption coefficient and $\Psi = (h\nu)\Phi$ is the energy fluence due to a photon particle fluence Φ carrying energy $(h\nu)$. The dose distribution can be calculated by attenuating an incident energy fluence Ψ_0 to a depth d and calculating the dose at that depth with the energy absorption coefficient, $D(x',d) = (\mu_{en}/\rho) \Psi_0(x')e^{-\mu d}$ where μ is the linear attenuation coefficient (Boyer and Mok, 1985). $P(x',\theta)$ is the dose profile at the axis of rotation along the x' axis rotated through an angle θ at $y' = 0$ in Figure 10. It can be shown (Bortfeld and Boyer, 1995) that the total dose delivered by a complete rotation of a beam can be calculated using

$$D(\vec{r}) = \int_{\theta=0}^{2\pi} D_{\theta}(\vec{r}') d\theta = \int_{\theta=0}^{2\pi} P(x',\theta) e^{-\mu x'} d\theta$$

where

$$P(x', \theta) = \frac{\mu_{en}}{\rho} \Psi_0(x', \theta) e^{+\mu z'_0}$$

is the beam profile associated with beam angle θ . Here we have written dose as if it were all deposited at the interaction point. This approximation neglects transport of dose in all directions by photons and electrons produced by the primary interaction. As this investigation continues, we will refine this approximation using rotation dose kernels (Desobry, 1991). The inverse treatment planning problem can be considered to be the inversion of this integral to calculate $P(x', \theta)$ for any dose distribution $D(\vec{r})$. The circular integral is formally an exponential back-projection followed by integration over the rotation angle θ . This process is used in image reconstruction in the context of the Radon transform. To apply image reconstruction theory to the dose calculation problem, consider the Fourier transform of the dose distribution

$$F(u, v) = \int_{-\infty}^{+\infty} \int_{-\infty}^{+\infty} D(x, y) e^{-2\pi i(xu + yv)} dx dy = \mathbf{F}_2 \{D(x, y)\}$$

The Fourier slice theorem provides a relationship between the two-dimensional Fourier transform of the dose distribution and the one-dimensional Fourier transform of a single profile,

$$S_\theta(u') = \int_{-\infty}^{+\infty} P(x', \theta) e^{-2\pi i u' x'} dx' = \mathbf{F}_1 \{P(x', \theta)\}$$

This is a single "slice" through the frequency domain distribution. The relationship can be expressed as

$$S_\theta(u') = F(\delta[u - u' \cos \theta], \delta[v - v' \sin \theta])$$

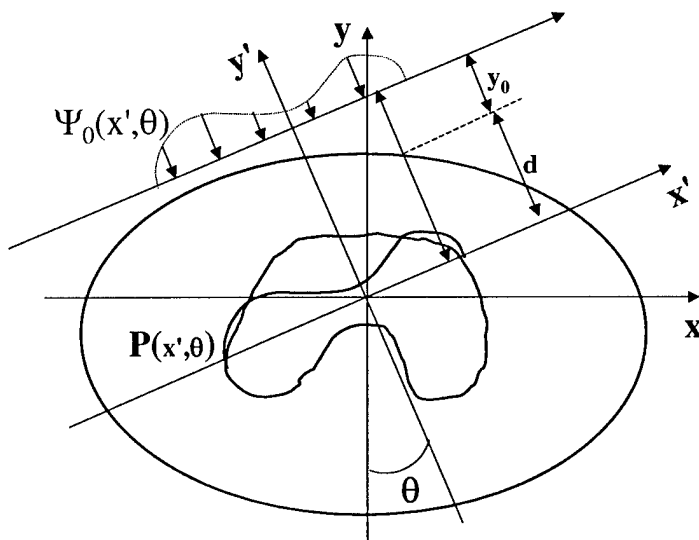


Figure 10. Geometry showing the calculation of dose using the exponential Radon transform.

One can formally construct the entire dose distribution from the one-dimensional Fourier transforms of the beam profiles. In diagnostic imaging, the Fourier slice theorem cannot be applied to image reconstruction because it is not feasible to interpolate from the polar coordinate system in which the single slices are computed to the rectilinear coordinate system in which the two-dimensional image is computed. However, we can compute the Fourier transform of the projection of the dose from a leaf gap using closed analytic functions.

Inverse transformation of analytic functions with the FFT. The proposed investigations will employ use of the inverse fast Fourier transform (IFFT) on data that has been calculated analytically. It is easy to transform real data

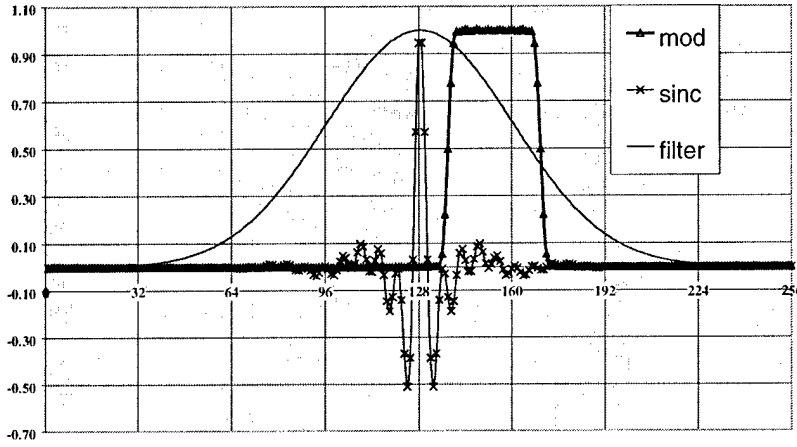


Figure 11. Demonstration of the formation of a square wave from an analytically calculated sinc function in the frequency domain.

from the spatial domain to the frequency domain and back again using a fast Fourier transform (FFT) algorithm followed by application of the complementary IFFT. In what is proposed here, the data will be computed analytically in the frequency domain *de novo*. It is essential that application of the IFFT to this computed data will yield the correct functional forms in the spatial domain. This section reports the demonstration of this capability by the investigators. The function of primary interest here is the rect function,

$$\Pi(x) = \frac{1+2x}{2|1+2x|} + \frac{1-2x}{2|1-2x|}$$

The function is a square-wave pulse of unit height and unit width. It has the property that $\Pi(x)=1$ when $|x| \leq 1/2$ and zero otherwise. Its Fourier transform is $\text{sinc}(x) = \sin(\pi x)/\pi x$. We are interested in using the rect function to represent the fluence produced by the gap between two MLC leaves. Consider a MLC leaf that projects to a width W_0 in the plane at isocenter. The m^{th} pair of leaves travel on a line offset from the field center a distance M_m^y . The fluence in this plane due to a gap between the m^{th} pair of leaves set to a width $W_m(\theta)$ can be expressed as

$$\Phi(x, y) = \int_{x'} \int_{y'} \Pi\left(\frac{x' - M_l(\theta) - x}{W_l(\theta)}\right) e^{-\frac{\pi}{2}\left(\frac{x'}{\sigma_x}\right)^2} \Pi\left(\frac{y' - M_l^y - y}{W_0}\right) e^{-\frac{\pi}{2}\left(\frac{y'}{\sigma_y}\right)^2} dx' dy'$$

where the Gaussian functions produce the penumbra due to a finite x-ray target size and leakage through the ends and sides of the leaves. This expression for $\Phi(x, y)$ is a convolution. It is composed of functions with known analytic Fourier transforms. Using the Fourier convolution theorem, the Fourier transform of the fluence can be written directly as

$$P(u, v) = W_l(\theta) \text{sinc}(W_l(\theta)) W_0(\theta) \text{sinc}(W_0(\theta)) e^{-2\pi i (u M_l(\theta) + v M_l^y)} e^{-2\pi (\sigma_x u^2 + \sigma_y v^2)}$$

Figure 11 is a demonstration of the proof of the principle that calculation of the sinc function analytically in the frequency domain yields, upon discrete Fourier transformation, the numerical values for the rect function in the spatial domain. The curve labeled sinc was calculated analytically for a pulse of width 32 using the expression for $P(u, v)$ given above. The offset was calculated as a complex exponential phase factor for a shift of 25 units. The real part of the frequency domain labeled sinc in Figure 11 demonstrates the modulation of the sinc function by the cosine term in the phase factor. The values were multiplied by a Gaussian (labeled filter in Figure xx) to produce the convolution accounting for edge blurring. The resulting numerical values were processed using the discrete Cooley-Tukey IFFT. The results are plotted in Figure 11. The resulting square pulse (labeled mod in Figure 11) demonstrates clearly that a rect function with the intended width and offset

: was generated. Usually the frequency domain must be padded with zeros when transforming both with an FFT and an IFT. We found that the zero padding was unnecessary if the frequency domain was calculated purely analytically. The exercise demonstrated that we could carry out the steps properly to compute analytically in the frequency domain, and then transform to the spatial domain with the IFFT.

Since we know the closed analytic form of the Fourier transform of the profile at any desired gantry angle, we can calculate the transform values exactly at every rectilinear grid point in the frequency domain. We have shown above that we can inverse transform an analytically calculated frequency domain distribution back into the spatial domain using the discrete fast Fourier transform. Therefore, we can compute dose distributions by calculating the frequency domain representation analytically and inverse transforming the resulting array to obtain the dose distribution. We can calculate the frequency domain for a fluence distribution produced by a multileaf collimator as a sum of sinc functions for the gaps and offsets produce by the leaves.

We return to the problem of direct computation of the solution to the inversion of the rotation integral for the dose distribution. It is possible to compute this inversion analytically. Formally the process can be described as follows. One computes the projection profiles as the exponential Radon transform of the dose distribution at all projection angles,

$$P^*(x', \theta) = \int_{-\infty}^{+\infty} D_{\theta}(x') e^{\mu y'} dy' = R_{\mu} \{D(x, y)\}$$

One then computes the one-dimensional Fourier transforms of the projection profiles

$$P(u', \theta) = F_1 \{P^*(x', \theta)\}$$

One then filters the transformed profiles

$$P(u', \theta) = K(u') P^*(u', \theta)$$

where $K = \frac{1}{2} |u'| \cdot H(|u'| - \mu/2\pi)$ is a filter function that is related to the conversion to polar coordinates.

The resulting frequency domain array is then inverse transformed to obtain the incident beam profile that will result in the desired dose distribution.

$$P(x', \theta) = F_1^{-1} \{P(u', \theta)\}$$

This process has been applied to the example given in Figure 12. The results are not the same as the intuitive solution. In the center of the field, for $|x| < W/2$, the optimal profile is $D_0/(2\pi) \cdot \cos(\mu r)$. For typical therapy beam energies, $\mu = 0.02/\text{cm}$ and this factor is essentially constant as anticipated. However, beyond the edge of the target volume, the optimal solution is

$$P(r) = \frac{D_0}{2\pi} \left[\cos(\mu r) - \frac{|r|}{\sqrt{r^2 + (W/2)^2}} \cos\left(\mu \sqrt{r^2 + (W/2)^2}\right) \right]$$

This solution takes on negative values and is therefore not feasible to deliver in practice. In the work we propose, we will not try to obtain the profiles by direct inversion of the Radon transforms of the prescribed dose distribution. Instead a search procedure will be investigated that seeks deliverable solutions based on the projections of MLC leaf gaps.

For a gap between two leaves, the fluence distribution is simply the product of rect functions. Consider the beam's-eye-view of a gap between two MLC leaves as in Figure 4.

$$\Phi_l(x', z', \theta) = \Phi_o \Pi\left(\frac{x' - M_l(\theta)}{W_l(\theta)}\right) \Pi\left(\frac{z' - M_l^z}{W_o}\right)$$

where M_l^z is the offset of leaf pair l (a constant for each leaf pair) and M_o is the width of the leaf (in the plane of projection) and is a constant across all leaves of the same width. The function $M_l(\theta) = \frac{1}{2}(x_i^A(\theta) + x_i^B(\theta))$ is the trajectory of the middle of the gap as a function of gantry angle θ . The function $W_l(\theta) = (x_i^B(\theta) - x_i^A(\theta))$ is the width of the gap between the leaves. These two functions constitute the solution sought by the inverse planning process for SWAT. The incident fluence within the cone beam formed by the MLC at a given gantry angle is

$$\Phi(x', z', \theta) = \sum_l \Phi_l(x', z', \theta)$$

The Fourier transform of this function, $F\{\Phi(x', z', \theta)\}$, is well known and is

$$S_o(u', v') = \sum_l W_l(\theta) \sin c(W_l(\theta)u') \cdot W_o \sin c(W_o v') e^{-2\pi i(u'M_l(\theta) + v'M_l^z)}$$

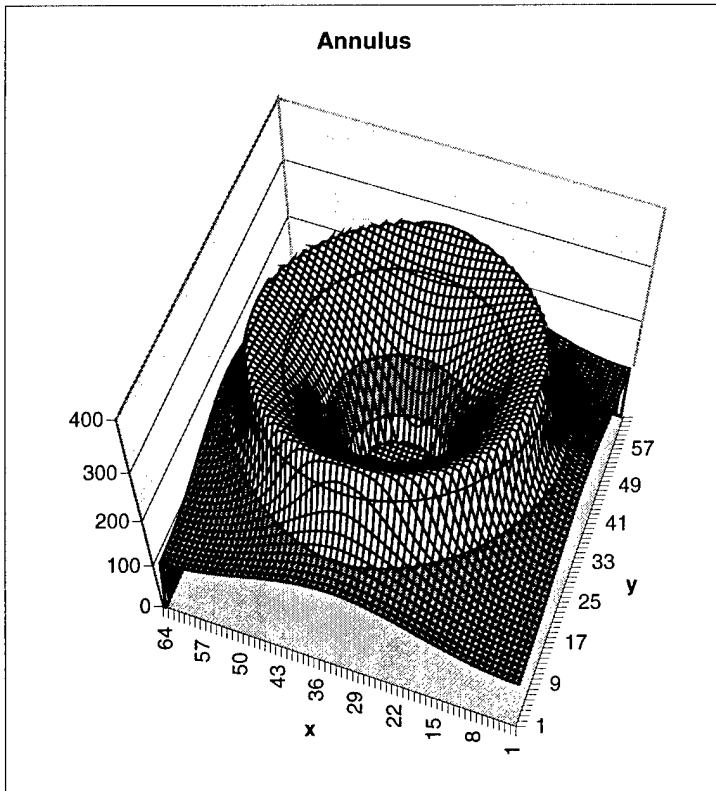


Figure 12. Dose in axial plane in the spatial domain due to a rotated gap. The gap was specified in the frequency domain and then inverse transformed to obtain the results in the figure.

The Fourier frequency domain representation of the MLC leaf trajectory can be calculated using analytic functions directly in the frequency domain without having to transform from the spatial domain. As a consequence, the frequency domain representation of the fluence (and dose) in the spatial domain can be calculated exactly for any point in the frequency domain. This is achieved by calculating the frequency domain profile $P(u', \theta)$ at angles $\theta_{i,j}$ corresponding to profile radii that pass through the rectilinear coordinate points at indices i,j . This allows one to fill the rectilinear space with analytically calculated Fourier transforms. Then one may use the Fourier slice theorem to use a three-dimensional discrete fast Fourier transform to directly calculate the spatial domain fluence (and dose) distribution.

A full three-dimensional calculation model was coded incorporating a three-dimensional IFFT. The parallel beam model was retained for the purposes of preliminary investigations. Sinc functions were generated for gaps

- corresponding the MLC leaves where the direction of the leaf motion was parallel to the axis of rotation. Thus each gap between a leaf pair used a sinc function in the direction of the rotation axis and another sinc function computed in profiles corresponding to the rotation about the axis. The results for an offset gap is shown in Figure 12. The central region out to a radius R_1 is blocked, and the dose rises to a rim at a radius R_2 before falling off as a skirt of dose as expected. This demonstrates that we can calculate the frequency domain representation of a dose distribution for a given MLC leaf configuration during a complete arc rotation.

Optimization in the frequency domain.

Using Fourier transforms is a strategy that has been described in standard texts on optimization theory (Pierre1969). The technique was used by Bortfeld to investigate optimization of beam orientations in the frequency domain (Bortfeld, 1993). The basic approach is the same here. Let the cost function to be optimized be

$$G = \sum_x \sum_y \sum_z [D_p(x, y, z) - D_c(x, y, z)]^2$$

where $D_p(x, y, z)$ is the prescribed dose distribution and $D_c(x, y, z)$ is the calculated dose distribution. Define the Fourier transforms of these dose distributions to be $D_p(u, v, w) = F \{D_p(x, y, z)\}$ and $D_c(u, v, w) = F \{D_c(x, y, z)\}$. Using these functions one can define a cost function in the frequency domain,

$$G = \sum_u \sum_v \sum_w [D_p - D_c]^2$$

The advantage of calculating the cost function in the frequency domain is that one may cut off the sum used to calculate G at some low frequencies, $u_{cut}, v_{cut}, w_{cut}$, e.g.

$$G \cong \sum_{u=1}^{u-cut} \sum_{v=1}^{v-cut} \sum_{w=1}^{w-cut} [D_p - D_c]^2$$

Demonstration that optimization in the frequency domain is equivalent to optimization in the spatial domain.

We now demonstrated the proof of the principle that optimization in the frequency domain yields the same results as optimization in the spatial domain for a simple example. In the example in Figure xx, we sought the width of a rect function that would minimize the least square difference between itself and a Gaussian with a

fixed σ . The cost function in the frequency domain was constructed from the analytic forms of the Fourier transforms of the rect function and the Gaussian function. Functions were chosen with known analytic Fourier transforms. The frequency domain cost function was

$$G = \sum_s \left[\frac{\sin(\pi \cdot W u)}{\pi u} - \sqrt{2} \sigma e^{-(2\pi\sigma^2 u^2)} \right]^2$$

The corresponding cost function in the spatial domain cost function was

$$G = \sum_x \left[\Pi\left(\frac{x}{W}\right) - e^{-\frac{\pi}{2}\left(\frac{x}{\sigma}\right)^2} \right]^2$$

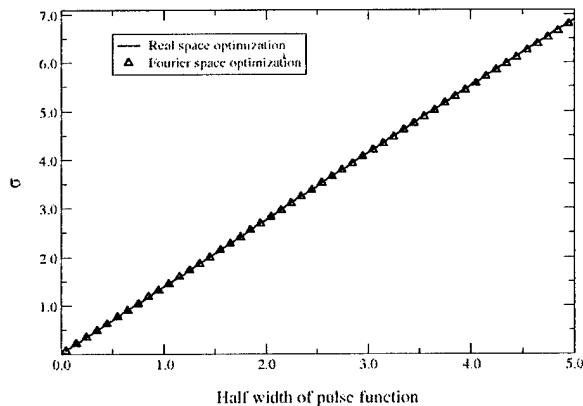


Figure 13. Precisely the same rect function width W was obtained in both the spatial and frequency domains.

A parabolic search algorithm was used to find the value of

W that minimized the cost functions in each domain for a range of values of the variance of the Gaussian function. The results are given in Figure 13. Precisely same values of the rect function widths were obtained by independent optimizations in both domains, as Parsaval's theorem predicts.

Demonstration that optimization need only be carried out for low frequencies.

This principal can be demonstrated using the same simple example as above. The Gaussian and rect functions are to be made as similar as possible as measured by the least squares cost function. In this second example, both the width and the height of the rect function were taken as variable parameters. This provided a two-dimensional search space with a minimum as shown in Figure 14. The optimal widths and amplitudes of the rect function were determined in both the frequency and spatial domains and were found to be the same consistent with the previous section. The calculation was then repeated in the frequency domain restricting the summation to ever decreasing cut-off limits.

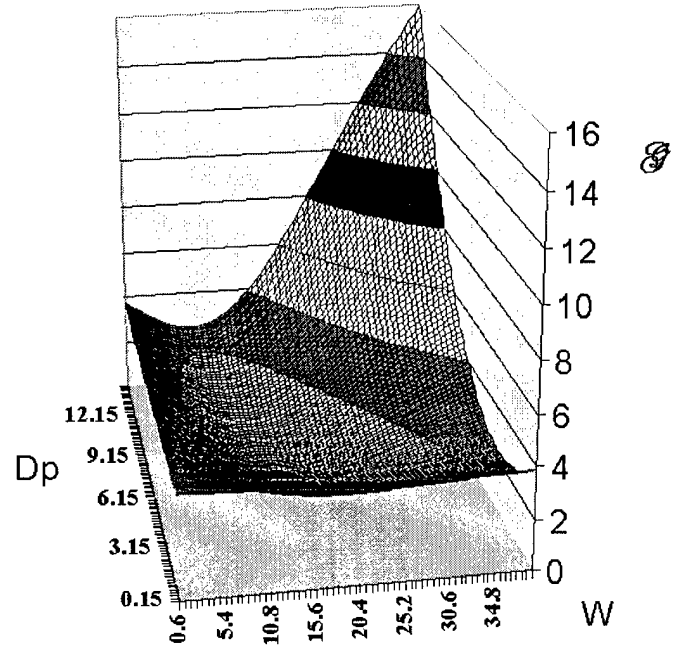


Figure 14. Cost function computed in the frequency domain as function of rect function amplitude (D_p) and width (W).

$$G = \sum_s^{s-cut} \left[\frac{\sin(\pi \cdot W s)}{\pi s} - \sqrt{2} \sigma e^{-(2\pi \sigma^2 s^2)} \right]^2$$

The results are plotted in Figure 15. Figure 15 demonstrates that as the upper limit of the summation over the frequency domain, s-cut, was lowered from 128 (the size of the frequency domain array used in this case) to

about 32, the results of the search for the optimum values of W and D_p (the minimum in Figure 13) remained fairly stable. This suggests a search strategy that begins iteratively optimizing the treatment parameters with very low cutoff frequency. If one starts with $1/4$ of each frequency domain axis or about 1.5% of the frequency domain volume, the search time will be reduced by a factor of approximately 100. As one approaches a final optimal value, the cut off frequency can be gradually raised to refine the precision of the final optimization parameters. By eliminating summation over a substantial volume of the frequency domain each time G is recomputed in the iterative search for its minimal value, a substantial savings in computation time can be realized. Once the final values of the leaf trajectories are computed, a final dose calculation will be carried out in the spatial domain using a Monte Carlo calculation.

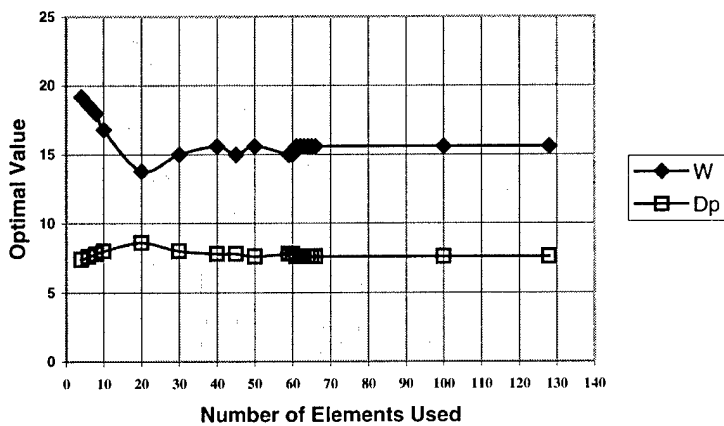


Figure 15. Demonstration of the stability of the optimization with an increasingly lower cutoff frequency, s_{cut}

substantial savings in computation time can be realized. Once the final values of the leaf trajectories are computed, a final dose calculation will be carried out in the spatial domain using a Monte Carlo calculation.

Conclusions

A line of investigation is described here that offers a strategy to seek means to plan and deliver IMRT more rapidly and efficiently than current methods using a continuous arc. The sweeping window produces a dose distribution within an unmodulated volume that is nearly the same as that produced by a Takahashi arc. However, the sweeping window offers opportunities to modulate the dose distribution at many angles to either shield structures or add dose to improve homogeneity within the target. Optimization of the gaps used in the arcs can be carried out by standard optimization methods. Optimization in the frequency domain may offer an opportunity to increase the computation speed. The efficacy of the ideas must be tested by developing the methodology and comparing the results with techniques presently in use. A definitive comparison cannot be made without first developing the SWAT technique to approximately the same level of sophistication as the fixed gantry and tomotherapy methods currently in use.

References

- Bortfeld T, Schlegel W (1993). Optimization of beam orientations in radiation therapy: some theoretical considerations. *Phys. Med. Biol.* 38:291-304.
- Bortfeld T, Boyer AL (1995). The exponential radon transform and projection filtering in radiotherapy planning. *Intl. J. of Imaging Systems & Tech.*, Vol. 6, 62-70.
- Brahme A, Roos JE, Lax I (1982). Solution of an integral equation in rotation therapy. *Phys. Med. Biol.* 27:1221-1229.
- Cormack AM. (1987) A problem in rotation therapy with x-rays. *Int. J. Radiat. Oncol. Biol. Phys.* 13:623-630.
- Cormack AM, Cormack RA (1987). A problem in rotation therapy with x-rays: Dose distributions with an axis of symmetry. *Int. J. Radiat. Oncol. Biol. Phys.* 13:1921-1925.
- Desobry GE, Wells NH, Boyer AL (1991). Rotational kernels for conformal therapy. *Medical Physics* 18(3):481-487.
- Oelfke U, Bortfeld T (1999). Inverse planning for x-ray rotation therapy: a general solution of the inverse problem. *Phys. Med. Biol.* 44: 1089-1104.
- Pierre D (1969). *Optimization Theory with Applications* (New York: Dover Publications, Inc).
- Takahashi S. Conformation radiotherapy (1965). rotation techniques as applied to radiography and radiotherapy of cancer. *Acta Radiol. Suppl.*;242:1-4.
- Webb S (2001). *Intensity-Modulated Radiation Therapy* (Bristol and Philadelphia: Institute of Physics Publishing).
- Yu CX (1995). Intensity modulated arc therapy with dynamic multileaf collimation : an alternative to tomotherapy. *Phys. Med. Biol.* 40:1435-1449.
- Xia P, Geis P, Xing L, Ma C, Findley D, Forster K, Boyer AL (1999). Physical characteristics of a miniature multileaf collimator. *Med. Phys.* 26(1):65-70.

A MULTILEAF COLLIMATOR FOR MODULATED ELECTRON RADIATION THERAPY (MERT) FOR BREAST CANCER

Yulin Song¹, Steve B. Jiang², Michael C. Lee¹, C-M Charlie Ma³, and Arthur. L. Boyer¹

*Departments of Radiation Oncology,
¹Stanford University School of Medicine, Stanford, CA 94305*

*²Massachusetts General Hospital
Harvard Medical School, Boston, MA 02114*

³Fox Chase Cancer Center, Philadelphia, PA 19111

E-mail: yulin@reyes.stanford.edu

Results from recent clinical trials have shown that irradiation is an effective adjuvant therapy to lumpectomy, mastectomy, and chemotherapy for breast cancers of different stages. However, the conventional tangential photon beam treatment has two major limitations. Firstly, part of the lung and heart (in the case of the left breast treatment) may be exposed to high radiation dose. Secondly, the contralateral breast may receive a significant amount of scatter dose. Consequently, irradiation-related complications such as arm edema, myocardial infarction, severe breast fibrosis, and secondary breast cancer may occur in the patients who have undergone conventional photon beam treatment. To reduce radiation dose to normal structures and, thus, the complications, we have investigated treating breast cancers using modulated electron radiation therapy (MERT), making use of the rapid depth dose falloff characteristics of electron beams. To deliver MERT plans effectively, we designed and manufactured a prototype electron multileaf collimator (EMLC). The performance of the EMLC was experimentally evaluated and the results were compared with those of Monte Carlo simulations.

Based on the results of Monte Carlo simulations, an experimental EMLC was fabricated by modifying a conventional 25 x 25 cm² electron cone (Varian Medical Systems, Palo Alto, CA). The EMLC consisted of 30 steel leaf pairs, with each leaf being 0.476 cm wide, 20.0 cm long, and 2.54 cm thick. The maximum opening was 14.2 x 15.5 cm² when all leaves were completely retracted, giving the largest radiation field of 15.0 x 16.3 cm² projected at 100 cm source-surface distance (SSD). Film dosimetry was performed at energies of 6, 12, and 20 MeV in a solid water phantom to evaluate the quality of the electron beams collimated by the EMLC. Based on the manufacturer's specifications of the beam production system and the EMLC design, the electron beams were also simulated using the EGS4/BEAM code. MERT plans for breast cancer with five nominal energies (6, 9, 12, 16, and 20 MeV) were created using modified EGS4/MCDOSE code. The calculated doses were checked against a commercially available Monte Carlo dose calculation engine (NXEGS, NX Medical Software LLC, New York, NY) and measurements. The MERT plans were also compared with x-ray intensity-modulated radiation therapy (IMRT) in terms of target coverage and normal tissue sparing.

Our results showed that there was an excellent agreement between the film measurements and the Monte Carlo simulated data at all electron energies in terms of dose distribution. We found that the EMLC provided significant improvements in dose penumbras and field resolution as compared to the photon MLC. We also found that MERT was able to provide similar or better target dose coverage compared with x-ray IMRT. However, MERT could significantly reduce the dose to critical structures.

We conclude that EMLC was able to provide sufficient beam collimation for MERT and for superficial targets, such as breast cancers, MERT showed excellent target coverage and normal tissue sparing.

This work was supported in part by The U.S. Army Medical Research and Materiel Command under DAMD17-00-1-0443 and NX Medical Software LLC, a subsidiary of NumeriX LLC.

COMBINING ELECTRON WITH INTENSITY MODULATED PHOTON BEAMS FOR BREAST CANCER

Lei Xing¹, Jonathan G. Li², Yulin Song¹, David Y. Yang¹, Don Goffinet¹, and Arthur L. Boyer¹

*Departments of Radiation Oncology,
¹Stanford University School of Medicine, Stanford, CA 94305-5304
²University of Florida
Gainesville, FL 32610-0385*

E-mail: lei@reyes.stanford.edu

Radiation therapy following removal of the tumor (lumpectomy) is accepted as an effective treatment modality in the management of both invasive and non-invasive breast cancer. Radiation therapy also plays an important role in the multi-modality management of locally advanced or inflammatory breast cancer as well as in the treatment for women with medial lesions and positive axillary nodes and those patients undergoing adjuvant bone marrow transplantation. With an increasing incidence of breast cancers and with the advantage of breast preservation, more women are choosing lumpectomy and radiation treatment as an alternative to mastectomy. In practice, however, there are many reports indicating undesired radiation effects in the intra-thoracic structures (such as the heart, lung and ribs) and risk of second cancers in the contra-lateral breast. A more effective radiation treatment method to reduce the dose to the sensitive structures is thus clinically important. In this work we report development of a breast cancer treatment technique using the combination of conventional electron beam(s) and intensity modulated photon beams.

In the stated treatment technique, an electron beam with appropriate energy was combined with 2 to 4 intensity modulated photon beams. An iterative algorithm was developed which optimizes the weight of the electron beam as well as the fluence profiles of the photon beams for a given patient. Three breast cancer patients with early-stage breast tumors were planned with the new technique and the results were compared with those from 3D planning using tangential fields as well as 9-field intensity-modulated radiotherapy (IMRT) techniques. The combined electron and IMRT plans showed better dose conformity to the target with significantly reduced dose to the ipsilateral lung, and in the case of the left-breast patient, reduced dose to the heart, than the tangential field plans. In both the right-sided and left-sided breast plans, the dose to other normal structures was similar to that from conventional plans and was significantly smaller than that from the 9-field IMRT plans. The optimized electron beam provided between 70% to 80% of the tumor dose at d_{\max} of the electron beam.

In summary, the use of electron provides an effective method to limit the exit dose from the adjacent sensitive structures and the combined electron and IMRT technique showed significant improvement over the conventional treatment technique using tangential fields with markedly reduced dose to the ipsilateral lung and the heart. Optimization of the composite treatment may result in highly conformal radiation doses to the primary tumor target volume while significantly reducing doses to the normal structures and therefore minimizing side effects. This combination provides a unique opportunity to take advantage of the two types of radiation and to produce conformal dose distributions that would otherwise be impossible and has the potential to improve significantly the way that the breast cancer is treated and to avoid or greatly reduce the treatment complications and side effects.

This work was supported in part by The U.S. Army Medical Research and Materiel Command under BC996645.

In the second case, a familiar interface to more arcane devices (e.g. digitizers) motivates the WWW-DICOM interface for the creation of teaching files. Since it is straightforward to Save a Web page or image, window width and center controls, together with zooming and grayscale inversion perhaps, can be applied until a satisfactory image is presented. This image may be saved at a much reduced capacity compared to the original. Thus, multi-image teaching files may be built without immediate storage problems.

[1] McColl R, Lane T. The DICOM-WWW gateway: implementation, configuration, security and privacy. *Medical Physics* 25(7):A216, 1998.

Continuing Education Course MRI - 3

Room: Taylor

TU-C5-01

Acceptance Testing of MRI Systems

Edward Jackson, U.T. M.D. Anderson Cancer Center, Houston, TX

Suggested elements of a general acceptance testing procedure for MRI systems will be presented. Specific tests of each subsystem, including the static magnetic field, gradient magnetic field subsystem, radiofrequency field subsystem, and computer systems, will be discussed. Available published guidelines for acceptance testing will be reviewed and acceptance criteria from such guidelines will be presented. Additional tests and acceptance criteria required for evaluating the performance of modern high-speed MRI scanners will also be suggested.

While the large diversity in capabilities of scanners from various vendors precludes the presentation of a single comprehensive acceptance test procedure, generalized testing procedures for all major subsystems using phantoms that are easily manufactured or commercially available to clinical medical physicists will be described. Acceptance tests that are difficult, or impossible, for typical practicing clinical medical physicists to independently perform without assistance of the vendor's installation or field service engineers will also be discussed, along with suggested approaches to incorporate vendor tests with independent evaluations.

Educational Objectives:

The clinical medical physicist will understand and be prepared to implement a general acceptance testing procedure that will evaluate all major subsystems of modern MRI scanners.

Upon completion of this course, participants will be prepared to:

1. Understand the tests needed to evaluate the performance of the static magnetic field, gradient magnetic field, radiofrequency field, and computer subsystems.
2. Understand typical acceptance criteria.
3. Develop a set of acceptance tests and acceptance criteria that are specific to the capabilities of the MRI system to be evaluated.
4. Determine the feasibility of measuring specific acceptance test parameters independently as opposed to using evaluation tools provided by the vendor to its installation and/or field service engineers.

Scientific Session

Room: Pearl

Calculations - Treatment Planning

TU-D1-01

Clinical Validation of a Monte Carlo Dose Calculation Tool for Radiotherapy Treatment Planning

JS Li*, T Pawlicki, J Deng, SB Jiang, A Kapur, E Mok, C-M Ma, Stanford University School of Medicine, Stanford, CA

A Monte Carlo program, MCDOSE, was developed at Stanford for radiotherapy treatment planning (RTP). MCDOSE was designed as a dose calculation module for easy implementation into any RTP system. We have implemented MCDOSE on an existing commercial RTP system for conventional photon/electron beams and intensity modulated radiotherapy (IMRT) dose verification. Features of MCDOSE included a multiple-source model to reconstruct the beam phase space, inclusion of beam modifiers

such as jaws, wedges, blocks, electron cutouts and bolus in the patient simulation, and the implementation of several variance reduction techniques. Vigorous testing and clinical commissioning of MCDOSE has been carried out. Photon and electron dose calculations using MCDOSE were tested for two Varian accelerators, a Clinac 2100C and a 2300C/D. Comparisons of the dose distributions for 4-15 MV photons and 6-20 MeV electrons calculated by MCDOSE and the well-benchmarked EGS4 user code DOSXYZ showed excellent agreement (within statistical uncertainty of 0.3%). The CPU time for a given calculation was generally a factor of 10 less for MCDOSE compared to DOSXYZ. The MCDOSE calculated heterogeneity correction factors for layered-lung or layered-bone phantoms were consistent with results from measurement to within 1%. Specifically designed inhomogeneous phantoms were used to test MCDOSE computed IMRT plans. The results showed that the dose calculated by MCDOSE agreed to within 3% measured results while the dose to critical structures was underestimated by a commercial inverse planning system by up to 100%.

TU-D1-02

Beam Characterization and Modeling for Photon Monte Carlo Treatment Planning

J Deng*, S Jiang, A Kapur, J Li, T Pawlicki, C Ma, Stanford University School of Medicine, Stanford, CA

Photon beams of 4, 6, and 15 MV from Varian Clinac 2100C and 2300C/D accelerators were simulated using the EGS4/BEAM system. The accelerator was modeled as a combination of component modules (CMs) consisting of a target, primary collimator, flattening filter, monitor chamber, mirror and jaws. A full phase space file was scored directly above the upper jaws and analyzed using a program, BEAMDP (BEAM Data Processor), to derive the particle planar fluence, angular distribution, energy spectrum and the fractional contributions of each individual CM. A multiple sub-source model was further developed to reconstruct the phase space. Separate sub-sources were used for the target, primary collimator and flattening filter components with accurate source intensity, energy, fluence and angular distributions. Good agreement (within 2%) was achieved in the dose distributions for field sizes 2 cm x 2 cm - 40 cm x 40 cm and source surface distances 80 cm - 120 cm between the Monte Carlo calculations with the source model and those with the original phase space, and measurements. The source model was implemented in an EGS4 user code, MCDOSE, for photon beam Monte Carlo treatment planning, which computes the dose distributions in a 3D rectilinear phantom built from the patient CT data and simulates the effect of beam modifiers such as wedges, multileaf collimator and blocks. The source model was also employed in the Monte Carlo beamlet profile calculation for inverse planning for intensity modulated radiotherapy (IMRT).

TU-D1-03

Experimental Validation of Dose Calculation Algorithms for the GliaSite (TM) RTS, a Novel ¹²⁵I Liquid-Filled Balloon Brachytherapy Applicator

J Monroe*, J Dempsey, J Dorton, S Mutic, J Markman, J Williamson, Washington University, Mallinckrodt Institute of Radiology, St. Louis, MO

We present the experimental validation of dose calculation algorithms for a novel ¹²⁵I liquid-filled brachytherapy balloon applicator (the GliaSite RTS) designed for the treatment of malignant brain-tumor resection-cavity margins. A solid water phantom machined for catheter conformity (verified by Computed Tomography (CT) imaging) was used to perform absolute low dose-rate radiochromic film (RCF) measurements in coronal planes about the applicator. The results were used to validate Monte Carlo photon transport (MCPT) simulations and a point-source dose-kernel model algorithm. Densitometry of RCFs employed a validated optical densitometry system with an artifact elimination process. The absolute activity of the ¹²⁵I solution was determined by inter-comparing a National Institute of Standards and Technology (NIST) ¹²⁵I standard with a known mass of radiotherapy solution (IotrexTM) in an identical vial and geometry. Agreement between RCF and MCPT was found to be within $\pm 5\%$. This significantly improves upon earlier reports of absolute RCF film dose measurements about ¹²⁵I sources. Agreement between the simple semi-empirical dose-kernel model and the MCPT and, by extension between the RCF measurements and semi-empirical model, was better than 5% except very near the applicator surface where 8-10% discrepancies were observed.

Measurement also confirmed no dose-distribution deviation from equatorial isotropy as predicted.

This work was supported by a grant from Proxima Therapeutics Inc.

TU-D1-04

CT-Guided Brachytherapy Using a Correlated 3D Stereotactic Arm

J Hevezi*, J Mira¹, J Marbach, S Chopra², R Vasquez³, (1)Cancer Therapy & Research Center, San Antonio, Texas, (2)University of Texas Health Science Center, San Antonio, Texas, (3)SW Texas Methodist Hospital, San Antonio, TX

Several patients have been treated on an outpatient basis implanting I-125 seeds under CT guidance for recurrent disease. The coordinates for the seed implantation sites are preplanned using the patient's CT data set. On implant day, the I-125 seeds are inserted through a needle guide with the Mick applicator. The interventional radiologist (RV,SC) uses a local anesthetic along the needle tracks and requires multiple CT slices to follow the needle trajectories to the preplanned coordinates. Needle tracks are optimized on the preplan to deposit multiple seeds along each track. An average of 10 seeds were deposited in our first 8 patients. Recurrent paraspinal tumors post full-course radiotherapy were the most frequent case encountered. Recently, a 3D stereotactic arm attached to the CT scanner (PQ5000, Picker International) and correlated in space with the CT data set has been used to locate needle trajectories and seed deposit coordinates. The patient must be immobilized in the treatment position for the preplan data set and aligned to this position for the implant procedure. Postplans after seed deposition have correlated well with the preplan dose distribution. Several methods are being evaluated to test the congruence postplan to preplan including interseed distance matrices and dose-volume histograms.

TU-D1-05

Incorporating Organ Motion Due to Breathing into 3D Dose Calculations: Sensitivity to Variations in Motion

A Lujan*, R Ten Haken, J Balter, E Larsen, University of Michigan, Ann Arbor, MI

We have previously described a method to incorporate the effects of organ motion due to breathing into 3D dose calculations for treatment of liver disease. This method uses an analytic function to describe inferior-superior liver motion during free breathing. Although periodic, each cycle is generally asymmetric, with the majority of time spent near the exhale position. Our analytic function includes parameters that describe the amplitude (exhale to inhale) of the motion and the degree of asymmetry (time at exhale relative to inhale). Representative parameter values are selected by observation for each patient. However, these parameters may vary from the representative values over the course of treatment (e.g. patient may take a few deep breaths over the course of treatment). This study demonstrates the effects such variations may have on the predicted outcome in dose. Monte Carlo-based direct simulations were used to compute 3D dose distributions that included the effects of liver motion due to breathing. The amplitude and/or shape of the breathing cycle function was changed from the representative values for various fractions of the total treatment. The significance of differences in the liver dose distribution was judged by changes (if any) in our normal tissue-based protocol for prescribing dose. Quantification of these effects will be useful in directing future efforts in describing and controlling organ motion due to breathing.

Work supported by NIH grant no. P01-CA59827 and the Sidney Kimmel Foundation

TU-D1-06

A Multiple Source Model for Monte Carlo Photon Dose Calculations in Radiotherapy

M Fix*, M Stampanoni, H Keller¹, E Born, R Mini², P Rueggsegger¹, (1)Institute for Biomedical Engineering and Medical Informatics, ETH Zurich, Switzerland, (2)Division of Med. Radiation Physics, Clinic of Radio-Oncology, Inselspital-University of Berne, Switzerland

A multiple source model (MSM) for MC dose calculations in radiotherapy was developed for the 6 MV photon beam of a Varian Clinac 2300 accelerator. The MSM consists of 12 planar and linear sources representing the main elements of the beam defining system. The characteristics of the sources for all square fields were extracted from phase space data resulting from MC simulations of the radiation transport through the treatment head for a set of square fields.

Using the MSM, phase space data, depth doses, lateral dose profiles and output factors were calculated and compared to measured data or to the original phase space data, respectively. Comparison of the depth dose curves at the depth of 10 cm showed deviations of less than 2% for all field sizes. The lateral dose distributions and the reconstructed phase space data showed good agreement with the measurements or original data, respectively. Also, the deviations between measured and calculated output factors for 10 cm water depth were less than 2%.

In summary, the MSM showed good agreement between measured and calculated data for square fields. The MSM has the potential to characterize more complex geometries for MC photon dose calculations.

TU-D1-07

The Generalization of a Photon Pencil Beam Algorithm for Electron Beam Dose Calculations

E Wong*, G Garvey¹, J Cunningham², J Sun², J Van Dyk¹, J Battista¹, (1) London Regional Cancer Centre, London, ON, Canada, (2) Theratronics, Kanata, ON, Canada

The semi-empirical pencil beam dose calculation algorithm for photon beams based on Scatter-Air-Ratios (SAR) has become the conceptual basis for dose computation in some modern treatment planning systems. For electron beams, the adoption of the SAR algorithm was first proposed by Dutreix et al. and more recently by re-introduced by Cunningham. This provides the possibility of using the same photon beam codes for electron dose calculations. Perhaps, the most deterring factor in such application is the ambiguity of Peak-Scatter-Factor or zero area Tissue-Air-Ratio concepts for electron beams. In contrast, the most widely used algorithm for electron beams in treatment planning was devised by Hogstrom. It is the solution to a superposition integral in which the kernel describes the spatial spread of dose from a pencil beam incident on the surface of a phantom. Hogstrom's formulation is based on Eyges whose analytical solution had a number of simplifying assumptions. The SAR algorithm on the other hand does not contain such assumptions. In this work, we expressed the SAR algorithm in the nomenclature of Hogstrom's analytical solution and defined the Peak Scatter Factor and zero area Tissue-Air-Ratio. We compared the kernels used in the two formalisms and their dose predictions against measurements made in water and inhomogeneous phantoms at different energies. We conclude that SAR and the Hogstrom formalism are similar in concept and performance, their difference lies in how the kernels are obtained.

TU-D1-08

Electron Beam Modeling and Commissioning for Monte Carlo Treatment Planning

S. B. Jiang*, A. Kapur, C.-M. Ma, Stanford University School of Medicine, Stanford, CA

A hybrid approach for commissioning electron beam Monte Carlo treatment planning systems is studied. The approach is based on the assumption that accelerators with similar designs have similar electron beam characteristics. For one type of accelerators, a reference machine is selected and simulated with the Monte Carlo method. A beam model, which is based on a multiple source model, is built for this type of accelerators using the Monte Carlo simulated phase space information for the reference machine. When commissioning another accelerator of the same type, the appropriate